UNDERSTANDING THE COMPOSITIONAL AND STRUCTURAL DRIVERS GOVERNING THE AQUEOUS CORROSION OF MULTICOMPONENT OXIDE GLASSES

By

NICHOLAS M. STONE-WEISS

A dissertation submitted to the

School of Graduate Studies

Rutgers, The State University of New Jersey

In partial fulfillment of the requirements

For the degree of

Doctor of Philosophy

Graduate Program in Materials Science and Engineering

Written under the direction of

Ashutosh Goel

And approved by

_____

_____

_____

_____

New Brunswick, New Jersey

May, 2020

ABSTRACT OF THE DISSERTATION

Understanding the Compositional and Structural Drivers Governing the Aqueous Corrosion of Multicomponent Oxide Glasses

by NICHOLAS M. STONE-WEISS

Dissertation Director:

Ashutosh Goel

The chemical durability of glass is a topic that, while being actively important for identifiable applications such as nuclear waste containment and bioactive glasses, is imperative to understand for predicting the long-term performance of both everyday and cutting-edge technological glass applications. Multicomponent glasses containing multiple network-forming oxides (i.e. SiO_2, B_2O_3, Al_2O_3, P_2O_5) comprise the vast majority of technologically-relevant glasses whose behavior in surrounding chemical environments must be well-predicted. These glasses, however, typically have significant compositional and structural complexity which complicates the development of straightforward models to understand their chemical durability. Given the intricacy of this topic and its multifaceted importance for technological glass applications, it is vital to move from an understanding based upon simple composition-dependent models to those based upon *composition-structure-property* relationships. The necessity for a deeper knowledge of this topic has been propelled by the notion that understanding the relationships between the

glass chemistry and their structure at the atomic level will help us in unearthing the fundamental mechanisms of glass corrosion. Based on this viewpoint, this research aims to elucidate the fundamental science governing the aqueous corrosion of multicomponent oxide glasses. With this goal in mind, this research focuses on understanding *composition-structure-chemical durability* relationships in simplified ternary and quaternary glass systems and addressing some of the remaining fundamental challenges / open questions relating to glass corrosion. Accordingly, glasses designed in the Na_2O-B_2O_3-SiO_2, Na_2O-Al_2O_3-B_2O_3-SiO_2, and Na_2O-P_2O_5-B_2O_3-SiO_2 systems have been the subject of this research.

Dissolution studies of sodium borosilicate glasses indicate that thermal history dictates the glass structure and dissolution rate, as the methodology used to quench the glass was shown to impact the dissolution rates by 1.5× to 3×, depending on the composition and molecular structure variations. Studies of the corrosion behavior of wide-ranged sodium aluminoborosilicate glass compositions in acidic environments display that stepwise B_2O_3 substitutions into nepheline ($NaAlSiO_4$) glass, although causing non-linear changes in glass structure network structural features, lead to strikingly linear increases in the forward dissolution rate in acidic environments resulting from similar aqueous corrosion mechanisms. The strengths of MAS NMR and MD simulations converge to develop an in-depth understanding of the short- and intermediate-range structural features in the sodium borosilicate and sodium phospho-borosilicate glass systems. Furthermore, through careful compositional design in these systems, it is shown that the structural drivers of glass dissolution can be uncovered, which can be applied to develop novel borosilicate bioactive glasses with controlled ionic release. Studies on a sodium borosilicate glass

dissolved in multiple solution environments display that buffer solution chemistry impacts dissolution behavior, where kinetics are controlled by acid/buffer composition in the solution. Future work recommended for this topic involves (i) the development of quantitative structure-property relationships (QSPR) from further exploration of the chemical durability of complex mixed network-former glasses and (ii) understanding the kinetics and fundamental mechanisms of glass corrosion from *in situ* studies or high-resolution examination of the reactive interface/gel layers.

Keywords: Bioactive glass; Dissolution; Thermal history; Structure; Chemical durability; Solution chemistry

Acknowledgments

This experience completing my Ph.D. has been extremely fulfilling and full of great experiences which I will never forget. It has been, without a doubt, the most challenging feat of my life, but I would not trade any of the experiences I have had for anything. Through my Ph.D. I feel that I have been able to grow tremendously, as a researcher, student, mentor, professional, etc. These accomplishments, however, would never have taken place without the amazing people around me during my time at Rutgers. First, I would like to graciously thank my advisor, Dr. Ashutosh Goel, for giving me the opportunity to develop under his guidance, for aiding me when I ran into problems, for believing in me, and for providing me with many great opportunities to learn and to develop as both a student and person. The accomplishments that I have made during my Ph.D. would definitely not have been possible without your help and guidance.

Furthermore, I would like to thank all of the amazing people I have had the pleasure of meeting and working with during my Ph.D., at Rutgers, in São Carlos, and through the countless contributions via scientific collaborations which have made many of my accomplishments possible. In particular, I would especially like to thank everyone I worked with while in Prof. Goel's group at Rutgers, you all have been amazingly supportive helpful, and kind through all the ups and downs of grad school. I have definitely made a lot of connections while here that I will always remember and cherish. I would like to also thank Prof. Hellmut Eckert and his students, who graciously accepted me as a visiting Ph.D. student in their lab in Brazil, from which I was able to learn tremendously and gain invaluable experiences. I would like to particularly thank collaborators Dr. Randall Youngman and Dr. Nicholas Smith from Corning, as well as Dr. Eric Pierce from ORNL,

who have all been consistently very helpful and supportive throughout my Ph.D. My studies here at Rutgers would not have been possible without all the support and guidance from the professors, fellow students, staff, administrators, etc., particularly Bob Horvath, Arya Tewatia, Ross Rucker, Dr. Lehman, Dr. Klein, Dr. Mann, Dr. Akdogan, Nahed Assal, Sheela Sekhar, as well as countless others.

I would not be to the place I am today without all the love and support from my family and friends. Above all, I would like to especially thank my parents for the opportunities they have given me, the undying support they have had during my life, and the belief they always had in me to be successful and pursue what I enjoyed most in life.

Dedication

This thesis is dedicated to my parents.

Table of Contents

List of Abbreviations

BO – **B**ridging **o**xygen

CP – **C**ross **p**olarization

DSC – **D**ifferential **s**canning **c**alorimetry

ERDA – **E**lastic **r**ecoil **d**etection **a**nalysis

INADEQUATE – **I**ncredible **n**atural **a**bundance **d**oubl**e qua**ntum **t**ransf**e**r

MAS – **M**agic **a**ngle **s**pinning

NBO – **N**on-**b**ridging **o**xygen

NMR – **N**uclear **m**agnetic **r**esonance

REAPDOR – **R**otational **e**cho **a**diabatic **p**assage **do**uble **r**esonance

REDOR – **R**otational **e**cho **do**uble **r**esonance

RBS – **R**utherford **b**ackscattering **s**pectrometry

SEM-EDS – **S**canning **e**lectron **mi**croscopy – **e**nergy **d**ispersive **s**pectroscopy

XPS – **X**-ray **p**hotoelectron **s**pectroscopy

XRD – **X**-**r**ay **d**iffraction

List of Figures

List of Tables

Chapter 1. Introduction

1.1 Significance of understanding the chemical durability of glasses

The chemical durability of glass is a topic that, while being actively important for identifiable applications such as nuclear waste containment and bioactive glasses, is imperative to understand for predicting the long-term performance of both everyday and cutting-edge technological glass applications.[1] Multicomponent glasses containing multiple network forming oxides (i.e. SiO_2, B_2O_3, Al_2O_3, P_2O_5) comprise the vast majority of technologically-relevant glasses whose behavior in surrounding chemical environments must be well-predicted, given their use in a wide range of commercial glasses which may necessitate either inherently high chemical durability or carefully controlled dissolution behavior.[2-7] These glasses, however, can have significant compositional complexity due to their ability to incorporate many different components into their structure, where each component contributes its part to the glass structure and resulting aqueous corrosion behavior. For this reason, a progression in the understanding of the chemical dissolution behavior of glasses in aqueous solutions has proceeded from simple *composition* dependent (analytical or geochemical) models[8-12] to those based on *composition-structure-property* relationships.[13-17] This evolution has been propelled by the notion that understanding the relationships between the chemical composition of glasses and their structure at the atomistic level will help us in unearthing the fundamental mechanisms of glass corrosion. However, despite the ongoing strenuous effort in this direction, our predominant reliance on empirical data from literature does not currently put us in a position to develop scientifically robust and statistically accurate models to predict the chemical dissolution behavior of glasses. This may be attributed to the fact that individual investigations have

approached these problems with specific aims that are best suited for their targeted application and desired goals (i.e. biological for bioactive glasses and geochemical for nuclear waste glasses). This divergence in approach does not facilitate the creation of a holistic dataset in which predictive models of glass corrosion can be developed which elucidate composition-structure-chemical durability relationships in multicomponent oxide glasses. Thus, it is imperative to generate comprehensive glass dissolution datasets across a wide composition-space which can provide the basis for predictive model development, and can in turn facilitate and significantly expedite the process of designing novel glasses and chemical treatments (i.e. chemical strengthening and isochemical etching).[1]

1.2 Current understanding of the basic mechanisms controlling aqueous corrosion of glasses

As glass is brought in contact with aqueous solutions, several physico-chemical processes occur simultaneously near the glass-fluid interface and in solution. Early models by Boksay[18] and Doremus[19] in the 1960s and 1970s, respectively, which discussed silicate glass–water interactions were based on diffusion kinetics and focused on developing a more quantitative description of alkali release and the elemental concentration profiles in the hydrated layers as observed in aqueous corrosion experiments. Although these early models described the inter-diffusion process well for simple alkali silicate glasses, the application of a simplified diffusion kinetics model for describing the elemental release behavior of multicomponent silicate glasses has not been successful. Since then, a considerable and dedicated effort has been made to understand the kinetics and governing mechanisms of glass corrosion. Silicate glasses, which are undoubtedly the most well-

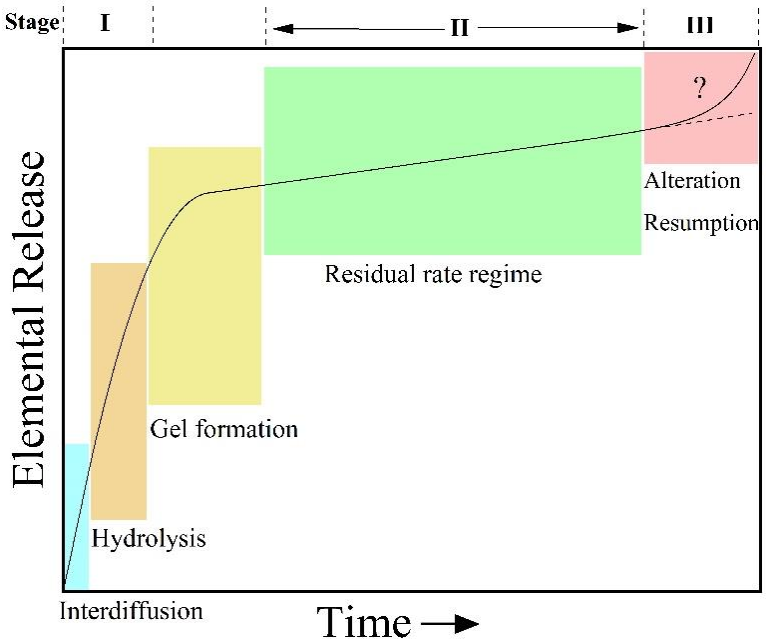

Figure 1.1. *Elemental release profile over time for typical silicate glasses*

studied oxide glass system, are observed to exhibit two (or sometimes three) main stages of dissolution (as displayed in Figure 1): (I) forward rate regime, marked by rapid linear elemental release, and (II) residual rate regime, characterized by slow, steady release from the glass.[20,21] Stage III, which only occurs in rare scenarios/conditions, involves a sudden resumption and acceleration in elemental release behavior. These kinetic trends are observed in most glasses, however, there is still no complete consensus on the basic mechanisms of glass dissolution explaining the aforementioned trends, particularly those which apply to a wide composition space.

The most recent literature on this subject debate two basic mechanisms for silicate glass corrosion: (i) the classical multi-step inter-diffusion-based mechanism and (ii) the interfacial dissolution–re-precipitation mechanism (IDPM).[22] The former describes the mechanism of corrosion as a multi-step process that includes the release of mobile glass modifying cations (such as Na^+) through ion exchange with protons in solution to form

hydrated Si-OH bonds (forming an inter-diffusion layer), followed by the protonation and hydrolysis of bridging bonds (i.e., Si-O-Si or Si-O-Al) and restructuring of the hydrated silica network into a gel layer via re-polymerization reactions.[19,20,23,24] The IDPM, on the other hand, suggests that glass corrosion proceeds as an inward-moving reaction front in which all bonds at the glass–fluid interface break and are immediately re-precipitated to form an amorphous gel layer.[22] The supersaturated water at the interface not only promotes alkali/alkaline-earth release from the glass but in fact releases all elements in the outermost surface layer only to reorganize as a secondary phase of network forming species such as Si and Al.[22] Both models agree that the "rate drop" from the rapid forward rate regime to a pseudo-equilibrium residual rate regime primarily occurs as a result of gel layer formation; however, their fundamental disagreement lies in the manner by which this layer develops. While the classical inter-diffusion-based mechanism has been widely accepted in the glass community, recent studies using highly advanced analytical techniques to track the gel layer characteristics suggest that a basic mechanism describing silicate glass corrosion may be more complicated than assumed in either individual mechanisms, with high dependence upon glass composition and surrounding leaching conditions.[24-26] This highlights the necessity to perform further studies using advanced techniques and a wide composition-space to elucidate and converge on the fundamental mechanisms governing aqueous corrosion of glasses.

1.3 Challenges and open questions in understanding the chemical durability of glass

In the preface to the technical details of the proposed doctoral research, we must emphasize that although the topic of glass corrosion has been studied for a long time, it is riddled with a variety of complexities that makes a holistic understanding deceptively

difficult. Glass corrosion is controlled by several intrinsic and extrinsic parameters, where the former includes glass composition, structure, and reactive surface area and the latter includes parameters such as temperature, pH, saturated vs. unsaturated conditions, solution chemistry, and flow rate. To effectively study the chemical dissolution behavior of glasses, each of the aforementioned variables must be carefully controlled and accounted for throughout corrosion experiments. However, experiments in place that probe chemical durability can be plagued by potential complications including vital aspects such as surface preparation, method of glass synthesis, glass/media combinations, characterization, and evolution of solution concentration. Likewise, a majority of the literature attempting to understand the chemical durability of glasses covers only a limited range of silicate-based compositions in neutral-to-alkaline media, which do not allow for the development of a unifying model of aqueous corrosion behavior which applies to a large composition-space and range of aqueous media. Based on our experience and relevant literature on these topics, we review in the following at least four considerations and/or open questions that need to be carefully navigated to unearth the mechanisms governing chemical durability of glasses and accurately understand composition-structure-property relationships.

(1) Thermal history: The thermal history of glass is known to have a significant influence on the chemical reactivity its surface,[27] as dictated by the impact that changes in fictive temperature have upon bulk/surface atomic structure as well as the tendency towards phase separation.[28-29] Changes in glass structure and speciation as a function of thermal history have been well-documented. For example, the cooling/quenching rate of melts through the glass transition range has been shown to significantly influence the structural coordination of boron[30] and alkali clustering[31] in borosilicate glasses. Phase separation in glasses often

leads to unique and unpredictable macroscopic properties.[32,33] Interestingly, a recent literature review finds numerous studies where glasses of different thermal histories have been used to study glass corrosion, with the embedded assumption in the *composition-dependent* dissolution models that the solid being modeled comprises a single phase (i.e. assumes no phase separation).[34]

(2) Pushing the boundaries of glass corrosion literature: Upon a thorough literature review, a large fraction of the aqueous corrosion studies performed have focused on silicate glass chemistries in neutral-to-alkaline environments, owing to their relevance in the fields of nuclear waste immobilization and biomaterials.[35,36] Significantly fewer studies, however, have aimed to understand glass corrosion either (i) in acidic media or (ii) of glasses rich in non-silicate glass-forming species. The handful of studies that discuss corrosion of silicate glasses in the acidic regime are mainly based upon a narrow set of glass chemistries[37-46] and, to our knowledge, the literature on the corrosion of borate- or phosphate-rich glasses in acidic media is non-existent. Moreover, studies aiming to unearth the fundamental science governing the dissolution behavior of glasses rich in non-silicate oxides in aqueous media are particularly scarce. For example, a minimal number of research articles devoted to studying the mechanisms governing the dissolution behavior of multi-component borate glasses in aqueous solutions have been published in the last five decades.[47-56] Similarly, although phosphate glasses have been used successfully in a wide range of technological applications,[57-62] there are very few papers that have tried to unearth the kinetics and mechanisms controlling the dissolution behavior of phosphate glasses in aqueous solutions.[63-67] Accordingly, since there is still no complete consensus on the basic mechanisms of glass dissolution which apply to a wide composition space and across

aqueous media, it is vital to "bridge the gap" (1) from silicate-rich to non-silicate-rich glasses and (2) from neutral to acidic dissolution media, to provide an overarching view of corrosion behavior which applies to technologically-relevant or potentially-relevant (yet unexplored) oxide glass compositions across a full range of pH environments.

(3) Structural design of novel glasses: Since glass chemistry and molecular structure are so intimately tied to a glass's chemical durability,[68,69] it is vital to understand the structural drivers of aqueous dissolution to design novel glasses with a controlled chemical resistance. As an example, third generation bioactive glasses are designed such that, when in contact with body fluids, the glass provides (i) structural support (i.e. scaffolding) to provide binding sites for the onset of regenerated human tissue and (ii) ionic dissolution products which release from the glass into the body to stimulate specific and wide-ranging biological responses.[36,70,71] Thus, the design of novel glasses with tunable release behavior requires a thorough understanding of structure–solubility relationships. However, the predominant reliance in the literature on a traditional "trial-and-error" approach, as opposed to a "materials-by-design" approach (as laid out in the White House's Materials Genome Initiative[72]), has made it difficult to design novel glasses using a systematic approach. Thus, adopting a "materials-by-design" approach in which the strengths of rigorous experimental datasets combined with computational methods can facilitate the generation of predictive models in which a novel glass's functions and properties can be predicted from first principles. Therefore, to design and predict the chemical durability of a novel glass based upon its chemistry,[16] a new degree of conceptual understanding of the glass systems of interest is required, which involves comprehensive experimental data and an understanding of the compositional and structural drivers of glass dissolution.

(4) Influence of solution chemistry – Buffered vs. Non-buffered solutions: The influence of pH on the dissolution kinetics and congruency of extraction in borosilicate and aluminosilicate glasses has been well reported in the literature.[38,42,73,74] To adequately control pH during dissolution experiments, buffered aqueous solutions comprising mixtures of both organic and inorganic salts have been used in many such studies across many glass applications.[11,13,73,75,76] This has a significant impact, however, on the interpretation of corrosion data, as the impact of such additives on the dissolution behavior of glasses has been largely ignored or unverified. For example, the tendency of organic anions to form complexes with aluminum ions and borate species (formed either at the glass surface or in the contact solution) has been well documented.[77-79] Accordingly, it has been observed that glasses exposed to buffer solutions with the same pH but different dissolved constituents undergo noticeably distinct dissolution behavior.[80-84] Similarly, the presence of alkali ions in the contact solution (from NaOH or other alkali containing salts)[74,85] will not only affect its ionic strength but will also slow down the process of chemical dissolution by shifting the equilibrium of ion exchange reaction ($\equiv Si - O - Na + H_3O^+ \leftrightharpoons \equiv Si - OH + Na^+ + H_2O$) towards the left in glasses sharing the common cation (e.g. Na-containing glasses, in this example). To understand the influence of pH on the dissolution kinetics of glasses, it is essential to choose aqueous solutions in which solution chemistry has a minimal impact on the chemical dissolution behavior.

1.4 Summary of contents

This doctoral thesis focuses on systematically exploring ternary and quaternary mixed network former glass systems (Na_2O-B_2O_3-SiO_2, Na_2O-Al_2O_3-B_2O_3-SiO_2, Na_2O-P_2O_5-B_2O_3-SiO_2), such that for each system we can generate a comprehensive dataset

combining information on short- and medium-range order glass structure with their dissolution behavior across a range of compositions and structural regimes. Along with the pursuit of understanding *composition-structure-chemical durability* relationships in mixed network former systems with wide-ranged compositions, we consider and explore specific experimental challenges previously observed in the literature, with specific emphasis on unearthing the impact of glass thermal history, glass surface structure and chemistry, and the influence of solution pH and chemistry upon glass corrosion, as described for each chapter below.

Chapter 2 focuses on understanding the impact of thermal history upon molecular structure and dissolution behavior of sodium borosilicate glasses. The choice of study is made based upon literature suggesting that thermal history can affect both chemical reactivity of surfaces as well as glass structural characteristics. Additionally, a thorough literature review reveals that glasses prepared with significantly different thermal histories (i.e. water quenched vs. quenched and annealed) have been synthesized and studied for dissolution experiments with similar aims. However, uncertainty still exists concerning if glasses with varied thermal history will behave similarly when in contact with aqueous environments. To address this topic, glasses are synthesized with varying B_2O_3/SiO_2 ratio in the Na_2O-B_2O_3-SiO_2 ternary system including two binary end-members. Each glass is synthesized using two separate routes: (1) splat quenching between two copper plates and (2) quenching on a metallic plate, followed by annealing to remove all residual stress. The aim is to synthesize glasses with the same compositions but different fictive temperatures. The effect of thermal history upon glass structure and fictive temperature is quantified using ^{23}Na, ^{11}B, and ^{29}Si magic angle spinning – nuclear magnetic resonance (MAS NMR)

spectroscopy and differential scanning calorimetry (DSC) through our collaboration with Corning, Inc. Rigorous dissolution experiments at constant sample surface area-to-solution volume (SA/V) are performed on these samples in DI water, in which glass structural changes and liquid evolution are tracked using X-ray diffraction (XRD), Fourier transform infrared spectroscopy (FT-IR), pH measurements, inductively coupled plasma – optical emission spectroscopy (ICP-OES). We find that the methodology of preparing the glass significantly impacts the glass structure and dissolution behavior, as the methodology used to quench the glass was shown to impact the dissolution rates by 1.5× to 3×, depending on the composition and molecular structure variations. The research work has been published in Acta Biomaterialia *(Stone-Weiss et al., Acta Biomater. 65 436-449 (2018)).*

Chapter 3 focuses on understanding the corrosion of silicate-based glass chemistries over a broad composition space in the acidic pH regime. This choice of study is made since the majority of literature on glass corrosion is focused on silicate glass chemistries in the neutral-to-alkaline aqueous regime owing to its relevance in the fields of nuclear waste immobilization and biomaterials. However, understanding the corrosion of glasses in the acidic pH regime is essential for glass packaging and touch screen electronic display industries. A thorough literature review on this topic reveals only a handful of studies that discuss acid corrosion of silicate glasses and their derivatives—these include only a narrow set of silicate-based glass chemistries. Accordingly, this study focuses on understanding the corrosion mechanisms governing metaluminous (Na/Al = 1) Na_2O-Al_2O_3-B_2O_3-SiO_2 glasses in acidic environments (pH = 0-4) across a wide composition-space (ranging from SiO_2-rich to B_2O_3-rich compositions), with particular emphasis on understanding the reactions taking place near the glass–fluid interface. Using state-of-the-

art characterization techniques including MAS NMR spectroscopy (performed in collaboration with Corning, Inc.), Rutherford backscattering, X-ray photoelectron spectroscopy (XPS), and elastic recoil detection analysis (ERDA), it is shown that stepwise B_2O_3 substitutions into nepheline ($NaAlSiO_4$) glass, although causing non-linear changes in glass structure network structural features, leads to strikingly linear increases in the forward dissolution rate in acidic environments. While the glasses undergo congruent dissolution in the forward rate regime, the residual rate regime displays evidence of preferential extraction near the glass surface (i.e., enrichment in aluminum content upon corrosion through $AlO_4 \rightarrow Al(OH)_3$ evolution) implying that dissolution–re-precipitation processes may occur at the glass–fluid interface in both B_2O_3-rich and SiO_2-rich glass compositions—albeit with vastly dissimilar reaction kinetics. The research work has recently been published in Physical Chemistry Chemical Physics *(Stone-Weiss et al., Phys. Chem. Chem. Phys. 22 1881-1896 (2020)).*

Chapters 4 and 5 focus on the structural design of borosilicate bioactive glasses, which have emerged as potential candidates as third generation bioactive glasses due to the potential advantages they possess as compared to silicate-based compositions. To develop novel borosilicate bioactive glasses, it is critical to understand composition-structure-degradation behavior relationships in this system, covering a wide range of compositions and properties with significant structural complexity. This study focuses on understanding the structure (Chapter 4) and degradation behavior (Chapter 5) of glasses in the Na_2O-P_2O_5-B_2O_3-SiO_2 system. Specifically, we explore the effect of incremental additions of P_2O_5 into perboric (R = Na/B; R < 1), metaboric (R = 1), and per-alkaline (R >1) glass compositions. In Chapter 4, the glass structure before degradation is rigorously explored

using both experimental and computational methods, including advanced single and double resonance MAS NMR techniques, MD simulations, and DFT calculations based on advanced algorithms. NMR experiments presented are performed in collaboration with Prof. Hellmut Eckert at the University of São Paulo in São Carlos, Brazil and Dr. Randall Youngman at Corning, Inc., meanwhile computational work is performed in collaboration with Prof. Alfonso Pedone at the University of Modena and Reggio Emilia in Modena, Italy. We observe in these studies that P_2O_5 tended to attract the network former species preferentially, resulting in a re-polymerization of the silicate and a re-structuring of the borate components. These processes eventually lead to phase separation and crystallization of sodium phosphate, at levels above 3 mol. % to 7 mol. %, respectively, in the peralkaline and perboric glasses investigated. $^{11}B\{^{31}P\}$ rotational echo double resonance results indicate that the ability of glasses to incorporate P_2O_5 without phase separation is related to the formation of P-O-B(IV) linkages that are integrated into the borosilicate glass network. In Chapter 5, selected glasses are studied for their degradation behavior in model bodily environments (pH = 7.4; 37 ºC) by tracking elemental release characteristics and in-depth structural details during dissolution using ICP-OES and MAS NMR, among other spectroscopic techniques. Through these studies, we meaningfully attribute the effects that specific structural features have upon degradation behavior, giving insight into the structural features desired in glasses tuned to particular biomedical applications. Combining the studies performed in Chapters 4 and 5, a comprehensive understanding of compositional and structural drivers of glass degradation in the studied system is developed which can be utilized to facilitate the design of novel borosilicate bioactive glasses.

Chapter 6 focuses on understanding the impact that buffer solution chemistry has upon glass dissolution behavior. In particular, the buffer solutions most commonly used in near-neutral environments across many glass applications in literature are Tris-based ($C_4O_3NH_{11}$, in combination with acids such as HCl or HNO_3). Tris buffer solutions are commonly chosen as aqueous media for dissolution studies since these solutions are effective in maintaining a constant solution pH in the absence of dissolved cations (i.e. Na^+ or Ca^{2+}) which can convolute experimental results due to solution feedback effects. However, Tris has a well-known tendency to complex with boron, which results in a significant impact on the dissolution kinetics of borosilicate glasses, which are important to a range of applications, including bioactive glasses and glasses for nuclear waste containment. Since the present consensus in the glass community is that Tris-based solutions are the best choice when studying this pH regime, our study focused on understanding the impact of Tris solution chemistry upon dissolution behavior of a sodium borosilicate glass. Accordingly, the present study focuses on the dissolution behavior of a sodium borosilicate glass in Tris-based (pH 7-9) solution environments with varied Tris concentrations (0.01 – 0.5 M) and acid identities (HCl vs. HNO_3). Elemental release and structural evolution are tracked using ICP-OES, liquid NMR, and MAS NMR spectroscopies. MAS NMR data is collected at Corning, Inc. We determine in this study that the identity of acid used in Tris-based solutions does not significantly impact dissolution behavior, however, increased contents of Tris in solution were observed to suppress glass dissolution tendencies. Notably, we are not able to determine the presence of Tris-boron complexes in the solution above room temperature, thus bringing into

question the formerly proposed complexation mechanism by which Tris was suggested to impact borosilicate dissolution kinetics.

Chapter 7 provides a summary of the key conclusions of this doctoral research, while Chapter 8 discusses the recommendation for future work.

References

1. Mauro, J. C.; Philip, C. S.; Vaughn, D. J.; Pambianchi, M. S., Glass Science in the United States: Current Status and Future Directions. *International Journal of Applied Glass Science* 2014, *5* (1), 2-15.
2. Hamilton, J. P.; Pantano, C. G., Effects of glass structure on the corrosion behavior of sodium-aluminosilicate glasses. *Journal of Non-Crystalline Solids* 1997, *222* (0), 167-174.
3. Du, L.-S.; Stebbins, J. F., Network connectivity in aluminoborosilicate glasses: A high-resolution 11B, 27Al and 17O NMR study. *Journal of Non-Crystalline Solids* 2005, *351* (43–45), 3508-3520.
4. Pierce, E. M.; Rodriguez, E. A.; Calligan, L. J.; Shaw, W. J.; Pete McGrail, B., An experimental study of the dissolution rates of simulated aluminoborosilicate waste glasses as a function of pH and temperature under dilute conditions. *Applied Geochemistry* 2008, *23* (9), 2559-2573.
5. Yamashita, H.; Inoue, K.; Nakajin, T.; Inoue, H.; Maekawa, T., Nuclear magnetic resonance studies of 0.139 MO (or M′ 2 O)· 0.673 SiO 2·(0.188− x) Al 2 O 3· xB 2 O 3 (M= Mg, Ca, Sr and Ba, M′= Na and K) glasses. *Journal of non-crystalline solids* 2003, *331* (1), 128-136.
6. El-Egili, K. Infrared studies of Na2O–B2O3–SiO2 and Al2O3–Na2O–B2O3–SiO2 glasses *Physica B* [Online], 2003, p. 340-348.
7. Rahaman, M. N.; Day, D. E.; Bal, B. S.; Fu, Q.; Jung, S. B.; Bonewald, L. F.; Tomsia, A. P., Bioactive glass in tissue engineering. *Acta Biomaterialia* 2011, *7* (6), 2355-2373.
8. Newton, R. G.; Paul, A., A new approach to predicting the durability of glasses from their chemical compositions. *Glass Technology* 1980, *21* (6), 307-309.
9. Paul, A., Chemical durability of glasses; a thermodynamic approach. *Journal of Materials Science* 1977, *12* (11), 2246-2268.
10. Strachan, D. M.; Croak, T. L., Compositional effects on long-term dissolution of borosilicate glass. *Journal of Non-Crystalline Solids* 2000, *272* (1), 22-33.
11. Kinoshita, M.; Harada, M.; Sato, Y.; Hariguchi, Y., Percolation Phenomenon for Dissolution of Sodium Borosilicate Glasses in Aqueous Solutions. *J Am Ceram Soc* 1991, *74* (4), 783-787.
12. Ojovan, M. I.; Hand, R. J.; Ojovan, N. V.; Lee, W. E., Corrosion of alkali–borosilicate waste glass K-26 in non-saturated conditions. *Journal of Nuclear Materials* 2005, *340* (1), 12-24.
13. Pierce, E. M.; Reed, L. R.; Shaw, W. J.; McGrail, B. P.; Icenhower, J. P.; Windisch, C. F.; Cordova, E. A.; Broady, J., Experimental determination of the effect of

the ratio of B/Al on glass dissolution along the nepheline (NaAlSiO4)–malinkoite (NaBSiO4) join. *Geochimica et Cosmochimica Acta* 2010, *74* (9), 2634-2654.
14. Kapoor, S.; Goel, A.; Tilocca, A.; Dhuna, V.; Bhatia, G.; Dhuna, K.; Ferreira, J. M. F., Role of glass structure in defining the chemical dissolution behavior, bioactivity and antioxidant properties of zinc and strontium co-doped alkali-free phosphosilicate glasses. *Acta Biomaterialia* 2014, *10* (7), 3264-3278.
15. Schaut, R. A. The effect of boron oxide on the composition, structure and adsorptivity of glass surfaces. Pennsylvania State University, 2008.
16. Lusvardi, G.; Malavasi, G.; Tarsitano, F.; Menabue, L.; Menziani, M. C.; Pedone, A., Quantitative Structure-Property Relationships of Potentially Bioactive Fluoro Phospho-silicate Glasses. *Journal of Physical Chemistry B* 2009, *113* (30), 10331-10338.
17. Aertsens, M.; Ghaleb, D., New techniques for modelling glass dissolution. *Journal of Nuclear Materials* 2001, *298* (1-2), 37-46.
18. Boksay, Z.; Bouquet, G.; Dobos, S., Kinetics of formation of leached layers on glass surfaces. *Physics and Chemistry of Glasses* 1968, *9* (2), 69.
19. Doremus, R. H., Interdiffusion of hydrogen and alkali ions in a glass surface. *Journal of Non-Crystalline Solids* 1975, *19*, 137-144.
20. Vienna, J. D.; Ryan, J. V.; Gin, S.; Inagaki, Y., Current Understanding and Remaining Challenges in Modeling Long-Term Degradation of Borosilicate Nuclear Waste Glasses. *International Journal of Applied Glass Science* 2013, *4* (4), 283-294.
21. Gin, S.; Abdelouas, A.; Criscenti, L. J.; Ebert, W. L.; Ferrand, K.; Geisler, T.; Harrison, M. T.; Inagaki, Y.; Mitsui, S.; Mueller, K. T., An international initiative on long-term behavior of high-level nuclear waste glass. *Materials Today* 2013, *16* (6), 243-248.
22. Geisler, T.; Janssen, A.; Scheiter, D.; Stephan, T.; Berndt, J.; Putnis, A., Aqueous corrosion of borosilicate glass under acidic conditions: a new corrosion mechanism. *Journal of Non-Crystalline Solids* 2010, *356* (28-30), 1458-1465.
23. Bunker, B. C., Molecular mechanisms for corrosion of silica and silicate glasses. *Journal of Non-Crystalline Solids* 1994, *179*, 300-308.
24. Hopf, J.; Eskelsen, J. R.; Chiu, M.; Ievlev, A.; Ovchinnikova, O. S.; Leonard, D.; Pierce, E. M., Toward an understanding of surface layer formation, growth, and transformation at the glass–fluid interface. *Geochimica et Cosmochimica Acta* 2018, *229*, 65-84.
25. Lenting, C.; Plümper, O.; Kilburn, M.; Guagliardo, P.; Klinkenberg, M.; Geisler, T., Towards a unifying mechanistic model for silicate glass corrosion. *npj Materials Degradation* 2018, *2* (1), 28.
26. Gin, S.; Neill, L.; Fournier, M.; Frugier, P.; Ducasse, T.; Tribet, M.; Abdelouas, A.; Parruzot, B.; Neeway, J.; Wall, N., The controversial role of inter-diffusion in glass alteration. *Chemical Geology* 2016, *440*, 115-123.
27. Pantano, C. G., What Do We Know about Glass Surfaces? In *A Collection of Papers Presented at the 61st Conference on Glass Problems: Ceramic Engineering and Science Proceedings*, John Wiley & Sons, Inc.: 2001; pp 137-148.
28. Moncke, D.; Ehrt, D.; Eckert, H.; Mertens, V., Influence of melting and annealing conditions on the structure of borosilicate glasses. *Physics and Chemistry of Glasses* 2003, *44* (2), 113-116.

29. Wheaton, B. R.; Clare, A. G., Evaluation of phase separation in glasses with the use of atomic force microscopy. *J Non-Cryst Solids* 2007, *353* (52–54), 4767-4778.
30. Gupta, P. K.; Lur, M. L.; Bray, P. J., Boron Coordination in Rapidly Cooled and in Annealed Aluminum Borosilicate Glass Fibers. *J Am Ceram Soc* 1985, *68* (3), C-82-C-82.
31. Angeli, F.; Villain, O.; Schuller, S.; Charpentier, T.; de Ligny, D.; Bressel, L.; Wondraczek, L., Effect of temperature and thermal history on borosilicate glass structure. *Physical Review B* 2012, *85* (5), 054110.
32. Taylor, P.; Ashmore, S. D.; Owen, D. G., Chemical Durability of Some Sodium Borosilicate Glasses Improved by Phase Separation*. *J Am Ceram Soc* 1987, *70* (5), 333-338.
33. Jantzen, C. M.; Pickett, J. B.; Brown, K. G.; Edwards, T. B. *Impact of phase separation of waste glass durability*; Westinghouse Savannah River Company: Aiken, SC, 29808, USA, 1999.
34. Jantzen, C. M.; Brown, K. G.; Pickett, J. B., Durable Glass for Thousands of Years. *International Journal of Applied Glass Science* 2010, *1* (1), 38-62.
35. Burger, E.; Rebiscoul, D.; Bruguier, F.; Jublot, M.; Lartigue, J. E.; Gin, S., Impact of iron on nuclear glass alteration in geological repository conditions: A multiscale approach. *Applied Geochemistry* 2013, *31* (Supplement C), 159-170.
36. Hoppe, A.; Gueldal, N. S.; Boccaccini, A. R., A review of the biological response to ionic dissolution products from bioactive glasses and glass-ceramics. *Biomaterials* 2011, *32* (11), 2757-2774.
37. Tsomaia, N.; Brantley, S. L.; Hamilton, J. P.; Pantano, C. G.; Mueller, K. T., NMR evidence for formation of octahedral and tetrahedral Al and repolymerization of the Si network during dissolution of aluminosilicate glass and crystal. *American Mineralogist* 2003, *88* (1), 54-67.
38. Hamilton, J. P.; Brantley, S. L.; Pantano, C. G.; Criscenti, L. J.; Kubicki, J. D., Dissolution of nepheline, jadeite and albite glasses: toward better models for aluminosilicate dissolution. *Geochimica et Cosmochimica Acta* 2001, *65* (21), 3683-3702.
39. Hamilton, J. P.; Pantano, C. G.; Brantley, S. L., Dissolution of albite glass and crystal. *Geochimica et Cosmochimica Acta* 2000, *64* (15), 2603-2615.
40. Hamilton, J. P.; Pantano, C. G., Effects of glass structure on the corrosion behavior of sodium-aluminosilicate glasses. *Journal of Non-Crystalline Solids* 1997, *222*, 167-174.
41. Declercq, J.; Diedrich, T.; Perrot, M.; Gislason, S. R.; Oelkers, E. H., Experimental determination of rhyolitic glass dissolution rates at 40–200 C and 2< pH< 10.1. *Geochimica et Cosmochimica Acta* 2013, *100*, 251-263.
42. Wolff-Boenisch, D.; Gislason, S. R.; Oelkers, E. H.; Putnis, C. V., The dissolution rates of natural glasses as a function of their composition at pH 4 and 10.6, and temperatures from 25 to 74 degrees C. *Geochimica Et Cosmochimica Acta* 2004, *68* (23), 4843-4858.
43. Wolff-Boenisch, D.; Gislason, S. R.; Oelkers, E. H., The effect of fluoride on the dissolution rates of natural glasses at pH 4 and 25 degrees C. *Geochimica Et Cosmochimica Acta* 2004, *68* (22), 4571-4582.
44. Gislason, S. R.; Oelkers, E. H., Mechanism, rates, and consequences of basaltic glass dissolution: II. An experimental study of the dissolution rates of basaltic glass as a

function of pH and temperature. *Geochimica et Cosmochimica Acta* 2003, *67* (20), 3817-3832.
45. Oelkers, E. H.; Gislason, S. R., The mechanism, rates and consequences of basaltic glass dissolution: I. An experimental study of the dissolution rates of basaltic glass as a function of aqueous Al, Si and oxalic acid concentration at 25 C and pH= 3 and 11. *Geochimica et Cosmochimica Acta* 2001, *65* (21), 3671-3681.
46. Berger, G.; Claparols, C.; Guy, C.; Daux, V., Dissolution rate of a basalt glass in silica-rich solutions: implications for long-term alteration. *Geochimica et Cosmochimica Acta* 1994, *58* (22), 4875-4886.
47. Adams, P. B.; Evans, D. L., Chemical Durability of Borate Glasses. In *Borate Glasses*, Pye, L. D.; Fréchette, V. D.; Kreidl, N. J., Eds. Springer US: 1978; Vol. 12, pp 525-537.
48. Das, C. R., The Reaction Between Borate Glass and Attacking Agents—Part III: Equilibrium pH of the Alkali Borate Glasses and Their Relationship with Chemical Durability and the Glass Composition. *Transactions of the Indian Ceramic Society* 1967, *26* (1), 155-158.
49. Velez, M. H.; Tuller, H. L.; Uhlmann, D. R., Chemical durability of lithium borate glasses. *J Non-Cryst Solids* 1982, *49* (1–3), 351 - 362.
50. Velez, M. H.; Uhlmann, D. R.; Tuller, H. L., Chemical durability of glasses. *Revista Latinoamericana de Metalurgia y Materiales* 1982, *2* (1), 3-15.
51. Bengisu, M.; Brow, R. K.; Yimaz, E.; Mogus-Milankovic, A.; Reis, S. T., Aluminoborate and aluminoboro silicate glasses with high chemical durability and the effect Of P2O5 additions on the properties. *J Non-Cryst Solids* 2006, *352* (32-35), 3668-3676.
52. George, J. L.; Brow, R. K., In-situ characterization of borate glass dissolution kinetics by mu-Raman spectroscopy. *J Non-Cryst Solids* 2015, *426*, 116-124.
53. Kapoor, S.; Youngman, R. E.; Zakharchuk, K.; Yaremchenko, A.; Smith, N. J.; Goel, A., A structural approach towards understanding the aqueous corrosion of alkali aluminoborate glasses. *Journal of Physical Chemistry B* 2018, *Submitted*.
54. Fernandes, H. R.; Kapoor, S.; Patel, Y.; Ngai, K.; Levin, K.; Germanov, Y.; Krishtopa, L.; Kroeker, S.; Goel, A., Composition-structure-property relationships in Li2O–Al2O3–B2O3 glasses. *Journal of Non-Crystalline Solids* 2018, *502*, 142-151.
55. Mascaraque, N.; Januchta, K.; Frederiksen, K. F.; Youngman, R. E.; Bauchy, M.; Smedskjaer, M. M., Structural dependence of chemical durability in modified aluminoborate glasses. *Journal of the American Ceramic Society* 2018, *In press*.
56. Mascaraque, N.; Frederiksen, K. F.; Januchta, K.; Youngman, R. E.; Bauchy, M.; Smedskjaer, M. M., Competitive effects of modifier charge and size on mechanical and chemical resistance of aluminoborate glasses. *Journal of Non-Crystalline Solids* 2018, *499*, 264-271.
57. Fletcher, L. B.; Witcher, J. J.; Troy, N.; Brow, R. K.; Krol, D. M., Single-pass waveguide amplifiers in Er-Yb doped zinc polyphosphate glass fabricated with femtosecond laser pulses. *Optics Letters* 2012, *37* (7), 1148-1150.
58. Brow, R. K.; Tallant, D. R., Structural design of sealing glasses. *Journal of Non-Crystalline Solids* 1997, *222* (0), 396-406.
59. Metcalfe, B. L.; Donald, I. W., Candidate wasteforms for the immobilization of chloride-containing radioactive waste. *J Non-Cryst Solids* 2004, *348* (0), 225-229.

60. Ahmed, I.; Lewis, M.; Olsen, I.; Knowles, J. C., Phosphate glasses for tissue engineering: Part 1. Processing and characterisation of a ternary-based P2O5–CaO–Na2O glass system. *Biomaterials* 2004, *25* (3), 491-499.
61. Ahmed, I.; Lewis, M.; Olsen, I.; Knowles, J. C., Phosphate glasses for tissue engineering: Part 2. Processing and characterisation of a ternary-based P2O5–CaO–Na2O glass fibre system. *Biomaterials* 2004, *25* (3), 501-507.
62. Martin, S. W., Ionic Conduction in Phosphate Glasses. *Journal of the American Ceramic Society* 1991, *74* (8), 1767-1784.
63. Delahaye, F.; Montagne, L.; Palavit, G.; Touray, J. C.; Baillif, P., Acid dissolution of sodium-calcium metaphosphate glasses. *J Non-Cryst Solids* 1998, *242* (1), 25-32.
64. Döhler, F.; Mandlule, A.; van Wüllen, L.; Friedrich, M.; Brauer, D. S., 31 P NMR characterisation of phosphate fragments during dissolution of calcium sodium phosphate glasses. *Journal of Materials Chemistry B* 2015, *3* (6), 1125-1134.
65. Bunker, B. C.; Arnold, G. W.; Wilder, J. A., PHOSPHATE-GLASS DISSOLUTION IN AQUEOUS-SOLUTIONS. *Journal of Non-Crystalline Solids* 1984, *64* (3), 291-316.
66. Gao, H.; Tan, T.; Wang, D., Effect of composition on the release kinetics of phosphate controlled release glasses in aqueous medium. *J Control Release* 2004, *96* (1), 21-28.
67. Gao, H. S.; Tan, T. N.; Wang, D. H., Dissolution mechanism and release kinetics of phosphate controlled release glasses in aqueous medium. *Journal of Controlled Release* 2004, *96* (1), 29-36.
68. Tilocca, A., Structural models of bioactive glasses from molecular dynamics simulations. *Proceedings of the Royal Society a-Mathematical Physical and Engineering Sciences* 2009, *465* (2104), 1003-1027.
69. Goel, A.; Kapoor, S.; Tilocca, A.; Rajagopal, R. R.; Ferreira, J. M. F., Structural role of zinc in biodegradation of alkali-free bioactive glasses. *Journal of Materials Chemistry B* 2013, *1* (24), 3073-3082.
70. Gorustovich, A.; Guglielmotti, M. B.; Lopez, J. M. P.; Cabrini, R. L., Increased osteogenesis elicited by boron-modified bioactive glass particles in the SiO2-CaO-P2O5-Na2O system: A histomorphometric study in rats. *Bioceramics, Vol 17* 2005, *284-286*, 913-916.
71. Xynos, I.; Edgar, A.; Buttery, L.; Hench, L.; Polak, J., Ionic Products of Bioactive Glass Dissolution Increase Proliferation of Human Osteoblasts and Induce Insulin-like Growth Factor II mRNA Expression and Protein Synthesis. *Biochemical and Biophysical Research Communications* 2000, *276* (2), 461-465.
72. White, A., The Materials Genome Initiative: One year on. *Mrs Bulletin* 2012, *37* (8), 715-716.
73. Perera, G.; Doremus, R. H., Dissolution Rates of Commercial Soda–Lime and Pyrex Borosilicate Glasses: Influence of Solution pH. *J Am Ceram Soc* 1991, *74* (7), 1554-1558.
74. Inagaki, Y.; Kikunaga, T.; Idemitsu, K.; Arima, T., Initial Dissolution Rate of the International Simple Glass as a Function of pH and Temperature Measured Using Microchannel Flow-Through Test Method. *International Journal of Applied Glass Science* 2013, *4* (4), 317-327.

75. Ebert, W. L. *Comparison of the results of short-term static tests and single-pass flow-through tests with LRM glass (ANL-06/51)*; Argonne National Laboratory: Argonne, IL, USA, 2006.
76. Chêne, J.; Trocellier, P., Investigation of alkali borosilicate glass durability using tritium tracing, β-autoradiography, scanning electron microscopy and ion beam analysis. *J Non-Cryst Solids* 2004, *337* (1), 86-96.
77. Steenberg, T.; Hjenner, H. K.; Jensen, S. L.; Guldberg, M.; Knudsen, T., Dissolution behaviour of biosoluble HT stone wool fibres. *Glastech. Ber. Glass Sci. Technol.* 2001, *74*, 97-105.
78. Violante, A.; Violante, P., Influence of pH, concentration, and chelating power of organic-anions on the synthesis of aluminum hydroxides and oxyhydroxides. *Clays and Clay Minerals* 1980, *28* (6), 425-434.
79. Tournié, A.; Majérus, O.; Lefèvre, G.; Rager, M. N.; Walmé, S.; Caurant, D.; Barboux, P., Impact of boron complexation by Tris buffer on the initial dissolution rate of borosilicate glasses. *Journal of Colloid and Interface Science* 2013, *400*, 161-167.
80. Horkavcová, D.; Rohanová, D.; Stříbny, A.; Schuhladen, K.; Boccaccini, A. R.; Bezdička, P., Interaction of MOPS buffer with glass–ceramic scaffold: Effect of (PO4) 3− ions in SBF on kinetics and morphology of formatted hydroxyapatite. *Journal of Biomedical Materials Research Part B: Applied Biomaterials* 2019.
81. Rohanová, D.; Horkavcova, D.; Paidere, L.; Boccaccini, A. R.; Bozděchová, P.; Bezdička, P., Interaction of HEPES buffer with glass-ceramic scaffold: Can HEPES replace TRIS in SBF? *Journal of Biomedical Materials Research Part B: Applied Biomaterials* 2018, *106* (1), 143-152.
82. Rohanová, D.; Boccaccini, A. R.; Yunos, D. M.; Horkavcová, D.; Březovská, I.; Helebrant, A., TRIS buffer in simulated body fluid distorts the assessment of glass–ceramic scaffold bioactivity. *Acta biomaterialia* 2011, *7* (6), 2623-2630.
83. Gomori, G., Buffers in the Range of pH 6.5 to 9.6. *Proceedings of the Society for Experimental Biology and Medicine* 1946, *62* (1), 33-34.
84. Kirste, G.; Brandt-Slowik, J.; Bocker, C.; Steinert, M.; Geiss, R.; Brauer, D. S., Effect of chloride ions in Tris buffer solution on bioactive glass apatite mineralization. *International Journal of Applied Glass Science* 2017, *8* (4), 438-449.
85. Kansal, I.; Goel, A.; Tulyaganov, D. U.; Santos, L. F.; Ferreira, J. M. F., Structure, surface reactivity and physico-chemical degradation of fluoride containing phospho-silicate glasses. *J Mater Chem* 2011, *21* (22), 8074-8084.

Chapter 2. Understanding the structural drivers governing glass – water interactions in borosilicate based model bioactive glasses

Nicholas Stone-Weiss,[1] Eric M. Pierce,[2] Randall E. Youngman,[3] Ozgur Gulbiten,[3] Nicholas J. Smith,[3] Jincheng Du,[4] Ashutosh Goel[1,*]

[1]Department of Materials Science and Engineering, Rutgers, The State University of New Jersey, Piscataway, NJ, 08854, USA

[2]Environmental Sciences Division, Oak Ridge National Laboratory, Oak Ridge, TN, 37831, USA

[3]Science and Technology Division, Corning Incorporated, Corning, NY, 14831, USA

[4]Department of Materials Science and Engineering, University of North Texas

[*] Email: ag1179@soe.rutgers.edu; Ph: +1-848-333-1523

Abstract

The past decade has witnessed a significant upsurge in the development of borate and borosilicate based resorbable bioactive glasses owing to their faster degradation rate in comparison to their silicate counterparts. However, due to our lack of understanding about the fundamental science governing the aqueous corrosion of these glasses, most of the borate/borosilicate based bioactive glasses reported in the literature have been designed by "trial–and–error" approach. With an ever-increasing demand for their application in treating a broad spectrum of non-skeletal health problems, it is becoming increasingly difficult to design advanced glass formulations using the same conventional approach. Therefore, a paradigm shift from the "trial–and–error" approach to "materials–by–design" approach is required to develop new-generations of bioactive glasses with controlled release of functional ions tailored for specific patients and disease states, whereby material functions and properties can be predicted from first principles. Realizing this goal, however, requires a thorough understanding of the complex sequence of reactions that control the dissolution kinetics of bioactive glasses and the structural drivers that govern them. While there is a considerable amount of literature published on chemical dissolution behavior and apatite-forming ability of potentially bioactive glasses, the majority of this literature has been produced on silicate glass chemistries using different experimental and measurement protocols. It follows that inter-comparison of different datasets reveals inconsistencies between experimental groups. There are also some major experimental challenges or choices that need to be carefully navigated to unearth the mechanisms governing the chemical degradation behavior and kinetics of boron-containing bioactive glasses, and to accurately determine the composition–structure–property relationships. In order to address these challenges, a simplified borosilicate based model melt-quenched bioactive glass system has been studied to depict the impact of thermal history on its molecular structure and dissolution behavior in water. It has been shown that the methodology of quenching of the glass melt impacts the dissolution rate of the studied glasses by 1.5× to 3× times depending on the changes induced in their molecular structure due to variation in thermal history. Further, a recommendation has been made to study dissolution behavior of bioactive glasses using surface area of the sample – to – volume of solution (SA/V) approach instead of the currently followed mass of sample – to – volume of solution approach. The structural and chemical dissolution data obtained from bioactive glasses following the approach presented in this paper can be used to develop the structural descriptors and potential energy functions over a broad range of bioactive glass compositions.

Keywords: bioactive glass; dissolution; thermal history; structure.

2.1 Introduction

The approach to accelerate materials discovery and development by enabling "materials–by–design", as laid out in White House's Materials Genome Initiative (MGI),[1] is highly promising from the viewpoint of developing third generation resorbable bioactive glasses, especially considering the advancements made in using computational models to predict glass structure and properties.[2,3] Boron-containing bioactive glasses (borates and borosilicates), which undergo faster degradation rates (than silicates) when in contact with physiological fluids, are potential candidates for design and development of third generation bioactive glasses.[4-10] However, there are two major challenges that retard the pace of development of resorbable borate/borosilicate based bioactive glasses – **(1)** lack of reliable computational models to predict the structure–property relationships in these glasses over a wide compositional space,[11] **(2)** lack of knowledge of the fundamental science and rigorous experimental data pertaining to corrosion of these glasses in aqueous solutions. It follows that most of the boron containing bioactive glasses reported in the literature (including the most well-known 13-93B3 glass[10]) have been designed by a "trial–and–error" approach, with partial or complete replacement of SiO_2 by B_2O_3 in 45S5, 13-93 or other silicate glass compositions.[7,12] While strenuous efforts are being made to develop scientifically robust computational models for predicting structure–property relationships in borate/borosilicate glasses,[13,14] there is a dearth of rigorous experimental datasets on chemical dissolution (or biodegradation) of boron-containing bioactive glasses to validate these models.

From the perspective of collecting rigorous experimental datasets to establish structure – property relationships in borate/borosilicate based bioactive glass, it is

necessary to recognize that while the degradation behavior of bioactive glasses has been studied for a long time, it is riddled with complexity that makes a holistic understanding deceptively difficult. For example, the majority of data published to date has been produced on silicate bioactive glass chemistries using a variety of experimental and measurement protocols. As a result, inter-comparison of different datasets reveals inconsistencies between experimental groups. This issue has also been highlighted in a recent round robin study by Macon et al.,[15] where the authors recommended that the community adopt a standardized experimental procedure to support the evaluation of dissolution mechanisms and *in vitro* bioactivity. The presence of boron in glasses further complicates the situation, as the experimental and measurement protocols developed for studying chemical dissolution behavior of silicate-based bioactive glasses may not be directly extended to study the dissolution behavior of boron-containing glass chemistries. Based on our experience and relevant literature, in the following section we briefly describe the major experimental challenges or choices that need to be carefully navigated to unearth the mechanisms governing the aqueous corrosion of boron-containing bioactive glasses and accurately determine their composition–structure–property relationships.

(1) Impact of methodology of glass synthesis – alteration in composition and thermal history: Most of the commercial bioactive glasses (including 45S5 Bioglass) are synthesized using the melt-quench technique. During the synthesis of glasses, one crucial aspect that is not carefully considered is the method for quenching the melt. There are several studies reported in the literature where glass melts have been quenched in water (see references[16-25]). While rapid quenching of the glass melt is required to prevent devitrification, the quenching of a bioactive glass melt in water results in significant

changes in its surface chemical composition. Cerruti et al.[26] demonstrated that the pH of deionized water increases from 6 to 10 in 30 seconds after 0.3 g of 45S5 Bioglass is immersed in 200 mL of water. This observation suggests the rapid release of alkali ions into water, even during brief exposures, thus risking significant changes to the glass melt surface composition of specimens. The chemical degradation and alteration in the glass composition will be even more severe in the case of boron-containing glass melts quenched in water, for example, see references.[27-29] This unintentional error can result in significant differences between batched and experimental glass compositions—facts which are rarely considered during analysis of results, translating to irreproducible results and potentially a flawed interpretation. Accordingly, alternative routes for rapid quenching of glass melts—for example splat quenching between two metallic plates—need to be adopted to maintain consistency between batched vs. experimental glass compositions.

Another crucial aspect that is highly governed by the methodology of glass synthesis is the thermal history. The thermal history of a glass is known to have significant influence on the chemical reactivity of a glass surface,[30-31] as dictated by its impact on bulk/surface atomic structure (vis-à-vis, changes in fictive temperature), as well as the tendency towards phase separation.[32-33] In particular, boron coordination in glasses is known to be highly sensitive to their chemical composition and thermal histories.[34-35] A thorough literature review reveals numerous studies where bioactive glasses with different thermal histories have been synthesized and studied, for example quenching of glass melt in water[16-25] vs. splat quenching between metallic plates[36-37] vs. quenching on a metallic plate followed by annealing.[22,23,25,38-40] While quenching of melts (e.g. in water, or between two metallic plates), is bound to generate residual stresses in the glasses, approaches to

alleviate these stresses are not always done effectively or in a standardized manner. Figure 2.1 presents an image of a sodium aluminoborosilicate glass (under polarimeter) after casting of the melt on a metallic plate followed by annealing. The colored fringes seen in Figure 2.1a demonstrate the level of residual stress after annealing the glass at a temperature corresponding to T_g–50 °C (where, T_g is the glass transition temperature as obtained from differential scanning calorimeter), as is usually done in most of the studies reported in the literature. On the other hand, Figure 2.1b presents an image of the same glass (under polarimeter) after complete removal of residual stress by annealing at ~T_g-50 °C for several hours and slow-cooling from this temperature, while also properly accounting for sample thickness. Figure 2.1c illustrates a borosilicate glass which has been splat-quenched between metallic plates; stress-induced birefringence bands of varying magnitudes can be seen throughout the glass. These residual stresses in glasses have been shown to have significant impact on their degradation rate in aqueous solutions.[41,42] Variations in annealing protocol thus potentially introduce additional complexity when comparing dissolution behavior of bioactive glasses, even with similar compositions processed through different routes.

(2) Surface area – to – volume ratio (SA/V) vs. mass – to – volume ratio: Generally, the literature on chemical dissolution studies of glasses in aqueous solutions can be divided into two categories based on the type of glass specimen used—i.e. powder or monolith—and wherein the majority of studies focus on powdered glass samples.[15,19-23,43,44] While powdered specimens offer certain practical advantages and can provide useful information, these experiments can be subjected to complications that lead to significant error.[45] To date there is still no complete consensus in the bioglass community on criteria to select the

powdered samples for dissolution studies. While ISO 23317:2014 suggests to follow the approach of surface area (SA) of sample – to – volume (V) of simulated body fluid (SBF) as a criterion to calculate the amount of sample required to study the in vitro bioactivity, a recent round robin study by TC04 (International Commision on Glass Technical Committee on biomedical glasses) members has suggested the mass of sample (M) –to– volume (V) of solution (M/V) ratio as the best practice to study the apatite-forming ability of bioactive glasses in vitro.[15] Most of the literature on bioactive glasses follows the approach of using M/V ratio to study their dissolution behavior and in vitro bioactivity. Although convenient, this approach does not account for the glass density and influence of particle size on the rate of chemical degradation of bioactive glasses, therefore making it difficult to compare the results from different studies.[46] As per our literature review, glass powders with particle sizes varying between <5 μm – 700 μm have been used for studying dissolution behavior and in vitro bioactivity.[18,22,23,25,47-53] In our opinion, designing experimental protocols on the basis of SA/V ratio are more appropriate, as it allows for the glass dissolution kinetics to be studied (when correlated with elemental analysis of solutions), which is difficult with the M/V ratio approach. It is worth noting that the SA/V approach has its own challenges, as also highlighted by Macon et al.[15]—one example being that geometric SA methods approximate glass particles as spherical, underestimating the SA due to the angularity of ground glass powders. However, it has also previously been demonstrated that a careful and rigorous methodology to calculate geometric SA of glass powders based on the sieve size fraction provides an adequate estimate of the actual SA within the range of typical testing uncertainities.[54-56] In this study, we have used an

approach to measure the geometric SA of glass powders using optical microscopy and image processing software (ImageJ).

(3) Choice of dissolution solution: Most of the in vitro dissolution studies reported in the literature use buffer solutions like SBF or Tris-HCl to study chemical degradation of bioactive glasses in order to maintain constant pH and simulate the conditions of body plasma. While serious concerns are being raised about the validity of SBF tests and hydroxyapatite-forming ability on glass surfaces being the marker of bioactivity,[57,58] the choice of other buffer solutions (for example, Tris-HCl) can have a pronounced impact on the dissolution behavior of bioactive glasses. For example, Tris-HCl—a widely used buffer solution—does not exhibit a significant impact on dissolution behavior of boron-free bioactive glass chemistries (for example, 45S5, 13-93). However, it has been shown to form a Tris-boron complex (in the stoichiometry of 1:1) with boron-containing glass chemistries, thus increasing the degradation rate of these glasses by at least 8 times (when compared with glass degradation in Tris-free buffer solution).[59] Another problem with using biological buffers like SBF is that these solutions are already calcium- and phosphate-rich. The affinity of phosphate chains in SBF to chelate with divalent calcium thus extracts calcium from the hydrated layer of glass (if CaO is present in the glass) into SBF solution, and results in the deposition of apatite and calcium carbonate phases on the altered glass surface.[60,61] The deposition of crystalline phases acts as a barrier over the hydrated layer, limiting the diffusion of molecular water into the bulk glass.[60] Similarly, the presence of alkali ions common to both the glass and the contact solution (from NaOH or other alkali containing salts) will affect the solution ionic strength. With the goal of understanding the genuine material dissolution kinetics of bioactive glasses and linking to structure, it is

essential to choose aqueous solutions that minimize the impact of solution chemistry on dissolution. Such a foundational understanding can then be expanded upon with studies in more complex biological-simulant systems.

(4) Static tests vs. dynamic tests: Historically, the majority of dissolution studies on bioactive glasses have been performed in static media,[15,19,22,43,62,63] while more recent literature suggests the use of continuous flow mechanism based on single pass flow through (SPFT) tests in order to mitigate or control solution feedback effects observed in the former, and mimic the in vivo chemical degradation behavior of glasses.[40,56,64,65] According to a round robin study (coordinated by Argonne National Laboratory) comparing static dissolution tests vs. SPFT tests for studying forward dissolution rate, the general practice of neglecting solution feedback effects in SPFT tests (which are small but not insignificant) can lead to some uncertainty in this approach.[54] According to this report, static tests, if performed carefully, provide an easier and economical alternative to continuous flow tests for measuring the forward dissolution rate of glasses.[54] Although dissolved glass components will accumulate over time in static tests, the rate at which they accumulate and their effect on the rate can be minimized with very low (optimized) SA/V ratios and short test durations (t) for a given glass—in other words, with customized experiments designed to restrict the solution concentration of dissolved species to a low-but-measurable range far from saturation, where rate-suppression effects are minimized.

With the aforementioned perspective, the work presented in this paper is focused on proposing a rigorous approach to understand the dissolution behavior and kinetics of boron-containing bioactive glasses from the fundamentals of glass structure. Accordingly, a borosilicate-based model bioactive glass series has been studied in the ternary system

Na_2O-B_2O_3-SiO_2 (Figure S1) where glasses with varying thermal histories have been synthesized to demonstrate their impact on the structure and dissolution behavior. The borosilicate glass system has been selected because of its high potential for application in bone regeneration and tissue engineering.[9,36,66,67] The incorporation of P_2O_5—a typical component of bioactive glasses–to the studied glass system has been avoided, since CaO-B_2O_3-P_2O_5-SiO_2 and Na_2O-B_2O_3-P_2O_5-SiO_2 based quaternary systems have limited glass forming regions.[68-71] Additionally, while most bioactive glasses contain CaO as a major component, we have chosen a glass system devoid of calcium due to the following reasons:

(i) Glasses have not been designed in the Na_2O-CaO-B_2O_3-SiO_2 system to avoid competition between two network modifying cations (Na^+ and Ca^{2+}) for charge balancing BO^{4-} units, as this would introduce additional complexity to the structural and chemical interpretation of dissolution results.

(ii) Glasses could have been designed in the CaO-B_2O_3-SiO_2 system, but this glass system does not have as extensive of a glass forming region as the Na_2O-B_2O_3-SiO_2 system (Figure S1). For example, it is difficult to obtain both the binary end-member glasses in the CaO-B_2O_3-SiO_2 system. Moreover, CaO, though an important component (favors osteoblast proliferation, differentiation and extracellular matrix mineralization), is not a necessary component of bioactive glasses and other bioceramics. CaO-free bioactive glasses[72-74] and bioceramics[75,76] have also been proposed in the literature.

The dissolution experiments have been performed in deionized (DI) water at a temperature of 65 °C in order to expedite the reaction processes. This protocol deviates from the more typical 37 °C condition common to bioglass studies, though the same design of experiments

can also be implemented at 37 °C. Similar dissolution experiments to study degeradation behavior of phosphate-based bioactive glasses in DI water at 98 °C have been reported in literature.[77-79] The choice of dissolution medium was made considering that DI water does not chelate or form complexes with glass dissolution products to alter the degradation rates. The importance of studying interactions between bioactive glasses and DI water has been highlighted by several other researchers.[77-85] Further it is worth mentioning that although the present study is focused on melt-quenched glasses, the issues pertaining to choice of dissolution medium, using SA/V vs. M/V approach, and static vs. dynamic tests are also valid for sol-gel-based bioactive glasses.

2.2 Experimental

2.2.1 Synthesis of the glasses

Glasses in the system 25 Na_2O – *x* B_2O_3 – (75-*x*) SiO_2 (*x* between 0 – 75 mol.%) with constant $Na_2O/(B_2O_3 + SiO_2)$ = 0.33 were synthesized using the melt-quench technique. High-purity powders of SiO_2 (Alfa Aesar; >99.5%), H_3BO_3 (Alfa Aesar; ≥98%), Na_2SiO_3 (Alfa Aesar; >99%) and Na_2CO_3 (Fisher Scientific; ≥99.5%) were used as precursors. Batches corresponding to 50 g oxides were melted in Pt-Rh crucibles for 1 h in air, at temperatures ranging from 1200-1650 ºC depending on B_2O_3/SiO_2 ratio in the glass composition. In order to elucidate the impact of thermal history, the glass melts were quenched by two routes: (1) splat quenched between two copper plates, so as to maximize fictive temperature and residual stress in the glass; versus (2) quenching on a metallic plate, followed by annealing to remove all residual stress (as shown in Figure 2.1). The procedure for annealing is described in the next section. Samples have been labeled as B–*x*–A, and B–*x*–Q, where *x* represents the batched B_2O_3 concentration while A and Q refer to annealed

and quenched, respectively. The amorphous nature of all glass samples was confirmed by X-ray diffraction (XRD) (PANalytical – X'Pert Pro; Cu K_α radiation; 2θ range: 10º–90º; step size: 0.01313º s–1). The concentration of SiO_2 and B_2O_3 in synthesized glasses was determined by inductively coupled plasma – optical emission spectroscopy (ICP – OES; PerkinElmer Optima 7300V), while sodium concentration in experimental glasses was determined by flame emission spectroscopy (PerkinElmer Flame Emission Analyst 200). The concentration of B_2O_3 in glasses was analyzed by digesting the glass samples in a 1:1 hydrofluoric acid to water matrix; meanwhile for SiO_2 analysis, samples were mixed with known quantities of sodium tetraborate flux and digested by stirring in a 1:1 hydrochloric acid to water matrix. Each solution was analyzed via ICP-OES against a matrix matched blank and standard. With regard to sodium analysis, samples were digested in perchloric/hydrofluoric acid mixtures using multiple heating and drying cycles; samples were ultimately mixed into hydrochloric acid and analyzed via flame emission spectroscopy against matrix matched blanks and standards. Table 2.1 presents the experimental glass compositions.

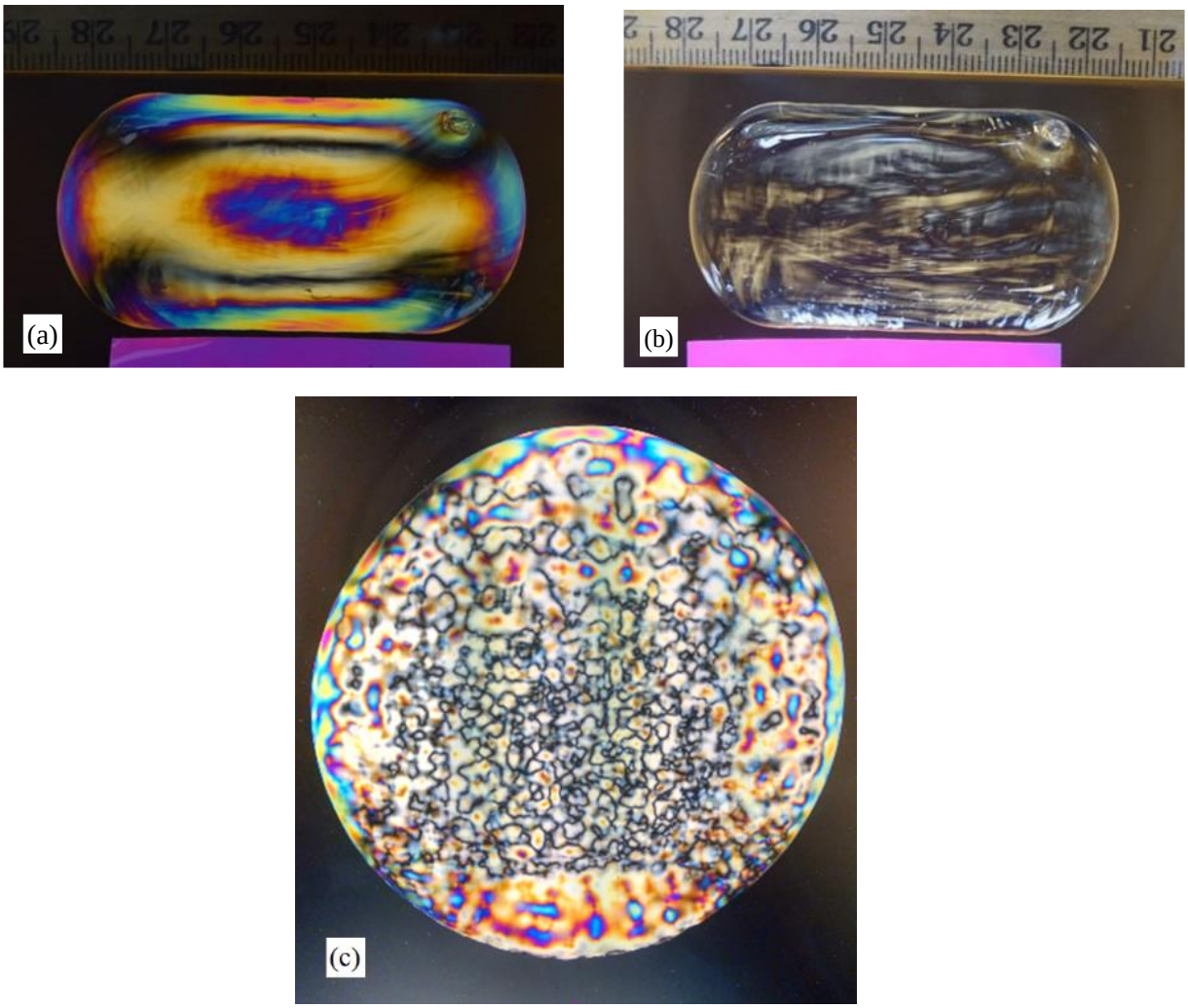

Figure 2.1. *An image of a sodium aluminoborosilicate glass as seen under a polarimeter (a) after annealing at T_g^* – 50 °C for 1 h, and (b) after annealing at T_g – 50 °C for several hours. Figure 1c shows the image of a splat-quenched (between two copper plates) sodium borosilicate glass under a polarimeter. The colored pattern observed in the glass (when view through polarized light) is created by stress and is divided into zero, first, second, and third order fringes. This pattern is used to obtain approximate retardation values.*

Table 2.1. *Experimental compositions (mol.%) and density (g/cm^3) of glasses. Note: The concentration of SiO_2 was calculated by subtracting the sum of experimentally measured concentration of Na_2O and B_2O_3 from 100, i.e. $SiO_2 = 100 – (Na_2O + B_2O_3)$.*

	Annealed				Quenched			
Glass	**Na_2O**	**B_2O_3**	**SiO_2**	**Density**	**Na_2O**	**B_2O_3**	**SiO_2**	**Density**
B-0	24.0	--	76.0	2.355±0.003	25.1	--	74.9	2.331±0.006
B-18.75	23.9	17.5	58.6	2.4588±0.0001	25.1	18.4	56.5	2.423±0.006
B-37.5	25.0	37.1	37.9	2.4191±0.0009	25.1	37.2	37.7	2.386±0.003
B-56.25	25.2	55.3	19.4	2.3167±0.0003	24.8	55.1	20.1	2.292±0.003
B-75	25.2	74.8	--	2.2044±0.0001	25.9	74.1	--	2.183±0.002

2.2.2 Methodology of annealing the glasses

The B-*x*-A series of glass melts were quenched on a metallic plate, followed by coarse annealing at temperatures corresponding to (T_g^* - 50) °C for 1 h, where T_g^* is the predicted glass transition temperature obtained from the SciGlass database.[86] The annealed glasses showed polariscopic evidence of residual stress, like that shown in Figure 2.1a. The glass transition temperature of these glasses was subsequently measured using differential scanning calorimetry (DSC; STA8000, PerkinElmer Inc.) at a heating rate of 20 °C per min under a continuous flow of N_2 gas (Pt pan, particle size of glass sample: 300 – 425 μm). The glasses were then annealed again at temperatures 10-50 °C below their respective glass transition temperatures for several hours and then slow-cooled to remove all the residual stress and obtain glass samples as shown in Figure 2.1b.

2.2.3 Glass transition and fictive temperature measurements

The specific heat capacity (C_p) of the glass samples was measured utilizing a differential scanning calorimeter (DSC; NETZSCH Pegasus 404 C). The absolute value of C_p was determined by subtraction of the empty Pt crucible baseline and adjustment of the heat flow values based on sapphire standard runs and corresponding literature values. The

enthalpic fictive temperature (T_f) of the samples was calculated by analysis of the temperature dependent specific heat capacity using the unified enthalpy matching method.[87,88] First, glasses were heated from room temperature to the supercooled liquid region above the glass transition temperature, with a heating rate of 20 °C/min, to obtain the original thermal-history-dependent C_p curve. Then, glasses were held isothermally at the equilibrium supercooled liquid region for 2 minutes to erase their thermal history. After that, the glasses were cooled from the supercooled liquid to room temperature at a cooling rate of 20 °C/min. Finally, glasses were reheated from room temperature to the supercooled liquid region above the glass transition temperature at the heating rate of 20 °C/min to obtain the C_p curve dependent on the thermal history defined by the 20 °C/min cooling rate. The second C_p curve can be used to estimate the fictive temperature of the defined thermal history, applying Moynihan's fictive temperature calculation method.[89] The area between the two C_p curves corresponds to the enthalpy difference between the two non-equilibrium states which is proportional to the fictive temperature difference. The fictive temperature of the original thermal history (quenched or annealed) was estimated by shifting the fictive temperature, as described by Guo et al.[87]

2.2.4 Structural analysis

The structure of both splat-quenched and annealed glasses has been studied using multi-nuclear magic angle spinning - nuclear magnetic resonance (MAS NMR) spectroscopy. The MAS NMR spectra of ^{11}B and ^{23}Na were acquired using commercial spectrometers (VNMRs, Agilent) and MAS NMR probes (Agilent). The samples were powdered in an agate mortar, packed into 3.2 mm zirconia rotors, and spun at 20 kHz for ^{11}B MAS NMR and 22 kHz for ^{23}Na MAS NMR. ^{23}Na MAS NMR data was collected at

16.4 T (185.10 MHz resonance frequency), using a 0.6 μs (~π/12 tip angle) pulse width for uniform excitation of the resonances. A range of 400 to 1000 acquisitions were co-added and the recycle delay between scans was 2 s. ^{11}B MAS NMR experiments were conducted at 11.7 T (160.34 MHz resonance frequency), incorporating a 4 s recycle delay, short rf pulses (0.6 μs) corresponding to a π/12 tip angle, and signal averaging of 400 to 1000 scans. The acquired spectra were processed with minimal apodization and referenced to aqueous boric acid (19.6 ppm) and aqueous NaCl (0 ppm). Fitting of the MAS NMR spectra was performed using DMFit[90] and, accounting for distributions in the quadrupolar coupling constant, the CzSimple model was utilized for ^{23}Na MAS NMR spectra. The "Q MAS ½" and Gaus/Lor functions were used to fit 3- and 4-fold coordinated boron resonances in the ^{11}B MAS NMR data, respectively, and N_4 was calculated from the relative areas of these peaks, with a small correction due to the overlapping satellite transition of the 4-fold coordinated boron peak.[91]

^{29}Si MAS NMR data were collected at 4.7 T (39.69 MHz resonance frequency) using a 5 mm MAS NMR probe. Powdered samples were packed into 5mm zirconia rotors and all measurements were conducted using 5 kHz sample spinning. Measurements were made with signal averaging of 320 to 2200 acquisitions, using π/6 pulse widths of 1.4 μs and recycle delays of 90 s. ^{29}Si spectra were processed without additional line broadening and referenced to tetramethylsilane at 0.0 ppm.

2.2.5 Chemical dissolution studies

2.2.5.1 Surface area analysis

The glasses were crushed and sieved to obtain powders with particle size varying between 300 – 425 μm. The powders were ultrasonicated in acetone to remove fines (i.e. fine powder). This process was repeated three times to ensure that all the fines sticking to

the surface of the larger glass particles were removed. The glass particles were dried overnight at 80 °C in ambient air and analyzed for any structural changes before and after acetone-washing using Fourier Transform Infrared (FTIR) spectroscopy. The IR spectra were acquired using a single-bounce diamond attenuated total reflectance (ATR) apparatus (FTIR-UATR, Frontier^{TM}, Perkin Elmer Inc.; scanning resolution: 4 cm^{-1}, 32 scans for background and samples). Geometric SA analysis of washed powders was performed using ImageJ software after capturing microscope of images of ~1000 particles per sample via an optical microscope (Zeiss Axioskop 40) at ~50X magnification. Figure S2 shows an optical microscope image of borosilicate glass particles used in this study for SA analysis. The high-contrast bright-field optical microscope images of the glass particles were analyzed by converting to grayscale and then applying a binary filter with custom intensity thresholds to capture particle edges. The two-dimensional (2D) SA projection and circularity of each particle was calculated from its displayed boundary outline as detected by ImageJ software. Further, using a spherical approximation of glass particles, the average three dimensional (3D) SA was calculated. These results were combined with experimental density values (measured using Archimedes' method by measuring mass of sample in air and in an organic solution; number of samples per composition = 5; standard deviation <0.009 g cm^{-3}) to determine the specific surface area of the washed powders (95% confidence interval: 4019-4453 mm^2/g). Finally, the mass of glass particles corresponding to SA/V = 5 m^{-1}, where V = 50 mL, was calculated. The suitability of the spherical shape approximation in this geometric SA measurement was verified by showing that most particle aspect ratios were near to 1, characteristic of a circle. Total uncertainty in SA in a

given experiment—based on the breadth of the particle distribution and density/mass error—was estimated to be on the order of 20%.

2.2.5.2 Chemical dissolution Behavior in DI Water

The chemical dissolution behavior of glasses was studied by immersing 56.0 mg of acetone-washed glass particles in 50 mL of DI water, corresponding to a SA/V = 5 m^{-1}. The powder – water mixtures were immediately sealed into sterilized polypropylene flasks and were placed in an oven at 65 °C. Parallel dissolution experiments were performed in time durations varying between 1 h to 14 days. In addition to analyses of neat (unused) and blank (glass-free) control solutions, all of the experiments were performed in duplicate to evaluate the uncertainty of final results. The glass powders remaining after dissolution experiments were dried for 2-3 days at 70 °C and then characterized by XRD and FTIR spectroscopy. The ATR-IR spectra were acquired using the same apparatus and procedure previously mentioned. The pH evolution of deionized water during glass corrosion was measured using a pH meter (Mettler Toledo InLab® Pro-ISM). The solutions obtained after dissolution experiments were chemically analyzed by inductively coupled plasma – optical emission spectroscopy (ICP-OES, PerkinElmer Optima 7300 DV). The normalized loss (*NL*) of sodium, boron and silicon ions from glasses into the DI water was calculated using equation (1),

$$NL_i = \frac{C_i}{\left(\frac{SA}{V}\right) f_i} \qquad (1)$$

where C_i is the concentration of element *i* in the solution as detected by ICP-OES, and f_i is the mass fraction of the element *i* in the glass. Normalized loss data was plotted against time and was linearly fit to determine Stage I dissolution rate.

Statistical significance of ICP-OES data was determined by performing t-tests on duplicate normalized loss and dissolution rates. In each case, one tailed test was performed to test a significance level of $p < 0.05$ (95 % confidence) in order to compare elemental release values and assess the influence of thermal history upon Stage I dissolution kinetics (*p* values can be seen in Table 2.4).

2.3 Results

2.3.1 Glass formation

All glasses synthesized during this study were transparent in appearance and verified as amorphous via XRD analysis (Figure S3). The experimental glass compositions, as analyzed by ICP-OES and flame emission spectroscopy, are in good agreement with their batched analogs (within ±1 mol. %) (Table 2.1). The stress levels in annealed and quenched glasses were analyzed using a polariscope. Based on the low level of stress-induced retardation in annealed glass samples with thickness of ~5mm, residual stresses were estimated to be less than 100 MPa (as shown in Figure 2.1b). Meanwhile, quenched samples exhibited first- and higher-order fringes indicative of significant residual stresses, as shown in Figure 2.1c.

2.3.2 Impact of thermal history on structure of glasses

Regarding compositional dependence of the glass transition temperature (T_g), initial addition of B_2O_3 (18.75 mol.%) in these glasses resulted in a substantial increase (~80 °C) in T_g values. However, further addition of B_2O_3 at the expense of SiO_2 resulted in a monotonic decrease in the T_g of glasses. The glass transition temperature as a function of B_2O_3 content is shown in Figure S4. It is preferred to display in terms of configurational heat capacity (Cp_{config}) to show the pronounced difference of the thermodynamics as a

function of glass composition. Cp_{config} of the glasses was calculated by subtracting the vibrational heat capacity from the total heat capacity. Temperature dependent vibrational heat capacity throughout the glass transition range was estimated by the extrapolation of the Maier-Kelley fit[92] of the glass heat capacity.

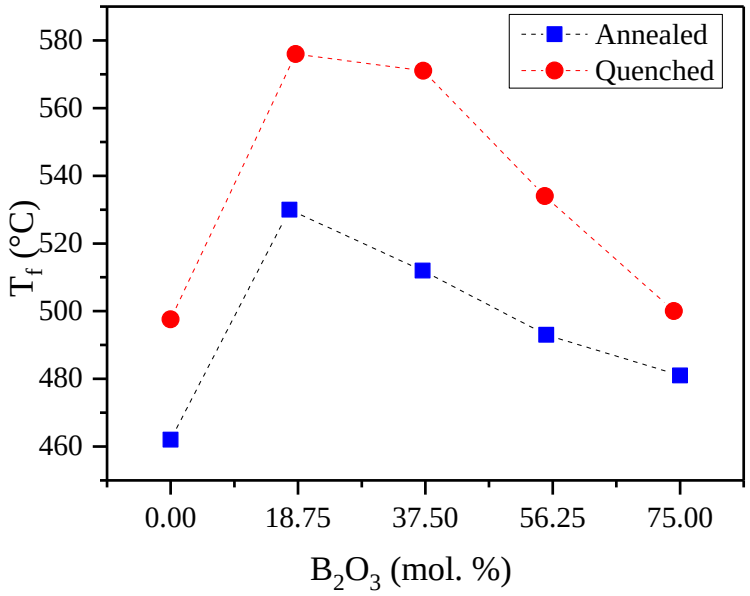

Figure 2.2. *Fictive temperature (T_f) as a function of experimental B_2O_3 (mol.%) content in glasses.*

Figure 2.2 presents the variation in fictive temperature (T_f) of both splat quenched and annealed glasses as a function of their B_2O_3 content. The fictive temperature corresponds to the temperature at which the structure of the equilibrium liquid freezes in the non-equilibrium solid. As expected, the T_f of all the quenched glasses was measured to be higher than their annealed analogues. However, a peculiar trend was observed with respect to variation of T_f as a function of SiO_2/B_2O_3 ratio in glasses. While glasses in the silica-rich region of the $Na_2O–B_2O_3–SiO_2$ ternary system demonstrated a marked influence of thermal history on their T_f values; this difference decreased with increasing B_2O_3

content. For example, $Na_2O–B_2O_3–SiO_2$ glass with 18.75 mol.% B_2O_3 exhibited a difference of ~46°C between the T_f values of quenched and annealed glasses, while binary Na_2O-B_2O_3 glass had a difference of ~19 °C between its two versions. This behavior can be correlated to the evolution of the fragility index[93] as a function of B_2O_3 content. The fragility index of the glass, which is defined by the temperature dependence of viscosity in the vicinity of the glass transition,[93,94] is scaled linearly with the ergodicity breaking process.[95] Upon quenching, fragile glass formers depart at a much faster rate than the strong glass formers[96] and show pronounced non-exponential relaxation behavior.[97] Heat capacity measurements can be used to make a comparison of thermodynamic fragility[93] as a function of composition. The normalized jump of Cp_{config} at the glass transition range is proportional to the fragility, while the normalized width of the glass transition ($\Delta T_g/T_g$) is inversely proportional to the fragility.[98] The Cp_{config} is an unscaled value[93] and a rigorous normalization procedure requires additional thermodynamic data such as configurational entropy. However, the width of the glass transition can be normalized by the glass transition temperature. Figure S5 displays the Cp_{config} of the three ternary glasses vs. temperature normalized by their glass transition temperatures. The temperature difference between the onset of the rise of the Cp at the glass transition and fall of the Cp at the glass transition was used to calculate the ΔT_g and it is normalized by the T_g for each composition. Figure S6 shows the linear correlation between the fragility $[(\Delta T_g/T_g)^{-1}]$ and fictive temperature change during the sub-T_g annealing of the glass. Thus, thermal history dependence should be evaluated as a function of the fragility of the glass forming liquid, which is controlled by the dimensionality of the network.

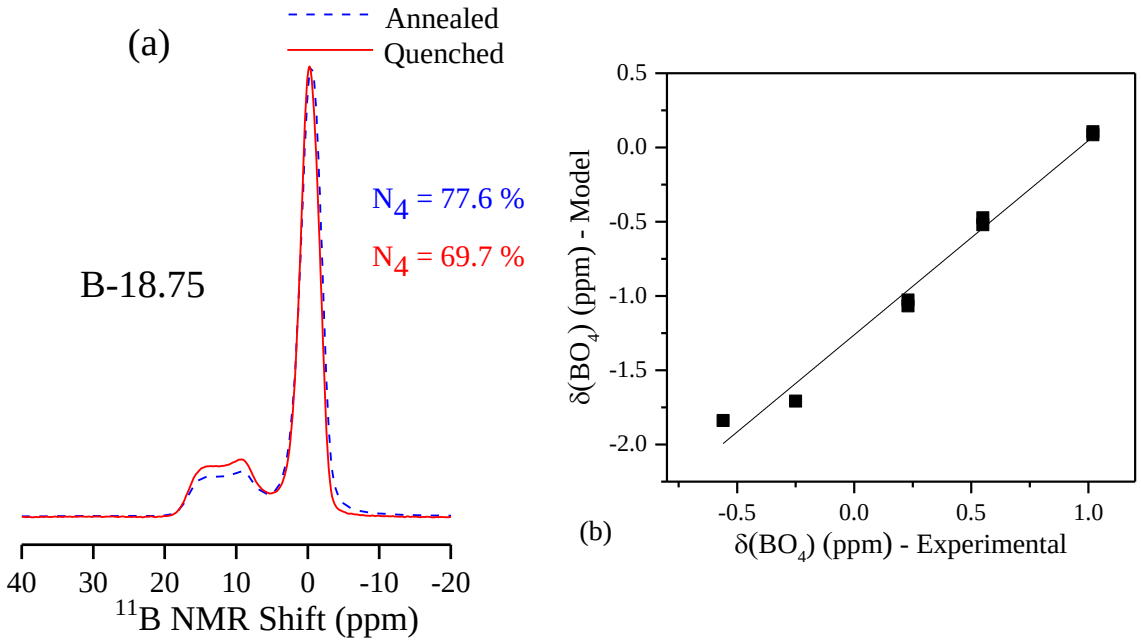

Figure 2.3. *(a) ^{11}B MAS NMR spectra of glasses B-18.75-A and B-18.75-Q. Samples were spun at 20 kHz and data was collected at 11.7 T. BO_4 peak position (near 0 ppm) was quantified for all glasses in order to linearly fit data (b) based upon the model by Martens and Müller-Warmuth.*[104]

Table 2.2. *Borate speciation in glasses as calculated from ^{11}B MAS NMR (Standard deviation: ±1 %)*

	Annealed		Quenched	
Glass	**N_3 (%)**	**N_4 (%)**	**N_3 (%)**	**N_4 (%)**
B-18.75	22.4	77.6	30.3	69.7
B-37.5	40.6	59.4	43.2	56.8
B-56.25	53.4	46.6	55.6	44.4
B-75	62.3	37.7	62.6	37.4

In order to obtain further insight into impact of chemical composition and thermal history on the structure of glasses, ^{23}Na, ^{11}B, and ^{29}Si MAS-NMR were employed. Figure 2.3a presents the ^{11}B MAS NMR spectra of glass B-18.75 (both annealed and quenched). The spectra show two main features, a broad doublet associated with BO_3 units centered at ~12 ppm and a peak at ~0 ppm attributed to BO_4 units.[32,99,100] The observed features in the

^{11}B spectra for the B-18.75 glasses are representative of all the glass samples discussed in this study. Table 2.2 provides the results of BO_3 and BO_4 fraction for all the glasses with varying SiO_2/B_2O_3 ratio and thermal history (annealed vs. quenched). The concentration of BO_4 units (N_4) in these glasses varies between 37 – 78% (irrespective of thermal history), wherein, the glass with lowest B_2O_3 concentration (B–18.75) exhibited the highest N_4 value, while an increase in boron content resulted in a gradual decrease in proportions of BO_4 unit. The BO_4 peak position shows a slight positive shift with increasing B_2O_3 content, which, in glasses, is usually attributed to intermixing between SiO_4 and BO_4 units. Multiple Quantum MAS NMR (MQMAS) and Raman data on borosilicate glasses have shown BO_4 units to have higher tendency to mix (in 2Si-2B or 3Si-1B units) with silicate units than BO_3 (either ring or non-ring variety).[100-103] Thus, for SiO_2-rich glasses, BO_4 units exist more readily and chemical shift is more negative due to the increase in shielding as SiO_4 replaces BO_3 with regard to BO_4 linkages.[104] The chemical shift data was fit using the model by Martens and Müller-Warmuth,[104] where molar fractions of SiO_2 and Na_2O were used in equation 2 to predict BO_4 chemical shift for any given composition.

$$\delta(BO_4)/\text{ppm} = -3.4x_{Si}+2.8x_{Na}-0.62 \qquad (2)$$

Figure 2.3b presents the comparison between experimental and model ^{11}B (BO_4) MAS NMR chemical shifts as calculated using equation 2. The linear relationship shown clearly demonstrates statistical mixing between silicate and borate groups. In other words, as the B_2O_3/SiO_2 ratio increases, there are fewer silicate tetrahedra available to mix with BO_4 groups, and a concomitant increase in chemical shift as the next-nearest neighbor cations shift towards a higher fraction of trigonal B.

Table 2.3. *Silicate speciation in glasses as calculated from a combination of ^{11}B MAS NMR, analyzed glass compositions, and the calculated fraction of sodium as a network modifier. B-56.25A was assumed to be 100 % Q^4 due to complete Na consumption as a charge compensator for N_4.*

	Annealed		Quenched	
Glass	Q^3	Q^4	Q^3	Q^4
B-0	63.3 %	36.7 %	67.1 %	32.9 %
B-18.75	23.0 %	77.0 %	28.2 %	71.8 %
B-37.5	6.0 %	94.0 %	8.2 %	91.8 %
B-56.25	--	100 %	1.4 %	98.6 %

Figure S7 presents the ^{29}Si MAS NMR spectra of glasses measured in this study. Due to the complications from Q^n (Q is the degree of polymerization in silicate network and n is the number of bridging oxygen) resonances with different next-nearest neighbor distributions, the ^{29}Si MAS NMR spectra of these glasses could not be de-convoluted. Therefore, the Q^n speciation in the studied glasses was calculated by a combination of experimental values of N_4 (from ^{11}B MAS NMR), analyzed glass compositions, and calculated Na fraction acting as a network modifier.[105-108] Table 2.3 presents the calculated silicate speciation for these glasses. In the binary sodium silicate glass (B-0), sodium is solely acting as a network modifier, thus creating non-bridging oxygen (NBO) in the silicate network. The silicate network of annealed glass B-0-A is dominated by 63.3% Q^3 units with the remaining 36.7% Q^4. The introduction of B_2O_3 in the silicate glass network (B-18.75) resulted in a significant increase in the fraction of Q^4 at the expense of Q^3 units, while further increase in B_2O_3 concentration to 37.5 mol.% resulted in nearly full polymerization of the silicate network (94.0% Q^4), and 56.25 mol.% resulted in complete polymerization (100% Q^4). These results can be explained on the basis of the Dell, Yun and Bray model[105-107] for structural speciation in borosilicate glasses, wherein the glass B-18.75 has R (Na_2O/B_2O_3) = 1.33, K (SiO_2/B_2O_3) = 3, and R* (0.5 + K/16) = 0.69, while

glass B-37.5 has R = 0.66, K = 1, and R* = 0.56. According to Dell, Yun and Bray model [104], if R > R*, the majority of sodium is expected to create NBOs in the silicate glass network.[104] On the other hand, for $R \leq R^*$, which is true for glasses B-56.25 and B-75, the alkali cations act as charge compensators for the four-coordinated boron atoms. These predictions can be validated by understanding the compositional dependence of ^{23}Na MAS NMR spectra of annealed glasses as presented in Figure 2.4. The ^{23}Na MAS NMR spectrum of binary Na_2O-SiO_2 glass exhibits a broad peak with a maximum at –4.7 ppm, and it shifts towards lower frequencies as B_2O_3 is substituted for SiO_2. This shift implies an increase in average Na–O bond length or coordination number (CN)[109,110] and a change in its structural role from network modifier to charge compensator.[111] While sodium acts either completely or partially as a silicate network modifier in glasses with B_2O_3 content varying between 0-37.5 mol.%, it exclusively acts as a charge compensator in glasses with B_2O_3 >37.5 mol.%, as is evident from the featureless broad peaks with maxima at –11.8 ppm shift for both B-56.25 and B-75 (see Figure 2.4). This trend can also be observed in the average coordination number of Na (as calculated using the formulas from Koller et al.[110] and Tagg et al.[112]), which varies from ~5.35-5.70 as B_2O_3 increases from 0 to 37.5 mol. % but holds constant at ~5.70 while sodium acts solely as a charge compensator in B_2O_3-rich compositions.

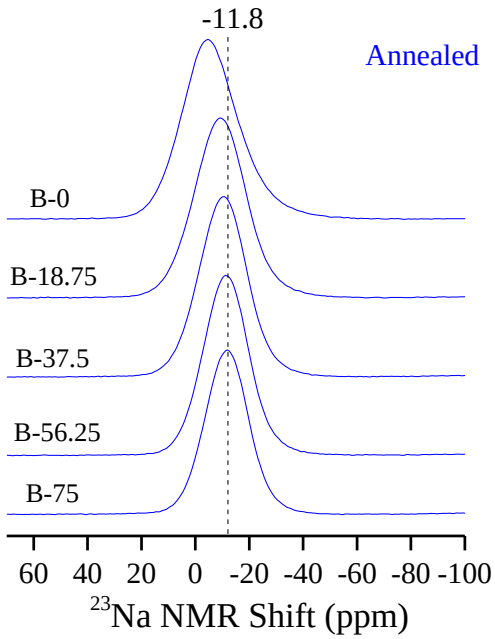

Figure 2.4. *^{23}Na MAS NMR spectra of annealed glasses. Samples were spun at 22 kHz and data was collected at 16.4 T.*

In terms of impact of thermal history on the structure of glasses, the most noticeable differences were observed in the borate speciation in SiO_2 rich glasses (as shown in Table 2.2). While the N_4 in glass B-18.75 was higher in the annealed sample (B–18.75–A) vs. its quenched (B–18.75–Q) analog by ~8%, this difference gradually decreased with an increase in B_2O_3/SiO_2 ratio, resulting in almost equal N_4 in the two B-75 glasses. These results may be explained on the basis of higher melt viscosity of SiO_2 rich glass compositions in comparison to their B_2O_3 rich analog. Therefore, rapid quenching of the SiO_2 rich glass will result in more disordered structure (higher T_f), thus higher number of BO_3 units. The other plausible reason for the minimal impact of thermal history on boron coordination in B_2O_3 rich glasses is the unavailability of oxygen atoms in the glass structure, normally required for the transformation of BO_3 to BO_4 units as shown in equation (3).[113,114]

$$\tfrac{1}{2}Na_2O + B\O_3 = Na^+ + B\O_4^- \quad (3)$$

2.3.3 Chemical dissolution behavior of glasses

All dissolution experiments were monitored for pH and B, Na, and Si concentration in reacted solutions. Table S1 and S2 presents the pH, elemental concentration, and normalized mass loss (NL) evolution as a function of time and glass composition for both the annealed and quenched samples, respectively. Static experiments with B-0, B-18.75, B-37.5, and B-56.25 were conducted for 336 hours, whereas the experiments with B-75 were conducted up to a maximum of 24 hours due to substantially faster dissolution rates. In the case of B-56.25 and B-75, the samples were completely dissolved at the end of the 14-day experiments, which is indicative of the relatively rapid dissolution of these glass compositions. The complete dissolution of the glass volume introduces not only an artificial plateau in solution concentration, but also implies substantially varying SA over the course of the experiment, complicating its interpretation. As a result, we focus our discussion on dissolution behavior of the B-0, B-18.75, and B-37.5 glasses. We have separated this section into the following subsections: (1) pH and elemental release rates, (2) relationship between normalized dissolution and structure, and (3) influence of thermal history on dissolution behavior of glasses.

2.3.3.1 Dependence of pH and normalized loss on composition and thermal history of glasses

As shown in Table S1, the pH increases for each sample, with the most rapid increase observed for binary sodium silicate (B-0) glass samples. The pH for the B-0 sample increased from 5.8 to ~10 after 1 hour of immersion in deionized water, and continued to increase to ~10.7 after 12 hours of immersion. The observed pH increase for

the B-0 samples occurs because of an increase in the dissolved Na concentration. Sodium is being preferentially released in the annealed B-0 samples, evident by the greater than 3× increase in the normalized Na release (80.7 ±0.5 g/m^2) in comparison to Si (26.6 ±2.8 g/m^2) after 6 hours of immersion in deionized water. The preferential release of Na is the result of an ion-exchange reaction mechanism, where Na ions are being exchanged by dissolved hydronium ions in the glass structure.[115,116] The aforementioned conclusion is also supported by the absorption band at ~1220 cm^{-1} in the FTIR spectra of reacted B-0-A and B-0-Q glass samples (Figure 2.5a) suggesting the formation of a Si–OH-rich hydration layer on the glass surface.[19] The higher-wavenumber regions of the same FTIR spectra shared in Figure 2.5b and 2.5c also show the development of bands at ~1630 cm^{-1} and ~3350 cm^{-1}, associated with H_2O bending modes and OH stretching, respectively.[117] This is consistent with the formation of hydrated silica gel like layer ($\equiv Si - O - Na + H_3O^+ \leftrightharpoons \equiv Si - OH + Na^+ + H_2O$) resulting from the exchange of hydronium ions for Na, typically characterized as Stage I of glass corrosion.[118] In comparison to the B-0 samples, the solution pH for B-18.75 and B-37.5 samples increased from 5.8 to ~7.5 after 1 hour and up to 9.5 after 12 hours (Table S1). The difference in the magnitude of the pH increase between glass compositions with and without boron may be the result of two interrelated factors: (i) the boron being released from glass forms an acidic species in solution that serves to neutralize the alkalinity created by the release of Na ions, and/or (ii) Na ions are being preferentially released slower in these glass compositions relative to the sodium silicate composition because Na ions that were originally present at Si non-bridging oxygen sites in the glass structure are now serving to charge compensate for the BO_4 units. A comparison of the average normalized loss for B (17.2 ±3.9 g/m^2) and Na (16.8 ±2.6 g/m^2)

for the annealed B-18.75 sample suggests congruent release of Na and B after six hours of immersion in deionized water, which is indicative of neutralization. However, B (204.5 ±1.2 g/m^2) is being released 1.3× faster than Na (155.6 ±10.7 g/m^2) from the B-37.5-A glass after six hours of immersion, indicative of slightly slower Na release relative to B, thus decreasing the pH and mitigating the effect of Na in solution. Similar results were obtained for the splat-quenched B-18.75 and B-37.5 analogues (Table S2). These results suggest that both processes may be occurring, and they are directly related to changes in glass composition and structure.

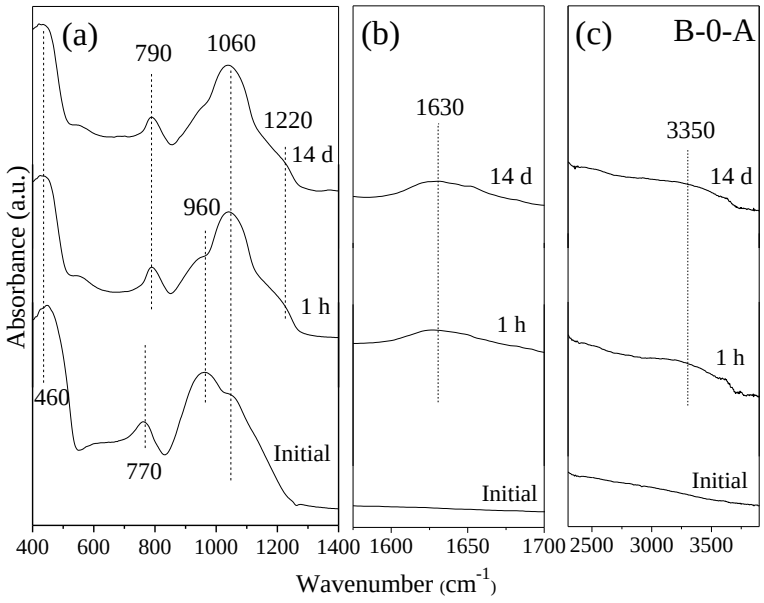

Figure 2.5. *FTIR spectra of glass B-0-A before and after immersion in deionized water for 1 h, and 14 days.*

With regard to impact of thermal history on the dissolution behavior of glasses, in the binary sodium silicate glass (B-0), Si is being released 2.3× faster from quenched (74.1 ±11.5 g/m^2) as compared to its annealed (33.2 ±3.1 g/m^2) analogue after 12 h, while Na release occurs 1.1× faster in quenched than annealed (147.5 ±4.4 vs. 133.5±0.7 g/m^2) during the same immersion time. Similarly, B-18.75 shows 1.5× (63.4 ±6.9 vs. 43.5 ±3.9

g/m^2) and 1.8× (73.8±5.9 vs. 41.4 ±2.9 g/m^2) faster Si and Na release from splat-quenched vs. annealed glasses after 12 h of immersion. However, thermal history had minimal impact on the dissolution behavior of Si and B from glass B-37.5. The normalized mass loss of Si from glass B-37.5-A was 73.6 ± 9.3 g/m^2 versus 99.1 ± 12.4 g/m^2 for B-37.5-Q after 6 h of immersion in water, thus, demonstrating the equivalent normalized loss for the quenched sample. However, with increasing immersion time to 12 h, the Si normalized mass loss was measured to be 90.0 ± 19.4 g/m^2 and 125.4 ± 5.0 g/m^2 for B-37.5-Q and B-37.5-A, respectively, depicting slightly slower degradation of the quenched sample in comparison to its annealed analogue. With further increase in immersion time to 24 h and 72 h, the NL of Si was measured to be almost equal (24 h: 142.6 ± 0.3 g/m^2; 72 h: 200.8 ± 3.8 g/m^2) for both quenched and annealed samples. For boron, both annealed and quenched samples showed almost equal NL after 12 h of immersion in water, for example, 271.5 ± 10.1 g/m^2 after 12 h, and 269.9 ± 0.9 g/m^2 after 24 h, thus, showing minimal impact of thermal history on their dissolution behavior. Here it needs to be highlighted that the normalized loss data for quenched vs. annealed glasses has been verified to be statistically dissimilar with $p < 0.05$.

2.3.3.2 Dependence of dissolution rates on composition and thermal history of glasses

To calculate the normalized dissolution rate, the averaged normalized loss data were plotted as a function of time (Figure 2.8), and a linear regression performed on the data collected from 6 to 24 hours. The slope of the line provides an estimate of the early-stage normalized dissolution rate. An example of the regression is displayed in Figure 2.6 for the glass B-0-A and the corresponding rates are provided in Table 2.4. These fits should only be considered estimates, since (many of) the curves, like Figure 2.6, showed some

evidence of nonlinear release and a non-zero intercept at t=0, and none of the fits were constrained to pass through (0,0). These limitations with fitting NL data with a single rate have been well-described in the literature.[119,120] Similar to the normalized loss, the average fitted rate of Na (4.1 g/[m^2 h]) is higher than Si (2.5 g/[m^2 h]), indicative of preferential Na extraction. Further, it is well known that for borosilicate glasses dissolved under alkaline conditions, one-unit increase in pH can result in as much as one order of magnitude increase in the normalized dissolution rate.[121,122] Due to this significant influence of pH on the rate of glass dissolution, direct comparison of the annealed and quenched samples is difficult because the pH evolution for the individual experiments was different (see Table S1 and S2). Therefore, to evaluate the influence of structure on the normalized dissolution rates, all rates were adjusted to a pH of 9.0 using equation 3.[122-123]

$$\log_{10} r_F = \log_{10} r_I + \eta(9 - pH_T) \quad (3)$$

In equation 3, r_F is the pH-adjusted rate in g/(m^2 h), r_I is the unadjusted rate in g/(m^2 h), η is the pH power law coefficient, and pH_T is the measured pH of test solution. Here we assumed a typical literature value for the pH power-law coefficient of 0.40 for all glass compositions.[122] For example, the glass B-0-A had an unadjusted Si normalized dissolution rate of 2.5 g/(m^2 h) at an average pH of 10.6 ±0.3 and an adjusted dissolution rate (at pH 9.0) of 0.6 g/(m^2 h). Table 2.4 presents the unadjusted and pH-adjusted rates for B, Na, and Si. Briefly, the pH adjustment resulted in a change in normalized loss rate between 1.2×−4× in magnitude. These results have been discussed in detail in the discussion section.

Table 2.4. *Average unadjusted and pH-adjusted release rate (g/[m^2 h]), respectively, based on B, Si, and Na release for both quenched and annealed samples. p values were calculated to assess significance of rate differences with varying thermal history.*

Unadjusted Release Rate, g/(m^{2}h)								**Statistical Comparison**		
		Annealed			**Quenched**			***p* values**		
Glass	**Avg. pH**	**B**	**Si**	**Na**	**B**	**Si**	**Na**	**B**	**Si**	**Na**
B-0	10.6±0.2	--	2.5±1.6	4.1±0.0	--	3.6±1.1	5.2±2.3	--	0.259	0.291
B-18.75	9.3±0.4	3.1±0.1	2.7±0.1	2.2±0.2	7.2±0.5	5.3±1.2	4.9±0.6	0.004	0.043	0.011
B-37.5	9.2±0.1	19.6±0.8	9.8±0.2	16.7±0.6	20.1±0.6	6.6±2.2	13.7±0.3	0.274	0.088	0.012
pH-Adjusted Release Rate, g/(m^{2}h)								**Statistical Comparison**		
		Annealed			**Quenched**			***p* values**		
Glass	**Avg. pH**	**B**	**Si**	**Na**	**B**	**Si**	**Na**	**B**	**Si**	**Na**
B-0	9.0	--	0.6±0.4	1.0±0.0	--	0.8±0.2	1.1±0.5	--	0.303	0.345
B-18.75	9.0	2.7±0.1	2.3±0.1	1.8±0.2	4.7±0.3	3.5±0.8	3.2±0.4	0.006	0.080	0.019
B-37.5	9.0	16.1±0.7	8.0±0.1	13.8±0.5	16.3±0.4	5.3±1.8	11.1±0.3	0.376	0.083	0.011

Note: The value of $p < 0.05$ depicts that the change between dissolution rate of a particular species from annealed vs. quenched glass is significant.

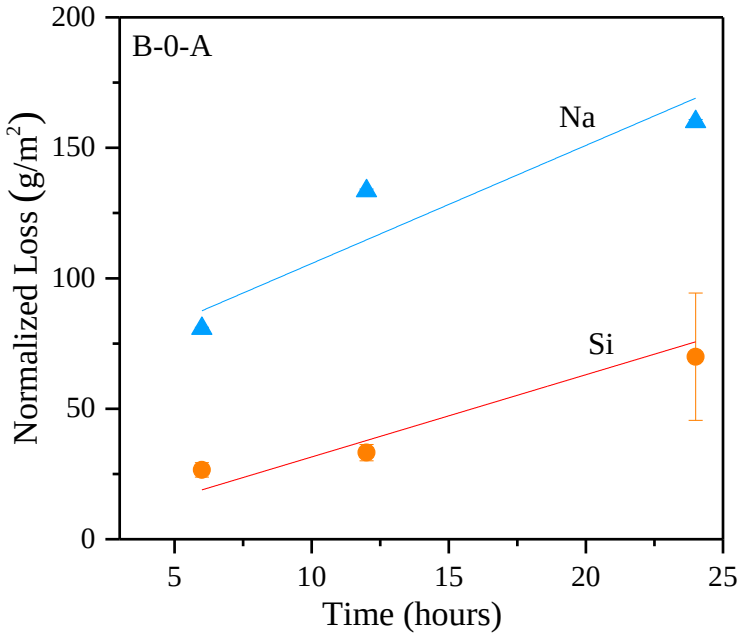

Figure 2.6. *Normalized loss of glass B-0-A as a function of immersion time in deionized water (up to 24 hours), fitted linearly to determine initial dissolution rate of each element. Each data point represents the average of two replicated experiments.*

2.4 Discussion

The ^{29}Si and ^{11}B MAS NMR spectra illustrate several changes in the distribution of key structural units and each of these changes can exert influence on the observed normalized dissolution rates. The main question we seek to address in this section is: how do observed structural changes that result from changes in the composition and thermal history impact the normalized dissolution rates? To answer this, we focus our attention on the pH-adjusted rates for B-0, B-18.75, and B-37.5 for both the annealed and quenched samples. Figure 2.7 shows the pH-adjusted normalized dissolution rate based on Na and Si release as a function of experimental B_2O_3 content. The results show that the dissolution of B-0-A and B-0-Q glasses are nearly equivalent, with B-0-A being slightly lower than B-0-Q. This is not surprising, given the slightly higher concentration of Q^4 units in B-0-A in comparison to B-0-Q.

The degradation rate of Si from glass B-18.75 (both annealed and quenched) is considerably higher when compared with glass B-0 despite significant increase in overall

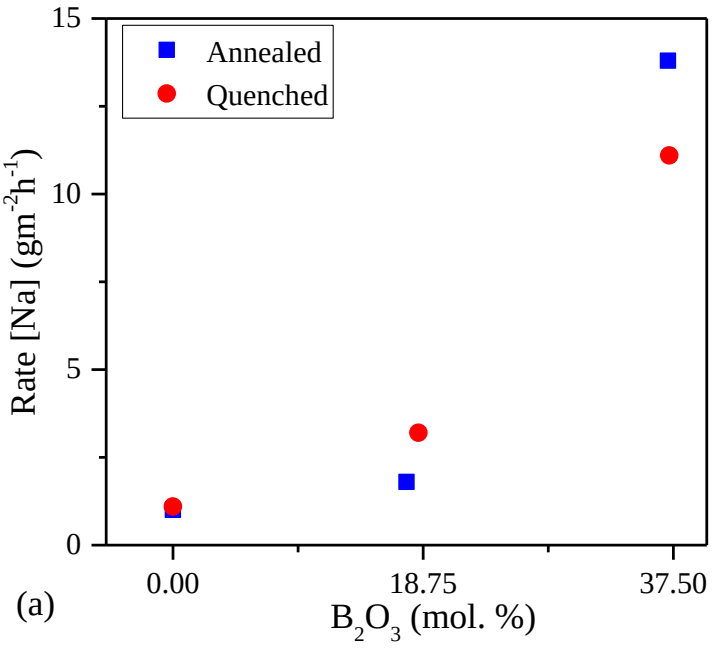

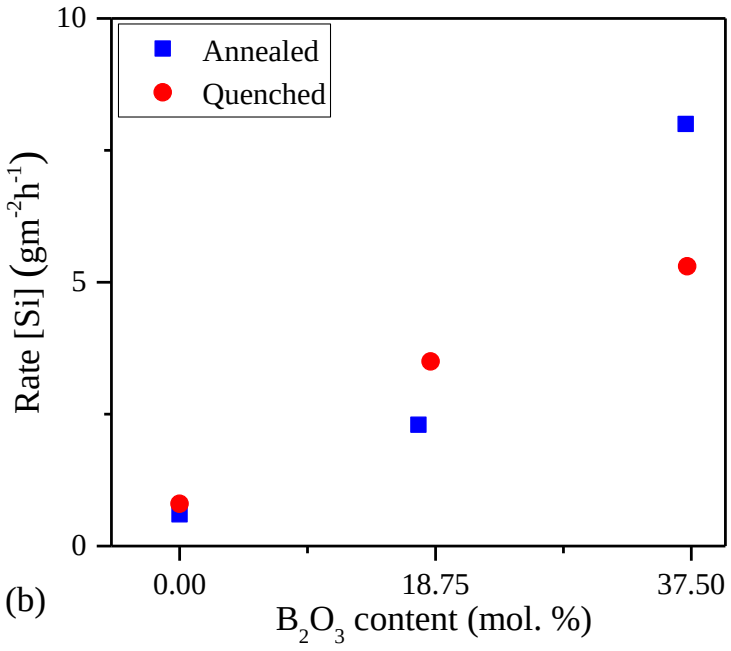

Figure 2.7. *pH-adjusted dissolution rates of (a) Na release and (b) Si release for quenched and annealed glasses as a function of their experimental B_2O_3 content.*

polymerization of the borosilicate glass matrix. The increase in release rate for glass B-18.75 may be attributed to the formation of Si–O–B linkages, which have lower resistance to hydrolysis in comparison to Si–O–Si bonds (resistance to hydrolysis: Si–O–Si > Si–O–B > B–O–B).[124] With reference to impact of thermal history, the annealed glass corrodes at a significantly slower rate than the quenched glass (B-18.75-Q). The most significant structural change that occurs between the B-18.75-A and B-18.75-Q that can account for the 1.5× difference in rate is the increased network connectivity and reduction in NBO concentration driven by the change in boron coordination between the two samples. The N_4 fraction is higher for the annealed sample (N_4 = 77.6% for B-18.75-A) versus the quenched sample (N_4 = 69.7% for B-18.75-Q). The increased fraction of tetrahedral boron induced by annealing "consumes" alkali through charge compensation of N_4 with an accompanying decrease in the amount of alkali available to form Q^3 with 1 NBO on Si (equating to a measured increase of ~5 % in Si Q^4 speciation). The substantially more

polymerized network in the annealed B-18.75-A glass resulted in a 1.5× decrease in the normalized dissolution rate.

As discussed above, thermal history had minimal impact on the dissolution behavior of glass B-37.5. It follows that the fitted dissolution rates of Na and B in this composition were quite similar for both annealed and quenched analogues (Table 2.4). This can be attributed to the rather insignificant change in the borate and silicate structural speciation in this glass as a function of thermal history (Table 2.2 and Table 2.3). That said, the fitted release rate of Si for glass B-37.5-A (8.0 g/(m^2 h)) was calculated to be 1.5× higher than its quenched (5.3 g/(m^2 h)) counterpart. At this time, we cannot fully explain the observed Si rate for the annealed sample being 1.5× higher than the quenched sample. It is conceivable that the observed difference in the Si release rate is the result of experimental uncertainty in the rate measurements, but this will require additional investigation.

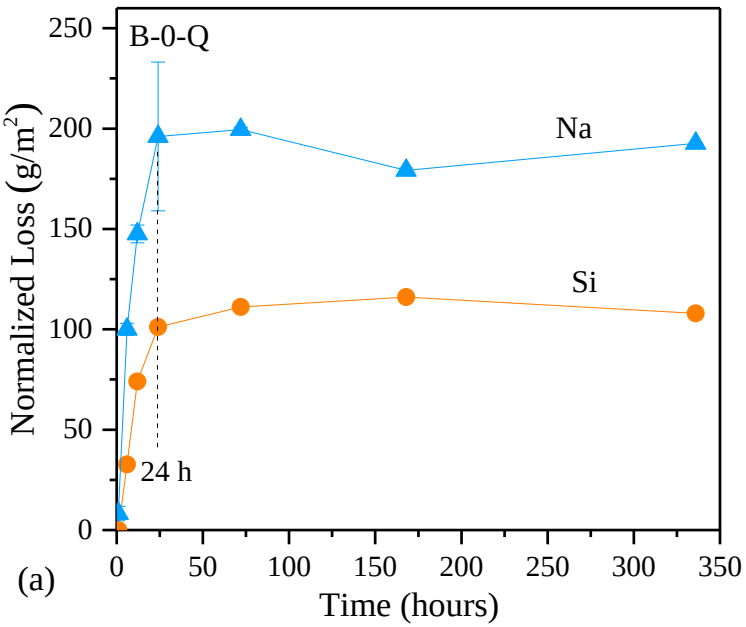

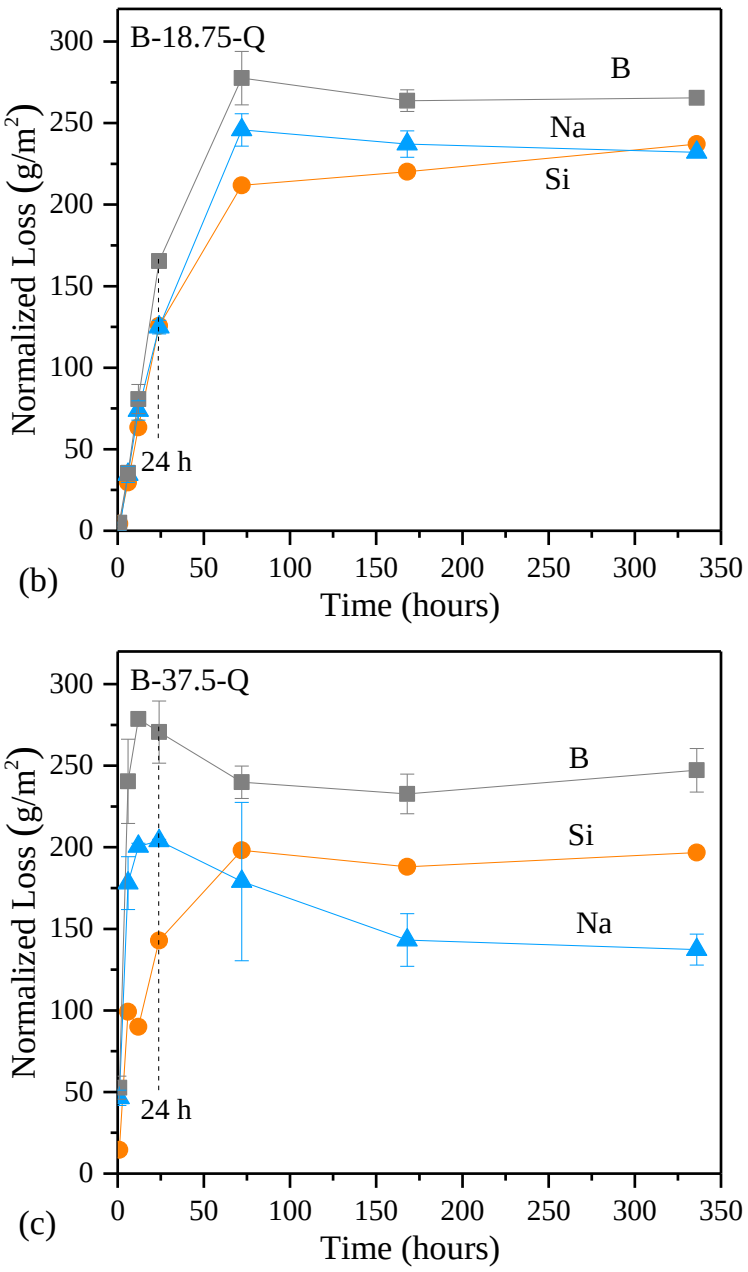

Figure 2.8. *Normalized loss of quenched glasses (a) B-0-Q, (b) B-18.75-Q, and (c) B-37.5-Q for the entire length of dissolution experiments (up to 14 days). Initial dissolution stages can be seen within the first 24 hours, marked by a dashed line.*

2.5 Implications of understanding dissolution behavior on design of borosilicate based bioactive glasses

First generation biomaterials were developed to be as bio-inert as possible to minimize rejection by host tissues. Second-generation biomaterials were designed to be either resorbable or bioactive, achieving positive interactions with the body. The next generation of biomaterials is combining these two properties, with the aim of developing materials that, once implanted, will help the body heal. While the function of first and second generation biomaterials is to replace diseased or damaged parts of the body, the concept of third–generation biomaterials is based on the principle of providing a scaffold and chemical conditions that initiate a synchronized sequence of cell level responses that result in the expression of genes required for living tissues regeneration.[125] Resorbable bioactive glasses are a subset of third–generation biomaterials, wherein, when in contact with body fluids, the glass resorbs in the body and the ionic dissolution products released from the glass stimulate specific biological responses, such as gene expression of human osteoblasts,[58] promotion of angiogenesis[126] and inducing insulin-like growth factor II mRNA expression,[127] to name a few examples. In the realm of borate/borosilicate based glasses, fundamental understanding of their dissolution behavior is thus of paramount importance to design next generation, gene-activating, bioactive glasses with controlled release of functional ions tailored for specific patient and disease states. For the same reason, there has been a recent surge in the number of studies focused on understanding mechanism and kinetics of dissolution of various bioactive glass compositions.[39,40,63,64,128,129] However, the chemical durability of glasses is a complex topic that lacks a consensus viewpoint on the basic mechanism that governs glass dissolution for

a wide composition space. While the validity of the basic assumptions of the existing composition-dependent models is still uncertain,[130] the models correlating the molecular structure of glasses with their dissolution behavior are still in their infancy.[131]

In this paper, we have highlighted the importance of thermal history and choice of experimental protocols on the dissolution behavior of borosilicate based model bioactive glasses. The methodology of glass synthesis has been shown to impact the dissolution rate of the studied glasses by 1.5× to 3× times depending on the changes induced in their molecular structure due to different thermal histories. It would have been difficult to obtain this correlation between dissolution behavior, and molecular structure of glasses by using M/V ratio as proposed by Macon et al.[15] Therefore, these parameters should be considered in conjunction with those proposed by Macon et al.[15] and Fagerlund et al.[40,64] while designing a unified approach for assessment of in vitro dissolution behavior and bioactivity of glasses.

From the perspective of structural design of bioactive glasses, most glasses have been traditionally designed empirically using trial-and-error experimentation, the latest example being a borate based glass, 13-93B3, wherein all the SiO_2 was replaced with B_2O_3 in a silicate glass named 13-93.[7] However, with the advent of third generation biomaterials, it is becoming difficult to design novel glass compositions using traditional empirical experimental techniques. It follows that a deeper level of conceptual understanding regarding the composition–structure–property relationships in these glass systems is required. Successfully accomplishing this goal will represent a leap forward in the design of glasses with controlled dissolution rates tailored for specific patient and disease states. The structural and chemical dissolution data obtained from bioactive glasses following the

approach presented in this paper can be used to develop the structural descriptors and potential energy functions over a broad range of bioactive glass compositions. This information can be used further in chemo-informatics methods to develop Quantitative Structure Property Relationship (QSPR) models for glass dissolution.[131]

2.6 Conclusions

An attempt has been made to discuss the experimental challenges that need to be carefully navigated to unearth the mechanisms governing the dissolution behavior and kinetics of boron-containing bioactive glasses. Accordingly, a series of model bioactive glasses with varying thermal histories in the $25Na_2O$-xB_2O_3-$(75-x)$ SiO_2 (x varies between 0 – 75 mol.%) system has been studied for its molecular structure (using MAS-NMR) and dissolution behavior in deionized water. It has been shown that the methodology of quenching of the glass melt impacts the dissolution rate of the studied glasses by 1.5× to 3× times (in the studied glass system) depending on the changes induced in their molecular structure due to variation in thermal history. It would have been difficult to obtain this correlation between dissolution behavior and molecular structure of glasses by adopting a sample M/V ratio approach to design the dissolution experiments. Therefore, recommendation has been made to study dissolution behavior of bioactive glasses using SA/V approach. The approach proposed to study dissolution of boron-containing bioactive glasses—which includes maintaining consistent thermal history, uniform glass particle size range, and following SA/V approach—allows us to gain a new level of conceptual understanding about the composition–structure–property relationships in these glass systems which can be applied to attain a significant leap in designing bioactive glasses with controlled dissolution rates tailored for specific patient and disease states.

Acknowledgments

This material is based upon work supported by the National Science Foundation under Grant No. 1507131. ORNL is operated by UT-Battelle, LLC for the US DOE under Contract No.'s DE-AC05-00OR22725. The authors also thank the Characterization Sciences group at Corning Incorporated for compositional analysis of the glasses.

Supplementary Information

The online version of this article contains supplementary information including glass formation regions of common ternary bioactive glass systems, XRD patterns, in addition to assorted dissolution data and heat capacity / fragility measurements. ^{29}Si MAS NMR data is also displayed in this section.

References

1. White, A., The Materials Genome Initiative: One year on. *Mrs Bulletin* 2012, *37* (8), 715-716.
2. Tilocca, A., Molecular Dynamics Simulations of Bioactive Glass Structure and In vitro Reactivity. In *Bioactive Glasses*, 2016; pp 89-104.
3. Tilocca, A., Rationalizing the Biodegradation of Glasses for Biomedical Applications Through Classical and Ab-initio Simulations. In *Molecular Dynamics Simulations of Disordered Materials: From Network Glasses to Phase-Change Memory Alloys*, Massobrio, C.; Du, J.; Bernasconi, M.; Salmon, P. S., Eds. Springer International Publishing: Cham, 2015; pp 255-273.
4. Lin, Y. N.; Brown, R. F.; Jung, S. B.; Day, D. E., Angiogenic effects of borate glass microfibers in a rodent model. *Journal of Biomedical Materials Research Part A* 2014, *102* (12), 4491-4499.
5. Jung, S. B., Bioactive Borate Glasses. In *Bio-Glasses*, John Wiley & Sons, Ltd: 2012; pp 75-95.
6. Jung, S. B.; Day, D. E.; Day, T.; Stoecker, W.; Taylor, P., Treatment of non-healing diabetic venous stasis ulcers with bioactive glass nanofibers. *Wound Repair and Regeneration* 2011, *19* (2), A30-A30.
7. Rahaman, M. N.; Day, D. E.; Bal, B. S.; Fu, Q.; Jung, S. B.; Bonewald, L. F.; Tomsia, A. P., Bioactive glass in tissue engineering. *Acta Biomater* 2011, *7* (6), 2355-2373.
8. Liu, X.; Xie, Z. P.; Zhang, C. Q.; Pan, H. B.; Rahaman, M. N.; Zhang, X.; Fu, Q.; Huang, W. H., Bioactive borate glass scaffolds: in vitro and in vivo evaluation for use as a drug delivery system in the treatment of bone infection. *J Mater Sci-Mater M* 2010, *21* (2), 575-582.
9. Fu, Q.; Rahaman, M. N.; Fu, H.; Liu, X., Silicate, borosilicate, and borate bioactive glass scaffolds with controllable degradation rate for bone tissue engineering applications. I. Preparation and in vitro degradation. *Journal of Biomedical Materials Research Part A* 2010, *95A* (1), 164-171.
10. Wray, P., 'Cotton candy' that heals? Borate glass nanofibers look promising. *American Ceramic Society Bulletin* 2011, *90* (4), 25-29.
11. Ferlat, G., Rings in Network Glasses: The B2O3 Case. In *Molecular Dynamics Simulations of Disordered Materials: From Network Glasses to Phase-Change Memory Alloys*, Massobrio, C.; Du, J.; Bernasconi, M.; Salmon, P. S., Eds. Springer International Publishing: Cham, 2015; pp 367-414.
12. Huang, W. H.; Day, D. E.; Kittiratanapiboon, K.; Rahaman, M. N., Kinetics and mechanisms of the conversion of silicate (45S5), borate, and borosilicate glasses to hydroxyapatite in dilute phosphate solutions. *J Mater Sci-Mater M* 2006, *17* (7), 583-596.
13. Ferlat, G.; Charpentier, T.; Seitsonen, A. P.; Takada, A.; Lazzeri, M.; Cormier, L.; Calas, G.; Mauri, F., Boroxol rings in liquid and vitreous B2O3 from first principles. *Physical Review Letters* 2008, *101* (6).
14. Ferlat, G.; Seitsonen, A. P.; Lazzeri, M.; Mauri, F., Hidden polymorphs drive vitrification in B2O3. *Nat Mater* 2012, *11* (11), 925-929.
15. Macon, A. L. B.; Kim, T. B.; Valliant, E. M.; Goetschius, K.; Brow, R. K.; Day, D. E.; Hoppe, A.; Boccaccini, A. R.; Kim, I. Y.; Ohtsuki, C.; Kokubo, T.; Osaka, A.; Vallet-Regi, M.; Arcos, D.; Fraile, L.; Salinas, A. J.; Teixeira, A. V.; Vueva, Y.; Almeida, R. M.; Miola, M.; Vitale-Brovarone, C.; Verne, E.; Holand, W.; Jones, J. R.,

A unified in vitro evaluation for apatite-forming ability of bioactive glasses and their variants. *J Mater Sci-Mater M* 2015, *26* (2).
16. Hashmi, M. U.; Shah, S. A., Dissolution behavior of bioactive glass ceramics with different CaO/MgO ratios in SBF-K9 and r-SBF. *Progress in Natural Science-Materials International* 2014, *24* (4), 354-363.
17. Shah, F. A.; Brauer, D. S.; Wilson, R. M.; Hill, R. G.; Hing, K. A., Influence of cell culture medium composition on in vitro dissolution behavior of a fluoride-containing bioactive glass. *Journal of Biomedical Materials Research Part A* 2014, *102* (3), 647-654.
18. Goel, A.; Kapoor, S.; Rajagopal, R. R.; Pascual, M. J.; Kim, H. W.; Ferreira, J. M. F., Alkali-free bioactive glasses for bone tissue engineering: A preliminary investigation. *Acta Biomater* 2012, *8* (1), 361-372.
19. Goel, A.; Kapoor, S.; Tilocca, A.; Rajagopal, R. R.; Ferreira, J. M. F., Structural role of zinc in biodegradation of alkali-free bioactive glasses. *Journal of Materials Chemistry B* 2013, *1* (24), 3073-3082.
20. Brauer, D. S.; Karpulthina, N.; O'Donnell, M. D.; Law, R. V.; Hill, R. G., Fluoride-containing bioactive glasses: Effect of glass design and structure on degradation, pH and apatite formation in simulated body fluid. *Acta Biomater* 2010, *6* (8), 3275-3282.
21. Mneimne, M.; Hill, R. G.; Bushby, A. J.; Brauer, D. S., High phosphate content significantly increases apatite formation of fluoride-containing bioactive glasses. *Acta Biomater* 2011, *7* (4), 1827-1834.
22. Kapoor, S.; Goel, A.; Tilocca, A.; Dhuna, V.; Bhatia, G.; Dhuna, K.; Ferreira, J. M. F., Role of glass structure in defining the chemical dissolution behavior, bioactivity and antioxidant properties of zinc and strontium co-doped alkali-free phosphosilicate glasses. *Acta Biomater* 2014, *10* (7), 3264-3278.
23. Kapoor, S.; Semitela, Â.; Goel, A.; Xiang, Y.; Du, J.; Lourenço, A. H.; Sousa, D. M.; Granja, P. L.; Ferreira, J. M. F., Understanding the composition-structure-bioactivity relationships in diopside ($CaO•MgO•2SiO_2$) - tricalcium phosphate ($3CaO•P_2O_5$) glass systemUnderstanding the composition-structure-bioactivity relationships in diopside (CaO•MgO•2SiO2) - tricalcium phosphate (3CaO•P2O5) glass system. *Acta Biomaterialia* 2014, *Accepted*.
24. Brauer, D. S.; Mneimne, M.; Hill, R. G., Fluoride-containing bioactive glasses: Fluoride loss during melting and ion release in tris buffer solution. *J Non-Cryst Solids* 2011, *357* (18), 3328-3333.
25. Miola, M.; Brovarone, C. V.; Maina, G.; Rossi, F.; Bergandi, L.; Ghigo, D.; Saracino, S.; Maggiora, M.; Canuto, R. A.; Muzio, G.; Vernè, E., In vitro study of manganese-doped bioactive glasses for bone regeneration. *Materials Science and Engineering: C* 2014, *38*, 107-118.
26. Cerruti, M.; Greenspan, D.; Powers, K., Effect of pH and ionic strength on the reactivity of Bioglass((R)) 45S5. *Biomaterials* 2005, *26* (14), 1665-1674.
27. Yazdi, A. R.; Towler, M., The effect of the addition of gallium on the structure of zinc borate glass with controlled gallium ion release. *Materials & Design* 2016, *92*, 1018-1027.
28. Rahimnejad Yazdi, A.; Torkan, L.; Stone, W.; Towler, M. R., The impact of gallium content on degradation, bioactivity, and antibacterial potency of zinc borate bioactive glass. *Journal of Biomedical Materials Research Part B: Applied Biomaterials* 2017, n/a-n/a.

29. Li, Y. M.; Stone, W.; Schemitsch, E. H.; Zalzal, P.; Papini, M.; Waldman, S. D.; Towler, M. R., Antibacterial and osteo-stimulatory effects of a borate-based glass series doped with strontium ions. *Journal of Biomaterials Applications* 2016, *31* (5), 674-683.
30. Pantano, C. G., What Do We Know about Glass Surfaces? In *A Collection of Papers Presented at the 61st Conference on Glass Problems: Ceramic Engineering and Science Proceedings*, John Wiley & Sons, Inc.: 2001; pp 137-148.
31. Amma, S.; Luo, J. W.; Kim, S. H.; Pantano, C. G., Effects of fictive temperature on the leaching of soda lime silica glass surfaces. *J Am Ceram Soc* 2017, *100* (4), 1424-1431.
32. Moncke, D.; Ehrt, D.; Eckert, H.; Mertens, V., Influence of melting and annealing conditions on the structure of borosilicate glassesInfluence of melting and annealing conditions on the structure of borosilicate glasses. *Physics and Chemistry of Glasses* 2003, *44* (2), 113-116.
33. Wheaton, B. R.; Clare, A. G., Evaluation of phase separation in glasses with the use of atomic force microscopy. *J Non-Cryst Solids* 2007, *353* (52–54), 4767-4778.
34. Angeli, F.; Villain, O.; Schuller, S.; Charpentier, T.; de Ligny, D.; Bressel, L.; Wondraczek, L., Effect of temperature and thermal history on borosilicate glass structure. *Physical Review B* 2012, *85* (5), 054110.
35. Gupta, P. K.; Lur, M. L.; Bray, P. J., Boron Coordination in Rapidly Cooled and in Annealed Aluminum Borosilicate Glass Fibers. *J Am Ceram Soc* 1985, *68* (3), C-82-C-82.
36. Singh, K.; Bala, I.; Kumar, V., Structural, optical and bioactive properties of calcium borosilicate glasses. *Ceramics International* 2009, *35* (8), 3401-3406.
37. Yao, A. H.; Wang, D. P.; Huang, W. H.; Fu, Q.; Rahaman, M. N.; Day, D. E., In vitro bioactive characteristics of borate-based glasses with controllable degradation behavior. *J Am Ceram Soc* 2007, *90* (1), 303-306.
38. Zhang, D.; Lepparanta, O.; Munukka, E.; Ylanen, H.; Viljanen, M. K.; Eerola, E.; Hupa, M.; Hupa, L., Antibacterial effects and dissolution behavior of six bioactive glasses. *Journal of Biomedical Materials Research Part A* 2010, *93A* (2), 475-483.
39. Hupa, L.; Fagerlund, S.; Massera, J.; Bjorkvik, L., Dissolution behavior of the bioactive glass S53P4 when sodium is replaced by potassium, and calcium with magnesium or strontium. *J Non-Cryst Solids* 2016, *432*, 41-46.
40. Fagerlund, S.; Ek, P.; Hupa, L.; Hupa, M., Dissolution Kinetics of a Bioactive Glass by Continuous Measurement. *J Am Ceram Soc* 2012, *95* (10), 3130-3137.
41. Cozien-Cazuc, S.; Parsons, A. J.; Walker, G. S.; Jones, I. A.; Rudd, C. D., Real-time dissolution of P40Na20Ca16Mg24 phosphate glass fibers. *J Non-Cryst Solids* 2009, *355* (50–51), 2514-2521.
42. Choueka, J.; Charvet, J. L.; Alexander, H.; Oh, Y. H.; Joseph, G. Effect of annealing temperature on the degradation of reinforcing fibers for absorbable implants *J Biomed Mater Res* [Online], 1995, p. 1309-1315.
43. Jones, J. R.; Sepulveda, P.; Hench, L. L., Dose-dependent behavior of bioactive glass dissolution. *J Biomed Mater Res* 2001, *58* (6), 720-726.
44. Lusvardi, G.; Malavasi, G.; Menabue, L.; Aina, V.; Morterra, C., Fluoride-containing bioactive glasses: Surface reactivity in simulated body fluids solutions. *Acta Biomater* 2009, *5* (9), 3548-3562.

45. Hench, L. L.; Clark, D. E., Physical chemistry of glass surfaces. *J Non-Cryst Solids* 1978, *28* (1), 83-105.
46. Hamed, N.; Hill, R.; Gillam, D.; Karpukhina, N., Effect of particle size and glass composition on bioactive glasses. In *94th General Session & Exhibition of the IADR*, Seoul, Republic of Korea, June 22-25, 2016, 2016.
47. Kansal, I.; Reddy, A.; Munoz, F.; Choi, S.-J.; Kim, H.-W.; Tulyaganov, D. U.; Ferreira, J. M. F., Structure, biodegradation behavior and cytotoxicity of alkali-containing alkaline-earth phosphosilicate glasses. *Materials science & engineering. C, Materials for biological applications* 2014, *44*, 159-65.
48. Tulyaganov, D. U.; Makhkamov, M. E.; Urazbaev, A.; Goel, A.; Ferreira, J. M. F., Synthesis, processing and characterization of a bioactive glass composition for bone regeneration. *Ceramics International* 2013, *39* (3), 2519-2526.
49. Tsigkou, O.; Jones, J. R.; Polak, J. M.; Stevens, M. M., Differentiation of fetal osteoblasts and formation of mineralized bone nodules by 45S5 Bioglass® conditioned medium in the absence of osteogenic supplements. *Biomaterials* 2009, *30* (21), 3542-3550.
50. Sun, J. Y.; Yang, Y. S.; Zhong, J.; Greenspan, D. C., The effect of the ionic products of Bioglass® dissolution on human osteoblasts growth cycle in vitro. *Journal of tissue engineering and regenerative medicine* 2007, *1* (4), 281-286.
51. Valerio, P.; Pereira, M. M.; Goes, A. M.; Leite, M. F., The effect of ionic products from bioactive glass dissolution on osteoblast proliferation and collagen production. *Biomaterials* 2004, *25* (15), 2941-2948.
52. Xynos, I. D.; Hukkanen, M. V. J.; Batten, J. J.; Buttery, L. D.; Hench, L. L.; Polak, J. M., Bioglass ®45S5 Stimulates Osteoblast Turnover and Enhances Bone Formation In Vitro: Implications and Applications for Bone Tissue Engineering. *Calcified Tissue International* 2000, *67* (4), 321-329.
53. Xynos, I. D.; Edgar, A. J.; Buttery, L. D. K.; Hench, L. L.; Polak, J. M., Gene-expression profiling of human osteoblasts following treatment with the ionic products of Bioglass (R) 45S5 dissolution. *J Biomed Mater Res* 2001, *55* (2), 151-157.
54. Ebert, W. L. *Comparison of the results of short-term static tests and single-pass flow-through tests with LRM glass (ANL-06/51)*; Argonne National Laboratory: Argonne, IL, USA, 2006.
55. Fournier, M.; Ull, A.; Nicoleau, E.; Inagaki, Y.; Odorico, M.; Frugier, P.; Gin, S., Glass dissolution rate measurement and calculation revisited. *J. Nucl. Mater.* 2016, *476*, 140-154.
56. Pierce, E. M.; Richards, E. L.; Davis, A. M.; Reed, L. R.; Rodriguez, E., Aluminoborosilicate waste glass dissolution under alkaline conditions at 40 C: implications for a chemical affinity-based rate equation. *Environmental Chemistry* 2008, *5* (1), 73-85.
57. Bohner, M.; Lemaitre, J., Can bioactivity be tested in vitro with SBF solution? *Biomaterials* 2009, *30* (12), 2175-2179.
58. Hoppe, A.; Gueldal, N. S.; Boccaccini, A. R., A review of the biological response to ionic dissolution products from bioactive glasses and glass-ceramics. *Biomaterials* 2011, *32* (11), 2757-2774.
59. Tournié, A.; Majérus, O.; Lefèvre, G.; Rager, M. N.; Walmé, S.; Caurant, D.; Barboux, P., Impact of boron complexation by Tris buffer on the initial dissolution rate of borosilicate glasses. *Journal of Colloid and Interface Science* 2013, *400*, 161-167.

60. Gao, H. S.; Tan, T. N.; Wang, D. H., Dissolution mechanism and release kinetics of phosphate controlled release glasses in aqueous medium. *Journal of Controlled Release* 2004, *96* (1), 29-36.
61. Christie, J. K.; Ainsworth, R. I.; Di Tommaso, D.; de Leeuw, N. H., Nanoscale Chains Control the Solubility of Phosphate Glasses for Biomedical Applications. *Journal of Physical Chemistry B* 2013, *117* (36), 10652-10657.
62. Hill, R., An alternative view of the degradation of bioglass. *Journal of Materials Science Letters* 1996, *15* (13), 1122-1125.
63. Döhler, F.; Mandlule, A.; van Wüllen, L.; Friedrich, M.; Brauer, D. S., 31 P NMR characterisation of phosphate fragments during dissolution of calcium sodium phosphate glasses. *Journal of Materials Chemistry B* 2015, *3* (6), 1125-1134.
64. Fagerlund, S.; Ek, P.; Hupa, M.; Hupa, L., On determining chemical durability of glasses. *Glass Technology-European Journal of Glass Science and Technology Part A* 2010, *51* (6), 235-240.
65. Pierce, E. M.; Rodriguez, E. A.; Calligan, L. J.; Shaw, W. J.; Pete McGrail, B., An experimental study of the dissolution rates of simulated aluminoborosilicate waste glasses as a function of pH and temperature under dilute conditions. *Applied Geochemistry* 2008, *23* (9), 2559-2573.
66. Huang, W.; Day, D. E.; Kittiratanapiboon, K.; Rahaman, M. N., Kinetics and mechanisms of the conversion of silicate (45S5), borate, and borosilicate glasses to hydroxyapatite in dilute phosphate solutions. *Journal of Materials Science: Materials in Medicine* 2006, *17* (7), 583-596.
67. Zhao, S.; Wang, H.; Zhang, Y.; Huang, W.; Rahaman, M. N.; Liu, Z.; Wang, D.; Zhang, C., Copper-doped borosilicate bioactive glass scaffolds with improved angiogenic and osteogenic capacity for repairing osseous defectse. *Acta Biomater* 2015, *14*, 185-196.
68. Gan, H.; Hess, P. C.; Kirkpatrick, R. J., Phosphorus and boron speciation in K2O-B2O3-SiO2-P2O5 glasses. *Geochimica et Cosmochimica Acta* 1994, *58* (21), 4633-4647.
69. Muñoz, F.; Montagne, L.; Delevoye, L.; Durán, A.; Pascual, L.; Cristol, S.; Paul, J.-F., Phosphate speciation in sodium borosilicate glasses studied by nuclear magnetic resonance. *J Non-Cryst Solids* 2006, *352* (28–29), 2958-2968.
70. Munoz, F.; Pascual, L.; Duran, A.; Montagne, L.; Delevoye, L., Structure-property relationships in phase separated borosilicate glasses containing P2O5. *Physics and Chemistry of Glasses-European Journal of Glass Science and Technology Part B* 2007, *48* (4), 296-301.
71. Munoz, F.; Montagne, L.; Delevoye, L., Influence of phosphorus speciation on the phase separation of Na2O-B2O3-SiO2 glasses. *Physics and Chemistry of Glasses-European Journal of Glass Science and Technology Part B* 2008, *49* (6), 339-345.
72. Magyari, K.; Stefan, R.; Vulpoi, A.; Baia, L., Bioactivity evolution of calcium-free borophosphate glass with addition of titanium dioxide. *J Non-Cryst Solids* 2015, *410*, 112-117.
73. Sriranganathan, D.; Kanwal, N.; Hing, K. A.; Hill, R. G., Strontium substituted bioactive glasses for tissue engineered scaffolds: the importance of octacalcium phosphate. *J Mater Sci-Mater M* 2016, *27* (2).
74. Wu, C. T.; Fan, W.; Gelinsky, M.; Xiao, Y.; Simon, P.; Schulze, R.; Doert, T.; Luo, Y. X.; Cuniberti, G., Bioactive SrO-SiO2 glass with well-ordered mesopores:

Characterization, physiochemistry and biological properties. *Acta Biomater* 2011, *7* (4), 1797-1806.
75. Weitzmann, M. N.; Ha, S.-W.; Vikulina, T.; Roser-Page, S.; Lee, J.-K.; Beck, G. R., Jr., Bioactive silica nanoparticles reverse age-associated bone loss in mice. *Nanomedicine: Nanotechnology, Biology and Medicine 11* (4), 959-967.
76. Ha, S.-W.; Weitzmann, M. N.; Beck, G. R., Bioactive Silica Nanoparticles Promote Osteoblast Differentiation through Stimulation of Autophagy and Direct Association with LC3 and p62. *ACS Nano* 2014, *8* (6), 5898-5910.
77. Brauer, D. S.; Rüssel, C.; Li, W.; Habelitz, S., Effect of degradation rates of resorbable phosphate invert glasses on in vitro osteoblast proliferation. WILEY-LISS: 2006.
78. Brauer, D. S.; Russel, C.; Kraft, J., Solubility of glasses in the system P2O5-CaO-MgO-Na2O-TiO2: Experimental and modeling using artificial neural networks. *J Non-Cryst Solids* 2007, *353* (3), 263-270.
79. Brauer, D. S.; Karpukhina, N.; Law, R. V.; Hill, R. G., Effect of TiO2 addition on structure, solubility and crystallisation of phosphate invert glasses for biomedical applications. *J Non-Cryst Solids* 2010, *356* (44-49), 2626-2633.
80. Tilocca, A.; Cormack, A. N., Modeling the Water−Bioglass Interface by Ab Initio Molecular Dynamics Simulations. *ACS Applied Materials & Interfaces* 2009, *1* (6), 1324-1333.
81. Tilocca, A.; Cormack, A. N., The initial stages of bioglass dissolution: a Car–Parrinello molecular-dynamics study of the glass–water interface. *Proceedings of the Royal Society A: Mathematical, Physical and Engineering Science* 2011, *467* (2131), 2102.
82. Zeitler, T. R.; Cormack, A. N., Interaction of water with bioactive glass surfaces. *Journal of Crystal Growth* 2006, *294* (1), 96-102.
83. Tilocca, A.; Cormack, A. N., Exploring the surface of bioactive glasses: Water adsorption and reactivity. *Journal of Physical Chemistry C* 2008, *112* (31), 11936-11945.
84. Shaharyar, Y.; Wein, E.; Kim, J. J.; Youngman, R. E.; Munoz, F.; Kim, H. W.; Tilocca, A.; Goel, A., Structure-solubility relationships in fluoride-containing phosphate based bioactive glasses. *Journal of Materials Chemistry B* 2015, *3* (48), 9360-9373.
85. Rajendran, V.; Devi, A. V. G.; Azooz, M.; El-Batal, F. H., Physicochemical studies of phosphate based P2O5-Na2O-CaO-TiO2 glasses for biomedical applications. *J Non-Cryst Solids* 2007, *353* (1), 77-84.
86. Mazurin, O.; Streltsina, M.; Shvaiko-Shvaikovskaya, T., Sci Glass-6.5 (Glass Property Information System). *Institute of Theoretical Chemistry, Shrewsbury, MA, USA* 2005.
87. Guo, X. J.; Potuzak, M.; Mauro, J. C.; Allan, D. C.; Kiczenski, T. J.; Yue, Y. Z., Unified approach for determining the enthalpic fictive temperature of glasses with arbitrary thermal history. *J Non-Cryst Solids* 2011, *357* (16-17), 3230-3236.
88. Yue, Y. Z.; Christiansen, J. D.; Jensen, S. L., Determination of the fictive temperature for a hyperquenched glass. *Chem Phys Lett* 2002, *357* (1-2), 20-24.
89. Moynihan, C. T.; Easteal, A. J.; Debolt, M. A.; Tucker, J., Dependence of Fictive Temperature of Glass on Cooling Rate. *J Am Ceram Soc* 1976, *59* (1-2), 12-16.
90. Massiot, D.; Fayon, F.; Capron, M.; King, I.; Le Calvé, S.; Alonso, B.; Durand, J. O.; Bujoli, B.; Gan, Z.; Hoatson, G., Modelling one-and two-dimensional solid-state NMR spectra. *Magnetic Resonance in Chemistry* 2002, *40* (1), 70-76.

91. Massiot, D.; Bessada, C.; Coutures, J.; Taulelle, F., A quantitative study of 27Al MAS NMR in crystalline YAG. *Journal of Magnetic Resonance (1969)* 1990, *90* (2), 231-242.
92. Maier, C. G.; Kelley, K., An equation for the representation of high-temperature heat content data1. *J. Amer. Chem. Soc.* 1932, *54* (8), 3243-3246.
93. Martinez, L. M.; Angell, C. A., A thermodynamic connection to the fragility of glass-forming liquids. *Nature* 2001, *410* (6829), 663-667.
94. Ediger, M. D.; Angell, C. A.; Nagel, S. R., Supercooled liquids and glasses. *Journal of Physical Chemistry* 1996, *100* (31), 13200-13212.
95. Guo, X. J.; Smedskjaer, M. M.; Mauro, J. C., Linking Equilibrium and Nonequilibrium Dynamics in Glass-Forming Systems. *J Phys Chem B* 2016, *120* (12), 3226-3231.
96. Wang, T.; Gulbiten, O.; Wang, R.; Yang, Z.; Smith, A.; Luther-Davies, B.; Lucas, P., Relative contribution of stoichiometry and mean coordination to the fragility of Ge–As–Se glass forming liquids. *The Journal of Physical Chemistry B* 2014, *118* (5), 1436-1442.
97. Gulbiten, O.; Mauro, J. C.; Lucas, P., Relaxation of enthalpy fluctuations during sub-T-g annealing of glassy selenium. *J Chem Phys* 2013, *138* (24).
98. Yang, G.; Gulbiten, O.; Gueguen, Y.; Bureau, B.; Sangleboeuf, J.-C.; Roiland, C.; King, E. A.; Lucas, P., Fragile-strong behavior in the As x Se 1− x glass forming system in relation to structural dimensionality. *Physical Review B* 2012, *85* (14), 144107.
99. Sen, S.; Xu, Z.; Stebbins, J. F., Temperature dependent structural changes in borate, borosilicate and boroaluminate liquids: high-resolution 11B, 29Si and 27Al NMR studies. *J Non-Cryst Solids* 1998, *226* (1–2), 29-40.
100. Du, L. S.; Stebbins, J. F., Nature of silicon-boron mixing in sodium borosilicate glasses: A high-resolution B-11 and O-17 NMR study. *Journal of Physical Chemistry B* 2003, *107* (37), 10063-10076.
101. Manara, D.; Grandjean, A.; Neuville, D., Advances in understanding the structure of borosilicate glasses: A Raman spectroscopy study. *Am Mineral* 2009, *94* (5-6), 777-784.
102. Du, L.-S.; Stebbins, J. F., Site preference and Si/B mixing in mixed-alkali borosilicate glasses: a high-resolution 11B and 17O NMR study. *Chem Mater* 2003, *15* (20), 3913-3921.
103. Pierce, E. M.; Reed, L. R.; Shaw, W. J.; McGrail, B. P.; Icenhower, J. P.; Windisch, C. F.; Cordova, E. A.; Broady, J., Experimental determination of the effect of the ratio of B/Al on glass dissolution along the nepheline (NaAlSiO4)–malinkoite (NaBSiO4) join. *Geochimica et Cosmochimica Acta* 2010, *74* (9), 2634-2654.
104. Martens, R.; Muller-Warmuth, W., Structural groups and their mixing in borosilicate glasses of various compositions - an NMR study. *J Non-Cryst Solids* 2000, *265* (1-2), 167-175.
105. Yun, Y. H.; Bray, P. J., Nuclear magnetic resonance studies of the glasses in the system Na2O-B2O3-SiO2. *J Non-Cryst Solids* 1978, *27* (3), 363-380.
106. Dell, W. J.; Bray, P. J.; Xiao, S. Z., 11B NMR studies and structural modeling of Na2O-B2O3-SiO2 glasses of high soda content. *J Non-Cryst Solids* 1983, *58* (1), 1-16.
107. Bray, P. J., Structural models for borate glasses. *J Non-Cryst Solids* 1985, *75* (1-3), 29-36.

108. Shelby, J. E., *Introduction to glass science and technology*. Royal Society of Chemistry: 2005.
109. Lee, S. K.; Stebbins, J. F., The distribution of sodium ions in aluminosilicate glasses: a high-field Na-23 MAS and 3Q MAS NMR study. *Geochimica et Cosmochimica Acta* 2003, *67* (9), 1699-1709.
110. Koller, H.; Engelhardt, G.; Kentgens, A. P.; Sauer, J., 23Na NMR spectroscopy of solids: Interpretation of quadrupole interaction parameters and chemical shifts. *The Journal of Physical Chemistry* 1994, *98* (6), 1544-1551.
111. Wu, J.; Stebbins, J. F., Effects of cation field strength on the structure of aluminoborosilicate glasses: High-resolution 11B, 27Al and 23Na MAS NMR. *J Non-Cryst Solids* 2009, *355* (9), 556-562.
112. Tagg, S.; Youngman, R.; Zwanziger, J., The structure of sodium tellurite glasses: sodium cation environments from sodium-23 NMR. *The Journal of Physical Chemistry* 1995, *99* (14), 5111-5116.
113. Kapoor, S.; Guo, X.; Youngman, R. E.; Hogue, C. L.; Mauro, J. C.; Rzoska, S. J.; Bockowski, M.; Jensen, L. R.; Smedskjaer, M. M., Network Glasses Under Pressure: Permanent Densification in Modifier-Free Al2O3 B2O3 P2O5 SiO2 Systems. *Physical Review Applied* 2017, *7* (5), 054011.
114. Kapoor, S.; Wondraczek, L.; Smedskjaer, M. M., Pressure-Induced Densification of Oxide Glasses at the Glass Transition. *Frontiers in Materials* 2017, *4* (1).
115. Boksay, Z.; Bouquet, G.; Dobos, S., Kinetics of formation of leached layers on glass surfaces. *Physics and Chemistry of Glasses* 1968, *9* (2), 69.
116. Doremus, R. H., Interdiffusion of hydrogen and alkali ions in a glass surface. *J Non-Cryst Solids* 1975, *19*, 137-144.
117. Kannan, S.; Lemos, A. F.; Ferreira, J. M. F., Synthesis and mechanical performance of biological-like hydroxyapatites. *Chem Mater* 2006, *18* (8), 2181-2186.
118. Gin, S.; Abdelouas, A.; Criscenti, L. J.; Ebert, W. L.; Ferrand, K.; Geisler, T.; Harrison, M. T.; Inagaki, Y.; Mitsui, S.; Mueller, K. T.; Marra, J. C.; Pantano, C. G.; Pierce, E. M.; Ryan, J. V.; Schofield, J. M.; Steefel, C. I.; Vienna, J. D., An international initiative on long-term behavior of high-level nuclear waste glass. *Materials Today* 2013, *16* (6), 243-248.
119. Ebert, W. L. *The effects of the glass surface area/solution volume ratio on glass corrosion: a critical review*; Argonne National Laboratory: 1995.
120. Ebert, W. L.; Bates, J. K., A comparison of glass reaction at high and low glass-surface solution volume. *Nucl. Tech.* 1993, *104* (3), 372-384.
121. Perera, G.; Doremus, R. H., Dissolution Rates of Commercial Soda–Lime and Pyrex Borosilicate Glasses: Influence of Solution pH. *J Am Ceram Soc* 1991, *74* (7), 1554-1558.
122. Icenhower, J. P.; McGrail, B. P.; Shaw, W. J.; Pierce, E. M.; Nachimuthu, P.; Shuh, D. K.; Rodriguez, E. A.; Steele, J. L., Experimentally determined dissolution kinetics of Na-rich borosilicate glass at far from equilibrium conditions: Implications for Transition State Theory. *Geochimica et Cosmochimica Acta* 2008, *72* (12), 2767-2788.
123. Hopf, J.; Kerisit, S. N.; Angeli, F.; Charpentier, T.; Icenhower, J. P.; McGrail, B. P.; Windisch, C. F.; Burton, S. D.; Pierce, E. M., Glass-water interaction: Effect of high-valence cations on glass structure and chemical durability. *Geochimica Et Cosmochimica Acta* 2016, *181*, 54-71.

124. Bunker, B. C.; Arnold, G. W.; Day, D. E.; Bray, P., The effect of molecular structure on borosilicate glass leaching. *J Non-Cryst Solids* 1986, *87* (1), 226-253.
125. Hench, L. L.; Polak, J. M., Third-generation biomedical materials. *Science* 2002, *295* (5557), 1014-+.
126. Boccaccini, A. R.; Gorustovich, A. A.; Roether, J. A., Effect of Bioactive Glasses on Angiogenesis: A Review of In Vitro and In Vivo Evidences. *Tissue Eng Part B-Re* 2010, *16* (2), 199-207.
127. Christodoulou, I.; Buttery, L. D. K.; Saravanapavan, P.; Tai, G. P.; Hench, L. L.; Polak, J. M., Dose- and time-dependent effect of bioactive gel-glass ionic-dissolution products on human fetal osteoblast-specific gene expression. *J Biomed Mater Res B* 2005, *74B* (1), 529-537.
128. Varila, L.; Fagerlund, S.; Lehtonen, T.; Tuominen, J.; Hupa, L., Surface reactions of bioactive glasses in buffered solutions. *J Eur Ceram Soc* 2012, *32* (11), 2757-2763.
129. George, J. L.; Brow, R. K., In-situ characterization of borate glass dissolution kinetics by mu-Raman spectroscopy. *J Non-Cryst Solids* 2015, *426*, 116-124.
130. Aertsens, M.; Ghaleb, D., New techniques for modelling glass dissolution. *J. Nucl. Mater.* 2001, *298* (1-2), 37-46.
131. Lusvardi, G.; Malavasi, G.; Tarsitano, F.; Menabue, L.; Menziani, M. C.; Pedone, A., Quantitative Structure-Property Relationships of Potentially Bioactive Fluoro Phospho-silicate Glasses. *Journal of Physical Chemistry B* 2009, *113* (30), 10331-10338.

Chapter 3. An insight into the corrosion of alkali aluminoborosilicate glasses in acidic environments

Nicholas Stone-Weiss,[1] Randall E. Youngman,[2] Ryan Thorpe,[3] Nicholas J. Smith,[2] Eric M. Pierce,[4] Ashutosh Goel[1†]

[1]Department of Materials Science and Engineering, Rutgers, The State University of New Jersey, Piscataway, NJ, 08854, United States

[2]Science and Technology Division, Corning Incorporated, Corning, NY 14831, United States

[3]Department of Physics and Astronomy and Laboratory for Surface Modification, Rutgers, The State University of New Jersey, Piscataway, NJ, 08854, United States

[4]Environmental Sciences Division, Oak Ridge National Laboratory, Oak Ridge, TN 37831, United States

[†] Email: ag1179@soe.rutgers.edu; Ph: +1-848-333-1523

Abstract

The majority of the literature on glass corrosion focuses on understanding the dissolution kinetics and mechanisms of silicate glass chemistries in the neutral–to–alkaline aqueous regime owing to its relevance in the fields of nuclear waste immobilization and biomaterials. However, understanding the corrosion of silicate-based glass chemistries over a broad composition space in the acidic pH regime is essential for glass packaging and touch screen electronic display industries. A thorough literature review on this topic reveals only a handful of studies that discuss acid corrosion of silicate glasses and their derivatives—these include only a narrow set of silicate-based glass chemistries. Although the current literature successfully explains the dissolution kinetics of glasses based upon classically understood aqueous corrosion mechanisms, more recent advancements in atomic-scale characterization techniques, have enabled a better understanding of reactions taking place directly at the pristine glass–fluid interface which has facilitated the development of a unifying model describing corrosion behavior of silicate glasses. Based on the corrosion mechanisms described and the questions raised in preceding literature, the present study focuses on understanding the corrosion mechanisms governing metaluminous (Na/Al = 1) sodium aluminoborosilicate glasses in acidic environments across a wide composition-space (ranging from SiO_2-rich to B_2O_3-rich compositions), with particular emphasis on understanding the reactions taking place near the glass–fluid interface. Using the state-of-the-art characterization techniques including nuclear magnetic resonance (NMR) spectroscopy, Rutherford backscattering, X-ray photoelectron spectroscopy (XPS) and elastic recoil detection analysis (ERDA), it has been shown that stepwise B_2O_3 substitutions into nepheline ($NaAlSiO_4$) glass, although causing non-linear changes in glass structure network structural features, leads to strikingly linear increases in the forward dissolution rate at pH = 2. While the glasses undergo congruent dissolution in the forward rate regime, the residual rate regime displays evidence of preferential extraction near the glass surface (i.e., enrichment in aluminum content upon corrosion through $AlO_4 \rightarrow Al(OH)_3$ evolution) implying that dissolution–re-precipitation processes may occur at the glass–fluid interface in both B_2O_3-rich and SiO_2-rich glass compositions—albeit with vastly dissimilar reaction kinetics.

Keywords: corrosion; structure; composition

3.1 Introduction

The chemical durability of glasses may seem like an "old" topic, but its fundamental understanding is of great concern for industry[1,2] and academia in order to find solutions to the problems relevant to the well-being of humanity and environment.[3,4] While the majority of literature on glass corrosion is focused on understanding dissolution kinetics and mechanisms of silicate glass chemistries in the neutral–to–alkaline aqueous regime owing to its relevance in the fields of nuclear waste immobilization (where the conditions in geological repository are expected to vary between neutral–to–highly alkaline)[5] and biomaterials (as the pH of the human body fluids varies between neutral to slightly alkaline),[6] understanding the corrosion of silicate-based glass chemistries over a broad composition space in the acidic pH regime is highly important for glass packaging and touch screen electronic display industries. Two important examples in the glass packaging industry where an understanding of acid corrosion is vital are (i) glasses for beverage containment and (ii) glasses for pharmaceutical packaging. The former is important because the pH of the majority of commercial alcoholic or non-alcoholic (non-dairy) drinks ranges from 2 to 7, with a significant portion (>90 %) being at pH < 4.[7] Since many of these drinks are packed in glass bottles/containers, it becomes imperative to understand the corrosion of silicate glasses in acidic environments. Similarly, window glasses are often packed with acidic interleaf materials to buffer against alkaline-pH corrosion during storage, but this acidic material can also facilitate leaching interactions in the presence of moisture.[8] While the majority of the container and window glass industries rely on conventional soda-lime silicate compositions, the glasses used in pharmaceutical packaging are designed mainly in the alkali borosilicate or aluminoborosilicate systems,

where these glasses encounter non-neutral pH during their service lifetime.[9] Glasses for display applications also require knowledge of dissolution behavior of glasses in acidic environments. For example, cover glasses used as the outer contact surface of touch-screen electronic displays are designed primarily in Na_2O–(K_2O)–Al_2O_3–B_2O_3–(P_2O_5)–SiO_2 systems, where they typically encounter pH varying between 2.5 and 6 (pH of human sweat and skin secretions) during their normal service lifetime.[10] Meanwhile, alkali-free glasses used as the substrates for electronic displays may encounter acidic cleaning chemistries during finishing to remove contaminants that could negatively influence performance of display transistor devices built into the display.

A thorough literature review on the topic of glass corrosion reveals only a handful of studies which discuss corrosion of silicate glasses and their derivatives in the acidic regime—these include only a narrow set of glass chemistries, with most of them being vitrified analogues of SiO_2-rich natural minerals,[11-20] a few being simplified borosilicate-based nuclear waste glasses,[21,22] and others being on aluminosilicate-based E-glass.[1,2] Consequently, there is a lack of consensus in the literature on the fundamental mechanisms of glass dissolution in acidic solutions that applies to a wide composition space. For example, according to Gislason and Oelkers,[18] the dissolution of basaltic glasses in solutions (far-from-equilibrium) with pH varying between 2 and 11 is controlled by a single mechanism, which includes (i) release of monovalent and divalent metal cations, (ii) exchange between H^+ in solution and Al in the glass, and (iii) considerably slower removal of silica from the glass. Berger et al.,[20] on the other hand, determined that solution affinity effects play a major role in the dissolution behavior of similar glasses, as their dissolution rates in acidic solutions were found to be driven by surrounding solution concentrations of

Al, meanwhile dissolution rate in neutral solutions were similarly driven by aqueous Si concentrations. While the aforementioned studies were able to successfully utilize solution and microstructural analyses to model glass corrosion kinetics in acid according to well-known kinetic theories and draw conclusions as to dissolution mechanisms, later studies discussed below have incorporated structural and chemical information of the evolving glass surface and bulk to give more insight into the fundamental corrosion mechanisms of silicate glasses in the acidic regime.

Multiple studies by Hamilton et al.[12-14] looked into the dissolution kinetics of feldspathoid-based sodium aluminosilicate minerals and glasses, including as a function of solution pH; from acidic to basic regimes. These studies correlated the dissolution behavior with glass structural descriptors according to the glass composition—such as the impact of non-bridging oxygen (NBOs) and Si–O–Si vs. Si–O–Al bonding upon ion exchange / hydrolysis rates near the glass–fluid interface, etc. along a specific walk of compositions in the ternary sodium aluminosilicate system. Similarly, Knauss et al.[21] studied a model nuclear waste glass in a range of solution pH, determining that fundamental differences in terms of rate of elemental release and altered layer characteristics (i.e. Si/Al release from the glass) occur as pH rises from acid to neutral environments. Tsomaia et al.[11] expanded upon these findings by performing an in-depth structural study on the surface of sodium aluminosilicate glasses at pH = 2, determining that silicate units are released only after release of Na and Al cations, and provided the first NMR evidence that aluminum tends to form octahedral coordination near the surface, either due to (i) a structural reorganization, involving *in situ* $AlO_4 \rightarrow AlO_5 \rightarrow AlO_6$ transformation or (ii) a re-precipitation mechanism from solution. More recent developments in understanding the kinetics and mechanisms

governing glass corrosion—for both acid and neutral-to-alkaline conditions—have attempted to use the latest advances in atomic-scale characterization techniques to generate a unifying model that describes corrosion behavior of silicate glasses, as communicated below.

The most recent literature on this subject debate two basic mechanisms for silicate glass corrosion: (i) the classical multi-step inter-diffusion-based mechanism and (ii) the interfacial dissolution – re-precipitation mechanism (IDPM).[22] The former describes the mechanism of corrosion as a multi-step process that includes release of mobile glass modifying cations (such as Na^+) through ion exchange with protons in solution to form hydrated Si-OH bonds (forming an inter-diffusion layer), followed by the protonation and hydrolysis of bridging bonds (i.e. Si-O-Si or Si-O-Al) and restructuring of the hydrated silica network into a gel layer via re-polymerization reactions.[23-26] The IDPM, on the other hand, suggests that glass corrosion proceeds as an inward-moving reaction front in which all bonds at the glass–fluid interface break and are immediately re-precipitated to form an amorphous gel layer.[22] The supersaturated water at the interface not only promotes alkali/alkaline-earth release from the glass, but in fact releases all elements in the outermost surface layer only to reorganize as a secondary phase of network forming species such as Si and Al.[22] While the classical inter-diffusion-based mechanism has been widely accepted in the glass community, recent studies using highly advanced analytical techniques to track the gel layer characteristics suggest that a basic mechanism describing silicate glass corrosion may be more complicated than assumed in either individual mechanisms, with high dependence upon glass composition and surrounding leaching conditions.[25,27,28] Based on previous findings and questions raised in the aforementioned literature, we aim to

address the following open questions in our study: (1) What mechanisms best describe the corrosion of alkali aluminoborosilicate glasses in acidic environment? (2) Does AlO_6 gel layer formation in acid occur by way of a structural transformation or re-precipitation? (3) Will the established corrosion mechanisms – multi-step inter-diffusion mechanism or IDPM – accurately describe the dissolution behavior of glasses far from the SiO_2-rich regime, i.e., glasses with B_2O_3 as the primary network former?

In light of the abovementioned questions, the present study is focused on understanding the kinetics and mechanisms of aqueous corrosion of sodium aluminoborosilicate glasses (with varying B_2O_3/SiO_2 ratio) in acidic solutions (HCl; pH = 2). Accordingly, the glass compositions have been designed in the 25 Na_2O–25 Al_2O_3–x B_2O_3–(50-x) SiO_2 (where x varies between 0 – 50 mol.%) quaternary system. The series of glass compositions was designed with the aim to understand the corrosion of oxide glasses with multiple network formers over a broad composition space. The choice of glasses along the metaluminous (Na/Al = 1) join was made with the understanding that alkali cations would, in general, first preferably serve to charge-compensate tetrahedral aluminum in the silicate network.[29] In the absence of "excess" Na_2O beyond the equimolar 1:1 proportion to Al_2O_3, structural complexities such as $BO_3 \rightarrow BO_4$ transformation or Si-NBO formation as a function of composition can be largely minimized, enabling a more direct interpretation of chemical and structural factors driving observed corrosion kinetics. A suite of state-of-the-art spectroscopic characterization techniques including inductively coupled plasma – optical emission spectroscopy (ICP-OES), magic angle spinning – nuclear magnetic resonance (MAS NMR) spectroscopy, X-ray photoelectron spectroscopy (XPS), Rutherford backscattering spectrometry (RBS), and elastic recoil detection analysis

(ERDA) have been employed to study changes in the bulk and surface structure/chemistry of corroded glasses as a function of solution chemistry. The results have been discussed taking into account the previously proposed mechanisms for glass corrosion, as discussed in depth in recent studies, namely in Gin et al.[4] and Geisler et al.,[22,30] alongside the additional literature.[25,27,28,31]

3.2 Experimental

3.2.1 Synthesis of the glasses

Glasses in this work were designed along the metaluminous join to maintain charge-balance between Na and Al (i.e. $Na_2O/Al_2O_3 = 1$) while replacing SiO_2 with B_2O_3 in the majority network, per the composition series 25 Na_2O–25 Al_2O_3–x B_2O_3–(50-x) SiO_2 (in mol. %, where x varies between 0–50 in 5 mol% increments). The silicate endpoint (x = 0) corresponds to the nepheline composition (25 Na_2O-25 Al_2O_3-50 SiO_2), whose dissolution rates have been previously well-studied.[11,12,32] All glasses were synthesized using the melt-quench technique, using high-purity powders of SiO_2 (Alfa Aesar; >99.5 %), H_3BO_3 (Alfa Aesar; ≥98 %), Al_2O_3 (Acros Organics; 99 %), Na_2SiO_3 (Alfa Aesar; >99 %) and Na_2CO_3 (Fisher Scientific; ≥99.5 %) as precursors. Oxide precursors were mixed in 70 g batches and melted in Pt-Rh crucibles for 1-2 h in air at temperatures ranging from 1400-1675 ºC, depending on B_2O_3/SiO_2 ratio in the glass composition. All glasses were quenched on a metallic plate and coarse-annealed at temperatures of T_g^* – 50 °C, where T_g^* is the estimated glass transition temperature obtained from the SciGlass database. Glasses were labeled according to the naming convention "B-x", where x represents the batched B_2O_3 concentration (mol.%). The amorphous nature of the glass samples was confirmed by X-ray diffraction (XRD) (PANalytical – X'Pert Pro; Cu K_α radiation; 2θ

range: 10–90º; step size: 0.01313º s^{-1}). The actual concentration of SiO_2, Al_2O_3, and B_2O_3 in the synthesized glasses was determined by ICP–OES (PerkinElmer Optima 7300V), while sodium concentration was determined by flame emission spectroscopy (Perkin Elmer Flame Emission Analyst 200). Table 3.1 presents the experimentally measured glass compositions, and agreement with batched targets are mostly within ±1 mol.%. The bulk water content in glasses was estimated from the maxima of the ~3500 cm^{-1} absorption band in the mid-infrared (IR) region, typical of molecular water.[33] The IR spectra were acquired using a single-bounce diamond attenuated total reflectance (ATR) apparatus attached to a Fourier Transform Infrared spectrometer (FTIR-UATR, Frontier™, PerkinElmer, Inc.; scanning resolution 4 cm^{-1}, 32 scans for background and samples).

3.2.2 Glass transition temperature measurements and annealing

Differential scanning calorimetry (DSC) data was collected on the fine glass powders (<45μm diameter) using a Simultaneous Thermal Analyzer (STA 8000; PerkinElmer) from room temperature to 1500 ºC at a heating rate of 20 ºC/min under a constant flow of nitrogen gas. The glass transition temperature (T_g) was deduced from the inflection point of the endothermic dip in the DSC spectra. The T_g values reported in this paper represents an average of at least two thermal scans. After experimental measurement of the T_g, each glass was re-annealed at a temperature corresponding to their T_g – 50 ºC for several hours and slow-cooled to room temperature until most of the residual stresses were removed, as visualized under a polariscope. A detailed methodology used to anneal the glasses has been described in our previous article.[3]

3.2.3 Bulk structural analysis of pre- and post-corroded glass samples

The structure of glass (both before and after chemical dissolution) has been studied using MAS NMR spectroscopy. The MAS NMR spectra of ^{27}Al, ^{11}B, and ^{23}Na for glasses and select post-dissolution samples were acquired using a commercial spectrometer (VNMRs, Agilent) and a 3.2-mm MAS NMR probe (Agilent). The samples were powdered in an agate mortar, packed into 3.2 mm zirconia rotors, and spun at 22 kHz for ^{23}Na and ^{27}Al MAS NMR, and 20 kHz for ^{11}B MAS NMR. ^{27}Al MAS NMR data were acquired at 16.4 T (182.34 MHz resonance frequency) using RF pulses of 0.6 μs (equivalent to a π/12 tip angle), recycle delays of 2 s, and signal averaging of 1000 acquisitions. Acquired data were processed without additional apodization and referenced to aqueous aluminum nitrate at 0.0 ppm. ^{23}Na MAS NMR data were collected at 16.4 T (185.10 MHz resonance frequency) using a 0.6 μs (~π/12 tip angle) pulse width for uniform excitation of the resonances. A range of 400 to 1000 acquisitions were co-added, and the recycle delay between scans was 2 s. The ^{11}B MAS NMR experiments were conducted at 16.4 T (224.52 MHz resonance frequency), incorporating a 4 s recycle delay, short rf pulses (0.6 μs) corresponding to a π/12 tip angle, and signal averaging of 400 to 1000 scans. Similar experimental conditions, but at 11.7 T (160.34 MHz resonance frequency), were used to collect ^{11}B MAS NMR spectra from post-dissolution samples. The acquired spectra were processed with minimal apodization and referenced to aqueous boric acid (19.6 ppm) and aqueous NaCl (0 ppm). Fitting of the MAS NMR spectra was performed using DMFit[34] and, accounting for distributions in the quadrupolar coupling constant, the CzSimple model was utilized for ^{23}Na and ^{27}Al MAS NMR spectra. The "Q MAS ½" and Gaus/Lor functions were used to fit 3- and 4-fold coordinated boron resonances in the ^{11}B MAS NMR

data, respectively, and N_4 was calculated from the relative areas of these peaks, with a small correction due to the overlapping satellite transition of the 4-fold coordinated boron peak.[35]

3.2.4 Sample preparation for glass corrosion tests

3.2.4.1 Glass powder specimens

The glasses were crushed and sieved to obtain powders with particle size varying between 300 – 425 μm. The glass particles were ultrasonicated in acetone to remove fine powder residue. The process was repeated at least thrice or until the supernatant was clear to ensure the removal of all the fine particles sticking to the surface of larger glass particles. The ultrasonicated glass particles were dried overnight at room temperature in ambient air and analyzed for any structural changes before versus after acetone-washing using FTIR spectroscopy (as has been described previously). Average three-dimensional (3D) geometric surface area of washed particles was determined using ImageJ software (as explained in more detail in Stone-Weiss et al.[3]) after capturing images of ~1000 particles via an optical microscope (Zeiss Axioskop 40) at ~50X magnification. Experimental density values (measured using Archimedes' method by measuring mass of sample in air and in d-limonene solution; number of samples = 3, standard deviation <0.009 g cm^{-3}; presented in Table 3.1) were used together with 3D surface area calculations to determine the specific surface area of the washed powders (4284-4781 mm^2/g). Finally, the mass of glass particles resulting in the desired surface area–to–volume ratio (SA/V) was calculated.

3.2.4.2 Monolithic glass coupons

Based on learnings from the corrosion studies of powder specimens, additional corrosion tests were performed on monolithic glass coupons from select compositions (B-5, B-25 and B-45). Two coupons of ~15 mm × 15 mm dimensions were cut from each glass

composition using a diamond blade. The polishing of the glass coupons was performed in accordance with the procedure described in the ASTM C1220-10,[36] wherein the glass specimens were ground in acetone sequentially on 120 – 600 grit sized SiC sheets, followed by polishing in a 6 µm non-aqueous diamond suspension until a mirror finish was acquired. The thickness of the polished samples was approximately between 2-3 mm. The dimensions of the polished samples were measured to calculate geometric surface areas.

3.2.5 Glass corrosion experiments in acidic pH

3.2.5.1 Dissolution behavior and kinetics of glass corrosion

The dissolution behavior and kinetics of glasses was studied at pH = 2±0.02 (hydrochloric acid; Alfa Aesar; ACS grade) by immersing 27.0 mg of acetone-washed glass particles in 50 mL solution, corresponding to SA/V = 2.5 m^{-1}. All powder–solution mixtures were immediately sealed into sterilized polypropylene flasks and placed in an oven at 35 ºC. Experiments ranged from 5 minutes to 72 hours. In addition to analyses of neat (unused) and blank (glass-free) control solutions, all experiments were performed in triplicate to evaluate the uncertainty of final results. The pH evolution of the solutions was measured at room temperature from solution aliquots using a pH meter (Mettler Toledo InLab® Pro-ISM). Separate aliquots of the corrosion solutions were chemically analyzed by ICP-OES (PerkinElmer Optima 8300). ICP-OES detection limits were <0.5 ppm for Na, <0.2 ppm for Al, <0.2 ppm for B, and <0.2 ppm for Si. The normalized loss (NL) of each element (Na, Al, B, and Si) released from glasses into the surrounding solution was calculated using equation (1),

$$NL_i = \frac{C_i - C_o}{\left(\frac{SA}{V}\right) f_i} \qquad (1)$$

where C_i is the mass concentration of element *i* in the solution as detected by ICP-OES; f_i is the mass fraction of the element *i* in the glass; and C_o is the background concentration (as determined from blank solutions). Normalized loss data were plotted against time and linearly fit over the apparent linear regimes of release at early times to evaluate forward dissolution rates as a function of glass composition and initial solution pH.

3.2.5.2 Structural transformations in the glasses due to aqueous corrosion

In order to study the mechanism of glass corrosion, both bulk and surface characterization of pre- and post-dissolution glass specimens was performed. The glass powders remaining after dissolution experiments *(from section 2.5.1)* were rinsed thoroughly with water thrice and dried overnight at 65 ºC followed by characterization using XRD and ^{27}Al and ^{11}B MAS NMR spectroscopy. On the other hand, the dissolution experiments on polished monolithic glass coupons were performed at pH = 2 for durations of either 12 hours, 1 day, or 3 days to match the maximum time duration performed with analogous glass grains. Corroded coupons were rinsed with DI water following the dissolution experiments and dried at room temperature to constant weight.

XPS measurements were performed on monolithic glass coupons in order to understand the composition and chemical environment of elements within the top 5-10 nm of the sample surfaces – both before and after corrosion processes. The XPS measurements utilized a Thermo Scientific K-Alpha equipment, which used a 1486.6 eV monochromated Al K_α x-ray source to excite core level electrons from the sample. A low energy dual electron/argon-ion beam flood gun was used for charge compensation during measurements. The kinetic energy of the photoelectrons was measured using a 180° double-focusing hemispherical analyzer with a 128-channel detector. Binding energies

were referenced to the main component of the adventitious carbon peak at 284.8 eV. Peak areas were converted to composition using suitable elemental relative sensitivity factors,[37] and corrected for attenuation through an adventitious carbonaceous overlayer using a calculation similar to the method described by Smith.[38] The probe depth of XPS, taken to be three times the inelastic mean free path of photoelectrons, varied from 3.6 nm for Na 1s to 9.3 nm for B 1s, Al 2p, and Si 2p photoelectrons.

RBS and ERDA measurements were similarly performed on pre- and post-corroded glass coupons in order to further evaluate the near-surface composition and hydrogen content of the corroded samples, respectively. These measurements were carried out using a General Ionex Tandetron accelerator using a 2.0 MeV He^{++} beam. For RBS, the beam was oriented normal to the sample surface and the energy of backscattered He ions was measured using a solid-state charged particle detector mounted at 17º with respect to the sample surface normal. For ERDA measurements, the beam was oriented in a grazing geometry with an angle of 75º between the incident beam and the surface normal. The detector was mounted 75º with respect to the surface normal in the specular direction, with a 40 μm mylar foil placed over the active area to block scattered He ions. Hence, only forward-scattered H ions were able to penetrate the detector. The probe depth of these ion scattering techniques was approximately 1 μm.

3.3 Results

3.3.1 Glass formation behavior and annealing

The melt-quenched glasses were transparent in appearance and XRD amorphous (as shown in Figure S1). The experimental compositions, as analyzed by ICP-OES, show

close agreement with batched compositions (±1.7 %) (see Table 3.1). The water content in B_2O_3-containing glasses was estimated to be less than 10 ppm (wt. %).[33]

In order to remove all residual stresses, glasses were annealed at $T_g^{\dagger}$-50 ºC for several hours followed by slow cooling to room temperature (where $T_g^{\dagger}$ refers to the onset point of the endothermic dip).[3] Residual stresses in the glasses, as analyzed under a polariscope, were estimated to be less than 10 MPa, taking into account the ~5 mm sample thickness and considering the absence of any first-order fringes under cross-polarized inspection.

Table 3.1. *Experimental compositions (within ±0.5 mol. %), density (ρ), molar volume (V_M), and T_g of the studied glass series.*

Sample ID	Experimental (mol. %)				ρ (±0.3 %) (g/cm^3)	V_M (±0.3 %) (cm^3/mol)	T_g (°C)
	Na_2O	Al_2O_3	B_2O_3	SiO_2			
B-0	25.1	25.9	--	49.0	2.458	29.05	839±2
B-5	25.2	25.4	5.1	44.3	2.433	29.46	719±5
B-10	24.8	26.0	9.1	40.0	2.415	29.94	679±11
B-15	24.6	26.6	14.0	34.8	2.391	30.54	635±4
B-20	25.0	26.1	19.2	29.7	2.369	30.95	591±2
B-25	25.1	26.0	24.3	24.6	2.339	31.54	549±3
B-30	24.8	26.0	28.6	20.5	2.318	32.00	532±1
B-35	24.8	25.7	33.8	15.7	2.296	32.47	513±1
B-40	25.0	25.6	38.7	10.7	2.261	33.15	502±1
B-45	24.8	25.3	44.7	5.2	2.246	33.58	491±1
B-50	25.2	25.5	49.3	--	2.227	34.11	486±1

3.3.2 Structural analysis of glasses

The density of glasses decreases linearly as a function of B_2O_3 content, while molar volume displays a linear increase, as shown in Table 3.1. These trends may be attributed to the introduction of lower bond density BO_3 units (as will be shown by MAS NMR

results) into the glass network in place of higher bond density SiO_4 tetrahedra. For this reason, the density of vitreous SiO_2 comprising a tetrahedral silica network is 2.2 g/cm^3, while that for vitreous B_2O_3 with corner-sharing planar BO_3 triangles is 1.8 g/cm^3.[39]

Figure 3.1a and b present the ^{11}B and ^{27}Al MAS NMR spectra of the annealed glasses. ^{23}Na MAS NMR spectra has been presented in Figure S2 and fitting parameters can be seen in Table S1. Since all the glasses studied in this work have been designed in the metaluminous regime (Na/Al = 1), we expect sodium to act in a charge compensating role to either AlO_4^- or BO_4^- network forming units, in preference to being used to form NBOs in the silicate network (i.e., silicate units are expected to be entirely Q^4). Studies have shown that aluminum tends to preferentially consume Na^+ relative to boron in SiO_2-

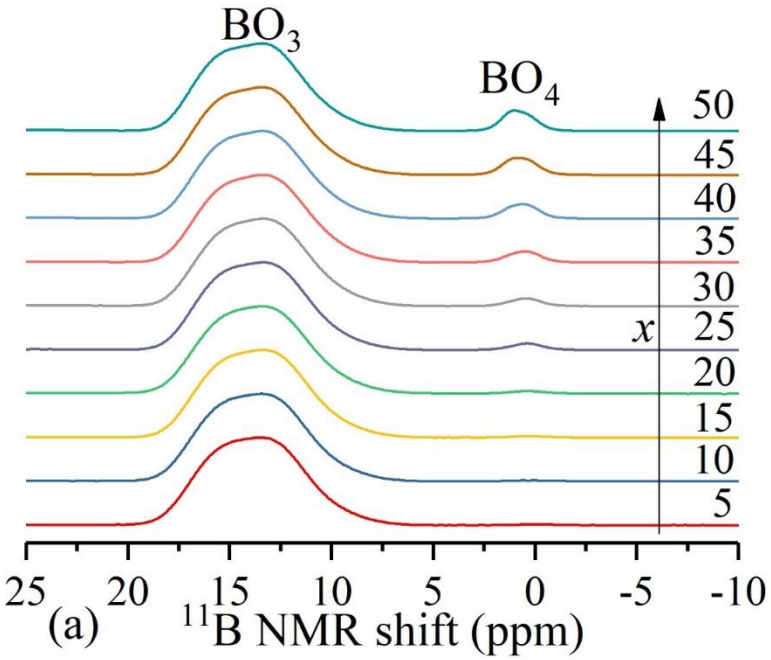

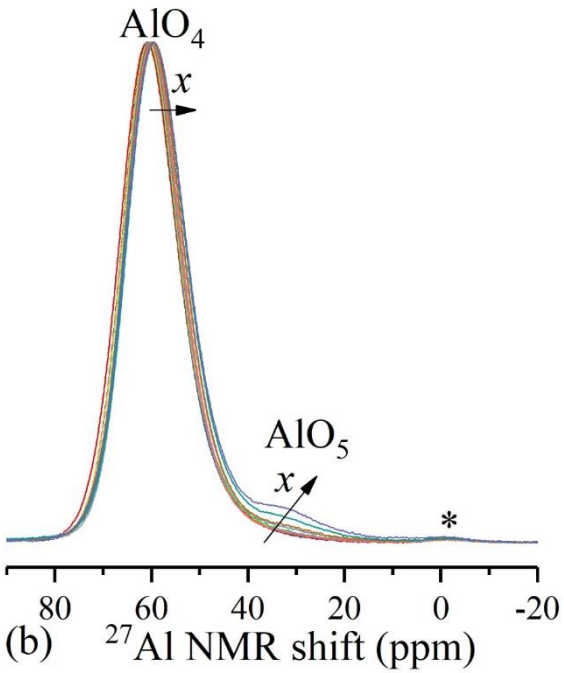

Figure 3.1. *(a) ^{11}B MAS NMR and (b) ^{27}Al MAS NMR spectral overlays of studied glasses. Trends according to increasing x (B_2O_3 content) can be seen in each plot. The (*) symbol in ^{27}Al spectra represents a background signal from the rotor.*

rich alkali aluminoborosilicate glasses.[29,32,40,41] However, it has also been shown that Al-vs-B competition for sodium may shift away from Al in favor of B more significantly in B_2O_3-rich glasses.[42,43] ^{11}B NMR spectra shown in Figure 3.1a display two main resonances: a broad quadrupolar-broadened peak centered at 14 ppm associated with BO_3 units, and a minor, relatively narrow peak centered at 2 ppm associated with BO_4 units. The BO_3 peak does not show any significant change in shape with increasing *x*, implying that ring vs. non-ring BO_3 species maintain similar ratios in the network. While the BO_4 peak mentioned is not clearly evident in SiO_2-rich glasses, this peak becomes more prominent as *x* increases beyond 20 mol.% depicting an increasing concentration of BO_4 units in the glasses with increasing B_2O_3. Table 3.2 presents the N_3 and N_4 fractions in glasses as

calculated from the fitting of ^{11}B MAS NMR spectra. The highest N_4 fraction of 6% was observed in the sodium aluminoborate glass (x = 50).

Sample ID	^{11}B MAS NMR		^{27}Al MAS NMR		% NBO in Network (Calculated)*
	N_3	N_4	AlO_4	AlO_5	
B-0	--	--	98.7	1.3	-0.5
B-5	99.6	0.4	98.8	1.2	0.1
B-10	99.5	0.5	98.3	1.7	-0.8
B-15	99.4	0.6	98.0	2.0	-1.5
B-20	98.9	1.1	98.7	1.3	-0.9
B-25	98.0	2.0	98.5	1.5	-1.0
B-30	97.6	2.4	98.6	1.4	-1.3
B-35	96.5	3.5	97.5	2.5	-1.2
B-40	95.3	4.7	97.3	2.7	-1.5
B-45	94.6	5.4	95.6	4.4	-1.5
B-50	94.0	6.0	94.1	5.9	-1.4

*Note: Negative NBO values displayed occur as a result of lower Na_2O content in the glass than that necessary to charge compensate AlO_4 and/or BO_4 units

Table 3.2. *B and Al % structural speciation in the glassy network (within ±0.5 %), as extracted from ^{11}B and ^{27}Al MAS NMR. Calculated NBO fractions as derived from Al and B speciation are also shown.*

It is important to note that any BO_4 units shown (experimentally) to develop in the structure of a metaluminous glass must consume Na^+ in its need for charge compensation, which consequently is expected to impact Al speciation in the network. In order to explore this, we also examined ^{27}Al MAS NMR spectra (shown in Figure 3.1b). At low B_2O_3 content, these spectra display a main resonance centered near 60 ppm (associated with AlO_4) and a very minor peak near 0 ppm associated with a background rotor signal. The AlO_4 peak

shifts towards higher shielding with increased B_2O_3 content, which we attribute to a systematic shift in next-nearest-neighbor identity as Al-O-B bonds begin to replace a predominantly Al-O-Si bonded network.[44] In keeping with trends in the ^{11}B MAS NMR spectra of B_2O_3-rich glasses, clear changes also occur in ^{27}Al MAS NMR spectra of B_2O_3-rich glasses, wherein, the development of a peak near 30 ppm associated with AlO_5 is evident. Table 3.2 presents the amount of 4- and 5- coordinated Al present in the glass network as deduced from the ^{27}Al MAS NMR spectra. While glasses with up to x = 30 show aluminum predominantly in tetrahedral coordination (98-99 %), increase in B_2O_3 concentration beyond 30 mol. % leads to a steady rise in AlO_5 content up to 6 % in the sodium aluminoborate glass (x = 50), thus, deviating from its expected tetrahedral role in metaluminous glasses. Although the existence of five-coordinated aluminum units in metaluminous and per-aluminous glasses or glasses with high ionic field strength cations has been widely reported,[43,45-48] its role in the structure—i.e. network former vs. network modifier—and properties of these glasses is still disputed. While higher (five- or six-) coordinated aluminum is conventionally considered to act as a network modifier,[49,50] the presence of AlO_5 units in the glass structure has been shown to result in an increase in their glass transition temperatures, melt viscosity, and hardness.[43,50-54] Interestingly, in our study, with increased B_2O_3 content, the fraction of higher coordinated Al and tetrahedral B units both rise, deviating from the expectation that aluminum tends to preferentially consume Na^+ for the charge compensation of AlO_4^- before boron can use them to convert BO_3 to BO_4. It is evident that in B_2O_3-rich (molar concentration of $B_2O_3 > SiO_2$) metaluminous glasses, the tetrahedral boron units begin to ‘steal’ Na^+ away from network forming Al units and cause higher-coordinated Al species to form.

In order to assess sodium's role around oxygen and verify the connectivity of the silicate network, we used analyzed compositions and the NMR-determined AlO_4 and BO_4 fractions to calculate NBO fractions, per the formula:

$$NBO\ Fraction = \frac{at.\%\ Na - at.\%\ B\ in\ BO_4 - at.\%\ Al\ in\ AlO_4}{at.\%\ O} \qquad (2)$$

In this formula, we assume that one Na^+ forms either one BO_4 or one AlO_4 unit, and that any excess alkali will begin to form NBOs in the silicate network on a 1-for-1 basis.[55] Results of these calculations are given in Table 3.2. It is important to note that, in this assumption, we have not taken into account AlO_5 units due to their small concentrations and uncertainties with regard to their impact on the NBO content in the glass network. It is evident from these calculations that, in each composition, the network contains less than 0.1% of NBOs, thus verifying sodium's primary role as a charge compensator, as well as the anticipated high connectivity of these glasses marked by Q^4 silicate structural units.

3.3.3 Glass structure vs T_g

In general, an increase in the B_2O_3 concentration in the studied glasses, at the expense of SiO_2, resulted in a significant reduction in their glass transition temperatures, as shown in Table 3.1. However, the variation in T_g with increasing B/(Al+Si) molar ratio is non-linear, as is evident from the close agreement between a fitted exponential function and the experimental data (as shown in Figure 3.2a).

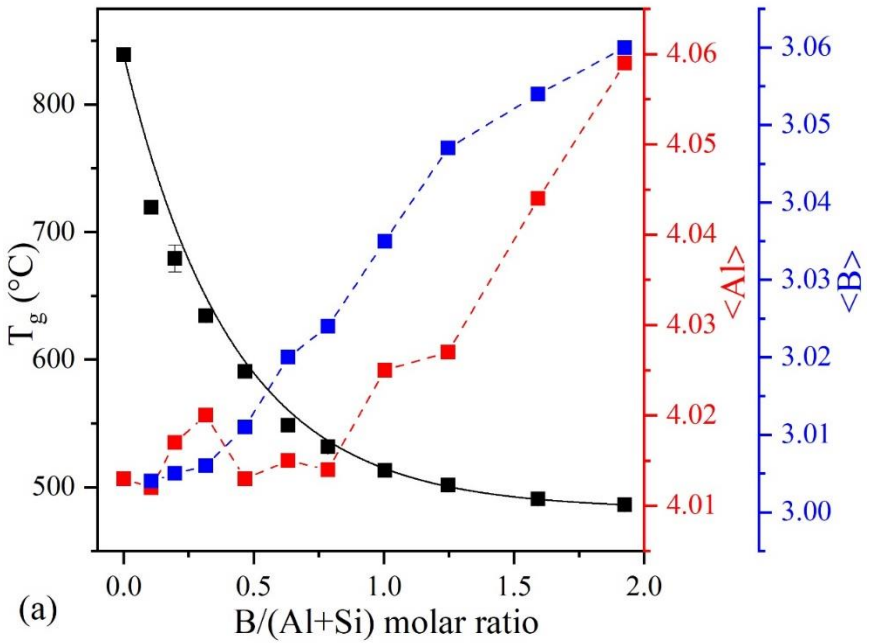

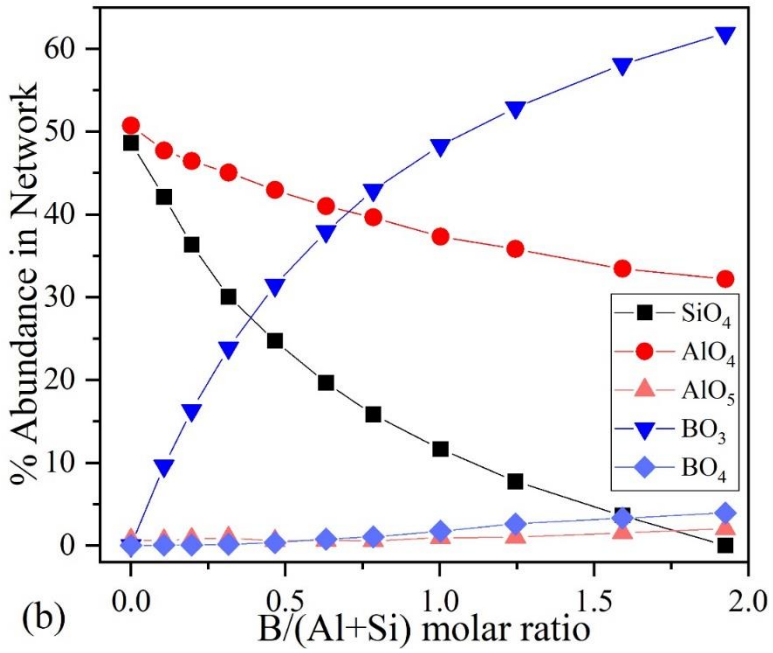

Figure 3.2. *(a) T_g and average Al and B coordination in the studied glasses as a function of B/(Al+Si) molar ratio. T_g is displayed on the left axis and both B and Al coordination are shown on the right axes. The fit of T_g displayed was performed using an exponential function to exhibit its non-linear behavior with composition. (b) Fractional display of network-forming species contained in the studied glass series according to B/(Al+Si) ratio, which have been normalized to 100 %.*

Since Na/Al = 1 in all batched compositions, it is expected that a variation in B_2O_3/SiO_2 ratio will result in a decline in T_g since tetrahedrally coordinated SiO_4 units will be replaced by less-constrained BO_3 units, leading to an overall reduction in network rigidity. However, the non-linear decrease in T_g shown with increasing B_2O_3 content in glasses is intriguing and may be explained based primarily on the following two viewpoints: (i) a gradual shift in the network topology with varying B_2O_3/SiO_2 ratio as tetrahedrally coordinated aluminosilicate glass network is being gradually converted to an aluminoborate network where trigonal BO_3 replaces tetrahedral SiO_4 as the main network forming unit, and (ii) an increasing average aluminum- and boron- coordination in the glass structure (in $x \geq 25$ compositions).

The first viewpoint can be argued according to Figure 3.2b which displays the percentage breakdown of the glass network into its constituent glass-forming species (normalized to 100 %). In the studied system, which we anticipate to have negligible NBO content, this breakdown represents a comprehensive depiction of the glass network evolution in a series of fully polymerized glasses. It is shown that while tetrahedral Al and Si are present in near-identical quantities at $x = 0$ (nepheline composition), substitution of B_2O_3 for SiO_2 leaves AlO_4 as the primary network component from $x = 5$ to $x = 20$, beyond which BO_3 units exist as the main network constituent ($x \geq 25$). The shift along this series from networks rich in tetrahedral Al and Si species to those rich in trigonal B contributes to a network with less constraints and higher degrees of freedom, thus contributing to gradual decreases in T_g.[56] However, it can also be noted in Figure 3.2b that concentration of SiO_4 and BO_3 units in the glass structure changes in a non-linear fashion as a function of B/(Al+Si) ratio, similar to what is seen for T_g in Figure 3.2a. For instance, although SiO_4 fractions initially reduce with a steep negative slope, the magnitude of the negative slope gradually decreases (as evidenced by ~30 % reductions from $x = 0$ to $x = 25$ and ~20 % reductions between $x = 25$ and $x = 50$). BO_3 unit fractions, on the other hand, first rise with a steep positive slope which continuously reduces as a function of B/(Al+Si) ratio. Thus, the non-linear trends in the variation of both SiO_4 and BO_3 network fractions may help to explain the non-linear decrease in T_g with increasing B_2O_3/SiO_2 ratio.

The second possible explanation for the non-linear trend observed in T_g is the rise in average Al and B coordination, especially in glasses with $x \geq 25$ mol.%. As evident from the secondary y-axes of Figure 3.2a, the average aluminum and boron coordination (hereafter referred to as <Al> and <B>, respectively) varies between 4.01-4.02 and 3.00-

3.02, respectively in glasses with $x \leq 25$ mol.%. However, <Al> and <B> increases from 4.01 to 4.06 and 3.02 to 3.06, respectively, with increasing B_2O_3 content in glasses with $x \geq 25$ mol.%. It has been well documented in the literature that rising BO_4 content leads to an increase in the glass network rigidity and a corresponding increase in T_g values.[3,57] However, uncertainty with respect to the impact of <Al> upon network rigidity may be addressed based on the T_g and structural data of glasses in the composition system 20 Na_2O–y Al_2O_3–(80-y) B_2O_3 (y varies between 5 – 25 mol.%) as reported in our previous publication.[43] The ^{11}B and ^{27}Al MAS NMR results on sodium aluminoborate glasses in our previous article had highlighted a decrease in the N_4 fraction from 24 % (y = 5) to 8 % (y = 25), and for AlO_4 fraction from 98% (y = 5) to 73% (y = 25) as shown in Figure S3a. Ideally, the decreasing N_4 and AlO_4 fractions should suggest decreasing connectivity in the glass network and thus, a reduced T_g. However, the T_g in these glasses was observed to increase with an increasing concentration of Al_2O_3, as has been shown in Figure S3b. This was explained to occur due to a rising fraction of five-coordinated aluminum in the glasses from 2 % (y = 5) to 23 % (y = 25), thus, increasing <Al> from 4.0 to 4.3. Similar results have been reported in the case of glasses in the Li_2O–Al_2O_3–B_2O_3 system[45] and several alkali and alkaline-earth aluminosilicate glass systems.[54] As discussed earlier, though the role of five-coordinated aluminum in the glass structure is still disputed, these findings indicate that AlO_5 units has a reticulating effect on the glass network. Thus, based on our previous results and the existing literature, the rise in <Al> in glasses with $x \geq 25$ mol. % (due to the formation of five-coordinated aluminum) in the present study may also be a contributing factor (along with the non-linear variation in SiO_4 and BO_3 units) to the non-linear variation in T_g.

3.3.4 Chemical dissolution behavior

3.3.4.1. Forward rate regime – Dissolution kinetics and solution analysis

Table S2 presents the pH, elemental concentrations, and normalized mass loss (NL) data for the glasses in this study as a function of time, while Figure 3.3a-e displays NL vs. time curves for compositions B-0, B-5, B-25, B-45, and B-50, respectively. The data points at each timestep represent an average elemental concentration from two duplicate experiments, and where the liquid aliquot from each experiment was measured three times by ICP-OES. In an attempt to capture the early release behavior, experiment durations were varied depending on the relative durability of each glass composition. The release of Na^+ cations and Al species occurs readily in acidic solutions due to ion-exchange / hydrolysis,[13] and has varying effects upon drift of solution pH from its initial value: Na^+ released from a glass tends to increase the alkalinity of solution, while alumina species (which exist as Al^{3+} or $Al(OH)_3$ in acidic environments) exhibit amphoteric behavior, depending on the acidity of solution and relative concentrations of Al species.[58,59] Meanwhile, the release of B—a species which is also released at elevated rates—has an opposite effect on the pH as its extraction is tantamount to additions of boric acid to solution. Beyond the initial buffering capacity of the pH = 2 solution imposed by the 0.01 M HCl concentration, the pH of a solution is thus subject to drift in accord with the concentration of elements released over time, and further moderated by the balance of different elemental species released as a function of glass composition (e.g. Na vs Al vs B). The spread of pH values over time is captured in Figure 3.4, which plots measured solution pH as a function of glass composition (via batched B_2O_3 content); corresponding pH data are listed in Table S2.

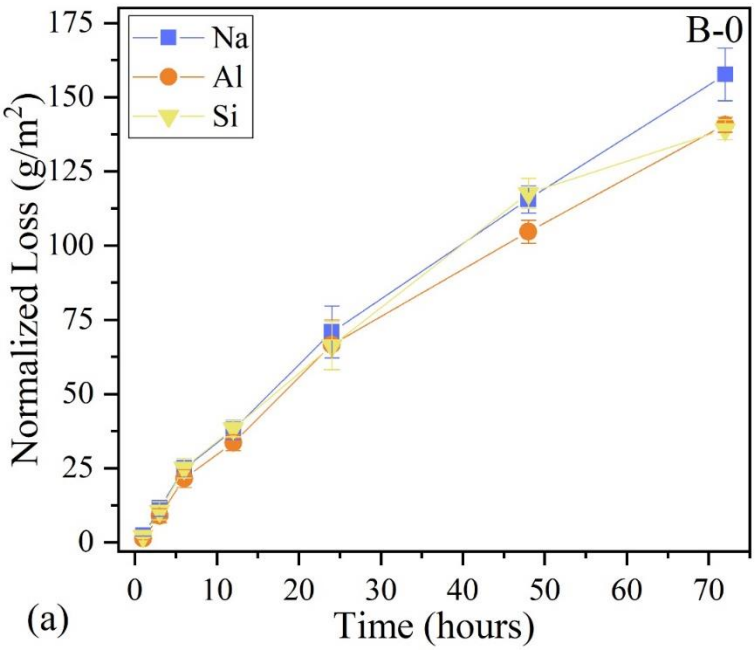
B-0
Na
Al
Si
Normalized Loss (g/m^2)
Time (hours)
0
25
50
75
100
125
150
175
0
10
20
30
40
50
60
70

(a)

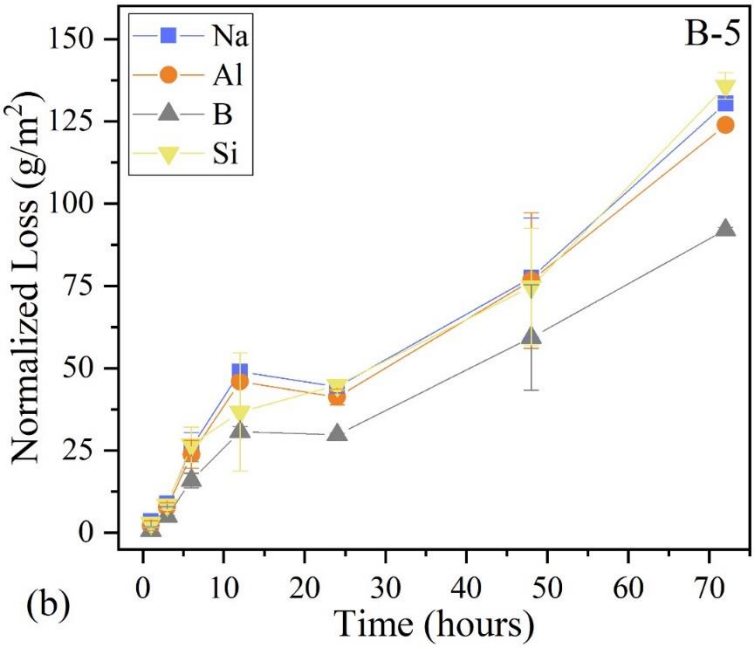
B-5
Na
Al
B
Si
Normalized Loss (g/m^2)
Time (hours)
0
25
50
75
100
125
150
0
10
20
30
40
50
60
70

(b)

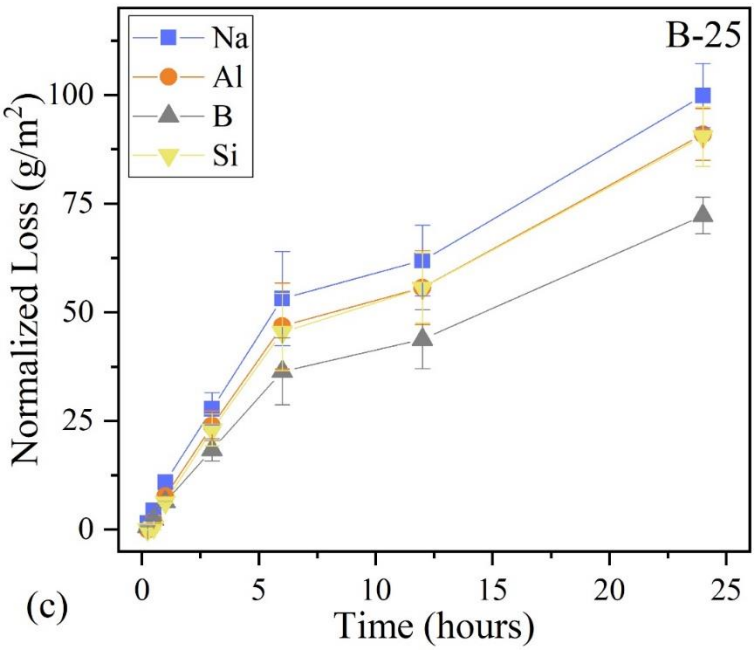
B-25
Na
Al
B
Si
Normalized Loss (g/m^2)
Time (hours)
0
25
50
75
100
0
5
10
15
20
25

(c)

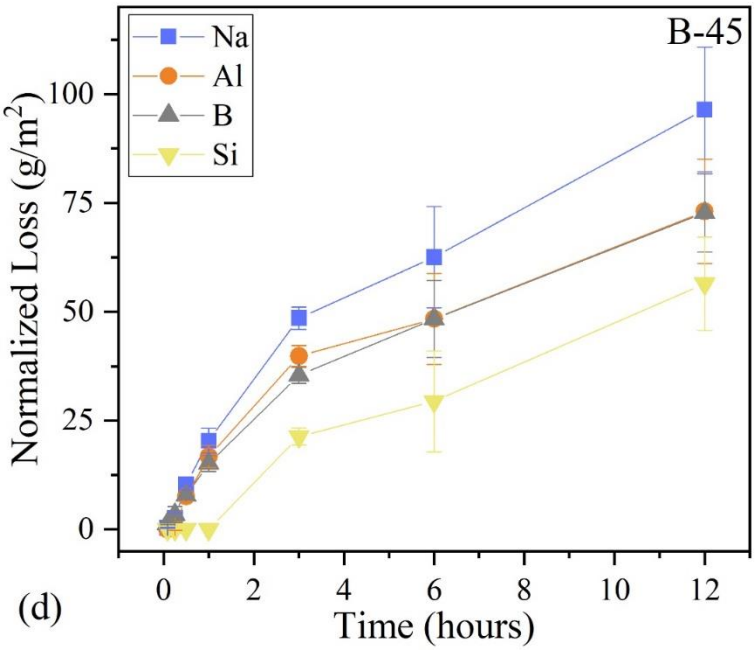
B-45
Na
Al
B
Si
Normalized Loss (g/m^2)
Time (hours)
0
25
50
75
100
0
2
4
6
8
10
12

(d)

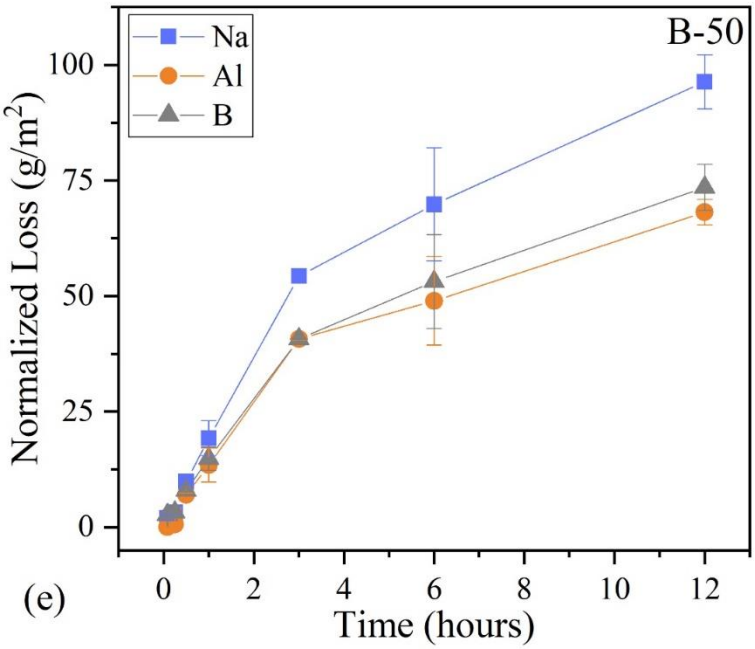

Figure 3.3. *Plots of normalized loss (g/m^2) of each element present in the glass as a function of time (hours) for (a) B-0, (b) B-5, (c) B-25, (d) B-45, and (e) B-50.*

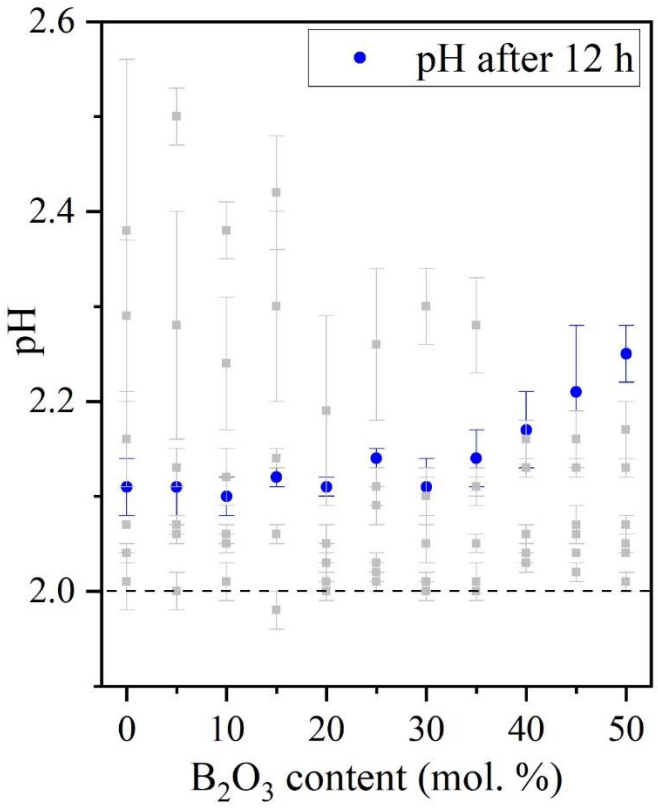

Figure 3.4. *Solution pH as a function of glass B_2O_3 content (mol. %) in pH = 2 starting solution. The data points highlighted in blue represent pH after 12 h dissolution experiments while points displayed in gray represent the pH data spread along the course of corrosion experiments for each glass composition.*

Dissolution experiments with an initial pH of 2 show a steady rise in pH over time, with ultimate values trending between 2.2-2.5. The spread of pH data in Figure 3.4 helps to additionally demonstrate the impact that glass composition has upon pH evolution, where 12 h time durations have been highlighted in a different color. It can be seen that while B_2O_3-rich compositions reach higher pH values within 12 h than SiO_2-rich counterparts, all compositions show pH change of less than ±0.3 within the same time duration, demonstrating the reasonable buffering capacity of pH = 2 solutions, and thus enabling assessment of acid dissolution behavior without the complication of more significant pH drift during a given experiment.

We utilized the curves shown in Figure 3.3 to compare the release kinetics between different elements and calculate forward dissolution rates for each composition, while also gaining relevant information related to the dissolution mechanisms of these glasses in acidic media. Acidic environments tend to promote ion exchange/hydrolysis of the glass network relative to solutions with near neutral pH, in this case with normalized loss values at pH = 2 reaching upwards of 100 g/m^2 within the first 12 hours of experiments. This tendency for rapid attack of the network is especially prominent in glasses with significant Al_2O_3 content, as Al-O bonds tend to undergo rapid hydrolysis in acids relative to neutral pH conditions.[24] In the studied acidic environment, we see in Figure 3.3 that all glasses show (i) an initial linear increase, followed by (ii) a concave downward behavior indicative of decreases in elemental release rates towards a slower residual rate. The reduction in apparent release rate in static experiments can result from several possible mechanisms, including formation of a protective gel/precipitate layer near the surface of the glass or solution feedback effects that manifest as elements approach saturation in the surrounding aqueous environment (we will explore this in more depth in the next section as we discuss residual rate).[24,26] From the NL data, it can be seen that SiO_2-rich compositions showed nearly 100 g/m^2 release in 72 h, while B_2O_3-rich compositions in the same environments saw this same magnitude of release in only 12-24 hours. In terms of elemental differences in release behavior, all glasses tend to show close agreement between NL values of Na, Al, B and Si (where present in the glass) within the forward rate regime, implying congruent release behavior. These similarities will become more apparent as we compare forward release rates and discuss experimental uncertainty.

Statistical uncertainty reported for each normalized loss point has been determined as 1σ standard deviation for duplicate samples; propagated uncertainty of corrosion experiments have also been calculated and these values approach as high as 50-60 % of the mean value. While standard deviation calculations only consider data from duplicate experiments and may need confirmation using larger sample sizes, propagation of uncertainty aims to encapsulate all systematic experimental uncertainties and estimate their combined sum—in our case, the vast majority arising from uncertainty in particle surface area. Since the vast majority of our NL standard deviations lie within 20 % of the mean value and NL/forward rate uncertainties typically seen in literature are less than 15-25 %[60-62] (for crushed glass in static conditions, using geometric SA, especially in high rate conditions), the propagated uncertainty we have calculated may overestimate uncertainties which arose from spherical approximations of crushed particles. Thus, we expect measured uncertainties from replicate experiments in our study to provide comparable estimates of total uncertainty, and will consider this amount of uncertainty when evaluating NL data in our dataset.

In order to further compare release kinetics for these glasses, we deduce forward dissolution rates on the basis of each element by performing linear regression on normalized loss vs. time plots in the early, linear portions of the release curves (within the first 3-12 hours). The slope of the line provides an estimate of the forward dissolution rate; these fits should only be considered estimates due to the somewhat subjective nature of determining the linear portion of the NL curve, as well as observing non-zero intercepts at t = 0 (with fits not being constrained to pass through (0,0)). Experimental error in fitting a single dissolution rate to NL data has been highlighted extensively in the literature.[63-64]

Rates and uncertainties according to B_2O_3 content (and B/(Al+Si) molar ratio) can be found in Table 3.3. In order to assess standard uncertainty in linear regression, the standard deviation of each NL data point was considered, and the relative impact of fitting a slope to uncertain data was summed to determine the overall fitted-slope uncertainty, similar to the method discussed by Kragten.[65] Normalized loss rates on the basis of each element varied between 3 – 18 g m^{-2} h^{-1}, showing a steady increase with increasing B/(Al+Si) ratio, as illustrated in Figure 3.5. This rate increase across the series was expected due to borate network incorporation. However, its relatively linear behavior according to B/(Al+Si) ratio (as seen in Figure 3.5) is a striking result considering the non-linear behavior observed in T_g and network structure (Figure 3.2). The non-linear trend detected for T_g has earlier been ascribed to either (i) shifts in network topology due to replacement of tetrahedral species (i.e. AlO_4 and SiO_4) by BO_3 or (ii) increases in coordination of both Al and B. The trends observed imply that although compositional evolution in the studied system impacts glass network connectivity and short-ranged structure, NL rates are relatively insensitive to these changes. Instead, we see that dissolution rates generally undergo linear variation according to B composition in the glass, indicating that B_2O_3-for-SiO_2 network former substitution promotes incremental changes in chemical durability.

Table 3.3. *Normalized loss rates of Na, Al, B, and Si for the studied glass in pH = 2 solutions. These rates were determined by linearly fitting normalized loss vs. time plots. Rates have been compared according to experimental B/(Al+Si) ratios in the glass.*

		Normalized Loss Rates (g-glass/[m^2h])							
Sample ID	**B/(Si+Al) Ratio**	**Na**	**Na-error**	**Al**	**Al-error**	**B**	**B-error**	**Si**	**Si-error**
B-0	0.00	3.2	±0.3	2.9	±0.3	--	--	3.3	±0.3
B-5	0.11	4.2	±0.1	4.1	±0.1	2.8	±0.2	3.2	±1.7
B-10	0.20	6.5	±0.3	6.3	±0.2	4.4	±0.2	7.0	±0.2
B-15	0.32	5.8	±0.3	5.4	±0.07	3.93	±0.06	6.0	±0.1
B-20	0.47	7.1	±0.5	6.6	±0.5	4.9	±0.4	6.8	±0.6
B-25	0.63	8.9	±1.8	8.1	±1.7	6.2	±1.3	8.0	±1.5
B-30	0.79	8.3	±0.2	7.7	±0.2	6.1	±0.2	8.45	±0.07
B-35	1.00	9.6	±0.2	8.9	±0.3	7.0	±0.2	8.8	±0.7
B-40	1.25	12.3	±2.2	11.2	±2.1	8.9	±1.8	9.9	±2.8
B-45	1.59	16.4	±0.9	13.7	±0.9	11.6	±0.7	*	*
B-50	1.93	18.2	±0.1	14.1	±0.1	13.26	±0.07	--	--

*Dissolution rate was not able to be extracted due to non-linear behavior in the forward rate regime and/or concentrations near the ICP-OES detection limits

In terms of elemental release comparisons, we see that while some glasses have deviations of up to 20-35 % between the NL rates of different elements, the studied glasses show a general NL rate similarity between Na, Al, B, and Si (where present in the glass),

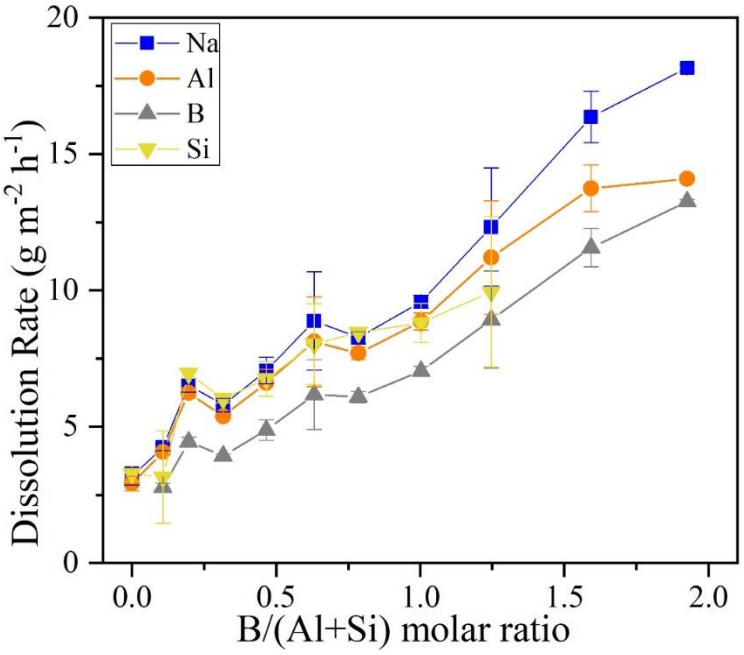

Figure 3.5. *Na, Al, B, and Si normalized loss rates in acidic solutions as a function of B/(Al+Si) molar ratio.*

indicative of an apparent congruent release in the forward rate regime when subjected to acidic environments. Slight differences in release rates may arise due to uncertainties typically estimated from dissolution experiments and the challenges with estimating forward rates from NL curves—surface sensitive experiments discussed later in this text will further explore release trends during the residual rate regime and aim to validate our kinetic observations near the glass–fluid interface.

3.3.4.2 Residual rate regime – Glass structural transformations due to aqueous corrosion

Although we see from the estimated dissolution rates that the glasses dissolve congruently in the forward rate regime, NL values for B in the majority of the compositions (x = 5 – 35) lie below Al, Si and/or Na at longer time durations in these experiments (12 – 72 h)—a time window taken to represent the residual rate regime. In order to further explore the structural and compositional changes taking place near the glass surface in this

regime, recovered glassy grains and bulk coupons were analyzed using multiple bulk and surface characterization techniques.

Grains recovered from the dissolution experiments were analyzed via XRD and MAS NMR to obtain insight into the structural evolution of glasses during corrosion. XRD analysis determined all grains recovered from experiments to be amorphous, ruling out the formation of significant crystalline secondary phases during corrosion. Meanwhile, ^{27}Al and ^{11}B MAS NMR were performed on selected samples, and results are summarized in Figures 3.6a and 3.6b. We chose to analyze grains obtained after the final timestep of corresponding static experiments, focusing on glass compositions B-0, B-25, and B-50—the goal being to investigate extremes of potential structural changes taking place as glasses across the composition series corrode. Figure 3.6a displays the ^{27}Al MAS NMR spectra of pre- and post-corroded glasses. In this figure, we see that B-0 and B-25 glasses show identical ^{27}Al spectra before versus after corrosion. The position of the peak corresponds

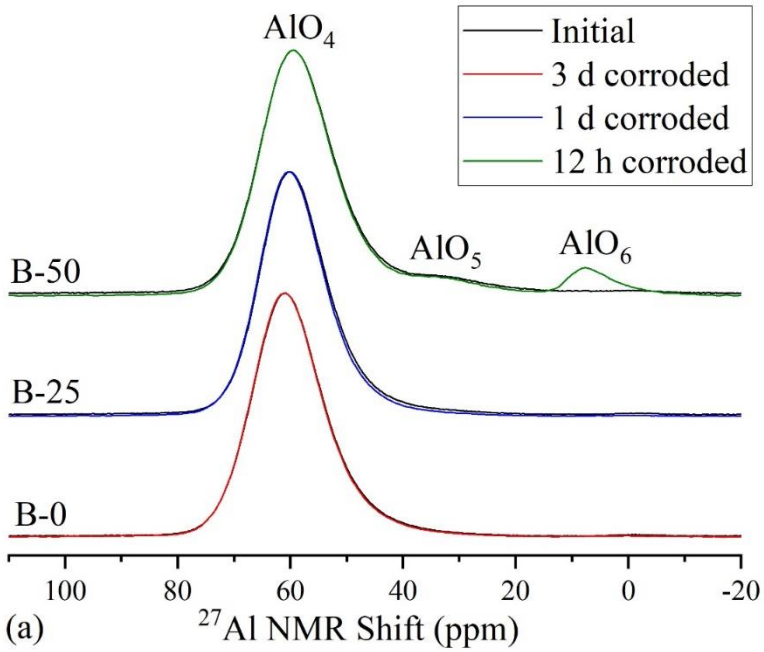

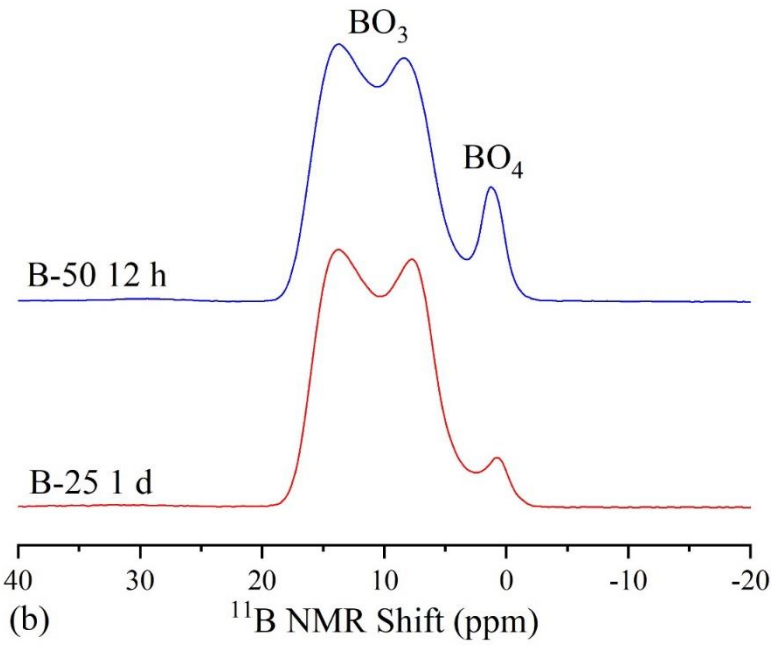

Figure 3.6. *(a) [27]Al MAS NMR spectra of B-0, B-25, and B-50 grains recovered from dissolution experiments, as compared with the pre-corroded glass spectra. (b) [11]B MAS NMR spectra of B-25 and B-50 grains recovered from dissolution experiments.*

to Al in a tetrahedral environment, and the consistency of the spectra indicate that the local environment around Al is not detectably altered in these glasses during

corrosion. In the composition B-50, on the other hand, while the AlO_4 and AlO_5 peaks appear identical before and after corrosion, development of a noteworthy peak near 5 ppm can also be seen after 12 h of corrosion. We associate the emergence of this peak with the development of hydrated AlO_6 secondary phases near the glass–fluid interface.[11,43,66] The breadth of the AlO_6 peak in the ^{27}Al MAS NMR spectra is indicative of an amorphous phase (corroborated by XRD), whereas crystalline $Al(OH)_3$ has been shown to form during corrosion of aluminoborate glasses in near-neutral–to–alkaline pH conditions due to significant decreases in alumina solubility.[43] It should be noted here that, despite significant amount of dissolution in samples from both SiO_2-rich and B_2O_3-rich glass compositions at pH = 2, the formation of AlO_6 units was observed only in the sodium aluminoborate end-

member sample (B-50). Although the formation of AlO_6 units in aluminosilicate glasses has also been reported in the literature (when corroded in acids for long durations),[11,66] our finding that AlO_6 only forms in B_2O_3-rich compositions (within the studied time durations) is attributed to the faster dissolution kinetics of aluminoborate glasses in comparison to their silicate analogues, which engenders a more rapid approach to corresponding solubility limit(s) within the timeframe of the experiment.

Figure 3.6b presents the ^{11}B MAS NMR spectra of B-25 and B-50 glasses after corrosion. These data were obtained at lower magnetic field than those for the pre-corroded glasses in Figure 3.1a, inhibiting direct spectral overlay due to known changes in peak shape with magnetic field. That said, when comparing the quantified results from Figure 3.6b to those from the pre-corroded glasses, calculated N_4 fractions are almost identical (± 0.5 %; within ± 0.5 % error limits typically associated with fitting MAS NMR spectra). This indicates an insignificant degree of structural change in the borate glass network (irrespective of the glass composition) during corrosion, as well as implying little to no precipitation of hydrated boron species from solution on the glass surface in this residual rate regime. Thus, acidic environments attacking the borate glass network seem to hydrolyze bonds with no preferential affinity for hydrolysis of BO_3 or BO_4 units despite differences in their typical bond energies.[43] While we have not discussed the silicate network, we expect silicate units in contact with acid to act in one of two ways: (i) hydration of Si-O bonds (Si-OH) or (ii) rapid apparent release of Si due to silicate "cluster" release following hydrolysis of the surrounding Al or B network, as network connectivity decreases significantly.[12,67-69] As mentioned in the previously proposed mechanisms for glass dissolution,[4,22,30] ultimate gel layer formation can occur through either method via

precipitation of partially bonded or free species at the glass – acid reaction front.[22,70] Surface analysis techniques will better explain the mechanism of silicate-acid interactions taking place.

Based on the NL results from glass grains, the polished coupons of glasses B-5, B-25, and B-45 were corroded in HCl (pH = 2) solutions for 3 days, 1 day, and 12 hours, respectively, creating samples with surfaces representative of the residual rate regime. The pre- and post-corroded glass coupons were analyzed using surface sensitive techniques. XPS spectra for the pre- and post-corroded B-45 samples are shown in Figure 3.7 and the corresponding elemental compositions (for B-5, B-25, and B-45, both pre- and post-corrosion) are summarized in Table 3.4. The measured surface compositions of the as-polished samples agree reasonably well with the bulk experimental compositions (as analyzed via ICP-OES) except for the B content of sample B-5, which shows a 2.5×

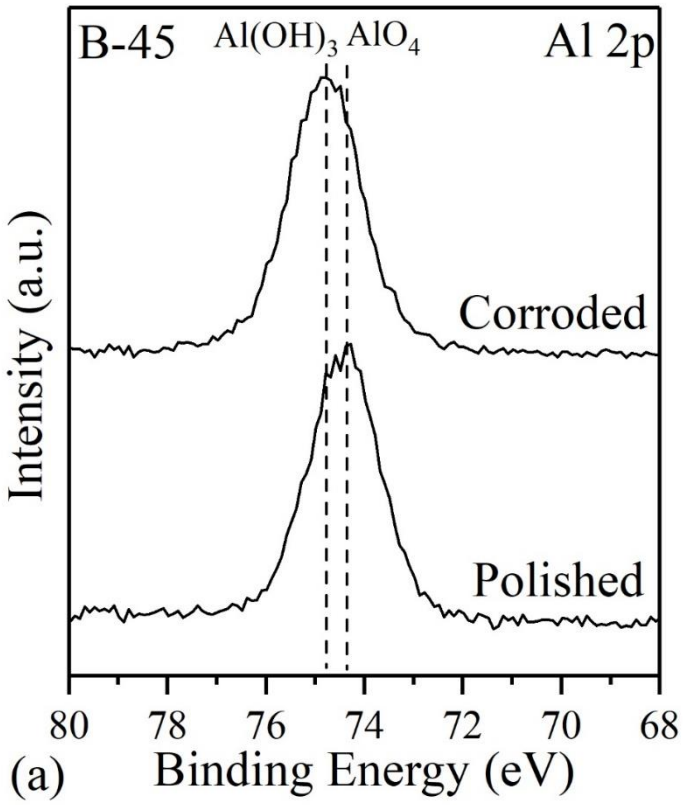

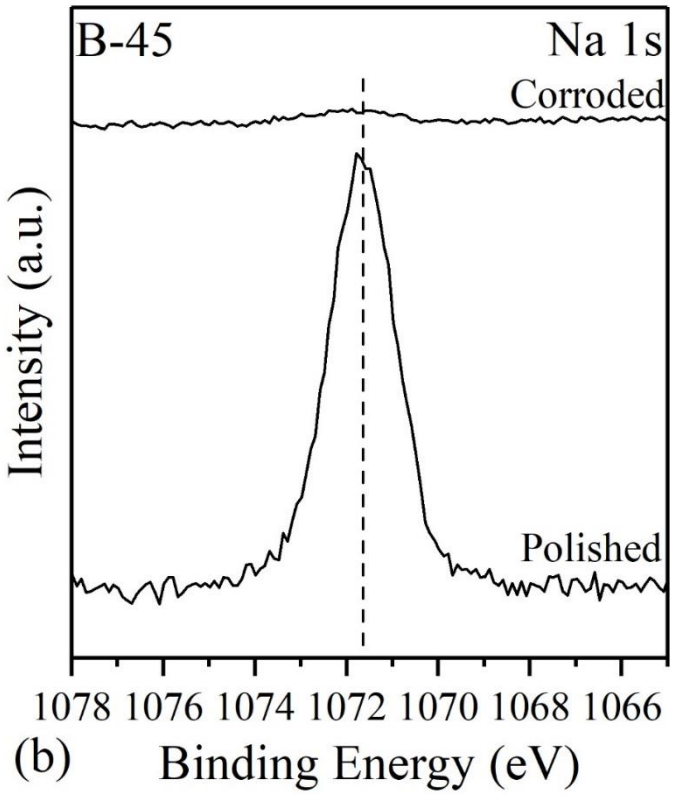
B-45
Na 1s
Corroded
Polished
Intensity (a.u.)
1078 1076 1074 1072 1070 1068 1066
Binding Energy (eV)

(b)

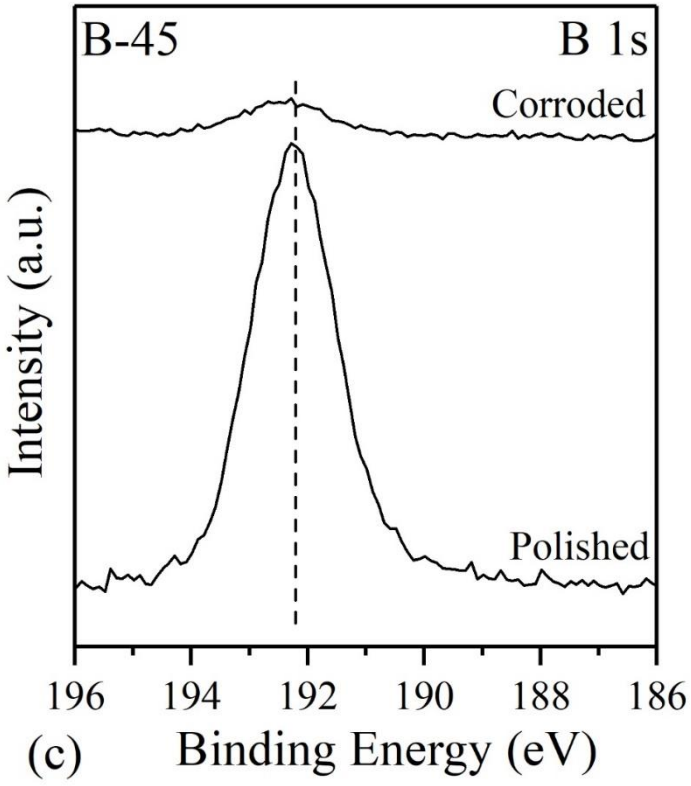
B-45
B 1s
Corroded
Polished
Intensity (a.u.)
196 194 192 190 188 186
Binding Energy (eV)

(c)

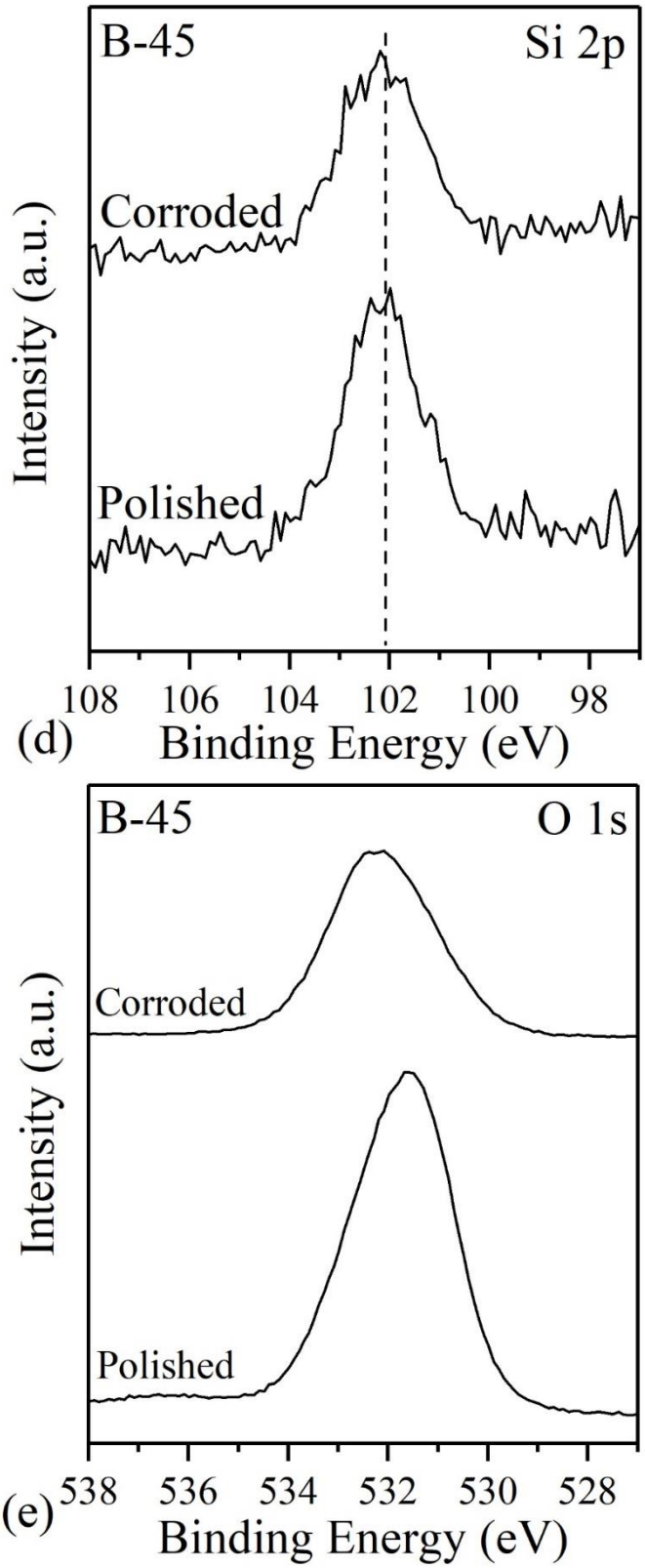

Figure 3.7. *(a) Al 2p, (b) Na 1s, (c) B 1s, (d) Si 2p, and (e) Al 2p XPS spectra of polished and corroded B-45 glass coupons (12 hours at pH = 2).*

enrichment at the surface. As this discrepancy is well outside the expected statistical error in the XPS measurements, this can be possibly attributed to slight segregation of B_2O_3 at the surface of the sample.

Table 3.4. *Surface compositions of B-5, B-25, and B-45 samples as measured in the top ~5-10 nm via XPS analysis (atomic percentages accurate within ±5 %). In each sample, we have compared compositions of polished and corroded samples to the bulk compositions measured using ICP-OES.*

Element (at. % by XPS)	**Sample**								
	B-5			**B-25**			**B-45**		
	Bulk	**Polished Surface**	**Corroded Surface**	**Bulk**	**Polished Surface**	**Corroded Surface**	**Bulk**	**Polished Surface**	**Corroded Surface**
Na	14.0	12.2	12.6	12.5	10.2	9.1	11.3	10.0	0.9
Al	14.1	13.0	13.2	13.0	11.7	13.6	11.5	10.9	26.3
B	2.8	7.0	3.8	12.1	13.7	9.7	20.3	22.6	4.1
Si	12.3	12.6	11.6	6.1	7.2	6.3	1.2	1.6	2.9
O	56.9	55.3	58.8	56.2	57.2	61.2	55.7	55.0	65.8

Upon exposure to acidic environments, the composition of sample B-5 was relatively unchanged in the surface layer, reverting largely to the composition expected from that of the bulk glass. However, samples B-25 and B-45 both showed moderate to significant reduction in their Na and B content. The surface of sample B-45 was almost entirely depleted in Na and B (80-90 %), while Al was enriched by a factor of ~2.4 after immersion. In Figure 3.7a, it is evident that while the polished Al 2p peak lies near 74.2 eV, the corroded sample shifts towards slightly higher binding energy (74.8 eV). This shift could indicate the presence of octahedral $Al(OH)_3$ units, as examined in Refs.[71-73] and may further correspond with a gradual shift in Al speciation from 4- to 6-coordination seen in MAS NMR of B-50 post-corroded grains.[74] O 1s spectra, meanwhile, show a significant change between pre- and post-corroded samples due to likely changes in mixed network former linkage ratios (i.e. Al-O-B, B-O-B, etc.), as well as surface hydration effects, during

corrosion. At these spectral resolutions, we also cannot rule out the possibility of the formation of NBOs near the surface due to bond hydrolysis (which normally contributes intensity near 531 eV).[75,76] Difficulties with deconvoluting the numerous species contained within the O1s peak of oxide glasses are well-documented, and thus no attempts to further quantify these effects have been made here.

Table 3.5. *Surface compositions of B-5, B-25, and B-45 samples as measured in the top 100-300 nm via RBS analysis (atomic percentages accurate within ±4 %). In each sample, we have compared compositions of polished and corroded samples to the bulk compositions measured using ICP-OES*

Element (at. % by RBS)	**Sample**								
	B-5			**B-25**			**B-45**		
	Bulk	**Polished Surface**	**Corroded Surface**	**Bulk**	**Polished Surface**	**Corroded Surface**	**Bulk**	**Polished Surface**	**Corroded Surface**
Na	14.0	13.9	13.0	12.5	12.1	11.8	11.3	11.3	4.8
Al	14.1	13.6	13.8	13.0	9.8	12.3	11.5	11.0	18.3
B*	2.8	2.8	3.0	12.1	15.8	12.6	20.3	21.8	18.8
Si	12.3	11.8	11.8	6.1	7.8	6.3	1.2	1.1	1.1
O	56.9	57.8	58.4	56.2	54.4	56.9	55.7	54.7	57.0

*Note: B concentration estimated by difference

The RBS spectrum of sample B-45 (polished and corroded) is shown in Table 3.5 and measured elemental compositions of B-5, B-25, and B-45 before and after corrosion are displayed in Figure 3.8a. Note that the RBS spectrum of corroded B-45 glass has been shifted downward in order to line up the intensities of the Al/Si onsets for ease of comparison. As a reminder to the reader, RBS measurements probe a depth of about 100-300 nm, and thus are expected to probe an information depth significantly further into the surface than in XPS. It can be seen that RBS-measured surface and bulk experimental compositions agree well in the polished samples. RBS results for the corroded samples, meanwhile, suggest that only the composition of sample B-45 changed significantly beyond the XPS-measured surface layers, as the loss of Na extended well into the RBS-

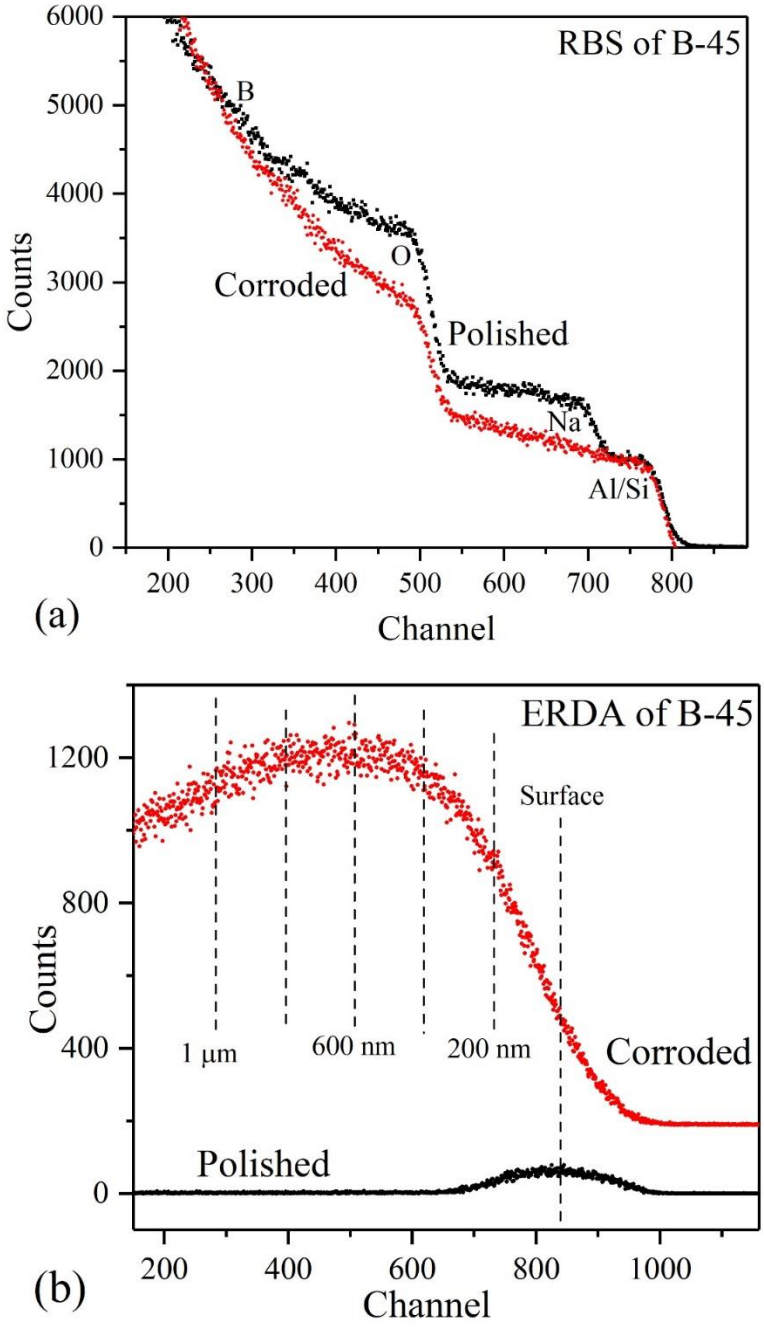

Figure 3.8. *(a) RBS and (b) ERDA spectra of polished and corroded B-45 glass coupons (12 hours at pH = 2).*

measured depth of the surface. Additionally, Al in B-45 was enriched by ~66 % in the bulk of the corroded sample as compared to the polished sample, implying that the Al enrichment in this sample may extend to a depth beyond that probed by XPS. Samples B-5 and B-25 showed no statistically significant changes in the bulk.

The ERDA spectrum shown in Figure 3.8b indicates that sample B-45 absorbed a significant amount of hydrogen upon exposure to acidic solutions, reaching a hydrogen content of 33% within the top 1 μm of the glass. The remaining samples showed only background levels of hydrogen both before and after immersion (see Figure S5). Note that the samples charged slightly during these measurements due to their relatively low conductivity and hence the energy onset of the surface peak was not consistent.

3.4 Discussion

The aim of this study was to address the open questions: (1) What mechanism(s) best describe the corrosion of glass in acidic environments? (2) Specifically, does AlO_6 gel layer formation in acid occur by way of a structural transformation or re-precipitation? (3) Will the established corrosion mechanisms – multi-step inter-diffusion mechanism or IDPM – accurately describe the dissolution behavior of glasses far from the extensively-studied SiO_2-rich compositional regime (i.e. B_2O_3-rich samples)?

In order to achieve this goal, we employed several state-of-the-art techniques to characterize the evolution of solution, bulk and surface chemistry, and structural features in glass samples after aqueous corrosion. We found that acid submersion (pH = 2) of sodium aluminoborosilicate glasses extending from silicate- to borate-rich endmembers resulted in a range of glass responses as were manifested in the elemental release behavior from the glass and structural/compositional modifications observed near the glass–fluid interface. As the batched glasses were designed in the metaluminous (Na/Al = 1) regime, Na^+ in the network was expected to play a charge compensating role for primarily AlO_4 and possibly BO_4 thus maintaining full connectivity of the silicate network. Furthermore, as high overall connectivity was maintained in these glasses (Table 3.2 estimates NBO

fractions in each glassy network), the structural drivers for network corrosion are anticipated to be highly dependent upon medium range order characteristics (i.e. Si-O-Al, Si-O-B, B-O-Al linkages), where composition and network former ratios play a major role in defining the extent of network mixing thus greatly affecting the rate of network hydrolysis and elemental release.

We particularly expected relative fractions of BO_3/BO_4 and AlO_4/AlO_5 species in the network to greatly affect network mixing characteristics in the studied compositions, which may be governed by stoichiometric mixing or by coordinated 'tetrahedral avoidance' rules, where bonds such as $Al^{[4]}$-O-$Al^{[4]}$ or $Al^{[4]}$-O-$B^{[4]}$ are generally avoided in the glass network.[40,48,77,78] In our system, we see in Table 3.2 that silicate-rich glasses show almost exclusively BO_3 and AlO_4 structural units (>98 %) with a completely polymerized silica backbone (~4 BO per tetrahedron), which is consistent with previous studies of similar mixed network former compositions.[32,40] However, as we enter the borate-rich region, we begin to see steady replacements of BO_3 and AlO_4 by BO_4 and AlO_5, respectively, up to ~6% of each in the aluminoborate endmember glass, the trend of which has also been previously observed in similar aluminoborate glasses.[44,79] In terms of medium range order, it has been observed that nepheline ($NaAlSiO_4$) glasses tend to form a highly interconnected aluminosilicate network, with roughly 4 bridging oxygens per Si tetrahedron connecting to Al.[12,48] As we introduce B_2O_3 for SiO_2, Si-O-B and Al-O-B bonds begin to replace the highly linked Si-O-Al network until the $NaAlB_2O_5$ endmember, where we expect an Al-O-B and B-O-B linked glassy network.[44] We deduce from Figure 3.2a and 3.2b that although T_g decreases along the series due to the replacement of tetrahedral Al and Si units by less-constrained BO_3 units, the non-linear behavior of T_g

(and network rigidity) is impacted either by the similarly non-linear evolution of the network former fractions (i.e. BO_3 substitution for SiO_4 and AlO_4; Figure 3.2b) along the glass series, or by an increase in aluminum and boron coordination (i.e. rises in AlO_5 and BO_4; Figure 3.2a) in B_2O_3-rich compositions ($x > 25$), which we have described to strengthen the glass network. In the following section we explore the influence changes in network structure can have on glass corrosion.

Glasses exposed to acidic solutions tend to undergo the process of ion exchange and hydrolysis at accelerated rates relative to neutral-pH solutions. Furthermore, due to the high Al solubility in acidic media, nepheline-based glasses will degrade quickly in acid due to rupture of Al-O-Si bonds which constitute the network. In tandem with H^+/H_3O^+ penetration to extract Na^+ from the glass, hydrolysis of Al-O bonds and subsequent release of Al^{3+} cations—species which previously held together isolated Si tetrahedra—will cause the network to degrade, leading to the rapid release of silicate units as silicic acid.[12] As B_2O_3 is substituted into the network in place of SiO_2, the introduction of more readily-hydrolyzed Al-O-B and Si-O-B linkages drives network hydrolysis to occur at a faster rate in comparison to Si-O-Al.[80] In Figure 3.5 and Table 3.3, we see that, in acidic environments, increasing B/(Al+Si) ratio in the glass leads to a general linear increase in forward dissolution rates by a factor of 4-6× proceeding from aluminosilicate to aluminoborate endmembers, despite non-linear evolution of the glass network structure and rigidity.

Comparing inter-elemental release patterns from the various glass compositions, we observe that acid attack leads to congruent release in the forward rate regime, as displayed by NL curves for Na, Al, B, and Si NL and the estimated forward rates being

within the experimental error of one another during the initial stages of dissolution (Figures 3.3 and 3.5). While previously reported findings suggest that silicate glasses in acid media dissolve congruently,[11,14,21,30] our results show that as B is added, signs of apparent incongruency emerge, and are especially evident in the residual rate regime of SiO_2-rich glasses as B release drops below that of Al, Si, and/or Na. In order to supplement our understanding of the elemental release mechanisms occurring at the glass–fluid interface in the residual rate regime, surface compositional and structural changes were uncovered by using a combination of multiple characterization techniques.

Although XRD studies of recovered grains detected that corroded glasses lacked significant crystalline secondary phases, the combination of MAS NMR and XPS / RBS / ERDA techniques enabled us to gain additional insight into the amorphous structural and chemical changes occurring near the glass–fluid interface. Through MAS NMR experiments, we observed that while B coordination in all glasses shows negligible changes, Al in B_2O_3-rich glasses begins to undergo a coordination change from predominantly AlO_4 to AlO_6, as determined from the development of a peak near 0 ppm in B-50 (as seen in Figure 3.6a) following corrosion. XPS studies corroborate these results by a marked enrichment of atom% Al and potential indications of AlO_6 units after 12 h of acid corrosion in B-45, as implied by a significant shift in the Al 2p peak towards higher binding energy,[71,72,74] and accompanied by the development of an O 1s peak likely associated with NBO (see Figure 3.7). An intriguing outcome of XPS / RBS experiments in the same sample (B-45) resides in that the following observation: Even though we have seen Al elemental release occur at similar rates to B in these experiments, as Na and B are significantly depleted (80-90 %) in the top ~10 nm, we see Al enrichment at the surface by

a factor of ~2.5 in the top ~10 nm (XPS) and a factor of ~1.5 in the top 100-300 nm (RBS) (presumably in a hydrated 6-coordinated form; see Table 3.4 and 3.5). ERDA performed on this sample confirmed the presence of H as either H^+/H_3O^+ or diffused H_2O species within the top ~1 μm of the glass surface. We should also note that Al enrichment and Na / B depletion from the surface was also seen in the B-25 (SiO_2 / B_2O_3 = 1) composition, although to a much less extent. Studies by Tsomaia et al.[11] and Criscenti et al.[66] in sodium aluminosilicate glasses at pH = 2 had previously determined that an enriched AlO_6 layer forming at the glass–fluid interface occurs upon corrosion by way of structural transformation at the glass surface. However, in our studied borate-rich glasses, we can alternatively explain the Al enriched surface formed either by a re-precipitation or adsorption process of Al species from solution following significant degradation of the borate network, which agrees with literature showing that dissolved Al exist in an octahedral form.[11,66] Thus, regardless of elemental release trends which seem to signal that the glass corrodes in a congruent fashion with regards to Al, we determine that these glasses begin to undergo a re-precipitation/gel layer formation mechanism on approach to the residual rate regime, even when silica is not present in significant amounts in the initial glass structure.

Our findings tend to show consistency with what was proposed by Geisler et al.[22] for experiments performed with a simplified glass composition at pH 0, which suggest that glass dissolution proceeds as an inward moving reaction front, where all elements are released congruently, followed by the formation of a re-precipitated gel layer. However, we are seeing an apparent shift in corrosion mechanism between SiO_2-rich and B_2O_3-rich samples, marked by the differences seen in the surface layers of borate-rich samples (in the

form of an AlO_6-rich hydrated layer)—while SiO_2-rich glasses ($x \leq 25$)—which undergo similar magnitudes of normalized loss—do not show clear evidence of hydrated layer formation. Aluminum in octahedral coordination near the surface of nepheline-based glasses, which has been found in glasses corroded at pH = 2 for longer time durations (near 1000 h),[11] may only occur in the latter stages of dissolution in which silica is saturated in solution and more significantly depleted from the glass–fluid interface. By comparison, in B_2O_3-rich samples, hydrated AlO_6 layers begin to form at the surface following degradation of the borate network, which occurs at an accelerated rate. Presumably, this breakdown promotes a dissolution–re-precipitation mechanism at the surface, as Al has been shown to release from the glass at similar rates to other network formers as opposed to remaining in the glass. Sodium aluminoborosilicate glasses dissolving in acidic conditions tend to act in ways that reflect their medium range order, and we have also shown that—while composition plays a clear role in the reaction kinetics and mechanisms occurring at the glass–fluid interface—recently proposed mechanisms for glass corrosion may provide the basis for understanding the way a wide range of glass compositions (extending into the B_2O_3-rich region) corrode under acidic conditions. Further examination of the pristine glass/hydrated layer interface, for instance through high-resolution depth profiling (i.e. TEM, ToF-SIMS, etc.), would provide valuable supplemental information about the molecular scale mechanisms and drivers governing corrosion of these glasses in acidic environments.

3.5 Conclusions

The current study has made an attempt to understand the mechanisms governing corrosion of glasses in acidic environments. Accordingly, a series of glasses in the 25

Na_2O–25 Al_2O_3–x B_2O_3–(50-x) SiO_2 (x varies between 0 and 50 mol. %) was subjected to pH = 2 environments, where the evolution of solution, bulk and surface chemistry, and structural characteristics of glass was studied using a suite of state-of-the-art spectroscopic characterization techniques. It has been shown that, although stepwise addition of B_2O_3 into the glass causes non-linear changes in network structural characteristics—i.e. T_g and fractions of AlO_5/BO_4 in the glass—noticeably linear increases in forward dissolution rates are observed. As has been seen in previous literature for SiO_2-rich compositions, we observed that glasses submerged in acid underwent an apparent congruent release in the forward rate regime. In the residual rate regime, however, deviations from congruency were detected, as Al enrichment through $AlO_4 \rightarrow Al(OH)_3$ evolution was observed at the surface of corroded B_2O_3-rich glasses. When comparing our results to the aforementioned studies, the findings imply that dissolution–re-precipitation processes occur at the glass–fluid interface in both B_2O_3-rich and SiO_2-rich glass compositions, notwithstanding vastly different reaction kinetics. The present investigation forms the basis for further study of the glass surface in wide-ranged glass compositions, as further implementing atomic-scale depth profiling can better probe the reactive interface and help to pinpoint molecular mechanisms governing aqueous corrosion.

Acknowledgements

This material is based upon work supported by the National Science Foundation under Grant No. 1507131, the US Department of Energy (DOE) – Offices of Nuclear Energy and Environmental Management through Nuclear Energy University Program under Grant No. DE-NE0008597, and US DOE – Office of River Protection under Grant No. DE-EM0003207. ORNL is operated by UT-Battelle, LLC, for the US DOE under Contract No.'s DE-AC05-00OR22725. The authors also thank the Characterization Sciences group at Corning Incorporated for compositional analysis of the glasses.

Supplementary Information

The online version of this article contains supplementary information including XRD and ^{23}Na MAS NMR of the as synthesized samples, T_g and ^{27}Al and ^{11}B MAS NMR speciation of a related glass system, among other miscellaneous chemical dissolution data as referred in the chapter. In this supplementary information, an additional section has also been added describing chemical dissolution behavior of pH = 0 and 4 solutions, which were not a part of the publication.

References

1. Qiu, Q.; Kumosa, M., Corrosion of E-glass fibers in acidic environments. *Composites Science and Technology* 1997, *57* (5), 497-507.
2. Jones, R.; Stewart, J., The kinetics of corrosion of e-glass fibres in sulphuric acid. *J Non-Cryst Solids* 2010, *356* (44-49), 2433-2436.
3. Stone-Weiss, N.; Pierce, E. M.; Youngman, R. E.; Gulbiten, O.; Smith, N. J.; Du, J.; Goel, A., Understanding the structural drivers governing glass–water interactions in borosilicate based model bioactive glasses. *Acta Biomater* 2018, *65* (Supplement C), 436-449.
4. Gin, S.; Abdelouas, A.; Criscenti, L. J.; Ebert, W. L.; Ferrand, K.; Geisler, T.; Harrison, M. T.; Inagaki, Y.; Mitsui, S.; Mueller, K. T., An international initiative on long-term behavior of high-level nuclear waste glass. *Materials Today* 2013, *16* (6), 243-248.
5. Burger, E.; Rebiscoul, D.; Bruguier, F.; Jublot, M.; Lartigue, J. E.; Gin, S., Impact of iron on nuclear glass alteration in geological repository conditions: A multiscale approach. *Applied Geochemistry* 2013, *31* (Supplement C), 159-170.
6. Hoppe, A.; Gueldal, N. S.; Boccaccini, A. R., A review of the biological response to ionic dissolution products from bioactive glasses and glass-ceramics. *Biomaterials* 2011, *32* (11), 2757-2774.
7. Reddy, A.; Norris, D. F.; Momeni, S. S.; Waldo, B.; Ruby, J. D., The pH of beverages in the United States. *The Journal of the American Dental Association* 2016, *147* (4), 255-263.
8. Smith, N. J.; Pantano, C. G., Leached layer formation on float glass surfaces in the presence of acid interleave coatings. *J Am Ceram Soc* 2008, *91* (3), 736-744.
9. Iacocca, R. G.; Allgeier, M., Corrosive attack of glass by a pharmaceutical compound. *J Mater Sci* 2007, *42* (3), 801-811.
10. Curto, V. F.; Coyle, S.; Byrne, R.; Angelov, N.; Diamond, D.; Benito-Lopez, F., Concept and development of an autonomous wearable micro-fluidic platform for real time pH sweat analysis. *Sensors and Actuators B: Chemical* 2012, *175*, 263-270.
11. Tsomaia, N.; Brantley, S. L.; Hamilton, J. P.; Pantano, C. G.; Mueller, K. T., NMR evidence for formation of octahedral and tetrahedral Al and repolymerization of the Si network during dissolution of aluminosilicate glass and crystal. *American Mineralogist* 2003, *88* (1), 54-67.
12. Hamilton, J. P.; Brantley, S. L.; Pantano, C. G.; Criscenti, L. J.; Kubicki, J. D., Dissolution of nepheline, jadeite and albite glasses: toward better models for aluminosilicate dissolution. *Geochimica et Cosmochimica Acta* 2001, *65* (21), 3683-3702.
13. Hamilton, J. P.; Pantano, C. G.; Brantley, S. L., Dissolution of albite glass and crystal. *Geochimica et Cosmochimica Acta* 2000, *64* (15), 2603-2615.
14. Hamilton, J. P.; Pantano, C. G., Effects of glass structure on the corrosion behavior of sodium-aluminosilicate glasses. *Journal of Non-Crystalline Solids* 1997, *222*, 167-174.
15. Declercq, J.; Diedrich, T.; Perrot, M.; Gislason, S. R.; Oelkers, E. H., Experimental determination of rhyolitic glass dissolution rates at 40–200 C and 2< pH< 10.1. *Geochimica et Cosmochimica Acta* 2013, *100*, 251-263.
16. Wolff-Boenisch, D.; Gislason, S. R.; Oelkers, E. H.; Putnis, C. V., The dissolution rates of natural glasses as a function of their composition at pH 4 and 10.6, and

temperatures from 25 to 74 degrees C. *Geochimica Et Cosmochimica Acta* 2004, *68* (23), 4843-4858.
17. Wolff-Boenisch, D.; Gislason, S. R.; Oelkers, E. H., The effect of fluoride on the dissolution rates of natural glasses at pH 4 and 25 degrees C. *Geochimica Et Cosmochimica Acta* 2004, *68* (22), 4571-4582.
18. Gislason, S. R.; Oelkers, E. H., Mechanism, rates, and consequences of basaltic glass dissolution: II. An experimental study of the dissolution rates of basaltic glass as a function of pH and temperature. *Geochimica et Cosmochimica Acta* 2003, *67* (20), 3817-3832.
19. Oelkers, E. H.; Gislason, S. R., The mechanism, rates and consequences of basaltic glass dissolution: I. An experimental study of the dissolution rates of basaltic glass as a function of aqueous Al, Si and oxalic acid concentration at 25 C and pH= 3 and 11. *Geochimica et Cosmochimica Acta* 2001, *65* (21), 3671-3681.
20. Berger, G.; Claparols, C.; Guy, C.; Daux, V., Dissolution rate of a basalt glass in silica-rich solutions: implications for long-term alteration. *Geochimica et Cosmochimica Acta* 1994, *58* (22), 4875-4886.
21. Knauss, K. G.; Bourcier, W. L.; McKeegan, K. D.; Merzbacher, C. I.; Nguyen, S. N.; Ryerson, F. J.; Smith, D. K.; Weed, H. C.; Newton, L. In *Dissolution kinetics of a simple analogue nuclear waste glass as a function of pH, time and temperature*, MRS Proceedings, Cambridge Univ Press: 1989; p 176.
22. Geisler, T.; Janssen, A.; Scheiter, D.; Stephan, T.; Berndt, J.; Putnis, A., Aqueous corrosion of borosilicate glass under acidic conditions: A new corrosion mechanism. *Journal of Non-Crystalline Solids* 2010, *356* (28-30), 1458-1465.
23. Doremus, R. H., Interdiffusion of hydrogen and alkali ions in a glass surface. *J Non-Cryst Solids* 1975, *19*, 137-144.
24. Bunker, B. C., Molecular mechanisms for corrosion of silica and silicate glasses. *Journal of Non-Crystalline Solids* 1994, *179*, 300-308.
25. Hopf, J.; Eskelsen, J. R.; Chiu, M.; Ievlev, A.; Ovchinnikova, O. S.; Leonard, D.; Pierce, E. M., Toward an understanding of surface layer formation, growth, and transformation at the glass–fluid interface. *Geochimica et Cosmochimica Acta* 2018, *229*, 65-84.
26. Vienna, J. D.; Ryan, J. V.; Gin, S.; Inagaki, Y., Current Understanding and Remaining Challenges in Modeling Long-Term Degradation of Borosilicate Nuclear Waste Glasses. *International Journal of Applied Glass Science* 2013, *4* (4), 283-294.
27. Lenting, C.; Plümper, O.; Kilburn, M.; Guagliardo, P.; Klinkenberg, M.; Geisler, T., Towards a unifying mechanistic model for silicate glass corrosion. *npj Materials Degradation* 2018, *2* (1), 28.
28. Gin, S.; Neill, L.; Fournier, M.; Frugier, P.; Ducasse, T.; Tribet, M.; Abdelouas, A.; Parruzot, B.; Neeway, J.; Wall, N., The controversial role of inter-diffusion in glass alteration. *Chemical Geology* 2016, *440*, 115-123.
29. Zheng, Q.; Youngman, R. E.; Hogue, C. L.; Mauro, J. C.; Potuzak, M.; Smedskjær, M. M.; Yue, Y., Structure of boroaluminosilicate glasses: impact of [Al 2 O 3]/[SiO 2] ratio on the structural role of sodium. *Physical Review B* 2012, *86* (5), 054203.
30. Geisler, T.; Nagel, T.; Kilburn, M. R.; Janssen, A.; Icenhower, J. P.; Fonseca, R. O.; Grange, M.; Nemchin, A. A., The mechanism of borosilicate glass corrosion revisited. *Geochimica et Cosmochimica Acta* 2015, *158*, 112-129.

31. Wang, Y.; Jove-Colon, C. F.; Kuhlman, K. L., Nonlinear dynamics and instability of aqueous dissolution of silicate glasses and minerals. *Scientific Reports* 2016, *6*, 30256.
32. Pierce, E. M.; Reed, L. R.; Shaw, W. J.; McGrail, B. P.; Icenhower, J. P.; Windisch, C. F.; Cordova, E. A.; Broady, J., Experimental determination of the effect of the ratio of B/Al on glass dissolution along the nepheline (NaAlSiO4)–malinkoite (NaBSiO4) join. *Geochimica et Cosmochimica Acta* 2010, *74* (9), 2634-2654.
33. Balzer, R.; Behrens, H.; Schuth, S.; Waurischk, T.; Reinsch, S.; Müller, R.; Fechtelkord, M.; Deubener, J., The influence of H2O and SiO2 on the structure of silicoborate glasses. *Journal of Non-Crystalline Solids* 2019, *519*, 119454.
34. Massiot, D.; Fayon, F.; Capron, M.; King, I.; Le Calvé, S.; Alonso, B.; Durand, J. O.; Bujoli, B.; Gan, Z.; Hoatson, G., Modelling one-and two-dimensional solid-state NMR spectra. *Magnetic Resonance in Chemistry* 2002, *40* (1), 70-76.
35. Massiot, D.; Bessada, C.; Coutures, J.; Taulelle, F., A quantitative study of 27Al MAS NMR in crystalline YAG. *Journal of Magnetic Resonance (1969)* 1990, *90* (2), 231-242.
36. ASTM, C., 1220. 1998. Standard Test Method for Static Leaching of Monolithic Waste Forms for Disposal of Radioactive Waste. *American Society for Testing and Materials, Annual Book of ASTM Standards* 1998, *12*, 609-624.
37. Scofield, J. H. *Theoretical photoionization cross sections from 1 to 1500 keV*; California Univ., Livermore. Lawrence Livermore Lab.: 1973.
38. Smith, G. C., Evaluation of a simple correction for the hydrocarbon contamination layer in quantitative surface analysis by XPS. *Journal of Electron Spectroscopy and Related Phenomena* 2005, *148* (1), 21-28.
39. Zeidler, A.; Wezka, K.; Whittaker, D. A. J.; Salmon, P. S.; Baroni, A.; Klotz, S.; Fischer, H. E.; Wilding, M. C.; Bull, C. L.; Tucker, M. G.; Salanne, M.; Ferlat, G.; Micoulaut, M., Density-driven structural transformations in B2O3 glass. *Physical Review B* 2014, *90* (2).
40. Du, L.-S.; Stebbins, J. F., Network connectivity in aluminoborosilicate glasses: A high-resolution 11B, 27Al and 17O NMR study. *Journal of Non-Crystalline Solids* 2005, *351* (43-45), 3508-3520.
41. Smedskjaer, M. M.; Zheng, Q.; Mauro, J. C.; Potuzak, M.; Mørup, S.; Yue, Y., Sodium diffusion in boroaluminosilicate glasses. *J Non-Cryst Solids* 2011, *357* (22), 3744-3750.
42. Züchner, L.; Chan, J. C. C.; Müller-Warmuth, W.; Eckert, H., Short-Range Order and Site Connectivities in Sodium Aluminoborate Glasses: I. Quantification of Local Environments by High-Resolution 11B, 23Na, and 27Al Solid-State NMR. *The Journal of Physical Chemistry B* 1998, *102* (23), 4495-4506.
43. Kapoor, S.; Youngman, R. E.; Zakharchuk, K.; Yaremchenko, A.; Smith, N. J.; Goel, A., Structural and Chemical Approach toward Understanding the Aqueous Corrosion of Sodium Aluminoborate Glasses. *The Journal of Physical Chemistry B* 2018, *122*, 10913-10927.
44. Bertmer, M.; Züchner, L.; Chan, J. C.; Eckert, H., Short and medium range order in sodium aluminoborate glasses. 2. Site connectivities and cation distributions studied by rotational echo double resonance NMR spectroscopy. *The Journal of Physical Chemistry B* 2000, *104* (28), 6541-6553.

45. Fernandes, H. R.; Kapoor, S.; Patel, Y.; Ngai, K.; Levin, K.; Germanov, Y.; Krishtopa, L.; Kroeker, S.; Goel, A., Composition-structure-property relationships in Li2O–Al2O3–B2O3 glasses. *Journal of Non-Crystalline Solids* 2018, *502*, 142-151.
46. Morin, E. I.; Stebbins, J. F., Separating the effects of composition and fictive temperature on Al and B coordination in Ca, La, Y aluminosilicate, aluminoborosilicate and aluminoborate glasses. *Journal of Non-Crystalline Solids* 2016, *432*, 384-392.
47. Morin, E. I.; Wu, J.; Stebbins, J. F., Modifier cation (Ba, Ca, La, Y) field strength effects on aluminum and boron coordination in aluminoborosilicate glasses: the roles of fictive temperature and boron content. *Applied Physics A* 2014, *116* (2), 479-490.
48. Lee, S. K.; Stebbins, J. F., The degree of aluminum avoidance in aluminosilicate glasses. *Am Mineral* 1999, *84* (5-6), 937-945.
49. Sen, S.; Youngman, R. E., High-resolution multinuclear NMR structural study of binary aluminosilicate and other related glasses. *Journal of Physical Chemistry B* 2004, *108* (23), 7557-7564.
50. Toplis, M. J.; Kohn, S. C.; Smith, M. E.; Poplett, I. J. F., Fivefold-coordinated aluminum in tectosilicate glasses observed by triple quantum MAS NMR. *American Mineralogist* 2000, *85* (10), 1556-1560.
51. Neuville, D. R.; Cormier, L.; Massiot, D., Al coordination and speciation in calcium aluminosilicate glasses: Effects of composition determined by 27Al MQ-MAS NMR and Raman spectroscopy. *Chemical Geology* 2006, *229* (1–3), 173-185.
52. Januchta, K.; Youngman, R. E.; Goel, A.; Bauchy, M.; Rzoska, S. J.; Bockowski, M.; Smedskjaer, M. M., Structural origin of high crack resistance in sodium aluminoborate glasses. *Journal of Non-Crystalline Solids* 2017, *460*, 54-65.
53. Thompson, L. M.; Stebbins, J. F., Non-stoichiometric non-bridging oxygens and five-coordinated aluminum in alkaline earth aluminosilicate glasses: Effect of modifier cation size. *Journal of Non-Crystalline Solids* 2012, *358* (15), 1783-1789.
54. Neuville, D. R., Al in five fold coordination in silicate glasses and melts: Myth or Reality? Proportion and role of Al in five fold coordination in silicate glasses and melts. In *ICG Annual Meeting 2018*, Yokohama, Japan, 2018.
55. Wu, J.; Stebbins, J. F., Effects of cation field strength on the structure of aluminoborosilicate glasses: High-resolution 11B, 27Al and 23Na MAS NMR. *Journal of Non-Crystalline Solids* 2009, *355* (9), 556-562.
56. Smedskjaer, M. M.; Mauro, J. C.; Youngman, R. E.; Hogue, C. L.; Potuzak, M.; Yue, Y., Topological Principles of Borosilicate Glass Chemistry. *Journal of Physical Chemistry B* 2011, *115* (44), 12930-12946.
57. Smedskjaer, M. M.; Youngman, R. E.; Striepe, S.; Potuzak, M.; Bauer, U.; Deubener, J.; Behrens, H.; Mauro , J. C.; Yue, Y., Irreversibility of Pressure Induced Boron Speciation Change in Glass. *Scientific records* 2014, *4*, 3770.
58. Wesolowski, D. J.; Palmer, D. A., Aluminum speciation and equilibria in aqueous solution: V. Gibbsite solubility at 50°C and pH 3–9 in 0.1 molal NaCl solutions (a general model for aluminum speciation; analytical methods). *Geochimica et Cosmochimica Acta* 1994, *58* (14), 2947-2969.
59. Paul, A., Chemical durability of glasses; a thermodynamic approach. *J Mater Sci* 1977, *12* (11), 2246-2268.

60. Ebert, W. L. *Comparison of the results of short-term static tests and single-pass flow-through tests with LRM glass (ANL-06/51)*; Argonne National Laboratory: Argonne, IL, USA, 2006.
61. Gin, S.; Frugier, P.; Jollivet, P.; Bruguier, F.; Curti, E., New Insight into the Residual Rate of Borosilicate Glasses: Effect of S/V and Glass Composition. *International Journal of Applied Glass Science* 2013, *4* (4), 371-382.
62. Fournier, M.; Ull, A.; Nicoleau, E.; Inagaki, Y.; Odorico, M.; Frugier, P.; Gin, S., Glass dissolution rate measurement and calculation revisited. *Journal of Nuclear Materials* 2016, *476*, 140-154.
63. Ebert, W. L.; Bates, J. K., A comparison of glass reaction at high and low glass-surface solution volume. *Nucl. Tech.* 1993, *104* (3), 372-384.
64. Ebert, W. L. *The effects of the glass surface area/solution volume ratio on glass corrosion: a critical review*; Argonne National Laboratory: 1995.
65. Kragten, J., Tutorial review. Calculating standard deviations and confidence intervals with a universally applicable spreadsheet technique. *Analyst* 1994, *119* (10), 2161-2165.
66. Criscenti, L. J.; Brantley, S. L.; Mueller, K. T.; Tsomaia, N.; Kubicki, J. D., Theoretical and 27Al CPMAS NMR investigation of aluminum coordination changes during aluminosilicate dissolution. *Geochimica et Cosmochimica Acta* 2005, *69* (9), 2205-2220.
67. Lee, S. K.; Musgrave, C. B.; Zhao, P.; Stebbins, J. F., Topological disorder and reactivity of borosilicate glasses: quantum chemical calculations and 17O and 11B NMR study. *The Journal of Physical Chemistry B* 2001, *105* (50), 12583-12595.
68. Casey, W. H.; Westrich, H. R.; Holdren, G. R., Dissolution rates of plagioclase at pH= 2 and 3. *American Mineralogist* 1991, *76* (1-2), 211-217.
69. Oelkers, E. H.; Schott, J., Experimental study of anorthite dissolution and the relative mechanism of feldspar hydrolysis. *Geochimica et Cosmochimica Acta* 1995, *59* (24), 5039-5053.
70. Devreux, F.; Barboux, P.; Filoche, M.; Sapoval, B., A simplified model for glass dissolution in water. *Journal of Materials Science* 2001, *36* (6), 1331-1341.
71. Bunker, B. C.; Arnold, G. W.; Day, D. E.; Bray, P., The effect of molecular structure on borosilicate glass leaching. *J Non-Cryst Solids* 1986, *87* (1), 226-253.
72. Kloprogge, J. T.; Duong, L. V.; Wood, B. J.; Frost, R. L., XPS study of the major minerals in bauxite: gibbsite, bayerite and (pseudo-) boehmite. *Journal of colloid and interface Science* 2006, *296* (2), 572-576.
73. Paparazzo, E., XPS analysis of oxides. *Surface and Interface Analysis* 1988, *12* (2), 115-118.
74. Remy, M.; Genet, M.; Notté, P.; Lardinois, P.; Poncelet, G., Characterisation of Al coordination at the outer surface of dealuminated mordenites by X-ray photoelectron spectroscopy. *Microporous Materials* 1993, *2* (1), 7-15.
75. Ebina, T.; Iwasaki, T.; Chatterjee, A.; Katagiri, M.; Stucky, G. D., Comparative study of XPS and DFT with reference to the distributions of Al in tetrahedral and octahedral sheets of phyllosilicates. *The Journal of Physical Chemistry B* 1997, *101* (7), 1125-1129.
76. Tasker, G. W.; Uhlmann, D. R.; Onorato, P. I. K.; Alexander, M. N.; Struck, C. W., Structure of sodium aluminosilicate glasses: X-ray photoelectron spectroscopy. *Le Journal de Physique Colloques* 1985, *46* (C8), C8-273.

77. Banerjee, J.; Kim, S. H.; Pantano, C. G., Elemental areal density calculation and oxygen speciation for flat glass surfaces using x-ray photoelectron spectroscopy. *J Non-Cryst Solids* 2016, *450*, 185-193.
78. Lee, S. K.; Stebbins, J. F., The structure of aluminosilicate glasses: High-resolution O-17 and Al-27 MAS and 3QMAS. *Journal of Physical Chemistry B* 2000, *104* (17), 4091-4100.
79. Loewenstein, W., The distribution of aluminum in the tetrahedra of silicates and aluminates. *Am Mineral* 1954, *39* (1-2), 92-96.
80. Du, L.-S.; Stebbins, J. F., Site connectivities in sodium aluminoborate glasses: multinuclear and multiple quantum NMR results. *Solid State Nuclear Magnetic Resonance* 2005, *27* (1–2), 37-49.

Chapter 4. Structural design of sodium borosilicate-based model bioactive glasses using advanced experimental and computational methods

Nicholas Stone-Weiss,[1] Henrik Bradtmüller,[2] Mariagrazia Fortino,[3] Marco Bertani,[3] Randall E. Youngman,[4] Alfonso Pedone,[3] Hellmut Eckert,[2,5] Ashutosh Goel[1,‡]

[1]Department of Materials Science and Engineering, Rutgers, The State University of New Jersey, Piscataway, NJ 08854, United States

[2]Institut für Physikalische Chemie, WWU Münster, Corrensstrasse 30, D48149 Münster, Germany.

[3]Department of Chemical and Geological Sciences, University of Modena and Reggio Emilia, via G. Campi 103, 41125, Modena, Italy

[4]Science and Technology Division, Corning Incorporated, Corning, NY 14831, United States

[5]São Carlos Institute of Physics, University of São Paulo, Avenida Trabalhador Saocarlense 400, São Carlos, SP 13566-590, Brazil

‡ Corresponding author:
Email: ag1179@soe.rutgers.edu; Ph: +1-848-333-1523

Abstract

Borosilicate glasses have emerged as potential candidates for third generation bioactive glasses due to the potential advantages they possess as compared to silicate-based compositions. In order to develop novel borosilicate bioactive glasses, it is critical to understand composition-structure-degradation behavior relationships in this system, covering a wide range of compositions and properties with significant structural complexity. In this pursuit, the structure of glasses in the Na_2O-P_2O_5-B_2O_3-SiO_2 system is studied by both experimental and computational methods. Specifically, we explore the effect of incremental additions of P_2O_5 into perboric (R = Na/B; R < 1), metaboric (R = 1), and per-alkaline (R >1) glass compositions, using advanced single and double resonance magic-angle spinning (MAS) NMR techniques, MD simulations, and DFT calculations based on advanced algorithms. P_2O_5 tends to attract the network former species preferentially, resulting in a re-polymerization of the silicate and a re-structuring of the borate components. These processes eventually lead to phase separation and crystallization of sodium phosphate, at levels above 3 mol. % to 7 mol. %, respectively, in the peralkaline and perboric glasses investigated. $^{11}B\{^{31}P\}$ rotational echo double resonance results indicate that the ability of glasses to incorporate P_2O_5 without phase separation is related to the formation of P-O-B(IV) linkages that are integrated into the borosilicate glass network.

Keywords: Structure, Bioactive glass, Compositional design

4.1 Introduction

The past 15+ years have experienced a tremendous upsurge in research interest of borosilicate-based bioactive glasses as potential candidates for the design and development of novel third generation biomaterials.[1-3] Borosilicate glasses, in particular, provide certain advantages over standard silicate-based compositions, including (i) a wider glass-forming range, (ii) tunable chemical durability over wide ranges,[1] and (iii) ease of processing into porous three-dimensional scaffolds for implantation into the body.[2,4] Recent studies have further shown their ability to promote angiogenesis and osteogenesis in vivo.[1,5] These features make borosilicate glasses very attractive for a wide scope of biomedical applications. Generally, third generation biomaterials are designed such that, when in contact with body fluids, ionic dissolution products that are released from the glass into the body stimulate specific biological responses,[6] such as gene activation for osteoblast proliferation,[7] enhancement of angiogenesis,[8] and expression of insulin-like growth factor II mRNA,[9] each of which facilitate body tissue regeneration. For maximizing healing effects, one needs to design materials whose functional ion release kinetics are tailored to the bodily rates of new tissue formation.[1] It is therefore of utmost importance to develop a fundamental understanding of the dissolution behavior in this glass system. Furthermore, since the degradation of glass in aqueous solutions is intimately related to its atomic and molecular structure,[10,11] a conceptual understanding of the compositional and structural drivers of glass degradation in the borosilicate glass system is required. The present contribution pursues this objective using the synergies of both experimental and computational methods.

Standard silicate glasses such as the 45S5 "gold standard" form a network dominated by metasilicate chains.[10] The introduction of B_2O_3 into silicate glasses, which tends to expedite degradation behavior,[1,2] adds significant structural complexity. Multiple new intermediate-range structural features involving three- and four-coordinate boron and their connectivities with each other and with silicon have been discussed,[12-15] but the relation of these features to dissolution rates are still largely unknown. Therefore, most borosilicate bioactive glass compositions reported in the literature have been developed systematically, by expanding the compositional parameter space, gradually replacing SiO_2 with B_2O_3 in known formulations such as 45S5 or 13-93.[1] If a "materials-by-design" approach (as laid out in the White House's Materials Genome Initiative[16]) is adopted instead of a "trial-and-error" approach, quantitative structure-property relationship (QSPR) models must be developed, which allow the prediction of glass structural details and degradation behavior based upon composition.

Our current study investigates the Na_2O-P_2O_5-B_2O_3-SiO_2 system. P_2O_5, like B_2O_3, plays a similarly vital role in bioactive glasses, as it enhances the bioactivity of most commercial bioactive glasses such as 45S5 and 13-93, largely due to its compatibility with mineral phosphate in bone tissue.[1,17] Although it is also an important component in borosilicate-based bioactive glasses,[1,2] the structural organization of P_2O_5-containing borosilicate glasses has never been comprehensively investigated. While commercial silicate-based bioactive glasses such as 45S5 contain predominantly isolated orthophosphate units,[1] the phosphate speciation in borosilicate-based bioglasses is still unknown over wide composition ranges. It is known, however, that small additions of P_2O_5 to borosilicate glass affect bulk physical properties and tend to promote phase separation

and/or crystallization processes.[18-21] Such changes have been explained in terms of an increased degree of polymerization of the silica and boria species and P-O-B intermixing in the network.[19,21] P_2O_5 is generally known as a cation scavenger in mixed network former glasses, attracting large amounts of modifier via multiply charged orthophosphate and diphosphate anions.[19,21,22] In the present contribution we obtain quantitative information from magic-angle spinning nuclear magnetic resonance (MAS NMR) and molecular dynamics (MD) simulations on the phosphate units present and their next nearest neighbor environments.[22,23] The discussion will be conducted in terms of the network former units (NFU-s) in the terminology T^n_{mX} (*T*, *X* = Si, B, P) where *n* denotes the number of bridging O atoms and $m \leq n$ specifies the number of linkages to other NFU-s of type X. Our studies aim to develop a comprehensive structural model relating sodium phospho-borosilicate glass compositions to their short- and intermediate-range order structural details.

4.2 Experimental

4.2.1 Glass synthesis and annealing

Glass series were designed in three different compositional regimes of $R = Na_2O/B_2O_3$ ratios, including perboric (PB, $R < 1$), metaboric (MB, $R = 1$), and peralkaline (PA, $R > 1$) compositions. Baseline compositions are (i) 25 Na_2O–30 B_2O_3–45 SiO_2 for PB ($R = 0.83$), (ii) 25 Na_2O–25 B_2O_3–50 SiO_2 for MB ($R = 1$), and (iii) 25 Na_2O–20 B_2O_3–55 SiO_2 for PA ($R = 1.25$). For each series, P_2O_5 was substituted into the baseline glass composition using three different ways (resulting in a total of nine series), as exemplified for MB glasses below:

Series MB1: (25-*x*/2) Na_2O–*x* P_2O_5–(25-*x*/2) B_2O_3–50 SiO_2
Series MB2: *x* P_2O_5–(100-*x*) (25 Na_2O–25 B_2O_3–50 SiO_2)
Series MB3: 25 Na_2O–*x* P_2O_5–25 B_2O_3–(50-*x*) SiO_2

In the first series, P_2O_5 is substituting for both Na_2O and B_2O_3, thus maintaining a constant *R* value. The second series features additions of *x* P_2O_5 in place of 100-*x* of the baseline compositions. The third series substitutes P_2O_5 in place of SiO_2 in the baseline glass. Batched P_2O_5 contents (*x*) vary between 0 and 9 mol. % within each series, however, only compositions resulting in homogeneous glasses were investigated further. For each batched composition, high purity powders of SiO_2 (Alfa Aesar; 99.5 %), H_3BO_3 (Alfa Aesar; ≥98 %), Na_2SiO_3 (Alfa Aesar; >99 %), and Na_2HPO_4 (Fisher Chemical; >99 %) were used as precursors. Batches corresponding to 70 g of oxides were melted in Pt-Rh crucibles for 1 h in air at temperatures between 1400 and 1500 ºC and quenched on a metallic plate. The amorphous nature of glasses was confirmed by X-ray diffraction (XRD) (PANalytical – X'Pert Pro; Cu K_α radiation; 2θ range: 10–90º; step size: 0.01313º s^{-1}). The glasses were then annealed for 1 hour near their glass transition temperatures (T_g*-50 ºC; where T_g* is predicted from the SciGlass database[24]) and slowly cooled to room temperature (see[26] for details). Residual stresses of less than 10 MPa were measured using a polariscope. Table 4.1 presents batched vs. experimental glass composition as analyzed on selected samples by inductively coupled plasma – optical emission spectroscopy (ICP – OES; PerkinElmer Optima 7300V) for B_2O_3, P_2O_5, and SiO_2, and flame emission spectroscopy (PerkinElmer Flame Emission Analyst 200) for Na_2O. Densities were measured using Archimedes's method for at least 3 pieces per sample weighed in both air and d-limonene. Differential scanning calorimetry (DSC) data was collected on fine glass powders (<45 μm diameter) using a simultaneous thermal analyzer (STA; Netzsch) from room temperature to 1400 °C at a heating rate of 20 °C/min under a constant flow of nitrogen gas. The experimental T_g was determined from the onset of the endothermic dip in the DSC curve.

Sample ID	Batched				ρ (g/cm^3) (±0.3 %)	V_M (±0.3 %) (cm^3/mol)	T_g (°C)
	Na_2O	P_2O_5	B_2O_3	SiO_2			
PB0	25.0 [25.3]	--	30.0 [29.7]	45.0 [45.0]	2.519	25.18	559
PB1-P1	24.6	1.0	29.5	45.0	2.509	25.58	
PB1-P3	23.6	3.0	28.4	45.0	2.479	26.50	
PB1-P5	22.7	5.0	27.27	45.0	2.462	27.30	
PB2-P1	24.8	1.0	29.7	44.6	2.518	25.50	549
PB2-P3	24.3 [25.9]	3.0 [3.0]	29.1 [29.0]	43.7 [42.2]	2.507	26.24	538
PB2-P5	23.8 [25.8]	5.0 [5.0]	28.5 [29.1]	42.8 [40.0]	2.476	27.20	506
PB3-P1	25.0	1.0	30.0	44.0	2.510	25.59	
PB3-P4	25.0	4.0	30.0	41.0	2.485	26.84	
PB3-P7	25.0	7.0	30.0	38.0	2.456	28.15	
MB0	25.0 [25.1]	--	25.0 [25.0]	50.0 [49.9]	2.531	24.87	561
MB1-P1	24.5	1.0	24.5	50.0	2.519	25.29	
MB1-P3	23.5	3.0	23.5	50.0	2.504	26.05	
MB1-P4	23.0	4.0	23.0	50.0	2.490	26.50	
MB2-P1	24.8	1.0	24.8	49.5	2.533	25.16	547
MB2-P3	24.3 [26.0]	3.0 [3.0]	24.3 [23.9]	48.5 [47.1]	2.518	25.94	543
MB2-P5	23.8 [24.7]	5.0 [5.0]	23.8 [23.9]	47.5 [46.3]	2.488	26.88	543
MB3-P1	25.0	1.0	25.0	49.0	2.519	25.31	
MB3-P3	25.0	3.0	25.0	47.0	2.510	26.05	
MB3-P5	25.0	5.0	25.0	45.0	2.487	26.95	
PA0	25.0 [25.1]	--	20.0 [20.1]	55.0 [54.8]	2.527	24.72	547
PA1-P1	24.4	1.0	19.6	55.0	2.501	25.28	
PA1-P3	23.3	3.0	18.7	55.0	2.497	25.94	
PA2-P1	24.8	1.0	19.8	54.5	2.526	25.04	548
PA2-P3	24.3 [25.1]	3.0 [3.1]	19.4 [19.3]	53.4 [52.6]	2.513	25.80	545
PA3-P1	25.0	1.0	20.0	49.0	2.515	25.16	
PA3-P3	25.0	3.0	20.0	47.0	2.506	25.91	

Table 4.1. *All batched compositions of studied glasses compared to selected experimental compositions (in brackets), as analyzed via ICP-OES (±0.5 mol. %). Density (ρ), molar volume (V_M), and T_g are also displayed.*

4.2.2 Structural analysis by NMR

NMR spectra were measured on an Agilent 240-MR DD2 spectrometer (5.7 T) using 3.2, 4.0, and 7.5 mm MAS NMR probes, Bruker Avance Neo 500 and 600 MHz spectrometers (11.7 and 14.1 T, respectively) using 2.5 and 4.0 mm MAS NMR probes, an Agilent DD2 system at 16.4 T equipped with a 3.2-mm MAS NMR probe, and an Agilent VNMRs system at 11.7 T equipped with a 5-mm MAS NMR probe. Table 4.2 specifies the conditions used for the various single resonance measurements. To probe the connectivity between phosphate units, one-dimensional refocused INADEQUATE experiments were employed on selected samples.[25] This technique uses double-quantum filtering, based on homonuclear indirect spin-spin ("J-coupling"), for selective detection of P-O-P linked species. These experiments were performed using a Bruker Avance Neo 600 MHz spectrometer at 14.1 T (243.0 MHz) (and a Bruker DSX 500 console interfaced with a 4.7 T magnet). with a 2.5 (4.0) mm probe using a spinning frequency of 15.0 (12.0) kHz, π/2 pulse lengths near 1.6 (4.0) μs, recycle delays of 5-10 s, and signal averaging over at least 4000 (24000) acquisitions. The double quantum coherence buildup time was set to 16 ms, corresponding to a $^{2}J(^{31}P\text{-}^{31}P)$ coupling constant of 30 Hz.

All the single resonance MAS NMR spectra were analyzed using the DMFit software,[26] utilizing the CzSimple model for ^{23}Na MAS NMR spectra, Gauss/Lorenz functions for ^{31}P and ^{29}Si MAS NMR spectra, and the "Q MAS ½" model and Gauss/Lorenz functions, respectively, for the ^{11}B resonances of 3- and 4-coordinated boron species. N_4 values were determined from the fractional areas of the peaks attributed to the

four-coordinated boron species, with a small correction for the overlapping satellite transition of the B(IV) species.[27]

Single Resonance Parameters		Perboric	Metaboric	Peralkaline
^{23}Na	Magnetic field (T) / Resonance frequency (MHz)	16.4 / 185.1	5.7 / 64.1	5.7 / 64.1 or 11.7 / 160.5
	Spinning frequency (kHz)	22.0	15.0	15.0
	Pulse length (μs) / Tip angle	0.6 / (π/12)	0.8-1.2 / (π/6)	0.8-1.2 / (π/6)
	Recycle delay (s)	2	0.25-0.5	0.25-0.5
	Number of acquisitions	200	≥2000	≥2000
	Reference standard	NaCl (aq.) (0.0 ppm)	NaCl (7.2 ppm)	NaCl (7.2 ppm)
^{11}B	Magnetic field (T) / Resonance frequency (MHz)	16.4 / 224.6	14.1 / 192.6	5.7 / 77.8
	Spinning frequency (kHz)	20.0	15.0	15.0
	Pulse length (μs) / (Tip Angle)	0.6 / (π/12)	0.5-1.0 / (π/6)	0.5-1.0 / (π/6)
	Recycle delay (s)	2	1-5	1-5
	Number of acquisitions	200	≥400	≥400
	Reference standard	H_3BO_3 (aq.) (19.6 ppm)	BPO_4 (-3.5 ppm)	BPO_4 (-3.5 ppm)
^{31}P	Magnetic field (T) / Resonance frequency (MHz)	16.4 / 283.3	5.7 / 98.1	5.7 / 98.1
	Spinning frequency (kHz)	20.0	12.0	12.0
	Pulse length (μs) / (Tip angle)	1.0 / (π/6)	4.0-5.2 / (π/2)	4.0-5.2 / (π/2)
	Recycle delay (s)	45	90-150	90-150
	Number of acquisitions	160-800	80	80
	Reference standard	85 % H_3PO_4 (0.0 ppm)	BPO_4 (-29.3 ppm)	BPO_4 (-29.3 ppm)
^{29}Si	Magnetic Field (T) / Resonance frequency (MHz)	11.7 / 99.3	5.7 / 48.2	5.7 / 48.2
	Spinning frequency (kHz)	6.0	5.0	5.0
	Pulse length (μs) / (Tip angle)	1.6 / (π/6)	5.0 / (π/2)	5.0 / (π/2)
	Recycle delay (s)	300	150	150
	Number of acquisitions	300-800	150	150
	Reference standard	Tetramethylsilane (0.0 ppm)	$CaSi_2O_5$ (-71.3 ppm)	$CaSi_2O_5$ (-71.3 ppm)

Table 4.2. *Summary of measurement conditions for all samples and nuclei studies by MAS NMR.*

Experimental Parameters of Double Resonance Experiments		
$^{11}B\{^{31}P\}$	$\nu_{nut.}$, observed (kHz)	71.0
	$\nu_{nut.}$, non-observed (kHz)	161.0
	Spinning frequency (kHz)	15.0
	π-Pulse length, observed (μs)	5.6-6.0
	π-Pulse length, non-observed (μs)	3.1
	Recycle delay (s)	1
	Number of acquisitions (per point)	≥112
$^{23}Na\{^{31}P\}$	$\nu_{nut.}$, observed (kHz)	31.3
	$\nu_{nut.}$, non-observed (kHz)	62.5
	Spinning frequency (kHz)	11.0
	π-Pulse length, observed (μs)	6.0
	π-Pulse length, non-observed (μs)	6.4
	Recycle delay (s)	0.5
	Number of acquisitions (per point)	512
$^{31}P\{^{23}Na\}$	$\nu_{nut.}$, observed (kHz)	62.5
	$\nu_{nut.}$, non-observed (kHz)	31.3
	Spinning frequency (kHz)	11.0
	π-Pulse length, observed (μs)	6.4
	π-Pulse length, non-observed (μs)	6.0
	Recycle delay (s)	40-100
	Number of acquisitions (per point)	256
$^{23}Na\{^{11}B\}$	$\nu_{nut.}$, observed (kHz)	34.2
	$\nu_{nut.}$, non-observed (kHz)	35.7
	Spinning frequency (kHz)	14.0
	π-Pulse length, observed (μs)	6.8
	π-Pulse length, non-observed (μs)	7.75 or 11.25*
	Recycle delay (s)	0.5
	Number of acquisitions (per point)	512
$^{31}P\{^{11}B\}$	$\nu_{nut.}$, observed (kHz)	161.0
	$\nu_{nut.}$, non-observed (kHz)	71.0
	Spinning frequency (kHz)	15.0
	π-Pulse length, observed (μs)	3.1
	π-Pulse length, non-observed (μs)	22.0
	Recycle delay (s)	90
	Number of acquisitions (per point)	192

*7.75 μs used for B(III) and 11.25 μs for B(IV)

Dipolar interactions between ^{11}B, ^{31}P, and ^{23}Na nuclei were probed using $^{11}B\{^{31}P\}$, $^{23}Na\{^{31}P\}$, $^{31}P\{^{23}Na\}$, and $^{23}Na\{^{11}B\}$ rotational echo double resonance (REDOR) experiments, in addition to $^{31}P\{^{11}B\}$ rotational echo adiabatic passage double resonance

(REAPDOR) spectroscopy, on selected samples. All REDOR experiments involving ^{23}Na-^{31}P nuclear interactions were conducted on a Bruker DSX 400 spectrometer using a 4.0 mm probe at 9.4 T, ^{23}Na{^{11}B} REDOR experiments were performed on a Bruker Avance Neo 500 MHz spectrometer using a 4.0 mm probe at 11.7 T, and ^{11}B/^{31}P double resonance measurements were conducted on a Bruker Avance Neo 600 MHz spectrometer using a 2.5 mm probe at 14.1 T. Table 4.2 specifies the conditions used for REDOR and REAPDOR experiments. The normalized REDOR and REAPDOR signal intensities $\Delta S = (S_0\text{-}S)/S_0$ (where S and S_0 are the signals (i) with and (ii) without recoupling π pulses, respectively) was plotted as a function of dipolar mixing time (NT_r), where N is the number of rotor cycles and T_r is the rotor period. REDOR experiments were performed using a rotor-synchronized spin echo sequence using π pulses as shown in Table 4.2. The compensation pulse scheme was used[28] and π pulses on the ^{31}P channel were phase cycled according to the XY-4 scheme.[29] Following previously established procedures,[28,30] dipolar second moments ($M_{2(S\text{-}I)}$) (where S represents the observed nucleus and I represents the non-observed nucleus) were determined by fitting the initial part of the REDOR curves ($\Delta S/S_0 \leq 0.20$) using the parabolic approximation[28]:

$$\frac{\Delta S}{S_0} = \frac{4}{3\pi^2} M_{2(S-I)} (NT_r)^2 \qquad (1)$$

Ultimately, the final $M_{2(S\text{-}I)}$ values are obtained by calibration with experimental data on the crystalline model compounds BPO_4, $Na_3P_3O_9$, and $Na_2B_4O_7$ for which the theoretical second moments can be calculated from crystallographic information.[31-33] The REAPDOR pulse sequence is typically used in the $S\{I\}$ case where the I-nuclei are quadrupolar, such as ^{11}B, producing more efficient dephasing by applying an adiabatic passage pulse lasting one-third of a rotor period in the middle of the dipolar recoupling period.[34] As the signal-

to-noise ratio of these experiments is limited by the long-spin-lattice relaxation times of the ^{31}P observe-nuclei, data were measured for 2 or 3 dipolar mixing times only, using rotor-synchronized π pulses in the ^{31}P channel and an adiabatic passage pulse on the ^{11}B channel. Additionally, a saturation comb of sixty 90° pulses ensured a stationary initial magnetization at the beginning of each experiment. Simulated REAPDOR curves for each sample were generated using the SIMPSON program package,[35] taking into account the experimentally determined spin-spin interaction parameters and the experimental conditions.

4.2.3 Molecular dynamics simulations

Classical molecular dynamics simulations have been employed to obtain further insight into the structure of the glass series PB2, MB2, PA2, and on the glass PB3-P7, using the batched compositions as reported in Table 4.1. Models containing about 3500 atoms have been generated (three replicas for each composition) by using the melt-quench approach.[36] The exact number of atoms and box dimensions are reported in Table S1 for these compositions, as well as for the compositions: (i) 55 Na_2O – 45 P_2O_5 and (ii) 40 Na_2O – 18 B_2O_3 – 42 P_2O_5, which were similarly modeled for NMR calculations (to be described below). The shell model force-fields have been used to describe the interatomic interactions between ionic pairs. In this model, which has been demonstrated to reproduce better the medium range structure of oxide glasses (especially in terms of T^n distributions and inter-tetrahedral bond angle distributions),[37-39] the more polarizable ions (oxygen in this case) are represented by a massive core connected to a massless shell by a harmonic spring. A charge is assigned to both the core and shell. The following functional form, which was already used in previous works, has been utilized:

$$U\left(r_{ij}, r_{c-s}, \theta_{ijk}\right) = k\frac{q_i q_j}{r_{ij}^2} + A_{ij}e^{-\left(\frac{r_{ij}}{\rho_{ij}}\right)} - \frac{C_{ij}}{r_{ij}^6} + \frac{1}{2}k_s\left(r_{core-shell}\right)^2 + \frac{1}{2}k_b\left(\theta_{ijk} - \theta_{ijk}^0\right)^2 \exp\left(-\frac{r_{ij}}{\rho} - \frac{r_{jk}}{\rho}\right)$$

(1)

where the first term describes Coulombic interactions between all ions (the core and shell belonging to the same ion are filtered out); the second term is a Buckingham function applied between the cation cores and oxygen shells; the third term represents the harmonic spring connecting the core and shell of the same oxygen ions whereas the last term is a three body interaction used to constrain the O-Si-O and O-P-O angles to 109°.

All the parameters used are included in Table S2 of the supplementary materials. It is important to highlight that all the parameters have been already used in previous investigations with the exception of the B-O parameter sets. The latter have been refined starting from those developed by Edén et al.[40] to be consistent with the other parameters and to better reproduce the N_4 fraction in borosilicate glasses with $[B_2O_3]/[SiO_2] \leq 0.33$. The leap-frog algorithm encoded in the DL_POLY2.14 package[41] has been used to integrate the equations of motion with a time step of 0.2 fs. The initial configurations were generated by randomly placing the number of atoms in a cubic box, whose dimension were constrained by the experimental densities. The systems were heated and held at 3200 K for 100 ps in the *NVT* ensemble ensuring a suitable melting of the samples. The liquids were then cooled to 300 K at a nominal cooling rate of 5 K/ps. The resulting glass structures were subjected to a final equilibration run of 200 ps. Velocity scaling was applied at every step during the quenching of the melt to control the kinetic energy (temperature) of the shells. Coulomb interactions were calculated by the Ewald summation method with a cut-off of 8 Å, whereas short range cut-off values of 7.5 Å were used.

4.2.4 NMR parameter calculations

To further guide the interpretation of the NMR experiments, we have also computed the NMR parameters of ^{17}O, ^{31}P, ^{29}Si, ^{11}B and ^{23}Na nuclei in the PB2-P5 glass composition. Three models of this glass containing 374 atoms each have been generated as was described above. Magnetic shielding and EFG tensors of the various NFU-s present were computed with the NMR-CASTEP[42] density functional theory (DFT) code using the GIPAW[43] and PAW[44] algorithms, respectively. The generalized gradient approximation (GGA) PBE[45] functional was employed, and the core-valence interactions were described by ultrasoft pseudopotentials generated on the fly. For ^{17}O, the 2s and 2p orbitals were considered as valence states with a core radius of 1.3 Å; for ^{29}Si and ^{31}P, a core radius of 1.8 a.u. was used with 3s and 3p valence orbitals; for ^{23}Na, a core radius of 1.3 a.u. was used with 2s, 2p and 3s valence orbitals; while for ^{11}B, a core radius of 1.405 a.u. was used with 2s and 2p valence states. For the PAW and GIPAW calculations we used two projectors in each s and p angular momentum channel for O and B, and in each s, p and d channel for Si and Na. Before computing the NMR parameters, constant volume geometry optimizations of the classically generated models were performed at the Γ point. Wave functions were expanded in plane waves with the kinetic energy cutoff of 610 eV; this has been demonstrated to be long enough to reach converged values for energy and NMR chemical shift.

In this work, to fix the ^{29}Si, ^{11}B, ^{31}P and ^{23}Na δ scale, the values of 322.1[46], 95.05[47], 278.8[46] and 554.05 ppm[48] have been used for $\sigma_{ref.}$. The experimentally determined quadrupolar moments, eQ, of 40.59 and 104×10^{-27} m^2 were used to calculate quadrupolar coupling constants C_Q for the ^{11}B and ^{23}Na nuclei.[49] However, since previous works

demonstrated that the C_Q values are overestimated using these values, we post-scaled the ^{11}B and ^{23}Na C_Q values by the factors 0.842 and 0.46, respectively, as suggested in previous studies.[47,48] NMR output parameters from CASTEP were analyzed using the SoSNMR software.[50]

4.3 Results and Discussion

4.3.1 Glass formation and bulk properties

Among the samples within a range of x = 0 to 9 for each series those ultimately selected for study passed the criteria of being transparent in appearance and showing no sharp X-ray diffraction peaks (Figure S1). Perboric glasses can incorporate P_2O_5 up to x = 5-7 while in metaboric and peralkaline glasses the limits are x = 4-5 and x = 3, respectively. Peralkaline glasses synthesized with more than 3 mol. % P_2O_5 showed XRD evidence of crystalline $Na_4P_2O_7$ phases—see Figure S1—in addition to being visibly phase separated. ICP-OES (see Table 4.1) analyses conducted on representative samples showed close agreement of their B and P contents with their batched compositions (within ±0.6 mol. %). Analyzed Na and Si concentrations in P_2O_5-free glasses are also very close to their batched values (within ±0.5 mol. %), however, larger variations are seen in x = 3-5 samples, with differences ranging between ±0.7 and 2.7 mol. The experimental density, molar volume, and T_g values of the synthesized glasses are also presented in Table 4.1. For the P-free glasses, density values agree with previous trends,[51] while upon successive introduction of P_2O_5 molar volumes tend to increase monotonically and T_g values tend to decrease with increasing x.

4.3.2 ^{11}B MAS NMR and ^{11}B{^{31}P} REDOR

The ^{11}B MAS NMR spectra of all perboric, metaboric, and peralkaline glasses are depicted in Figures 4.1 and S2. In all the spectra, two main features exist: a broad feature centered at ~14 ppm assigned to three-coordinate boron with all-bridging oxygen (B^3(III)) or two bridging and one non-bridging oxygen (B^2(III) units), and a narrower feature near 0 ppm attributed to four-coordinate boron (B(IV) units). It is generally accepted (and here also confirmed by MD simulations, see below), that all four oxygen atoms in the latter species are bridging (B^4(IV). Three- and four-coordinate boron will hereafter be shortly denoted as B(III) and B(IV), with the exception of discussing MD simulation results in which NBO/BO content is confirmed. With increasing phosphate content in the glass the fraction of four-coordinate boron, N_4, decreases moderately in PB and MB glasses, whereas no clear trend can be observed in the PA glasses. Each spectrum was fitted with two B(III) components tentatively assigned to B(III) ring and non-ring units, and two B(IV) components near zero and -2.5 ppm (e.g., see Figure 4.1a), accounting for the asymmetric shape of the B(IV) signal. Table 4.3 summarizes all the NMR interaction parameters. For the phosphate-free glasses PB0, MB0, and PA0 the fraction of B(IV) units, N_4, agrees very well with the previous results on borosilicate glasses, and predictions based on R and the SiO_2/B_2O_3 ratio K.[13] The decrease of N_4 as a function of x observed in the PB and MB glasses can be attributed to the need for extra charge compensation required for the anionic phosphate species formed. In the case of the PA glasses the situation is less clear, as the base glass is expected to contain a significant amount of anionic B^2(III) units. In this case, the invariance of N_4 may be due to depletion of both anionic four-coordinate B(IV) and anionic three-coordinate B^2(III) units. The chemical shifts of the B^4(IV) units, near 0 ppm

and -2.5 ppm, are close to those previously reported for $B^4_{3Si,1B}$ and B^4_{4Si} units, respectively.[19,52] While the chemical shift near -2.5 ppm might thus come from an increased number of Si neighbors around borate units, we can alternatively explain it to signify the formation of B-O-P linkages. This question is explored further using chemical shift calculations, MD simulations, and REDOR experiments. Computed isotropic chemical shifts δ_{CS}^{iso} of all B^3(III) and B^4(IV) species range between 14 and 18 ppm and -2.3 and 1.1 ppm, respectively, in excellent agreement with experimental values. Table 4.4 reveals that the δ_{CS}^{iso} values of both B^3(III) and B^4(IV) species are predicted to decrease when B(IV) units in the second coordination spheres are replaced by B(III), Si and/or P. For example, δ_{CS}^{iso} of B^3(III) species surrounded by three B(IV) units decreases from 17.2 ppm to 16.1/16.6/15.9 ppm upon replacing one B(IV) next-nearest neighbor by B(III), Si^4, or P^3, respectively. Likewise, δ_{CS}^{iso} of B^4(IV) units decreases from 1.1 to -0.8 ppm in going from $B^4_{3B(IV),1B(III)}$ to $B^4_{4B(III)}$ species and from -0.2 to -0.9 ppm in going from $B^4_{3B(IV),1Si(4)}$ to $B^4_{3B(III),1Si(4)}$ units. Finally, it is worth noting that in our models the most negative isotropic chemical shifts of B^4(IV) are found for species surrounded by one B(IV), one B(III), and two P atoms (-1.5 ppm) and by four Si atoms (-2.3 ppm). Thus, based on these calculations, the chemical shift near -2.5 ppm can be ascribed to either the formation of multiple B(IV)-O-Si or B(IV)-O-P linkages. To quantify the extent of B-O-P linkages, $^{11}B\{^{31}P\}$ REDOR experiments, which probe ^{11}B-^{31}P magnetic dipole-dipole interactions, were conducted on selected samples. Figures 4.2a and b compare the Fourier transformed ^{11}B MAS NMR spectra in the absence (S_0) and presence (S) of dipolar recoupling and the corresponding difference spectra (S_0 – S) for the samples PB3-P7 and MB3-P5, respectively. In these experiments dipolar mixing times of 4.0 ms (60 rotor cycles) were

used. In both samples, the four-coordinated boron species show strong dephasing, while dephasing is significantly weaker for the B(III) units. Based on this finding, we can conclude that only the B(IV) units are involved in B-O-P linkages, whereas B(III) units do not link to phosphate to any significant extent – the slight de-phasing observed here can be easily explained by weaker dipolar interactions with more remote ^{31}P nuclei. Also, Figures 4.2a and b indicate that a significant ^{11}B{^{31}P} REDOR effect is observed for both the B(IV) signal deconvolution components near 0 and -2.5 ppm, signifying B-O-P linking for both of them. For further quantification we turn to the REDOR curves (plots of $\Delta S/S_0$ versus dipolar mixing times NT_r, see Figure 4.2c-d). The initial data regime ($\Delta S/S_0 < 0.2$) was fitted to Equation 1 in order to extract dipolar second moments ($M_{2(B\text{-}P)}$) for each sample (see Table 4.5). Here, the very low $M_{2(B\text{-}P)}$ value (0.1×10^6 rad^2/s^2) obtained for the B(III) units can be taken as an estimate of a contribution arising from more remote nuclei, which also needs to be accounted for when analyzing the M_2 values measured for the B(IV) units in terms of the number of B(IV)-O-P linkages. By directly comparing the $M_{2(B\text{-}P)}$ values thus determined with that measured for crystalline BPO_4 (four B-O-P linkages at an internuclear distance of 270 pm),[53] we can deduce that the average number of B-O-P linkages per B(IV) species in PB3-P7 is $\langle m_P(B(IV))\rangle = 0.37$. Considering the N_4 value, we conclude that on the whole the 60 boron atoms of this glass formulation are involved in 12.5 B-O-P linkages. For the MB3-P5 glass, the average number of B-O-P linkages per B(IV) unit is $\langle m_P(B(IV))\rangle = 0.21$; in this case the 50 boron atoms of the glass formulation make a total of 6.7 B-O-P linkages.

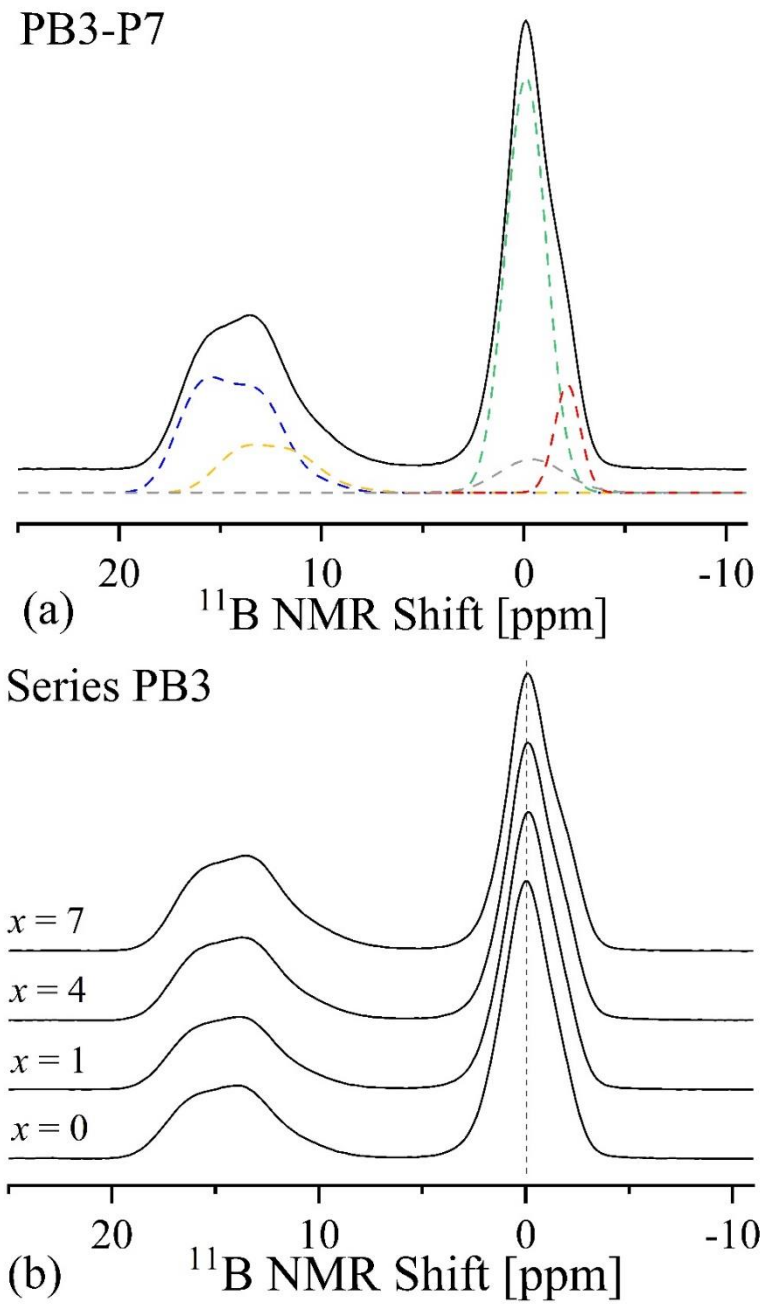
PB3-P7
20
10
0
-10
(a)
^{11}B NMR Shift [ppm]
Series PB3
x = 7
x = 4
x = 1
x = 0
20
10
0
-10
(b)
^{11}B NMR Shift [ppm]

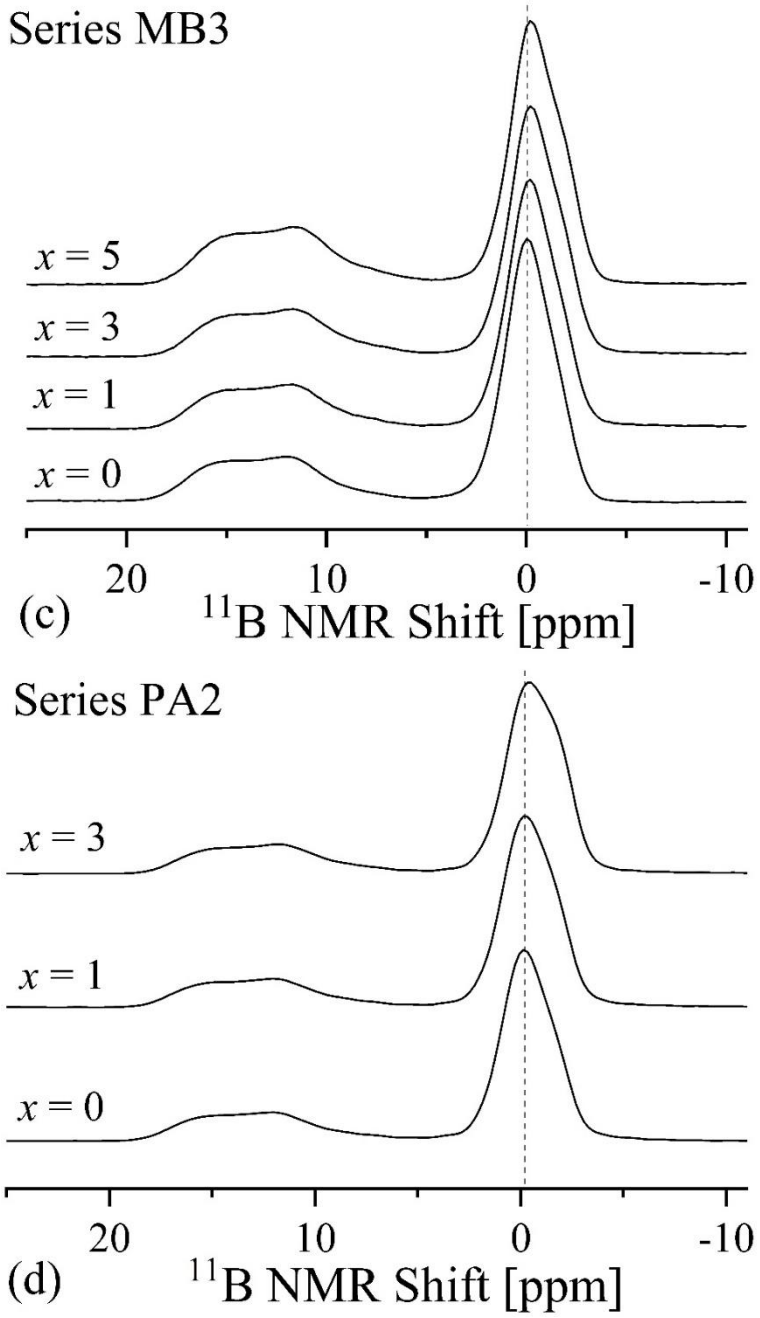

Figure 4.1. *(a) Exemplary lineshape deconvolution for the central transition of the ^{11}B MAS NMR spectra of PB3-P7 glass and ^{11}B MAS NMR spectra of Series (b) PB3, (c) MB3, and (d) PA3 glasses. Each ^{11}B MAS NMR spectra was fitted with two Q mas ½ peaks within the B(III) resonance and three Gauss/Lorentz functions within the B(IV) resonance. The minor fitted peak displayed near 0 ppm represents the overlapping satellite transition within the B(IV) resonance, whose area was not considered while calculating N_4 values for all samples.*

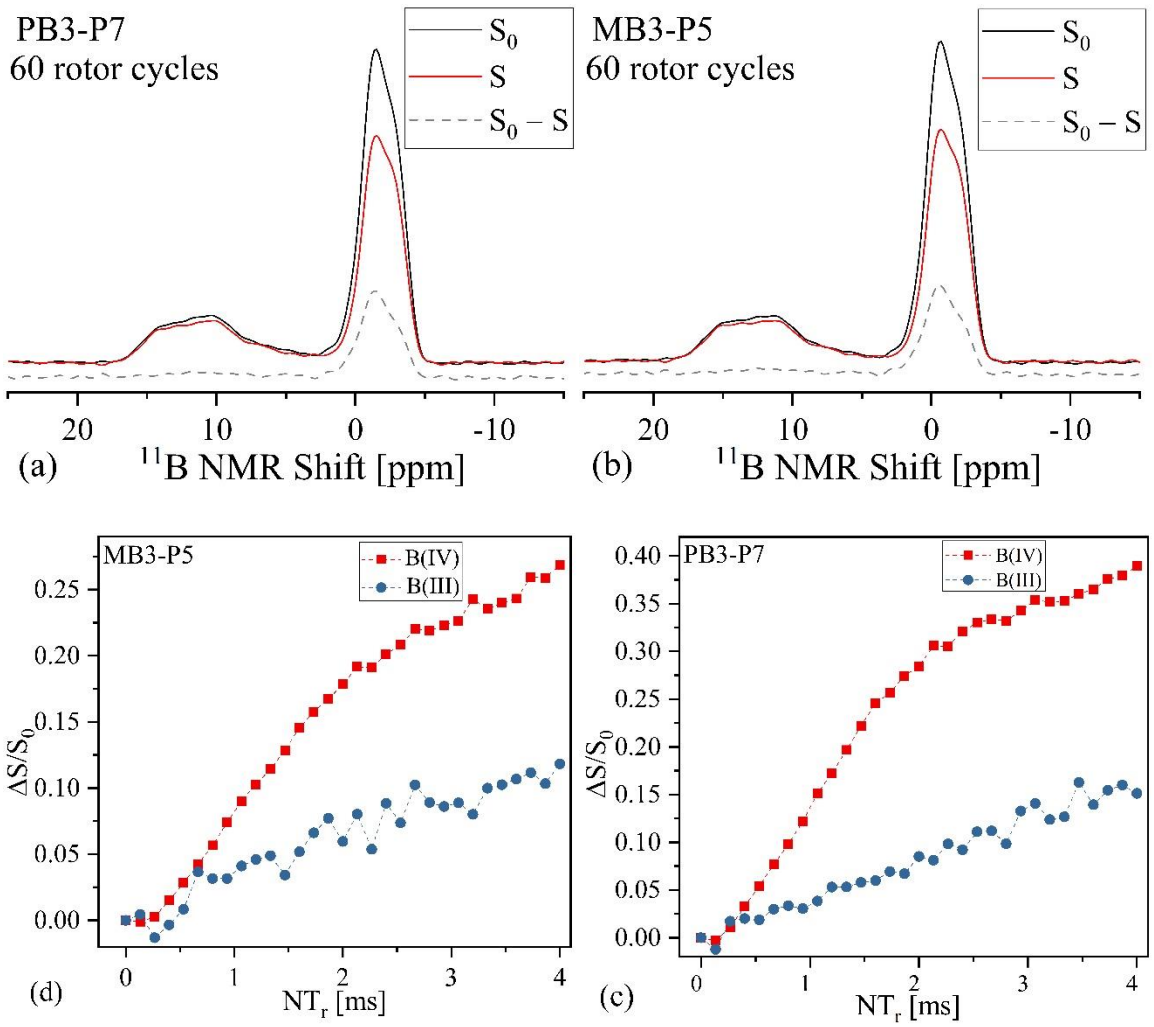

Figure 4.2. *Fourier Transforms of the ^{11}B MAS spin echoes obtained in a $^{11}B\{^{31}P\}$ REDOR experiment after 60 rotor cycles (NT_r = 4.0 ms): reference signal, S_0, signal with dipolar dephasing, S, and REDOR difference spectrum S_0-S, for (a) PB3-P7 glass and (b) MB3-P5 glass. (c) and (d) display $^{11}B\{^{31}P\}$ REDOR curves ($\Delta S/S_0$ vs. NT_r) for PB3-P7 and MB3-P5 samples, respectively.*

Table 4.3. *Fitting parameters of ^{11}B MAS NMR in the studied glasses, including fraction of each species f (± 1.0 %), isotropic chemical shift, δ_{CS}^{iso} (± 0.5 ppm), quadrupolar coupling constant, C_Q (± 0.2 MHz), η_Q (± 0.05), and overall N_4 fractions (± 1 %) where N_4, as simulated from MD models, are displayed in brackets.*

Sample ID	B(III) Ring				B(III) Non-Ring				B(IV)-I		B(IV)-II		N_4
	f (%)	δ_{CS}^{iso} (ppm)	C_Q (MHz)	η_Q	f (%)	δ_{CS}^{iso} (ppm)	C_Q (MHz)	η_Q	f (%)	δ_{CS}^{iso} (ppm)	f (%)	δ_{CS}^{iso} (ppm)	
PB0	27.8	18.5	2.7	0.3	9.3	16.2	2.6	0.3	59.3	-0.1	3.6	-2.1	62.9 [59.5]
PB1-P1	25.7	18.2	2.7	0.3	9.5	16.1	2.6	0.3	60.2	-0.2	4.6	-2.2	64.8
PB1-P3	28.2	18.1	2.7	0.3	10.1	15.8	2.6	0.3	55.3	-0.2	6.4	-2.2	61.7
PB1-P5	29.9	18.0	2.7	0.3	11.3	15.7	2.6	0.3	47.4	-0.1	11.4	-2.1	58.8
PB2-P1	26.2	18.4	2.7	0.3	10.3	16.4	2.7	0.3	60.1	-0.1	3.4	-2.1	63.5 [60.5]
PB2-P3	28.6	18.1	2.7	0.3	9.3	16.1	2.6	0.3	54.7	-0.1	7.4	-2.1	62.1 [58.6]
PB2-P5	28.7	18.1	2.7	0.3	12.2	16.1	2.6	0.3	49.9	-0.1	9.2	-2.1	59.1 [54.6]
PB3-P1	27.0	18.3	2.7	0.3	9.6	16.3	2.6	0.3	58.5	-0.1	4.9	-2.1	63.4
PB3-P4	29.4	18.2	2.7	0.3	10.6	16.1	2.6	0.3	53.8	-0.1	6.2	-2.2	60.0
PB3-P7	31.2	18.0	2.7	0.3	12.4	16.0	2.6	0.3	48.4	-0.1	8.0	-2.2	56.4 [53.8]
MB0	25.1	17.7	2.6	0.3	5.9	14.6	2.5	0.5	62.4	-0.5	6.6	-2.4	67.2 [61.7]
MB1-P1	23.6	17.7	2.6	0.3	6.5	14.6	2.5	0.5	61.9	-0.5	8.0	-2.4	69.9
MB1-P3	26.3	17.5	2.6	0.4	5.6	14.1	2.6	0.4	56.9	-0.6	11.2	-2.4	68.1
MB1-P4	26.8	17.4	2.6	0.3	7.7	14.0	2.5	0.5	50.6	-0.6	14.9	-2.4	65.5
MB2-P1	25.8	17.6	2.6	0.3	6.7	14.6	2.6	0.5	62.4	-0.6	5.1	-2.5	67.5 [63.4]
MB2-P3	25.5	17.4	2.6	0.3	7.3	14.8	2.6	0.5	59.6	-0.7	7.6	-2.6	67.2 [60.9]
MB2-P5	26.1	17.3	2.6	0.3	8.4	14.1	2.5	0.5	54.6	-0.7	10.9	-2.6	65.5 [60.3]
MB3-P1	23.1	17.5	2.6	0.3	9.3	15.2	2.6	0.5	62.6	-0.9	5.0	-2.8	67.6
MB3-P3	23.0	17.4	2.6	0.3	10.0	15.3	2.6	0.5	59.6	-0.9	7.4	-2.8	67.0
MB3-P5	26.6	17.2	2.6	0.3	9.4	14.2	2.4	0.5	56.0	-0.9	8.0	-2.9	64.0
PA0	21.7	18.2	2.6	0.4	6.4	15.2	2.6	0.4	60.8	-0.1	11.1	-1.9	71.0 [67.2]
PA1-P1	22.5	17.0	2.5	0.4	8.9	10.4	2.5	0.5	62.1	-1.2	6.4	-2.8	68.5
PA1-P3	22.0	17.0	2.5	0.4	10.1	10.4	2.5	0.5	59.3	-1.2	8.6	-2.8	67.9
PA2-P1	21.2	18.1	2.5	0.4	6.5	14.4	2.6	0.4	58.0	-0.1	14.3	-1.8	71.4 [58.9]
PA2-P3	21.9	18.0	2.6	0.4	5.5	14.4	2.6	0.4	57.7	-0.3	14.9	-2.1	71.9 [66.6]
PA3-P1	24.6	17.4	2.5	0.4	8.2	9.0	2.4	0.5	62.6	-1.0	4.6	-2.7	67.2
PA3-P1	23.5	17.2	2.5	0.4	9.1	9.3	2.4	0.5	61.7	-1.2	5.8	-2.8	67.4

4.3.3 ^{31}P MAS NMR, refocused INADEQUATE, ^{31}P{^{23}Na} REDOR, and ^{31}P{^{11}B} REAPDOR

Figure 4.3 shows the ^{31}P MAS NMR spectra of glasses from series PB2, PB3, MB2, and MB3, while Figure S3 displays the ^{31}P MAS NMR spectra of series PB1, MB1, and PA1-PA3. All the ^{31}P lineshape parameters and the assignment to the various P^n_{mX} species are summarized in Table 4.6. The spectra from all the series show three main features: a low intensity peak at ~16 ppm (P^0 units), a strong peak centered between 1 and 4 ppm (P^1 units), and a broader feature between -5 and -10 ppm (P^2 units). The chemical shift range associated with the latter suggests a mix of P^2_{2B} and $P^2_{1B,1P}$ units.[19] In addition, connectivity to Si must be considered. As *x* increases in the PB and MB series, we see a decrease in the P^0 signal intensity while the intensities of the P^2 species increase monotonically. Peralkaline glasses show a slight increase of the intensity of that peak as *x* increases from 1 to 3 mol% while P^0 signal intensity changes depend upon the substitution method used (see Figure S3). The spectra of glasses belonging to the series PA1 show a narrowing of the P^0 and P^1 resonance lines in going from $x = 1$ and $x = 3$ in addition to a low-frequency displacement and increased intensity of the P^0 peak. These changes may indicate the development of more highly ordered phosphate environments. XRD patterns of the $x = 5$ glasses show the formation of crystalline sodium pyrophosphate, a small amount of which appears to be present in the PA1-P3 glass (see Figure S1 for XRD patterns of PA1-P3 and PA1-P5 samples). Series PA2 and PA3, on the other hand, show similar or slightly decreased P^0 peak intensities from $x = 1$ to 3, alongside small low-frequency shifts in peak position. Additionally, in glasses of all regimes and series, the P^1 resonance center shifts towards lower frequencies with increasing P content. To aid in the assignments of those

signals to the various P^{n}_{mX} units, we have also computed the NMR parameters of the phosphate species found in three replicas of models containing about 400 atoms of the PB2-P5 glass (whose data is reported in Table 4.4). Additional chemical shift calculations were done on a phosphate and a borophosphate composition, 55 Na_2O – 45 P_2O_5 and 40 Na_2O – 18 B_2O_3 – 42 P_2O_5. Our results show that $P^1_{1B(IV)}$, P^1_{1Si} and P^1_{1P} species resonate at about 8.2, 4.3, and 3.8 ppm with standard deviations between 2 and 5 ppm, indicating that these units may not be clearly distinguishable in broadened MAS NMR spectra. Predicted chemical shifts for the four possible P^2 species, namely $P^2_{2B(IV)}$, $P^2_{1B(IV),1Si,}$ $P^2_{2Si,}$ and $P^2_{1B(IV),1P}$, are -3.5, -11.5, -10.8, and -14.8 ppm, respectively, while no value for $P^2_{1Si,1P}$ can be found as it was not generated in the MD simulation of the borophosphosilicate glass. To further understand the compositional evolution of these spectra, various advanced NMR experiments were conducted to re-couple homo- and heteronuclear spin-spin interactions, thereby providing direct evidence of P-O-P and P-O-B connectivities.

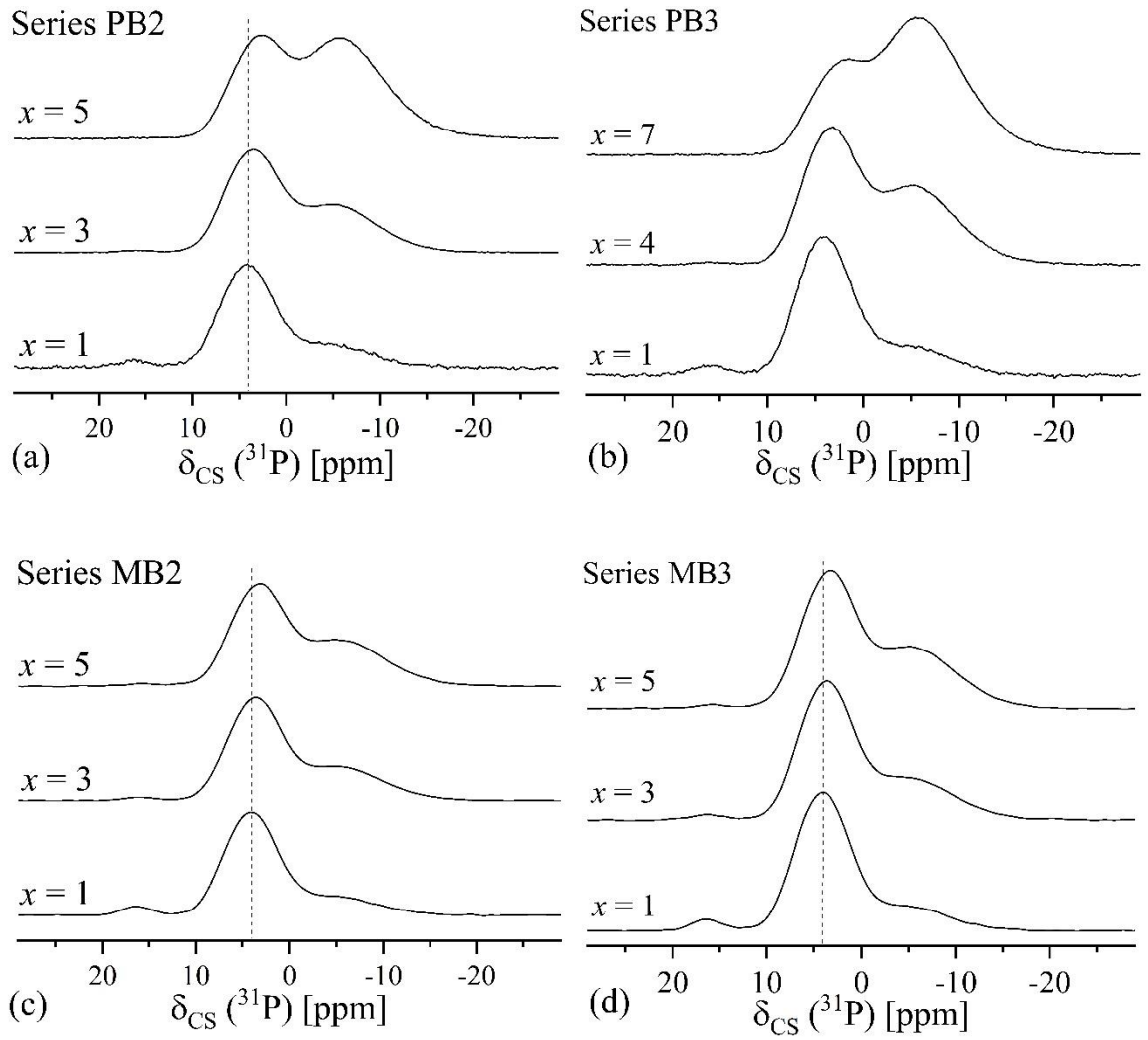

Figure 4.3. *^{31}P MAS NMR spectra of Series (a) PB2, (b) PB3, (c) MB2, and (d) MB3 glasses.*

Table 4.4. *Calculated isotropic chemical shifts of boron, silicon and phosphorus NFUs found in the PB2-P5 glass modeled at the MD-GIPAW level.*

Species	δ_{CS}^{iso} (ppm)	C_Q (MHz)
P^1(B(IV))	8.2 ± 4.8	-
P^1(B(III))	7.1 ± 5.1	-
P^1(Si)	4.3 ± 1.8	-
P^1(P)	3.8 ± 3.0*	-
P^2(2B(IV))	-3.5 ± 2.6	-
P^2(2Si)	-10.8 ± 3.7	-
P^2(SiB(IV))	-11.5 ± 1.7	-
P^2(B(IV)P)	-14.8 ± 4.4†	
P^3(3B(IV))	-18.8 ± 3.0	-
P^3(Si2B(IV))	-23.2 ±2.0	-
Si^4(4B(IV))	-82.0 ± 4.1	-
Si^4(3B(IV)B(III))	-92.0 ± 4.0	-
Si^4(SiB(III)2B(IV))	-95.5 ± 2.0	-
Si^4(2Si2B(IV))	-95.9 ± 1.0	-
Si^4(2B(IV)2B(III))	-98.6 ± 3.0	-
Si^4(B(III)B(IV)SiP)	-99.6 ± 2.5	-
Si^4(Si3B(IV))	-100.2 ± 4.0	-
Si^4(B(IV)3B(III))	-100.3 ± 3.5	-
Si^4(3SiB(IV))	-101.1 ± 3.0	-
Si^4(2SiB(IV)B(III))	-101.6 ± 1.1	-
Si^4(Si2B(III)B(IV))	-101.6 ± 3.0	-
Si^4(B(IV)2SiP)	-102.6 ± 2.0	-
Si^4(2Si2B(III))	-103.2 ± 1.0	-
Si^4(4Si)	-107.2 ± 4.0	-
Si^4(4B(III))	-107.6 ± 2.0‡ [39]	-
Si^4(3SiB(III))	-109.2 ± 2.0	-
B^3(2B(III)Si)	17.8 ± 0.5	2.85 ± 0.1
B^3(3B(IV))	17.2 ± 2.0	2.71 ± 0.1
B^3(B(IV)B(III)Si)	16.9 ± 1.8	2.67 ± 0.1
B^3(2B(IV)Si)	16.6 ± 1.3	2.65 ± 0.1
B^3(2B(IV)B(III))	16.1 ± 1.0	2.68 ± 0.1
B^3(2B(IV)P)	15.9 ± 1.4	2.73 ± 0.1
B^3(B(IV)2Si)	15.1 ± 1.0	2.67 ± 0.1
B^3(B(III)2Si)	14.6 ± 1.6	2.71 ± 0.1
B^4(3B(IV)B(III))	1.1 ± 0.5	0.26 ± 0.05
B^4(B(IV)3B(III))	0.6 ± 0.4	0.44 ± 0.05
B^4(2B(III)B(IV)Si)	0.5 ± 0.4	0.60 ± 0.05
B^4(3B(IV)Si)	-0.2 ± 0.3	0.37 ± 0.05
B^4(2B(IV)B(III)Si)	-0.3 ± 0.3	0.41 ± 0.05
B^4(4B(III))	-0.8 ± 0.4	0.19 ± 0.05
B^4(B(IV)3Si)	-0.8 ± 0.2	0.35 ± 0.05
B^4(3B(III)Si)	-0.9 ± 0.3	0.17 ± 0.05
B^4(B(III)3Si)	-1.0 ± 0.3	0.38 ± 0.05
B^4(B^4B(III)2P)	-1.5 ± 0.4	0.20 ± 0.05
B^4(4Si)	-2.3 ± 0.4	0.36 ± 0.05

* As calculated from MD simulations of a 55 Na_2O – 45 P_2O_5 glass

† As calculated from MD simulations of a 40 Na_2O – 18 B2O3 – 42 P_2O_5 glass

‡ As calculated from MD simulations of a 25 Na_2O – 56.25 B_2O_3 – 18.75 SiO_2 glass [39]

We probed indirect ^{31}P-^{31}P spin-spin interactions in the samples PB3-P7 and MB3-P5, by applying the 1-D refocused INADEQUATE pulse sequence. As this method relies on the existence of through-bond spin-spin interactions to generate double quantum coherences, it can serve as a filter for selectively detecting only those ^{31}P nuclei that are involved in P-O-P linkages. Figures 4.4a and 4.4b show direct comparisons between the ^{31}P MAS NMR and the INADEQUATE spectra for two selected glass compositions. The double-quantum filtered spectrum of MB3-P5 shows a single component near 2.5 ppm. The same peak is also identified in the INADEQUATE spectrum of sample PB3-P7; however, an additional component is observed near -10 ppm, whereas the difference spectrum shows components near 4.6 and -4.6 ppm. Using the lineshape parameters of these partial spectra as additional constraints, the overall ^{31}P MAS NMR spectrum can be fitted to a total of five Gaussian contributions I-V, whose parameters are summarized in Table 4.6 (see Figure 4.4). This particular deconvolution model was used to fit the ^{31}P MAS NMR spectra for all the samples by maintaining similar Gaussian line widths and positions. The chemical shift of component II agrees with that of pyrophosphate (P^1_{1P}) units. We further note that component II is narrower than the overall signal near 1-4 ppm observed in the single-pulse spectra, requiring the additional components I and III for a satisfactory deconvolution. Based on the $^{31}P\{^{11}B\}$ REAPDOR results detailed below, component I is tentatively assigned to P^1_{1B} units. For component III the possibilities include P^1_{1Si} and P^2_{2B}.

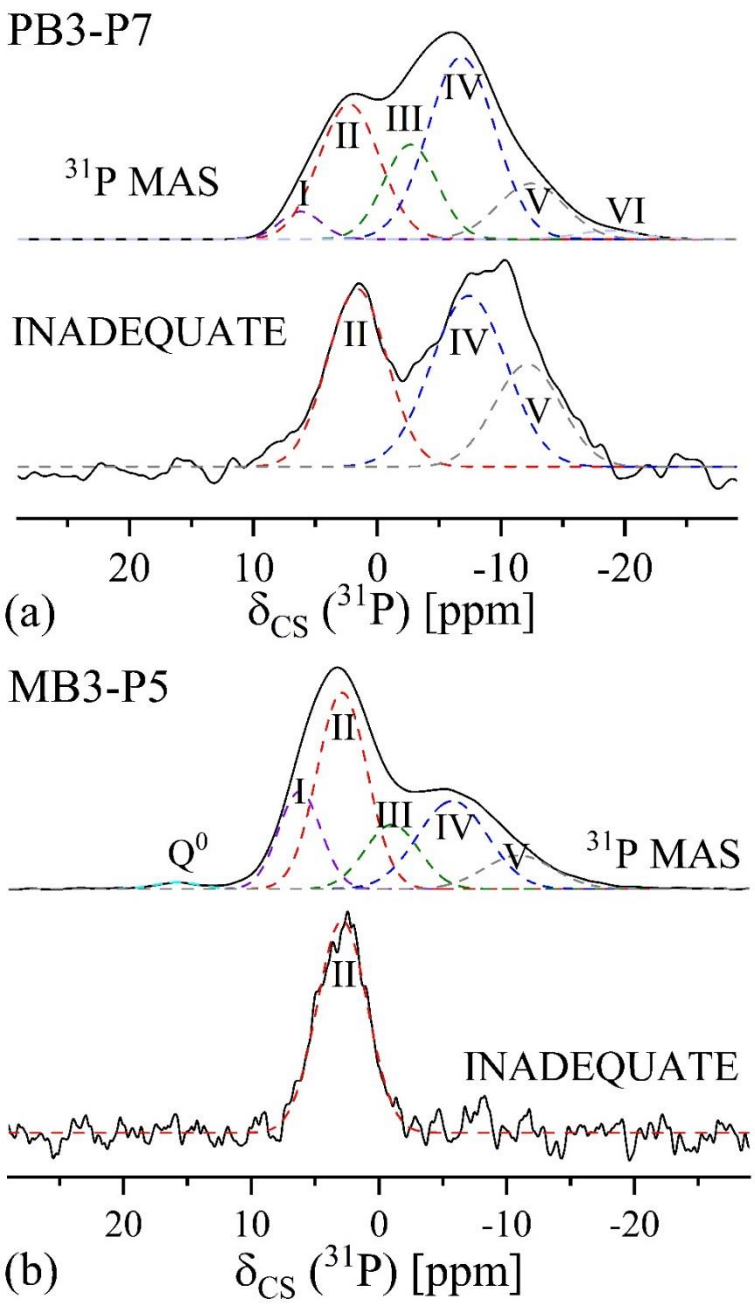

Figure 4.4. *Deconvolution of the ^{31}P MAS NMR and double-quantum filtered ^{31}P MAS NMR spectra, using the refocused INADEQUATE sequence: (a) PB3-P7 and (b) MB3-P5 samples. The double-quantum filtered spectra were utilized to guide the fitting of ^{31}P MAS NMR spectra. Red, blue, and green data points are the full spectra, the filtered spectra, and the difference spectra, respectively.*

Further insight into this question comes from $^{31}P\{^{11}B\}$ REAPDOR experiments. Figure 4.5a and b show the Fourier transforms of rotor-synchronized ^{31}P spin echoes without (S_0) and with (S) ^{11}B dipolar recoupling for the samples PB3-P7 and MB3-P5 after 16 and 22 rotor cycles. Also displayed are the difference spectra ($S_0 - S$), which indicate that the phosphate species contributing to both major resonances near 1-4 ppm and -5 to -10 ppm show significant ^{11}B-^{31}P dipole-dipole coupling. We conclude that these phosphate species have, at least in part, ^{11}B next nearest neighbors. Two and three points on the REAPDOR curve were measured for MB3-P5 and PB3-P7, respectively, and are compared with data generated from SIMPSON simulations taking into account the natural abundance of the ^{11}B isotope (80.4 %) (see Figure 4.5c-d). In these simulations, the P-B distance across a P-O-B linkage was assumed to be 270 pm, consistent with the shortest distance in BPO_4.[31] Simulations are based on a ^{11}B quadrupolar coupling constant of 0.52 MHz and 0.64 MHz for glasses MB3-P5 and PB3-P7, respectively. These values were taken from the overall spectral range of the spinning sideband pattern associated with the $|m| = ½ <-> |m| = 3/2$ satellite transitions (see Figure S4). For spin-3/2 nuclei, this overall spectral range is identical to the quadrupolar coupling constant, C_Q. We can see from the simulations that the signal near -5 to -10 ppm shows a stronger REAPDOR effect compared to that simulated for a single P-O-B linkage (about 1.1 and 1.2 per P unit in PB3-P7 and MB3-P5), whereas the signal in the 1 to 4 ppm range shows a weaker interaction (about 0.65 and 0.8 P-O-B linkages per P unit). While the P^0 peak also shows evidence of some weak dephasing in the MB3-P5 sample, this effect must be attributed to contributions from more remote ^{11}B nuclei in the glass.

Bearing in mind these findings, the most likely candidates for structural species detected in our experiments, based upon the studied compositional regime and the experimental ^{31}P chemical shifts, are $P^1_{1B(IV)}$ (component I), P^1_{1P} (component II), and P^2_{2B} (component III). In addition, P^1_{1Si} species may contribute to component II or III, which in the latter case would have the effect of weakening the overall REAPDOR response. Plausible assignments for component IV and V are the species $P^2_{1B,1P}$ and $P^3_{2B,1P}$ as these signals appear both in the refocused INADEQUATE experiments and in the REAPDOR difference spectra.[22] In addition, subtle differences arising from a detailed comparison of the refocused INADEQUATE spectra and the REAPDOR difference spectra suggest that the P^1_{1Si} and $P^2_{1B,1Si}$ units may be present as well, the former contributing intensity mostly to signals III and IV and latter contributing intensity mostly to signal V in the sample PB3-P7. Concerning the sample MB3-P5, we further believe that the resonances associated with $P^2_{1B,1P}$ and $P^3_{2B,1P}$ units may have eluded the double-quantum filtered detection in Figure 4.4b due to their low concentrations. Minor components labeled P^0 and VI are attributed to isolated monophosphate (P^0) or P^2_{2P} chain phosphate species which do not contain any linkages to B. Table 4.6 presents the proposed phosphate speciation of all the samples as determined from the spectral deconvolutions; in the case of sample PB3-P7 two separate sets of analyses including refocused INADEQUATE experiments were done; the deviations give an impression of the possible experimental error in the speciations.

Inspection of Table 4.6 reveals some universal trends, regardless of *R* regime: As *x* increases from 1 to higher values, the concentrations of P^0 and P^1 species decrease monotonically, while those of P^2 and P^3 increase. The concomitant increase in connectivity

can be expressed by the average number of bridging oxygen atoms per phosphate unit given by

$$<n> = 0\times f(P^0) + 1 \times f(P^1) + 2 \times f(P^2) + 3\times f(P^3)$$

which is listed at the bottom of Table 4.6. For all compositions, we also see a general rise in P-O-B linked phosphate units with increased P_2O_5 presence in the glass network, with a preference towards units that have at least 2 bridging oxygen atoms (P^2 units). While there is a decrease in the concentration of $P^1{}_{1B}$ units, those of other B linked P^2 units ($P^2{}_{2B}$, $P^2{}_{1B,1Si}$, $P^2{}_{1B,1P}$) and some $P^3{}_{2B,1P}$ units as well become more prominent, with the average number of B next nearest neighbors for each P in the glass rising from 0.5 to 0.9-1.2 in PB glasses, rising from 0.7 to 0.8-0.9 in MB glasses, and either remaining similar or rising from 0.6 to 0.7 in PA glasses (Table 4.6). These values were calculated from the $P^n{}_{mB}$ concentrations, according to the assessed speciation from ^{31}P MAS NMR. While in glasses with x = 1 about half (40-60 %) of the phosphate units have no linkages to boron (i.e. are either P^0 or $P^1{}_{1P}$), higher concentrations of P_2O_5 are linked more extensively with B, because of their larger concentrations of P^2 units. This effect is most pronounced in the perboric (PB) glasses having higher B_2O_3 contents.

To validate our results, we can compare the average dipolar interaction strengths measured in the ^{11}B{^{31}P} REDOR and the ^{31}P{^{11}B} REAPDOR experiments—both techniques should give consistent results, i.e. the total number of B-O-P linkages as determined from ^{11}B NMR should equal the total number of P-O-B linkages derived from ^{31}P NMR. From the ^{11}B{^{31}P} REDOR experiments yielding the average number of B-O-P linkages per B(IV) unit from the second moment $M_{2(B\text{-}P)}$ the total number of B-O-P linkages is given by:

$$\#(\text{B-O-P}) = N_4 \times 2 \text{ mol. \% } B_2O_3 \times \langle m_P(B) \rangle$$

neglecting any B(III)-O-P linkages in the network. As detailed above, the 60 boron atoms in glass PB3-P7 make a total of 12.5 B-O-P linkages whereas the 50 boron atoms in glass MB3-P5 make a total of 6.7 B-O-P linkages.

For comparison, the average number of B-O-P linkages per P can be deduced from the simulation of the REAPDOR dephasing observed for the total integrated ^{31}P MAS NMR signal (see Figure 4.5a and b). As shown in Figure 4.5c-d, this number is found near $\langle n_B(P) \rangle = 1.0$ for both samples. Thus, the total number of P-O-B linkages is given by: #(P-O-B) = 2x $\langle n_B(P) \rangle$. For example, the 14 phosphorus atoms in glass PB3-P7 make a total of 14 P-O-B linkages whereas the 10 phosphorus atoms in glass MB3-P5 make a total of 10 P-O-B linkages. Yet another independent estimate of #(P-O-B) is available from the phosphorus speciation as listed in Table 4.6. From the calculated values, $\langle n_B(P) \rangle$ shown near the bottom of this table we conclude that there are 14.3/16.8 and 8.6 P-O-B linkages in samples PB3-P7 and MB3-P5, respectively, in good agreement with the REAPDOR estimate. This consistency also confirms our ^{31}P MAS NMR peak assignments within the entire body of NMR data collected. Table 4.5 displays these comparisons for the two studied samples, expressing the results in terms of the average number of B-O-P linkages per B(IV) unit, as calculated from the phosphorus speciation according to:

$$\frac{Avg.\#\ B-O-P\ linkages}{B^4}$$

$$= \frac{(Avg.\#\ B\ per\ P) * (P\ content, mol.\%)}{(N_4\ fraction) * (B\ content, mol.\%)} \qquad (2)$$

All the results are summarized in Table 4.6.

Table 4.6 further shows that the rate of change of $<n_B(P)>$ as a function of x increases in the order PA->MB->PB, as does the number of P-O-B linkages formed for a fixed x-value. Thus, the more highly polymerized PB glasses tend to mix more extensively with P than the MB or PA glasses as the P_2O_5 content is increased. However, due to the well-known affinity of phosphate units towards sodium, the extent of P-O-B mixing is also highly dependent upon the Na^+ distribution in the network, which will be discussed further below.

Table 4.5. *Dipolar second moments ($M_{2(S-I)}$) of glasses and model compounds, as determined from a parabolic fit of $\Delta S/S_0 \leq 0.20$ from S{I} REDOR data, where S and I denote the observed and the non-observed nuclei. $M_{2(S-I)}$ values in parentheses are raw data obtained before model compound calibration Additionally, calculated values of the average number of P next nearest neighbors around B(IV) have been compared to prove consistency between the two double resonance techniques utilized and the calculated ^{31}P speciation based on fitted peak assignments.*

Sample ID	$M_{2(B-P)}$ / 10^6 rad^2/s^2 (±10 %)			$\sum r_{(B-P)}^{-6}$ / 10^{60} m^{-6}			$<m_P(B(IV))>$ (±10 %)*		
	B(III)	B(IV)	B(IV),net	B(III)	B(IV)	B(IV),net	$^{11}B\{^{31}P\}$ REDOR	^{31}P MAS	$^{31}P\{^{11}B\}$ REAPDOR
BPO_4	--	--	20.3 (11.2)	--	--	0.0105	--	--	--
PB3-P7	0.2 (0.1)	2.0 (1.1)	1.8 (1.0)	0.0001	0.0010	0.0009	0.37	0.42	0.41
MB3-P5	0.2 (0.1)	1.3 (0.7)	1.1 (0.6)	0.0001	0.0007	0.0006	0.21	0.26	0.31

Sample ID	$M_{2(Na-P)}$ / 10^6 rad^2/s^2	$\sum r_{(Na-P)}^{-6}$ / 10^{60}m^{-6}	$M_{2(P-Na)}$ / 10^6 rad^2/s^2	$\sum r_{(P-Na)}^{-6}$ / 10^{60}m^{-6}
$Na_3P_3O_9$	5.4 (3.4)	0.0041	26.7 (8.2)	0.0041
$Na_2B_4O_7$	--	--	--	--
PB0	--	--	--	--
PB3-P1	0.3 (0.2)	0.0002	27.8 (8.5)	0.0042
PB3-P4	1.1 (0.7)	0.0008	24.4 (7.5)	0.0037
PB3-P7	2.3 (1.4)	0.0018	23.0 (7.0)	0.0035

*Average number of B-O-P linkages per B(IV) unit

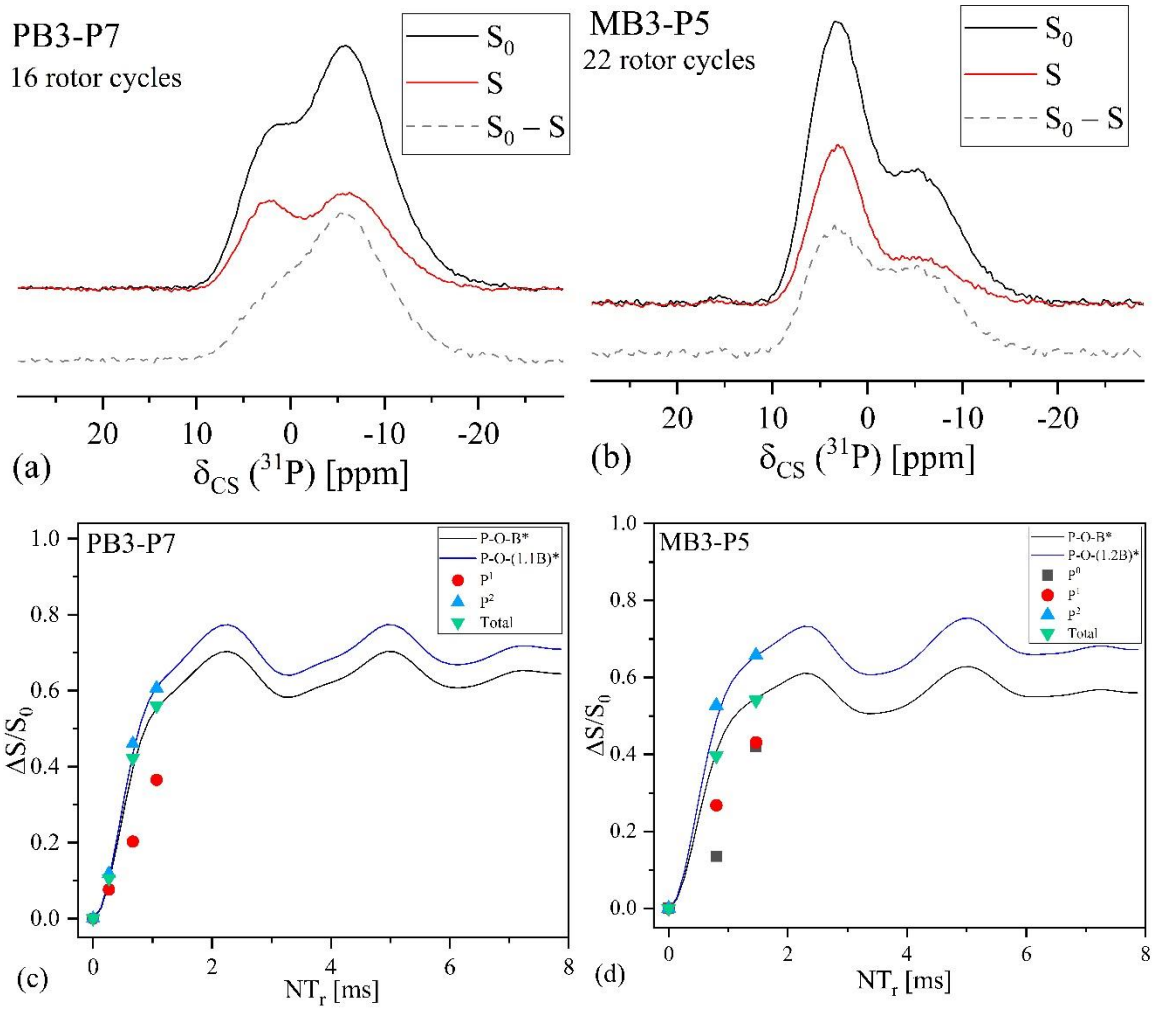

Figure 4.5. *Fourier Transforms of the ^{31}P MAS spin echoes obtained in a $^{31}P\{^{11}B\}$ REAPDOR experiment: reference signal, S_0, signal with dipolar dephasing, and REAPDOR difference spectra S_0-S: (a) PB3-P7 glass after 16 rotor cycles (NT_r = 1.1 ms) and (b) MB3-P5 glass after 22 rotor cycles (NT_r = 1.5 ms). (c) and (d) display $^{31}P\{^{11}B\}$ REAPDOR curves ($\Delta S/S_0$ vs. NT_r) for PB3-P7 and MB3-P5 samples, respectively, for the resolved resonances of P^0, P^1, P^2, and the integral, after a given evolution time. The solid lines represent the results from numerical simulations made with the SIMPSON software. The black curve represents the REAPDOR curves for a ^{11}B-^{31}P two-spin system assuming an internuclear distance equal to that of a P-O-B linkage found in BPO_4 (270 pm). The blue curve has been scaled to the experimental data of the P^2 species in order to deduce an average number of P-O-B linkages.*

Table 4.6. *Fitting parameters of ^{31}P MAS NMR in all studied glasses, including species designations, fraction of each species f (±1.0 %), isotropic chemical shift, δ_{CS}^{iso} (±0.2 ppm), FWHM (±0.1 ppm).*

Sample ID		^{31}P MAS NMR								
		PB1-P1	**PB1-P3**	**PB1-P5**	**PB2-P1**	**PB2-P3**	**PB2-P5**	**PB3-P1**	**PB3-P4**	**PB3-P7***
P^0	***f* (%)**	2.0	0.6	0.0	3.3	0.9	0.0	2.7	0.5	0.0/0.0
	δ_{CS}^{iso} (ppm)	16.0	16.0	--	16.3	15.9	--	16.0	16.0	--
	FWHM (ppm)	3.9	4.6	--	3.9	4.6	--	3.9	3.9	--
P^1_{1B}	***f* (%)**	11.3	6.2	4.3	12.0	7.8	4.7	12.0	10.2	3.2/4.2
	δ_{CS}^{iso} (ppm)	6.6	6.6	6.1	6.9	6.6	6.1	6.6	6.2	6.2/4.6
	FWHM (ppm)	4.0	4.0	4.0	4.0	4.0	4.0	4.0	4.0	3.9/3.8
P^1_{1P}	***f* (%)**	59.9	45.5	32.3	60.5	50.8	33.2	60.8	45.0	25.7/21.6
	δ_{CS}^{iso} (ppm)	3.4	3.1	2.6	3.6	3.2	2.6	3.5	2.8	2.3/1.6
	FWHM (ppm)	5.8	5.8	5.8	5.8	5.8	5.8	5.7	5.7	5.8/5.7
P^2_{2B}	***f* (%)**	8.7	11.7	12.4	9.1	12.0	12.1	9.7	12.4	16.6/32.7
	δ_{CS}^{iso} (ppm)	-2.1	-2.1	-2.1	-2.1	-2.1	-2.1	-2.1	-2.7	-2.7/-4.6
	FWHM (ppm)	5.1	5.1	5.1	5.1	5.1	5.1	5.1	5.1	5.1/8.0
$P^2_{1B,1P}$	***f* (%)**	15.1	26.5	36.5	12.8	23.4	36.1	12.7	25.6	40.4/26.8
	δ_{CS}^{iso} (ppm)	-6.4	-6.2	-6.3	-6.6	-6.5	-6.3	-6.6	-6.6	-6.8/7.4
	FWHM (ppm)	6.3	6.3	6.4	6.3	6.4	6.4	6.3	6.3	6.4/7.1
$P^3_{2B,1P}$	***f* (%)**	3.1	8.6	12.9	2.2	5.1	12.4	2.1	6.3	12.5/12.0
	δ_{CS}^{iso} (ppm)	-12.4	-11.5	-11.7	-12.4	-12.4	-11.7	-12.4	-12.4	-12.4/-12.1
	FWHM (ppm)	6.4	6.3	6.4	6.4	6.4	6.4	6.4	6.4	6.4/6.4
P^2_{2P}	***f* (%)**	0.0	0.8	1.7	0.0	0.0	1.4	0.0	0.0	1.5/2.8
	δ_{CS}^{iso} (ppm)	--	-18.7	-18.7	--	--	-18.7	--	--	-18.7/-17.5
	FWHM (ppm)	--	5.9	5.9	--	--	5.9	--	--	5.9/6.2
$\langle m_B(P) \rangle$ Av. # of B neighbors per P		0.50	0.73	0.91	0.47	0.65	0.90	0.48	0.73	1.02/1.20
$\langle n \rangle$		1.28	1.56	1.77	1.23	1.45	1.74	1.24	1.50	1.83/1.86

*two separate sets of measurements with fits constrained by refocused INADEQUATE experiments

Sample ID		^{31}P MAS NMR								
		MB1-P1	**MB1-P3**	**MB1-P4**	**MB2-P1**	**MB2-P3**	**MB2-P5**	**MB3-P1**	**MB3-P3**	**MB3-P5**
P^0	***f* (%)**	3.2	1.3	1.0	3.7	1.4	1.2	3.7	1.7	1.1
	δ_{CS}^{iso} **(ppm)**	16.4	16.3	16.3	16.4	16.3	15.6	16.4	16.3	15.8
	FWHM (ppm)	4.1	4.2	4.2	4.1	4.2	4.9	4.1	4.2	4.2
P^1_{1B}	***f* (%)**	29.6	20.4	18.1	31.6	22.5	14.5	32.5	23.4	15.2
	δ_{CS}^{iso} **(ppm)**	6.0	6.0	5.9	6.0	6.0	6.2	6.0	6.0	6.2
	FWHM (ppm)	4.5	4.5	4.5	4.5	4.5	3.9	4.5	4.5	3.9
P^1_{1P}	***f* (%)**	39.7	35.6	34.5	40.1	37.1	36.6	39.5	37.6	37.4
	δ_{CS}^{iso} **(ppm)**	2.9	2.9	2.9	2.9	2.9	2.9	2.9	2.9	2.9
	FWHM (ppm)	4.6	4.6	4.6	4.6	4.6	4.6	4.6	4.6	4.6
P^2_{2B}	***f* (%)**	10.3	13.1	13.4	9.0	12.4	14.1	9.5	12.5	13.5
	δ_{CS}^{iso} **(ppm)**	-0.9	-0.9	-0.5	-1.1	-0.9	-0.9	-0.8	-0.9	-1.0
	FWHM (ppm)	5.0	5.0	5.0	5.0	5.0	5.0	5.0	5.0	5.0
$P^2_{1B,1P}$	***f* (%)**	12.8	21.4	22.9	12.0	19.5	23.8	11.8	18.4	23.7
	δ_{CS}^{iso} **(ppm)**	-5.8	-5.8	-5.6	-5.6	-5.8	-5.8	-5.8	-5.8	-5.8
	FWHM (ppm)	6.5	6.5	6.5	6.5	6.5	6.4	6.5	6.5	6.5
$P^3_{2B,1P}$	***f* (%)**	4.4	8.2	10.1	3.6	7.1	9.8	3.0	6.4	9.2
	δ_{CS}^{iso} **(ppm)**	-10.9	-10.9	-10.9	-10.9	-10.9	-10.9	-10.9	-10.9	-10.9
	FWHM (ppm)	6.5	6.5	6.5	6.5	6.5	6.5	6.5	6.5	6.5
P^2_{2P}	***f* (%)**	0.0	0.0	0.0	0.0	0.0	0.0	0.0	0.0	0.0
	δ_{CS}^{iso} **(ppm)**	--	--	--	--	--	--	--	--	--
	FWHM (ppm)	--	--	--	--	--	--	--	--	--
$\langle m_B(P) \rangle$		0.72	0.84	0.88	0.69	0.81	0.86	0.69	0.80	0.84
$\langle n \rangle$		1.29	1.50	1.56	1.25	1.45	1.56	1.24	1.42	1.55

Sample ID		^{31}P MAS NMR					
		PA1-P1	**PA1-P3**	**PA2-P1**	**PA2-P3**	**PA3-P1**	**PA3-P3**
P^0	***f* (%)**	4.7	7.4	4.8	4.7	5.5	3.2
	δ_{CS}^{iso} (ppm)	16.0	14.8	16.4	15.3	16.5	16.3
	FWHM (ppm)	4.1	3.8	4.5	4.5	4.6	4.5
P^1_{1B}	***f* (%)**	27.6	16.5	26.8	21.1	29.0	23.1
	δ_{CS}^{iso} (ppm)	6.4	6.2	6.3	5.8	6.4	6.2
	FWHM (ppm)	4.6	4.3	4.6	4.6	4.6	4.6
P^1_{1P}	***f* (%)**	45.5	46.7	42.7	40.6	42.2	43.1
	δ_{CS}^{iso} (ppm)	3.1	2.8	3.1	2.9	3.1	3.1
	FWHM (ppm)	4.6	4.2	4.6	4.6	4.6	4.6
P^2_{2B}	***f* (%)**	8.0	7.9	11.1	12.2	9.9	11.7
	δ_{CS}^{iso} (ppm)	-1.0	-1.2	-0.5	-0.3	-0.7	-0.5
	FWHM (ppm)	5.0	5.0	5.0	5.0	5.0	5.0
$P^2_{1B,1P}$	***f* (%)**	10.8	13.6	10.9	14.4	9.6	13.2
	δ_{CS}^{iso} (ppm)	-5.8	-5.8	-5.8	-5.8	-5.8	-5.8
	FWHM (ppm)	6.5	6.5	6.5	6.5	6.5	6.5
$P^3_{2B,1P}$	***f* (%)**	3.4	7.9	3.6	7.1	3.8	5.7
	δ_{CS}^{iso} (ppm)	-10.9	-10.9	-10.9	-10.9	-10.9	-10.9
	FWHM (ppm)	6.5	6.5	6.5	6.5	6.5	6.5
P^2_{2P}	***f* (%)**	0.0	0.0	0.0	0.0	0.0	0.0
	δ_{CS}^{iso} (ppm)	--	--	--	--	--	--
	FWHM (ppm)	--	--	--	--	--	--
$\langle m_B(P) \rangle$		0.61	0.62	0.67	0.74	0.66	0.71
$\langle n \rangle$		1.21	1.30	1.24	1.39	1.21	1.33

4.3.4 ^{29}Si MAS NMR

Figures 4.6 and S5 present the ^{29}Si MAS NMR spectra of samples in the series MB3, PB3, and PA3 as well as MB1, MB2, PA1, and PA2 samples. Each series displays a broad peak centered near -92 ppm in the phosphate-free glass which shifts significantly towards lower frequency with increased P_2O_5 content. A similar trend has also been observed by Muñoz et al.[19] in a compositionally related borosilicate system. The signal positions we see in our samples are also consistent with previously studied P_2O_5-free and P_2O_5-containing alkali borosilicate glasses of similar *R* and *K* (= $[SiO_2]/[B_2O_3]$) values.[19,54,55] Owing to the poor resolution, no unambiguous lineshape deconvolution is possible here. Therefore, Table 4.7 lists the average ^{29}Si chemical shifts determined from the center of gravity. We clearly note that this quantity shifts significantly towards lower frequency with increasing P_2O_5 content. As the ^{29}Si chemical shifts in compositionally complex mixed-network former glasses are influenced by numerous different factors, including the number of non-bridging oxygen atoms and the number of next nearest neighbor linkages the trend observed here can be explained in different ways. Further guidance comes from quantum chemical calculations of chemical shifts done on PB2-P5 glass, which are summarized in Table 4.4 for various Si^4 species with different connectivities. They confirm the trends found by Fortino et al.[39]: While $\delta_{CS}^{iso}(^{29}Si)$ increases when Si atoms are replaced by borate species in the second coordination sphere the effect is significantly stronger for Si-O-B(IV) linkages than for Si-O-B(III) linkages. For example, the computed isotropic chemical shift for a $Si^4_{4B(IV)}$ species is -82.0 ppm while it is -107.6 ppm for a $Si^4_{4B(III)}$ species[39] (see Table 4.4). Intermediate values are found for Si^4 species with mixed B(III), B(IV), and Si^4 ligation. The chemical shift ranges of such

species overlap with those usually associated with Si^2 and Si^3 units in silicate glasses, making a corresponding assignment difficult. The situation is complicated further if ligation to phosphorus is considered, as replacement of a Si-O-Si linkage by a Si-O-P linkage produces a shift that is more negative than that of Si^4_{4Si}. Given this situation and the poorly resolved lineshapes, it is not possible to deduce detailed silicon speciations from the ^{29}Si MAS NMR spectra alone. Si^4 species connected to a mix of Si, B(III), and B(IV) are likely to be present; in addition, there may be some contribution from Si^3 units. In a similar sodium phospho-borosilicate glass glasses, Muñoz et al.[19] attributed the ^{29}Si chemical shift trend observed upon the addition of P_2O_5 to a decrease in silicate-borate network connectivity. However, it might also reflect a diminution of Si^3 units or, in principle, an increase in the number of Si-O-P linkages. From the charge balance constraint,

$$[Si^3] + [B(IV)] + [P^2] + 2[P^1] = [Na] \qquad (3)$$

we are able to deduce the concentration of Si^3 units if we neglect the B^2(III) units. These numbers, listed in Table 4.7, show that the addition of phosphate in these glasses tends to diminish $[Si^3]$, i.e. the concentration of NBOs attached to Si. Again this effect can be attributed to the successful competition of P_2O_5 over SiO_2 in attracting network modifier.

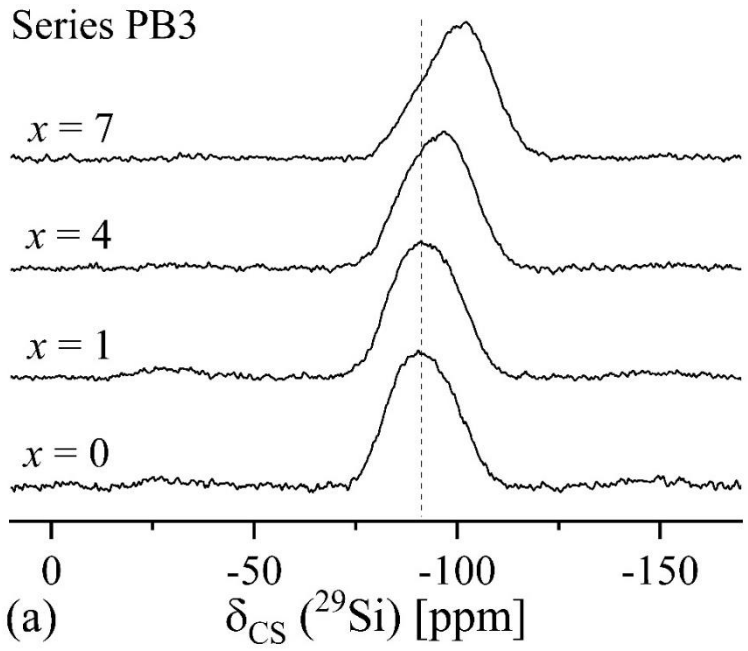
Series PB3
x = 7
x = 4
x = 1
x = 0
0
-50
-100
-150
(a)
δCS (29Si) [ppm]

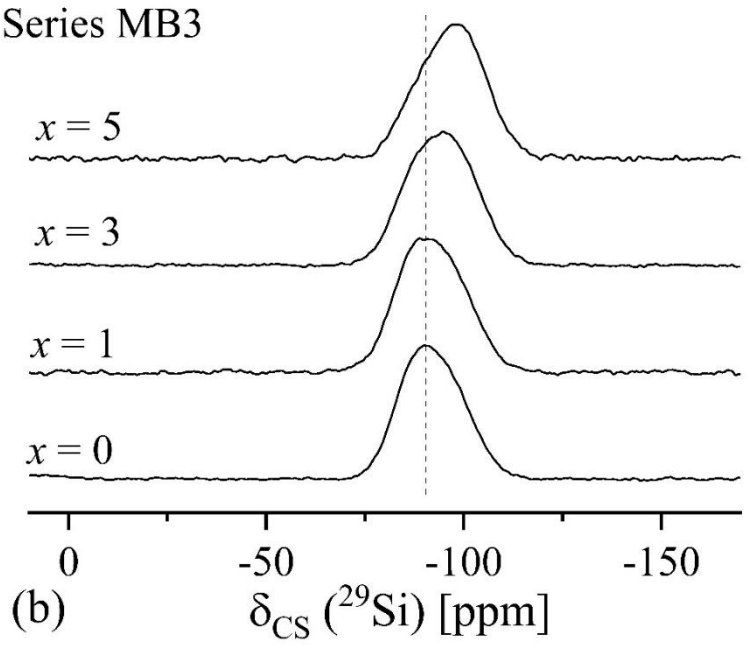
Series MB3
x = 5
x = 3
x = 1
x = 0
0
-50
-100
-150
(b)
δCS (29Si) [ppm]

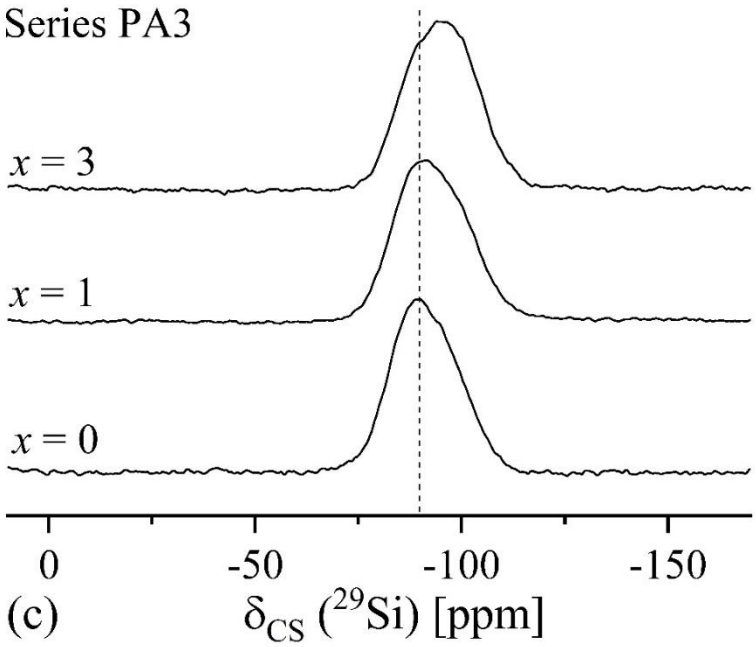

Figure 4.6. *^{29}Si MAS NMR spectra of Series (a) PB3, (b) MB3, and (c) PA3 glasses. The dashed lines are guides to the eye.*

Table 4.7. *^{29}Si chemical shifts δ_{cg} (center of gravity, ±0.5 ppm) and calculated Si^4 fractions (±1.0 %) based on charge balance, and average ^{23}Na isotropic chemical shifts, δ_{CS}^{iso} (± 0.5 ppm), and C_Q values (± 0.2 MHz).*

Sample ID	^{29}Si MAS NMR		^{23}Na MAS NMR	
	Si^4(calc.)	**δ_{cg}**	**δ_{CS}^{iso} (ppm)**	**C_Q (MHz)**
PB0	70.8	-91.9	-5.2	2.4
PB1-P1	83.4	n.d.*	-5.2	2.5
PB1-P3	92.0	n.d.	-5.8	2.5
PB1-P5	97.7	n.d.	-5.4	2.6
PB2-P1	81.5	n.d.	-5.3	2.4
PB2-P3	84.5	n.d.	-5.0	2.6
PB2-P5	88.3	n.d.	-5.7	2.5
PB3-P1	80.8	-92.3	-5.9	2.2
PB3-P4	95.1	-95.3	-6.5	2.2
PB3-P7	100.3	-99.7	-6.4	2.2
MB0	66.7	-92.1	-3.0	2.7
MB1-P1	77.4	-93.0	-6.4	2.9
MB1-P3	88.1	-96.2	-7.9	2.8
MB1-P4	91.4	-97.5	-8.8	2.8
MB2-P1	74.6	-92.5	-6.0	2.9
MB2-P3	77.8	-95.2	-7.8	2.8
MB2-P5	92.1	-97.4	-9.0	2.7
MB3-P1	74.1	-91.9	-5.8	2.8
MB3-P3	85.1	-94.1	-7.3	2.8
MB3-P5	92.3	-96.7	-9.0	2.7
PA0	61.7	-91.3	-4.8	2.9
PA1-P1	68.9	-94.6	-6.7	2.8
PA1-P3	84.0	-96.4	-6.8	2.8
PA2-P1	68.3	-92.8	-5.1	2.9
PA2-P3	77.3	-95.2	-7.0	2.8
PA3-P1	66.6	-92.7	-5.0	2.9
PA3-P3	77.8	-95.1	-6.2	2.8

*Not determined

4.3.5 ^{23}Na MAS NMR and ^{23}Na{^{31}P} and ^{31}P{^{23}Na} REDOR

Figure 4.7a-c presents the ^{23}Na MAS NMR spectra of series MB3, PB3, and PA3. Differences in appearance are attributed to the different magnetic field strengths used for data collection (MB and PA samples were measured at 5.7 T while PB samples were measured at 16.4 T, thus the extent of 2nd-order quadrupolar broadening is very different for the low and high field data). The ^{23}Na isotropic chemical shift (δ_{CS}^{iso}) and C_Q values listed in Table 4.7 were extracted from the fitted spectra using the Czjzek distribution model implemented in DMfit. Isotropic chemical shift values in MB glasses show a monotonic decrease from near -3 to -9 ppm with increasing *x*, while PB and PA glasses show much less pronounced effects. The isotropic chemical shift is expected to be highly dependent upon the distribution of sodium among the silicate, borate, and phosphate structural units, whose anionic charges it compensates. Based on the findings of the present study, the main change as a function of *x* in all three series is the increased participation of phosphate in the anionic inventory of the glass. The overall ^{23}Na chemical shift trend towards more negative values with increasing *x* reflects the increased importance of sodium/phosphate interactions, and the simultaneous decrease of the importance of B(IV)-Na and Si^3-Na interactions.

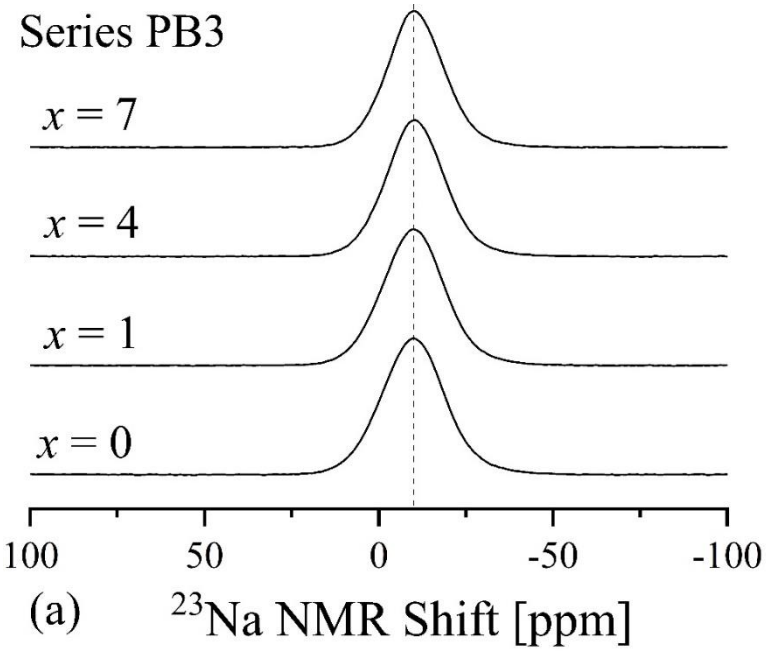
Series PB3
x = 7
x = 4
x = 1
x = 0
100
50
0
-50
-100
(a)
23Na NMR Shift [ppm]

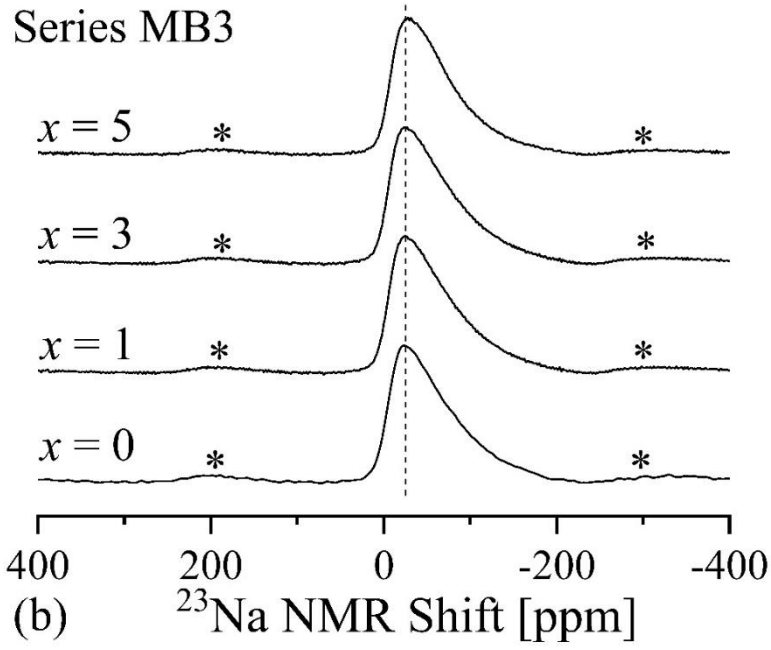
Series MB3
x = 5
x = 3
x = 1
x = 0
*
400
200
0
-200
-400
(b)
23Na NMR Shift [ppm]

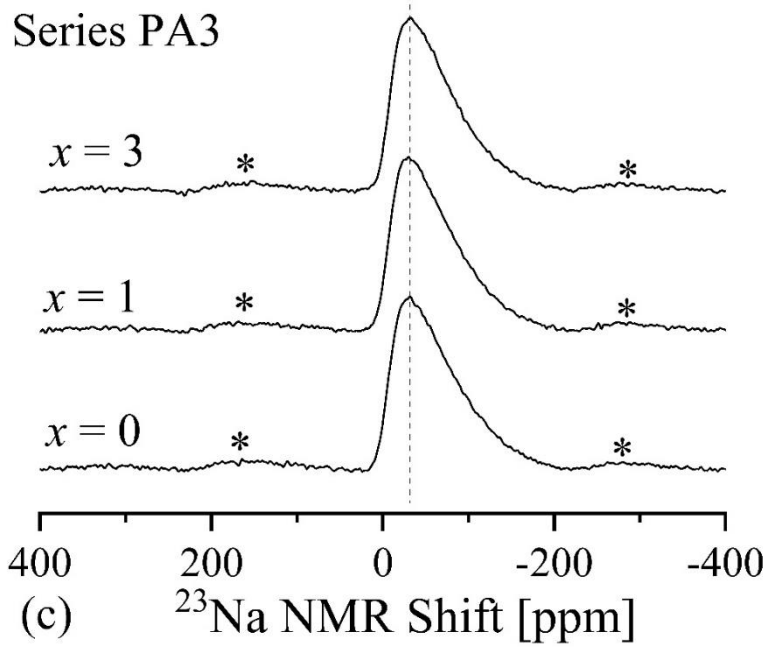

Figure 4.7*. [23]Na MAS NMR spectra of Series (a) PB3, (b) MB3, and (c) PA3 glasses. The asterisks mark spinning sidebands and the dashed lines serve as guides to the eye.*

To probe Na-P interactions in the glass network, we measured $^{23}Na\{^{31}P\}$, and $^{31}P\{^{23}Na\}$ dipole-dipole couplings in the glasses and the crystalline model compound $Na_3P_3O_9$ for calibration: Again, M_2 values were extracted via Equation (1) from the initial portion of each REDOR curve ($\Delta S/S_0 < 0.2$; see Figure 4.8); these values are displayed in Table 4.5. As anticipated, $M_{2(Na\text{-}P)}$ increases with increasing *x*. We estimate the average coordination of the sodium ions with phosphorus in the second coordination sphere at 0.3, 1.0, and 2.1 P for samples PB3-P1, PB3-P4, and PB3-P7, respectively. This trend in ^{23}Na-^{31}P proximity is accompanied by decreases in the Si^3 and N_4 fractions (see Tables 4.3 and 4.7), suggesting that Na^+ which had acted to charge compensate B(IV) units or to create NBOs in the silicate network in the phosphate-free glasses is now associated more closely with phosphate units. Consistent with this interpretation, the $M_{2(P\text{-}Na)}$ values measured in

the reverse $^{31}P\{^{23}Na\}$ REDOR experiments remain roughly constant as a function of *x*, suggesting a rather constant environment of the phosphate units with sodium ions.

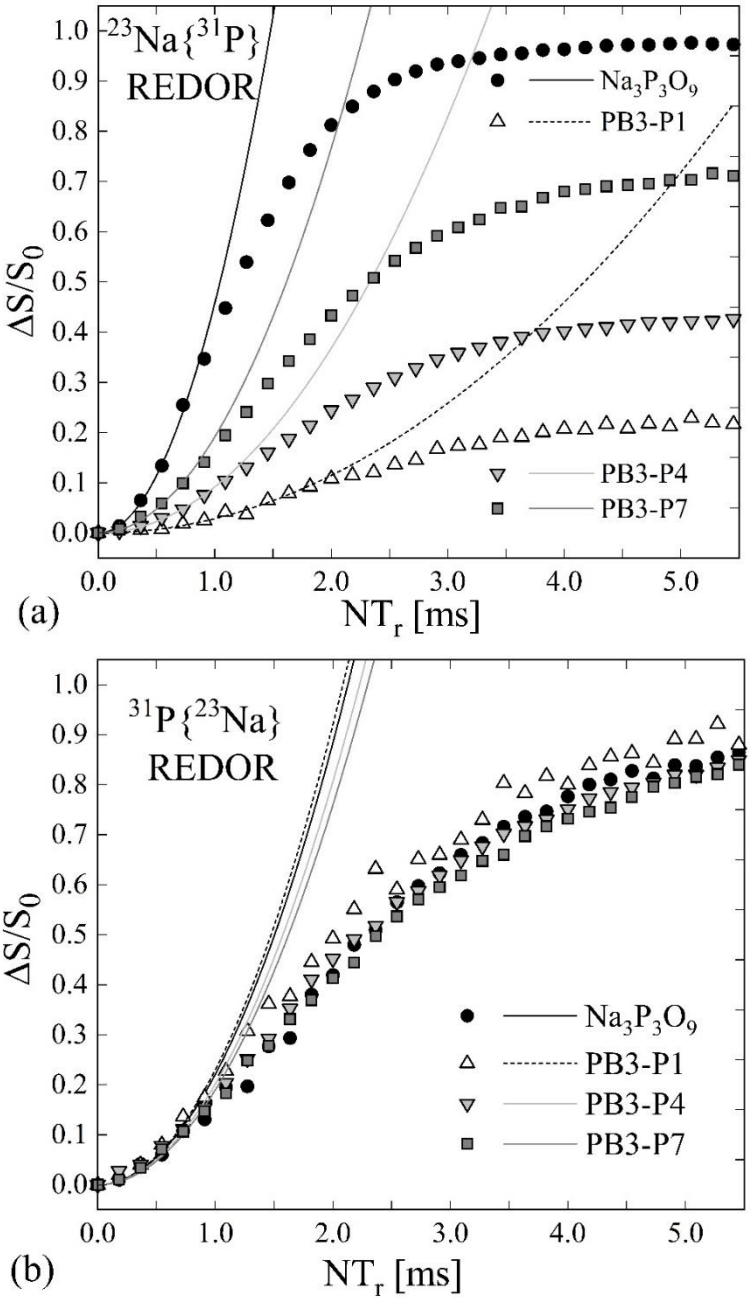

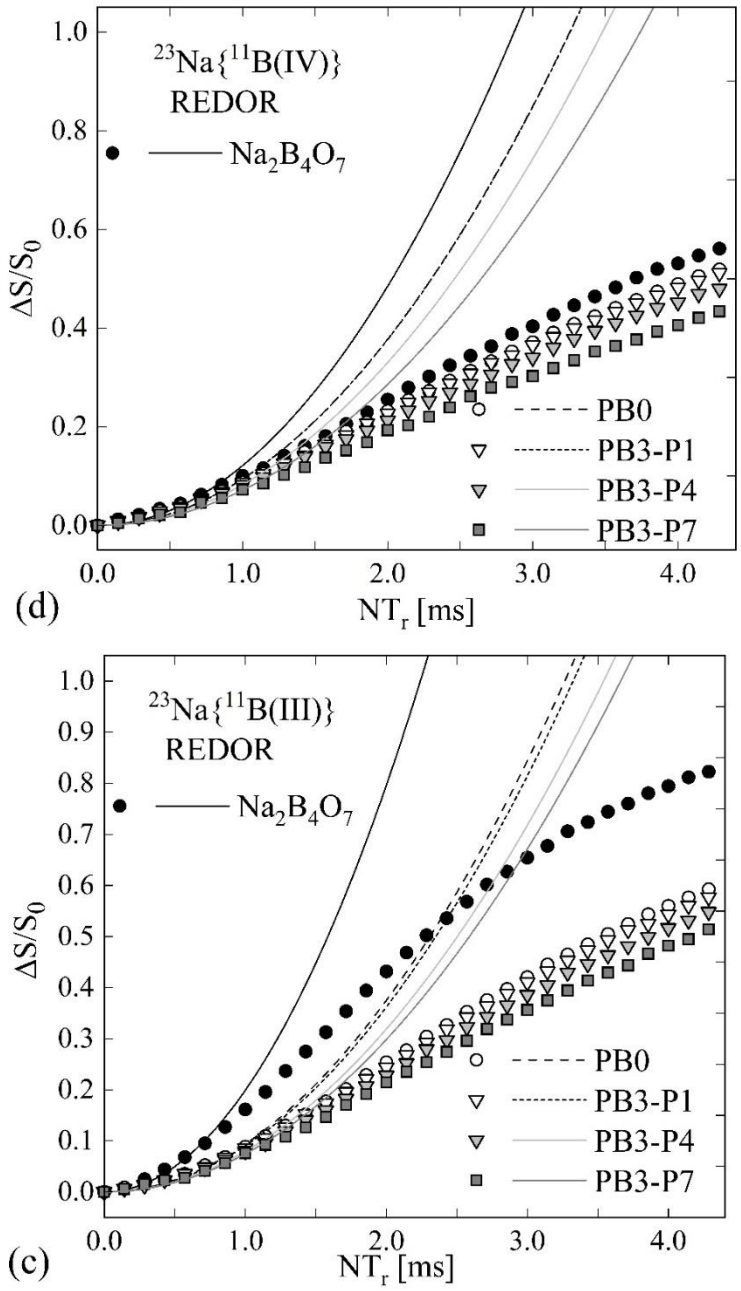

Figure 4.8. *(a) $^{23}Na\{^{31}P\}$, (b) $^{31}P\{^{23}Na\}$, (c) $^{23}Na\{^{11}B(III)\}$, and (d) $^{23}Na\{^{11}B(IV)\}$ REDOR curves for model compounds $Na_3P_3O_9$ and $Na_2B_4O_7$, and the glass samples PB0, PB3-P1, PB3-P4, and PB3-P7. The solid curves represent parabolic fits to the initial regime ($\Delta S/S_0 \leq 0.20$) from which the heteronuclear second moments are extracted via Equation (1).*

4.3.6 MD Simulations: Glass structure predictions

MD simulations were performed on one series per Na/B regime (Series PB2, MB2, and PA2; including the P_2O_5-free counterparts) in order to (i) compare and prove the validity of using MD simulations to reproduce and predict glass structures and (ii) obtain additional structural details which are not readily available from MAS NMR.

Boron environment: short range order. Reliable B-O interatomic parameters must first be validated by their ability to accurately reproduce the N_4 values as a function of composition. In this respect, Table 4.3 indicates good agreement between simulated and experimental data. For each series investigated, the majority of the boron atoms are four-coordinated ($N_4 > 0.53$), although the experimental N_4 values are always higher by 5-7% compared to the simulated data. Nevertheless, the simulations reflect the same trends observed experimentally: N_4 tends to decrease in the order PA-> MB->PB, and with increasing P_2O_5 content. Table 4.8 further indicates that the large majority (>91 %) of the four-coordinated boron species B(IV) are bound to four bridging oxygen atoms, i.e. they are B^4(IV)species. The fraction of B(IV) species linked to NBOs, denoted B^3(IV) species, is negligible. We note that this kind of information is not available from solid state NMR, as the NMR-parameters of four-coordinate boron atoms bound to non-bridging oxygen atoms are unknown and their spectra of both species are most likely overlapping.

The same kind of analysis has also been conducted on the three-coordinated boron (B(III)) species. Table 4.8 reveals that the majority of them are B^3(III) species (trigonal B unit with 3 BO), but the simulations also suggest that there are non-negligible amounts of B^2(III) units bearing a non-bridging oxygen. In this context it is important to note that small concentrations of B^2(III) units are difficult to detect and quantify by high-field ^{11}B MAS

NMR, and the low-field data by Yun and Bray based on their detailed analysis of ^{11}B and ^{10}B wideline NMR spectra[12] remain the best estimates known to date. In line with these wideline NMR results, the MD simulations indicate that the fraction of B^2(III) units decreases with decreasing *R* values, i.e. in the order PA->MB->PB. Furthermore, in agreement with these general trends, Table 4.8 reveals that the successive incorporation of P_2O_5 into these glasses has the effect of depleting the B^2(III) units drastically. Such information is currently not available experimentally from the ^{11}B NMR data presented here, even when analyzing boron speciation with ^{11}B 3QMAS NMR spectroscopy (data not shown).

Boron environment: connectivity. Table 4.8 lists the average number of each NFU around each B^4(IV) and B^3(III) unit, as extracted from the MD generated models. In general, B^4(IV) species are connected to 1.9-2.3 Si atoms and nearly equal amounts (between 0.7 and 1.1) of B(III) and B(IV) species in the PB2 and MB2 series. In both series, the number of P atoms connected to B^4(IV) species increases (up to 0.3 per B^4(IV) species) with the addition of P_2O_5. While the experimental data from NMR do not permit such an incisive numerical analysis, we can compare the simulated average number of B(IV)-O-P linkages per boron with the results from $^{11}B\{^{31}P\}$ REDOR. For the glass PB3-P7 we note excellent quantitative agreement. Also the MD simulations agree with the experimental REDOR result that there are very few if any B(III)-O-P linkages. Interestingly, we also see that P prefers to replace B(IV) and Si as opposed to B(III) species in the second coordination sphere of B^4(IV). In the PA2 series, the second coordination sphere of B^4(IV) has more Si atoms (2.5-2.7) and fewer B(IV) and B(III) units (0.6-0.8) compared to PB2

and MB2 series. In this case, P seems to preferentially replace Si instead of B(IV). Again, such detailed information is not currently available from solid-state NMR.

Overall, the MD simulations confirm the NMR result that phosphorus promotes a re-structuring of the borate component. B^4(IV) species are mainly surrounded by silicon atoms and phosphate units, whereas B^3(III) species are mainly connected to B(IV) species (between 1.4 and 1.7), silicon (1.0-1.4), and to a very small extent, other B(III) species (0.1-0.4). Unlike B(IV) species, B(III) species tend to avoid linking to phosphorus. While the MD simulations suggest that the fraction of B(III)-O-Si linkages tends to increase with *x*, no such information can be drawn from the NMR data, as they do not reveal any discernable spectroscopic trends for the B(III) units.

The effect of the network former mixing in the second coordination sphere of the boron atoms was thoroughly investigated in a previous theoretical study on 25 Na_2O *x* B_2O_3 (75-*x*) SiO_2 (*x* = 0 – 75 mol %) glasses.[39] That work showed that (i) the positions and areas of the B(III) and B(IV) peaks in the ^{11}B MAS NMR spectra of the simulated glasses are in good agreement with their experimental counterparts, which validates the accuracy of the structural models and NMR calculations, (ii) the ^{11}B isotropic chemical shift decreases with the B-O-T angle and with the amount of silicon in the second coordination sphere of boron, and (iii) the substitution of B(III)/B(IV)-O- B(III) bonds by B(III)/B(IV)-O-B(IV) bonds leads to an increase in the isotropic chemical shift. Unfortunately, the ^{11}B(III) NMR parameter analyses are not sufficiently distinctive to monitor the changes in the second coordination sphere of these units as P_2O_5 is added to these glasses. This may be possible, however, by ^{11}B{^{29}Si} REDOR experiments to be conducted on ^{29}Si enriched glasses in the future.

Table 4.8. N_4/N_3 *values and fractions of* $B^4(IV)$, $B^3(IV)$, $B^3(III)$, *and* $B^2(III)$ *units found in the MD-generated structural models of the investigated glasses and average numbers of network former cations bound to fully connected* $B^4(IV)$ *and* $B^3(III)$ *units. #P neighbors around* $B^4(IV)$ *has also been compared to the values as calculated from fitting of* ^{31}P *MAS NMR data.*

Sample ID	***N_4***	**$B^3(IV)$**	**$B^4(IV)$**	**#B(IV)**	**#B(III)**	**#Si**	**#P**	**#P (^{31}P MAS NMR)**
PB0	59.5	2.0	57.5	1.0	1.0	2.0	-	-
PB2-P1	60.5	1.6	58.9	0.9	1.0	2.1	0.0	0.0
PB2-P3	58.6	1.8	56.8	0.9	1.1	1.9	0.2	0.1
PB2-P5	54.6	1.3	53.3	0.7	1.1	1.9	0.3	0.3
PB3-P7	53.8	3.9	49.9	0.7	1.1	1.7	0.5	0.4
MB0	61.7	4.4	57.3	0.9	0.8	2.3	-	-
MB2-P1	63.4	3.4	60.0	1.0	0.9	2.1	0.0	0.0
MB2-P3	60.9	2.7	58.2	0.8	0.9	2.2	0.2	0.2
MB2-P5	60.3	2.2	58.1	0.7	0.9	2.2	0.3	0.3
PA0	67.2	5.8	61.4	0.8	0.6	2.7	-	-
PA2-P1	58.9	2.1	56.8	0.6	0.8	2.5	0.0	0.0
PA2-P3	66.6	3.4	63.2	0.8	0.6	2.5	0.2	0.2
Sample ID	***N_3***	**$B^2(III)$**	**$B^3(III)$**	**#B(IV)**	**#B(III)**	**#Si**	**#P**	
PB0	40.5	9.9	30.6	1.7	0.3	1.0	-	
PB2-P1	39.5	6.7	32.8	1.6	0.4	1.0	0.0	
PB2-P3	41.4	4.1	37.3	1.7	0.3	1.1	0.0	
PB2-P5	45.4	4.5	40.9	1.5	0.4	1.1	0.0	
PB3-P7	46.2	1.7	44.5	1.5	0.5	1.0	0.0	
MB0	38.3	12.5	25.8	1.6	0.3	1.1	-	
MB2-P1	36.6	7.5	29.1	1.6	0.2	1.2	0.0	
MB2-P3	39.1	7.4	31.7	1.5	0.3	1.2	0.0	
MB2-P5	39.7	4.7	35.0	1.4	0.3	1.2	0.1	
PA0	32.8	13.9	18.9	1.5	0.1	1.4	-	
PA2-P1	41.1	10.0	31.1	1.4	0.2	1.4	0.0	
PA2-P3	33.4	8.6	24.8	1.4	0.2	1.4	0.0	

Table 4.9. *Amounts of Si^4, Si^3, and Si^2 species (in % of the Si content) found in the MD-generated glasses and average number of NFU bound to Si^4 and Si^3 (±0.1).*

Sample ID	Si^4	#B(IV)	#B(III)	#Si	#P
PB0	84.2	1.7	0.5	1.8	-
PB2-P1	86.4	1.7	0.5	1.7	0.0
PB2-P3	88.5	1.6	0.6	1.7	0.1
PB2-P5	92.3	1.5	0.7	1.7	0.2
PB3-P7	94.8	1.5	0.7	1.5	0.2
MB0	78.8	1.6	0.4	2.1	-
MB2-P1	79.6	1.5	0.4	2.1	0.1
MB2-P3	85.9	1.5	0.5	2.0	0.1
MB2-P5	89.1	1.4	0.4	2.0	0.2
PA0	73.3	1.5	0.3	2.3	-
PA2-P1	83.2	1.2	0.4	2.4	0.0
PA2-P3	80.5	1.3	0.3	2.3	0.1

Sample ID	Si^2	Si^3	#B(IV)	#B(III)	#Si	#P
PB0	0.1	15.7	1.7	0.4	1.0	-
PB2-P1	0.0	13.7	1.6	0.4	1.0	0.0
PB2-P3	0.1	11.4	1.7	0.3	1.1	0.0
PB2-P5	0.0	7.7	1.5	0.4	1.1	0.0
PB3-P7	0.0	5.3	1.5	0.5	1.0	0.0
MB0	0.3	20.9	1.6	0.3	1.1	-
MB2-P1	0.3	20.1	1.6	0.2	1.2	0.0
MB2-P3	0.0	14.1	1.5	0.3	1.2	0.0
MB2-P5	0.5	10.4	1.4	0.4	1.2	0.1
PA0	1.0	25.7	1.5	0.3	1.2	-
PA2-P1	0.4	16.4	1.2	0.4	1.4	0.0
PA2-P3	0.6	18.9	1.3	0.3	1.3	0.1

Silicon environment and connectivity. Table 4.9 reports the Si^n distribution in the investigated glasses. In each series, Si is predominantly present as Si^4 species (>84, 78 and 73 % for the PB2, MB2, and PA2 series, respectively) and Si^3 species (16, 21, and 26 % for the PB2, MB2 and PA2 series, respectively) and small amounts of Si^2 species. While the Si^4 fractions extracted from the MD-generated models are roughly 3-15 % higher than those deduced from NMR (Table 4.7), the trends are the same: With increasing *x* the silicate network becomes more polymerized, reflecting the concomitant transfer of the Na^+ ions

towards the anionic phosphate component. Table 4.9 shows that Si^4 is mainly connected to other silica tetrahedrons (1.7-1.8 for Series PB2, 2.0-2.1 for Series MB2, and 2.3-2.4 for Series PA2) and B(IV) units (1.5-1.7 for PB2, 1.4-1.6 for MB2, and 1.2-1.5 for PA2). Si^3 units, on the other hand, have one NBO which effectively replaces one silicon neighbor in the second coordination sphere. Low levels of B(III) species are also connected to Si^3 and Si^4 (0.3-0.7). Additionally, there are small fractions of P (up to 0.2 for glasses with larger amounts of P_2O_5) that are second neighbors to Si^4 (minimal amounts of P are observed around Si^3 units). As was also observed for B(IV) species, upon addition of P_2O_5 to the glass, the environment of Si is depleted in B(IV) and Si species and enriched in B(III) species as the B(III) units tend to link with B(IV) and Si atoms.

Phosphorus environment: short-range order. Table 4.10 indicates that the phosphorus speciation in the present glasses is dominated by anionic P^1 and P^2 units reflecting the well-known fact that P preferentially attracts the anionic charges in mixed network former systems. Quantitative data on this effect are shown in Figure 4.9. Plotted are the fractions of NBOs bound to each NFU in the three glass series studied here, not counting the uncharged formally doubly bonded NBO already present for any phosphate unit. The data confirm the results of a previous study of sodium calcium phospho-borosilicate glasses[22,23] indicating that the attraction of anionic NBO decreases in the order P >> B(III) > Si > B(IV). The average number of bridging oxygen atoms, $\langle n \rangle$ as deduced from MD is found to be somewhat lower than the corresponding experimental values determined from NMR. Nevertheless, both data sets show that $\langle n \rangle$ consistently increases with increasing *x* in the MB2 and PB2 glass series. In contrast, NMR and MD speciation seem to follow opposite trends in the compositionally more limited series PA2.

Phosphorus environment: connectivity. Table 4.11 summarizes the NFU connectivities of the phosphate species, indicating a dominance of Si and B(IV) units. At variance with the MAS NMR data the MD results indicate very low levels of P-O-P linkages. One possible reason for this discrepancy can be seen in the low overall concentration of the P atoms in our glasses. As a consequence, their speciation and connectivities have little influence on the energy minimum sought in the simulation. Considering this situation, the correct prediction of the trend of <*n*> as a function of *x* and the consistent information on P-O-B linkages can be already considered a remarkable success.

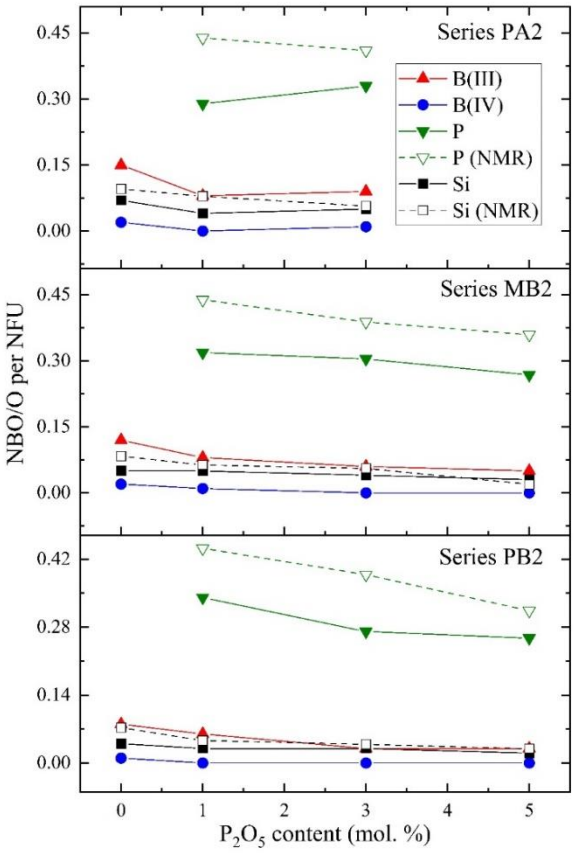

Figure 4.9. *MD-derived average numbers of NBOs per network-forming species B(III), B(IV), Si, and P plotted as a function of* x. *In the case of the P and Si speciation, results from NMR are shown for comparison.*

Table 4.10. *Structural speciation of phosphorus (in % of the P content) in the MD-generated glasses.*

Sample ID	P^0 Total	P^1 Total	P^2 Total	P^3 Total	P^4 Total
PB0	N/A	N/A	N/A	N/A	N/A
PB2-P1	0.0	47.5	41.5	11.0	0.1
PB2-P3	0.0	25.2	58.1	15.3	1.4
PB2-P5	0.4	20.7	60.6	17.2	1.2
PB3-P7	0.0	15.0	73.0	11.2	0.8
MB0	N/A	N/A	N/A	N/A	N/A
MB2-P1	0.0	35.4	56.7	8.0	0.0
MB2-P3	0.9	27.3	64.7	7.2	0.0
MB2-P5	0.0	19.4	68.4	11.8	0.4
PA0	N/A	N/A	N/A	N/A	N/A
PA2-P1	0.1	29.9	55.7	14.3	0.0
PA2-P3	0.9	38.4	52.6	8.3	0.0

Table 4.11. *Average numbers of network former units (B(IV), B(III), P, and Si) connected to P^1 and P^2 species in the MD-generated glasses.*

Sample ID	P^1			
	#B(IV)	**#B(III)**	**#Si**	**#P**
PB2-P1	0.3	0.1	0.6	0.0
PB2-P3	0.3	0.1	0.6	0.0
PB2-P5	0.3	0.1	0.5	0.1
PB3-P7	0.3	0.2	0.3	0.2
MB2-P1	0.5	0.1	0.4	0.0
MB2-P3	0.2	0.2	0.6	0.0
MB2-P5	0.3	0.1	0.6	0.0
PA2-P1	0.3	0.1	0.6	0.0
PA2-P3	0.2	0.0	0.7	0.1
Sample ID	P^2			
	#B(IV)	**#B(III)**	**#Si**	**#P**
PB2-P1	1.2	0.0	0.8	0.0
PB2-P3	1.2	0.2	0.6	0.0
PB2-P5	0.9	0.2	0.9	0.0
PB3-P7	1.0	0.2	0.7	0.1
MB2-P1	1.1	0.0	0.9	0.0
MB2-P3	1.1	0.1	0.8	0.0
MB2-P5	0.9	0.2	0.9	0.0
PA2-P1	0.9	0.2	0.9	0.0
PA2-P3	0.9	0.1	1.0	0.0

Table 4.12. *Contributions of P, B(III), B(IV), and Si to the second-nearest neighbor coordination of Na.*

Sample ID	#P	#B(III)	#B(IV)	#Si
PB0	-	1.7	2.5	2.3
PB2-P1	0.2	1.6	2.5	2.2
PB2-P3	0.6	1.5	2.2	2.0
PB2-P5	1.0	1.4	2.0	1.7
PB3-P7	1.3	1.3	1.9	1.4
MB0	-	1.4	2.2	2.6
MB2-P1	0.2	1.3	2.2	2.6
MB2-P3	0.7	1.2	1.9	2.3
MB2-P5	1.0	1.1	1.7	2.0
PA0	-	1.0	1.9	3.0
PA2-P1	0.2	0.9	1.7	2.9
PA2-P3	0.6	0.8	1.6	2.5

Sodium distribution. Our MD simulations reveal that sodium is surrounded by an average of 6.4 and 6.5 oxygen atoms at distances near 2.40 Å in MB0 and PB0 glasses. Upon addition of P_2O_5 to each glass series, both the average Na coordination numbers and Na-O distances tend to decrease to 6.2/6.3 and 2.37 Å, respectively. The coordination numbers and distances remain almost constant at 6.2 and 2.38 Å, respectively for Series PA2. Regarding the partitioning between NBO and BO in the studied glasses, the fraction of NBO around Na increases with increasing P_2O_5 content in the glass, indicating that sodium gradually shifts from its role as a charge compensator connected to boron-bonded BO species, to a charge compensator of anionic non-bridging oxygen atoms attached to phosphate species. To investigate the sodium distribution around each NFU in the glass, we have plotted the T-Na (T = Si, B(III), B(IV), P) pair distribution functions in Figure S6 and compared the T-Na coordination numbers extracted from the simulations to that computed according to homogeneously distributed sodium in the glass (see Figure S7). Figure S6 indicates that the most probable Si-Na distances range between 3.3-3.4 Å and no particular trend is observed with P_2O_5 content apart from a slight decrease of their

occurrence (evidenced by a decreased peak intensity). The B(III)-Na peak is centered at 3.0 Å and splits into two peaks (3.0 and 3.1 Å) upon P_2O_5 addition. While B(III)-Na interaction is not traditionally expected as these units are charge-neutral, their spatial proximity can be attributed to either B^2(III) units containing 1 NBO or B^3(III) units linked to B(IV) which contain a Na^+ charge compensator. The B(IV)-Na PDF peak, on the other hand, is narrower than the B(III)-Na peak and occurs at slightly shorter distances (2.9 Å), whereas the P-Na PDFs show a double peak centered at 3.1 and 3.4 Å. From the viewpoint of the Na^+ ions, their interactions with the NFUs in the second-nearest neighbor sphere are of particular interest. For defining this sphere, a cutoff distance of 3.6 Angstroms was found to yield stable results. Table 4.12 summarizes the development of the Na-NFU correlations extracted from the MD generated model. They show a clear dependence on P_2O_5 content, marked by monotonic decreases in Si, B(III), and B(IV) neighbors and increases in the quantity of P neighbors. Therefore, the sodium ions strongly prefer phosphate species over any other NFUs in the second coordination sphere of Na. This finding stands in excellent agreement with the conclusions from the $^{23}Na\{^{31}P\}$ REDOR studies. We can put this agreement into more quantitative terms, considering that the dipolar second moments $M_{2(S-I)}$, determined experimentally by REDOR via equation (1) and listed in Table 4.5 follow from the internuclear distance distribution according to the van Vleck equation[56]

$$M_{2(S-I)} = \frac{4}{15}\left(\frac{\mu_0}{4\pi}\right)^2 \gamma_I^2 \gamma_S^2 \hbar^2 I(I+1) \sum \frac{1}{r_{S-I}^6} \qquad (2)$$

where γ_I and γ_S are the gyromagnetic ratios of the nuclear species involved, and $r_{S\text{-}I}$ are the internuclear distances between the observe nuclei (S) and the nuclei (I) of spin quantum number I to which they are coupled, and all the other symbols have their usual meanings. As all of the constants in equation (2) are well-known, we can calculate experimental

values of $\sum \frac{1}{r_{S-I}^6}$ (NMR) from the numerical second moments $M_{2(\text{P-Na})}$ and $M_{2(\text{Na-P})}$ listed in Table 4.5. This value can be compared with values of $\sum \frac{1}{r_{S-I}^6}$ extracted from the MD generated models, by extending the summation to the convergence limit, which in the present case was found to be 15 Å, and results were averaged over a total of 451 ^{23}Na observe and 126 ^{31}P observe nuclei, respectively. For the glass PB3-P7, these numbers are in very good agreement: Specifically we find $\sum \frac{1}{r_{P-Na}^6}$ = 3.5 × 10^{57} m$^{\acute{}6}$ and 3.7 × 10^{57} m^{-6} from NMR, and MD output, while the corresponding results for $\sum \frac{1}{r_{Na-P}^6}$ are 1.8 × 10^{57} m^{-6} and 1.2 × 10^{57} m^{-6}, respectively. This preliminary result is very encouraging, showing good consistency between the MD and NMR data. Future studies will be devoted to a more systematic comparison of all the $M_{2(\text{S-I})}$ values (*S*, *I* = ^{11}B, ^{23}Na, ^{31}P) characterizing all the six possible pair correlations for a larger set of glasses in the Na_2O-SiO_2-B_2O_3-P_2O_5 system.

4.4 Implications on the design of novel borosilicate-based bioactive glasses

Through a systematic and dedicated approach, an in-depth understanding of the structure of borosilicate-based model bioactive glasses has been unearthed. It is well-known that the short-and intermediate-range order in multicomponent glasses greatly affects the glass degradation behavior in simulated body environments. For instance, weakly bound species (i.e. Na^+ at Si-NBO sites) readily release from the glass in aqueous environments via ion exchange,[57-59] meanwhile, B(III) species have been previously shown to hydrolyze at quicker rates in comparison to B(IV) species.[60,61] This knowledge may have the prospect to extend to phosphate species since *x* = 1 glasses exhibit high amounts of isolated phosphate species (P^0 and $P^1{}_{1P}$) which are weakly bound to the glass network,

meanwhile, $x > 1$ glasses contain elevated amounts of P-O-B^4 NFU linkages which can improve the chemical durability. Furthermore, the additional structural effects that P_2O_5 exhibit upon NFU mixing and speciation (i.e. N_4 and Si^4 fractions) can have unanticipated impacts upon ionic release characteristics and bioactivity which can benefit the design of novel bioactive glasses. Future studies examining *structure-degradation behavior* relationships in the present sodium phopsho-borosilicate glass system can help to unearth the ideal NFU structures necessary for tuning ionic release to elicit desired biological responses when in contact with human body fluids. Using the described approach, which necessitates a careful compositional design, can accelerate the development of borosilicate glasses for innovative applications.

4.5 Conclusions

The present combined MAS NMR and MD study provides a comprehensive structural understanding of the short- and intermediate-range order in the Na_2O-P_2O_5-B_2O_3-SiO_2 model bioactive glass system, and its evolution upon successive incorporation of P_2O_5. Three glass series, corresponding to perboric ($R < 1$), metaboric ($R = 1$), and peralkaline ($R > 1$) base compositions are investigated into which P_2O_5 is incorporated along three distinct substitution schemes, leading to a comprehensive data set of nine series in total. While levels above 5 mol. % P_2O_5 lead to phase separation and formation of crystalline $Na_4P_2O_7$, the tolerance of the glass network for P_2O_5 increases with decreasing *R*-value. Within this composition range P_2O_5 effects a significant re-polymerization of the silicon species and a re-structuring of the borate component in the network, driven by the additional demand of phosphate for charge compensation. In addition, the degree $<n>$ of phosphate polymerization increases as a function of P_2O_5 content, as increasing amounts

of B-O-P linkages are formed. The latter also serve to disperse the negative charges of the B(IV) units toward non-bridging oxygen atoms located on the phosphate species.[62,63]

The detailed analysis of ^{31}P-^{11}B dipole-dipole and ^{31}P-^{31}P indirect spin-spin couplings on selected samples suggests a general picture of the NFU connectivities, which stands in excellent agreement with those drawn from the MD simulations and expands significantly on previous findings on bioactive P_2O_5-containing silicate and borosilicate glasses.[22,63,64] In addition, the combined ^{23}Na- based double resonance experiments and the MD simulations portray a consistent and quantitative picture of the next-nearest neighbor coordination sphere of the modifier cations, featuring their preferred correlations with the phosphate component. Ultimately, our extensive knowledge of this system will not only facilitate the prediction of structural details and degradation behavior for bioactive glass applications, but also help in identifying novel borosilicate glasses tuned to particular biomedical applications.

Conflicts of interest

The authors confirm the absence of any conflict of interest with this submission.

Acknowledgements

This material is based upon work supported by the National Science Foundation under Grant No. 1507131, the US Department of Energy (DOE) – Offices of Nuclear Energy and Environmental Management through Nuclear Energy University Program under Grant No. DE-NE0008597, and US DOE – Office of River Protection under Grant No. DE-EM0003207. H.E. and H.B. thank FAPESP for support under Grant No. 2013/07793-6. H.B. also thanks the DFG for support. The authors also thank the Characterization Sciences group at Corning Incorporated for compositional analysis of glasses.

Supplementary Information

The supplementary information of this manuscript contains XRD patterns of as-synthesized glasses, additional MAS NMR spectra, in addition to further information related to the MD simulations performed on glass samples.

References

1. Rahaman, M. N.; Day, D. E.; Bal, B. S.; Fu, Q.; Jung, S. B.; Bonewald, L. F.; Tomsia, A. P., Bioactive glass in tissue engineering. *Acta Biomaterialia* 2011, *7* (6), 2355-2373.
2. Balasubramanian, P.; Buettner, T.; Pacheco, V. M.; Boccaccini, A. R., Boron-containing bioactive glasses in bone and soft tissue engineering. *Journal of the European Ceramic Society* 2018, *38* (3), 855-869.
3. Stone-Weiss, N.; Pierce, E. M.; Youngman, R. E.; Gulbiten, O.; Smith, N. J.; Du, J.; Goel, A., Understanding the structural drivers governing glass–water interactions in borosilicate based model bioactive glasses. *Acta Biomaterialia* 2018, *65*, 436-449.
4. Deshkar, A.; Marcial, J.; Southern, S. A.; Kobera, L.; Bryce, D. L.; McCloy, J. S.; Goel, A., Understanding the structural origin of crystalline phase transformations in nepheline (NaAlSiO4) based glass-ceramics. *Journal of the American Ceramic Society* 2017, *100* (7), 2859-2878.
5. Huang, W. H.; Day, D. E.; Kittiratanapiboon, K.; Rahaman, M. N., Kinetics and mechanisms of the conversion of silicate (45S5), borate, and borosilicate glasses to hydroxyapatite in dilute phosphate solutions. *Journal of Materials Science-Materials in Medicine* 2006, *17* (7), 583-596.
6. Hanson, B.; Murtagh, M.; Tandon, P., Alkali-doped optical fiber preform and method of making same. Google Patents: 2005.
7. Hoppe, A.; Gueldal, N. S.; Boccaccini, A. R., A review of the biological response to ionic dissolution products from bioactive glasses and glass-ceramics. *Biomaterials* 2011, *32* (11), 2757-2774.
8. Boccaccini, A. R.; Gorustovich, A. A.; Roether, J. A., Effect of Bioactive Glasses on Angiogenesis: A Review of In Vitro and In Vivo Evidences. *Tissue Engineering Part B-Reviews* 2010, *16* (2), 199-207.
9. Xynos, I.; Edgar, A.; Buttery, L.; Hench, L.; Polak, J., Ionic Products of Bioactive Glass Dissolution Increase Proliferation of Human Osteoblasts and Induce Insulin-like Growth Factor II mRNA Expression and Protein Synthesis. *Biochemical and Biophysical Research Communications* 2000, *276* (2), 461-465.
10. Tilocca, A., Structural models of bioactive glasses from molecular dynamics simulations. *Proceedings of the Royal Society a-Mathematical Physical and Engineering Sciences* 2009, *465* (2104), 1003-1027.
11. Goel, A.; Kapoor, S.; Tilocca, A.; Rajagopal, R. R.; Ferreira, J. M. F., Structural role of zinc in biodegradation of alkali-free bioactive glasses. *Journal of Materials Chemistry B* 2013, *1* (24), 3073-3082.
12. Yun, Y. H.; Bray, P. J., Nuclear magnetic resonance studies of the glasses in the system Na2O-B2O3-SiO2. *Journal of Non-Crystalline Solids* 1978, *27* (3), 363-380.
13. Dell, W. J.; Bray, P. J.; Xiao, S. Z., 11B NMR studies and structural modeling of Na2O-B2O3-SiO2 glasses of high soda content. *Journal of Non-Crystalline Solids* 1983, *58* (1), 1-16.
14. Bray, P. J., Structural models for borate glasses. *Journal of Non-Crystalline Solids* 1985, *75* (1-3), 29-36.
15. Manara, D.; Grandjean, A.; Neuville, D. R., Structure of borosilicate glasses and melts: A revision of the Yun, Bray and Dell model. *Journal of Non-Crystalline Solids* 2009, *355* (50–51), 2528-2531.

16. White, A., The Materials Genome Initiative: One year on. *Mrs Bulletin* 2012, *37* (8), 715-716.
17. Crovace, M. C.; Souza, M. T.; Chinaglia, C. R.; Peitl, O.; Zanotto, E. D., Biosilicate®—A multipurpose, highly bioactive glass-ceramic. In vitro, in vivo and clinical trials. *Journal of Non-Crystalline Solids* 2016, *432*, 90-110.
18. Christensen, R.; Byer, J.; Kaufmann, T.; Martin, S. W., Structure–property relationships in the mixed glass former system Na2O–B2O3–P2O5. *Physics and Chemistry of Glasses-European Journal of Glass Science and Technology Part B* 2009, *50* (4), 237-242.
19. Muñoz, F.; Montagne, L.; Delevoye, L.; Durán, A.; Pascual, L.; Cristol, S.; Paul, J.-F., Phosphate speciation in sodium borosilicate glasses studied by nuclear magnetic resonance. *Journal of Non-Crystalline Solids* 2006, *352* (28–29), 2958-2968.
20. Fluegel, A.; Spinelli, I. M.; LaCourse, W., Study of the Kinetics of Phase Separation in 3.25 Na2O-3.25 Li2O/Na2O-33.5 B2O3-60 SiO2 Glasses by Skeletonization. *Advances in Fusion and Processing of Glass III* 2006, *141*, 363-370.
21. Gan, H.; Hess, P. C.; Kirkpatrick, R. J., Phosphorus and boron speciation in K2O-B2O3-SiO2-P2O5 glasses. *Geochimica et Cosmochimica Acta* 1994, *58* (21), 4633-4647.
22. Yu, Y.; Stevensson, B.; Edén, M., Medium-Range Structural Organization of Phosphorus-Bearing Borosilicate Glasses Revealed by Advanced Solid-State NMR Experiments and MD Simulations: Consequences of B/Si Substitutions. *The Journal of Physical Chemistry B* 2017, *121* (41), 9737-9752.
23. Yu, Y.; Eden, M., Structure-composition relationships of bioactive borophosphosilicate glasses probed by multinuclear 11B, 29Si, and 31P solid state NMR. *RSC Advances* 2016, *6* (103), 101288-101303.
24. Mazurin, O.; Streltsina, M.; Shvaiko-Shvaikovskaya, T., Sci Glass-6.5 (Glass Property Information System). *Institute of Theoretical Chemistry, Shrewsbury, MA, USA* 2005.
25. Lesage, A.; Bardet, M.; Emsley, L., Through-bond carbon− carbon connectivities in disordered solids by NMR. *Journal of the American Chemical Society* 1999, *121* (47), 10987-10993.
26. Massiot, D.; Fayon, F.; Capron, M.; King, I.; Le Calvé, S.; Alonso, B.; Durand, J. O.; Bujoli, B.; Gan, Z.; Hoatson, G., Modelling one-and two-dimensional solid-state NMR spectra. *Magnetic Resonance in Chemistry* 2002, *40* (1), 70-76.
27. Massiot, D.; Bessada, C.; Coutures, J.; Taulelle, F., A quantitative study of 27Al MAS NMR in crystalline YAG. *Journal of Magnetic Resonance (1969)* 1990, *90* (2), 231-242.
28. Chan, J. C.; Eckert, H., Dipolar coupling information in multispin systems: Application of a compensated REDOR NMR approach to inorganic phosphates. *Journal of Magnetic Resonance* 2000, *147* (2), 170-178.
29. Gullion, T., Measurement of heteronuclear dipolar interactions by rotational-echo, double-resonance nuclear magnetic resonance. *ChemInform* 1998, *29* (4), no-no.
30. Bertmer, M.; Eckert, H., Dephasing of spin echoes by multiple heteronuclear dipolar interactions in rotational echo double resonance NMR experiments. *Solid State Nuclear Magnetic Resonance* 1999, *15* (3), 139-152.
31. Schulze, G. E., Die Kristallstruktur von BPO 4 und BAsO 4. *Naturwissenschaften* 1933, *21* (30), 562-562.

32. Ondik, H., The structure of anhydrous sodium trimetaphosphate Na3P3O9, and the monohydrate, Na3P3O9. H2O. *Acta Crystallographica* 1965, *18* (2), 226-232.
33. Krogh-Moe, J., The crystal structure of sodium diborate, Na2O. 2H2O3. *Acta Crystallographica Section B: Structural Crystallography and Crystal Chemistry* 1974, *30* (3), 578-582.
34. Ba, Y.; Kao, H.-M.; Grey, C. P.; Chopin, L.; Gullion, T., Optimizing the13C–14N REAPDOR NMR Experiment: A Theoretical and Experimental Study. *Journal of Magnetic Resonance* 1998, *133* (1), 104-114.
35. Bak, M.; Rasmussen, J. T.; Nielsen, N. C., SIMPSON: a general simulation program for solid-state NMR spectroscopy. *Journal of Magnetic Resonance* 2000, *147* (2), 296-330.
36. Pedone, A., Properties calculations of silica-based glasses by atomistic simulations techniques: a review. *The Journal of Physical Chemistry C* 2009, *113* (49), 20773-20784.
37. Tilocca, A.; de Leeuw, N. H.; Cormack, A. N., Shell-model molecular dynamics calculations of modified silicate glasses. *Physical Review B* 2006, *73* (10).
38. Tilocca, A., Short- and medium-range structure of multicomponent bioactive glasses and melts: An assessment of the performances of shell-model and rigid-ion potentials. *Journal of Chemical Physics* 2008, *129* (8).
39. Fortino, M.; Berselli, A.; Stone-Weiss, N.; Deng, L.; Goel, A.; Du, J. C.; Pedone, A., Assessment of interatomic parameters for the reproduction of borosilicate glass structures via DFT-GIPAW calculations. *Journal of the American Ceramic Society* 2019, *102* (12), 7225-7243.
40. Stevensson, B.; Yu, Y.; Edén, M., Structure–composition trends in multicomponent borosilicate-based glasses deduced from molecular dynamics simulations with improved B–O and P–O force fields. *Physical Chemistry Chemical Physics* 2018, *20* (12), 8192-8209.
41. Smith, W.; Forester, T. R., DL_POLY_2.0: A general-purpose parallel molecular dynamics simulation package. *Journal of Molecular Graphics* 1996, *14* (3), 136-141.
42. Segall, M. D.; Lindan, P. J. D.; Probert, M. J.; Pickard, C. J.; Hasnip, P. J.; Clark, S. J.; Payne, M. C., First-principles simulation: ideas, illustrations and the CASTEP code. *Journal of Physics-Condensed Matter* 2002, *14* (11), 2717-2744.
43. Yates, J. R.; Pickard, C. J.; Mauri, F., Calculation of NMR chemical shifts for extended systems using ultrasoft pseudopotentials. *Physical Review B* 2007, *76* (2), 024401.
44. Han, F., Projector-Augmented Plane-Wave Method. World Scientific: 2011; Vol. 50, pp 391-396.
45. Perdew, J. P.; Burke, K.; Ernzerhof, M., D. of Physics and NOL 70118 J. Quantum theory group Tulane University. *Phys. Rev. Lett* 1996, *77*, 3865-3868.
46. Pedone, A.; Charpentier, T.; Malavasi, G.; Menziani, M. C., New insights into the atomic structure of 45S5 bioglass by means of solid-state NMR spectroscopy and accurate first-principles simulations. *Chemistry of Materials* 2010, *22* (19), 5644-5652.
47. Alderman, O. L.; Iuga, D.; Howes, A. P.; Pike, K. J.; Holland, D.; Dupree, R., Spectral assignments and NMR parameter–structure relationships in borates using high-resolution 11B NMR and density functional theory. *Physical Chemistry Chemical Physics* 2013, *15* (21), 8208-8221.

48. Gambuzzi, E.; Charpentier, T.; Menziani, M. C.; Pedone, A., Computational interpretation of 23Na MQMAS NMR spectra: A comprehensive investigation of the Na environment in silicate glasses. *Chemical Physics Letters* 2014, *612*, 56-61.
49. Pyykkö, P., Spectroscopic nuclear quadrupole moments. *Molecular Physics* 2001, *99* (19), 1617-1629.
50. Presti, D.; Pedone, A.; Licari, D.; Barone, V., A Modular Implementation for the Simulation of 1D and 2D Solid-State NMR Spectra of Quadrupolar Nuclei in the Virtual Multifrequency Spectrometer–Draw Graphical Interface. *Journal of chemical theory and computation* 2017, *13* (5), 2215-2229.
51. Feller, S. A.; Kottke, J.; Welter, J.; Nijhawan, S.; Boekenhauer, R.; Zhang, H.; Feil, D.; Parameswar, C.; Budhwani, K.; Affatigato, M. In *Physical properties of alkali borosilicate glasses*, Proceedings of the Second International Conference on Borate Glasses, Crystals, and Melts, Abingdon, United Kingdom, Sheffield (United Kingdom): The Society of Glass Technology: 1997; pp 246-253.
52. Du, L. S.; Stebbins, J. F., Solid-state NMR study of metastable immiscibility in alkali borosilicate glasses. *Journal of Non-Crystalline Solids* 2003, *315* (3), 239-255.
53. Eckert, H., Structural characterization of bioactive glasses by solid state NMR. *Journal of Sol-Gel Science and Technology* 2018, *88* (2), 263-295.
54. El-Damrawi, G.; Müller-Warmuth, W.; Doweidar, H.; Gohar, I., Structure and heat treatment effects of sodium borosilicate glasses as studied by 29Si and 11B NMR. *Journal of non-crystalline solids* 1992, *146*, 137-144.
55. Martin, S. W., Si-29 MAS-NMR study of the short-range order in potassium borosilicate glasses. *Journal of the American Ceramic Society* 1995, *78* (4), 952-960.
56. Van Vleck, J., The dipolar broadening of magnetic resonance lines in crystals. *Physical Review* 1948, *74* (9), 1168.
57. Perera, G.; Doremus, R. H., Dissolution Rates of Commercial Soda–Lime and Pyrex Borosilicate Glasses: Influence of Solution pH. *Journal of the American Ceramic Society* 1991, *74* (7), 1554-1558.
58. Bunker, B. C., Molecular mechanisms for corrosion of silica and silicate glasses. *Journal of Non-Crystalline Solids* 1994, *179*, 300-308.
59. Hamilton, J. P.; Pantano, C. G., Effects of glass structure on the corrosion behavior of sodium-aluminosilicate glasses. *Journal of Non-Crystalline Solids* 1997, *222* (0), 167-174.
60. Kapoor, S.; Youngman, R. E.; Zakharchuk, K.; Yaremchenko, A.; Smith, N. J.; Goel, A., Structural and Chemical Approach toward Understanding the Aqueous Corrosion of Sodium Aluminoborate Glasses. *The Journal of Physical Chemistry B* 2018, *122* (48), 10913-10927.
61. Brauer, D. S.; Möncke, D., Introduction to the structure of silicate, phosphate and borate glasses. In *Bioactive Glasses*, 2016; pp 61-88.
62. Larink, D.; Eckert, H.; Reichert, M.; Martin, S. W., Mixed Network Former Effect in Ion-Conducting Alkali Borophosphate Glasses: Structure/Property Correlations in the System M2O (1/3) (B2O3)(x)(P2O5)(1-x) (2/3) (M = Li, K, Cs). *Journal of Physical Chemistry C* 2012, *116* (50), 26162-26176.
63. Funke, L. M.; Eckert, H., Charge compensation in sodium borophosphate glasses studied by 11B {23Na} and 31P {23Na} rotational echo double resonance spectroscopy. *The Journal of Physical Chemistry C* 2016, *120* (6), 3196-3205.

64. Fayon, F.; Duée, C.; Poumeyrol, T.; Allix, M.; Massiot, D., Evidence of nanometric-sized phosphate clusters in bioactive glasses as revealed by solid-state 31p nmr. *The Journal of Physical Chemistry C* 2013, *117* (5), 2283-2288.

Chapter 5. An insight into the structural and compositional drivers controlling ionic release kinetics of model borosilicate bioactive glasses

Nicholas Stone-Weiss,[1] Henrik Bradtmüller,[2] Randall E. Youngman,[3] Hellmut Eckert,[2] Ashutosh Goel[1,§]

[1]Department of Materials Science and Engineering, Rutgers, The State University of New Jersey, Piscataway, NJ 08854, United States

[2]São Carlos Institute of Physics, University of São Paulo, São Carlos, Brazil

[3]Science and Technology Division, Corning Incorporated, Corning, NY 14831, United States

§ Corresponding author:
Email: ag1179@soe.rutgers.edu; Ph: +1-848-333-1523

5.1 Introduction

Recent years have experienced a significant rise in the research interest of borosilicate-based bioactive glasses as potential candidates while designing novel third generation biomaterials.[1-3] Borosilicate glasses, for instance, offer particular advantages over traditional silicate-based compositions, such as (i) a broader glass-forming range, (ii) tunable chemical degradation over wide ranges,[1] and (iii) ease of processing into porous three-dimensional scaffolds for implantation into the body.[2, 4] Furthermore, borosilicate glasses have been shown to promote angiogenesis and osteogenesis in vivo;[1, 5] the aforementioned intrinsic characteristics and macroscale properties make borosilicate glasses very attractive for a wide scope of biomedical applications. Generally, third generation biomaterials are designed such that, when exposed to body fluids, ionic dissolution products are released from the glass into the body to initiate a synchronized sequence of cell-level responses that result in the expression of genes required for body tissue regeneration.[6] Since healing effects can be maximized by tailoring ion release kinetics to the bodily rates of new tissue formation,[1, 6] developing a fundamental understanding of the degradation behavior of borosilicate glasses in body fluids is of utmost importance. Likewise, since the degradation of glass in aqueous solutions is closely tied to its structure at the atomic level,[7, 8] a greater conceptual understanding of the compositional and structural drivers controlling glass degradation behavior is required for the development of novel borosilicate bioactive glasses.

It is well-known that the network structure of bioactive silicate glasses (such as the 45S5 “gold standard”) is dominated by metasilicate chains,[7] while the ideal structures in borosilicate bioactive glasses are not as well identified. For instance, the addition of B_2O_3

adds significant network structural complexity, which greatly affects aqueous degradation kinetics. Multiple studies on simplified sodium borosilicate glasses[9-14] have successfully described the local and intermediate-range structural features involving trigonal and tetrahedral boron and their connectivity with each other and with silicon, but the connection between these structural features and glass dissolution behavior is still largely unknown. Further, recent studies have been performed which identify comprehensive *composition-structure* relationships in P_2O_5-containing borosilicate compositions,[15-19] where P_2O_5 is known to vastly alter glass properties[17, 20-22] and is a vital component of borosilicate bioactive glasses due to its beneficial impact upon bioactivity and compatibility with mineral phosphate in bone tissue.[1, 23] Although the structure of borosilicate glasses is well-understood and phospho-borosilicate structure is fairly well-understood for a limited composition-space (i.e., compositions based upon 45S5[15, 16]), the links between glass structure and degradation behavior/bioactivity in both systems are still mostly uncertain. Additionally, building *structure-degradation behavior* relationships is elusively difficult since the majority of borosilicate bioactive glass literature focusing on glass dissolution mechanisms and bioactivity utilize a "trial-and-error" compositional design approach, which involves a partial or full replacement of SiO_2 by B_2O_3 in known formulations such as 45S5 or 13-93.[1, 24, 25] While this approach is successful in determining biocompatibility over the dedicated composition-space, it does not allow for the development of *composition-structure-property* relationships in which novel bioactive compositions can be designed using predictive models relating glass structure to its degradation behavior. Thus, a comprehensive "materials-by-design" approach (as laid out in the White House's Materials Genome Initiative[26]) must be instead adopted, in which intimate relationships

between glass structure and degradation behavior can be unearthed across systematically-designed borosilicate and phospho-borosilicate glass compositions. In this way, comprehensive datasets on model borosilicate bioactive glasses can be generated which facilitate the development of predictive models[27] allowing the prediction of glass degradation behavior based upon its composition.

Glasses in the current study were devised over a wide composition space in the baseline sodium borosilicate (P_2O_5-free) system, including perboric (Na/B < 1), metaboric (Na/B = 1), and peralkaline (Na/B > 1) regimes, substituting P_2O_5 into the glass using stepwise additions. Through a comprehensive study utilizing several state-of-the-art characterization techniques, including inductively coupled plasma – optical emission spectroscopy (ICP-OES), advanced magic-angle spinning nuclear magnetic resonance (MAS NMR) spectroscopy, among others, we aim to generate a comprehensive understanding of the elemental release behavior and glass structural evolution during degradation these glasses in simulated body environments. Accordingly, we aim to develop a comprehensive understanding of the compositional and structural drivers of glass degradation in the studied system, which we hope will contribute to the design of novel borosilicate-based bioactive glasses with controlled dissolution behavior (i.e. ionic release) for targeted biomedical applications.

5.2 Experimental

5.2.1 Compositional design and glass preparation

Glass series were designed in three different compositional regimes of $R = Na_2O/B_2O_3$, ratios, including perboric (PB, $R < 1$), metaboric (MB, $R = 1$), and peralkaline (PA, $R > 1$) compositions. The series explored are listed below (mol. %):

Series PB2: $x\ P_2O_5$–(25 Na_2O–30 B_2O_3–45 SiO_2) x = 0, 1, 3, 5

Series MB2: $x\ P_2O_5$–(25 Na_2O–25 B_2O_3–50 SiO_2) x = 0, 1, 3, 5

Series PA2: $x\ P_2O_5$–(25 Na_2O–20 B_2O_3–55 SiO_2) x = 0, 1, 3

The glass synthesis and annealing procedures have been described in Chapter 4. Table 5.1 presents the batched vs. experimental glass compositions as analyzed on selected samples by ICP-OES (PerkinElmer Optima 7300V) for B_2O_3, P_2O_5, and SiO_2 and flame emission spectroscopy (PerkinElmer Flame Emission Analyst 200) for Na_2O.

Table 5.1. *All batched compositions of studied glasses compared to selected experimental compositions (in brackets), as analyzed via ICP-OES (±0.5 mol. %). B^4 fraction from ^{11}B MAS NMR and calculated Si^4 fractions are also displayed.*

Sample ID	Batched				MAS NMR	
	Na_2O	**P_2O_5**	**B_2O_3**	**SiO_2**	**B^4**	**Si^4**
PB0	25.0 [25.3]	--	30.0 [29.7]	45.0 [45.0]	62.9	70.8
PB2-P1	24.8	1.0	29.7	44.6	63.5	81.5
PB2-P3	24.3 [25.9]	3.0 [3.0]	29.1 [29.0]	43.7 [42.2]	62.1	84.5
PB2-P5	23.8 [25.8]	5.0 [5.0]	28.5 [29.1]	42.8 [40.0]	59.1	88.3
MB0	25.0 [25.1]	--	25.0 [25.0]	50.0 [49.9]	67.2	66.7
MB2-P1	24.8	1.0	24.8	49.5	67.5	74.6
MB2-P3	24.3 [26.0]	3.0 [3.0]	24.3 [23.9]	48.5 [47.1]	67.2	77.8
MB2-P5	23.8 [24.7]	5.0 [5.0]	23.8 [23.9]	47.5 [46.3]	65.5	92.1
PA0	25.0 [25.1]	--	20.0 [20.1]	55.0 [54.8]	71.0	61.7
PA2-P1	24.8	1.0	19.8	54.5	71.4	68.3
PA2-P3	24.3 [25.1]	3.0 [3.1]	19.4 [19.3]	53.4 [52.6]	71.9	77.3

5.2.2 Sample preparation for chemical degradation experiments

5.2.2.1 Surface area analysis of glass powder specimens

The studied glass was crushed and sieved to obtain powders with particle size varying between 300 – 425 µm. The glass particles were ultrasonically washed in acetone to remove any fine powder residue sticking to the surface of larger particles. This process was repeated at least three times or until the supernatant was clear to ensure the removal of

all fine particles. The ultrasonically washed glass particles were dried overnight at room temperature in ambient air and analyzed for any structural changes before and after acetone-washing using Fourier Transform Infrared (FTIR) spectroscopy. The IR spectra were acquired using a single-bounce diamond attenuated total reflectance (ATR) apparatus (FTIR-UATR, Frontier™, PerkinElmer, Inc.; scanning resolution 4 cm^{-1}, 32 scans for background and samples). Average three-dimensional (3D) geometric surface area of washed particles was determined using ImageJ software (as explained in more detail in Ref.[3]) after capturing images of ~1000 particles via an optical microscope (Zeiss Axioskop 40) at ~50X magnification. Experimental density values (measured using Archimedes' method by measuring the mass of sample in air and d-limonene solution; number of samples = 4, standard deviation <0.009 g cm^{-3}) were used together with the 3D surface area calculations to determine the specific surface area of the washed powders (~4100-4400 mm^2/g). Finally, the mass of glass particles resulting in the desired surface area–to–volume ratio (SA/V) was calculated.

5.2.2.2 Monolithic glass coupons

Based on the results of the degradation behavior of powder samples, similar tests were performed on monolithic glass coupons. Three coupons with the dimensions ~10 mm × ~10 mm were cut for each glass composition using a diamond blade. The polishing of the glass coupons was performed according to the procedure described in ASTM C1220-10,[28] where the glass samples were ground in acetone sequentially using 120 – 600 grit sized SiC sheets followed by polishing in 6 µm and 3 µm non-aqueous diamond suspensions until a mirror finish was acquired. The thickness of the polished sample varied between 1-2 mm. The dimensions of the rectangular polished samples were measured to calculate the geometric surface areas.

5.2.3 Glass degradation experiments in simulated body environments

5.2.3.1 Degradation behavior and kinetics of glass corrosion

The degradation behavior and kinetics of glasses were studied in Tris-HCl and Tris-HNO_3 solutions with pH 7.4. Solutions were prepared by dissolving 13.25 g of Tris in DI water and adjusting the pH to the desired value with 1 M of HCl or HNO_3. Solutions were prepared as target pH ±0.02 in batches with a total volume of 1.00±0.05 L to maintain accurate Tris molarity in solution. In each experiment, 60.0 mg of acetone-washed glass particles were immersed in 50.0 mL of solution, corresponding to SA/V = 5 m^{-1}. All powder–solution mixtures were immediately sealed into sterilized polypropylene flasks and placed in an oven at 37±1 ºC. Solution preparation and experimental conditions were prepared according to ISO 10993-14, with the important addition of substituting HNO_3 instead of HCl as the acid utilized in Tris-based solutions. This decision was made according to our experience and relevant literature, in which Tournié et al.[29] determined that degradation kinetics in the forward rate regime accelerate by a factor of ~2 in Tris-HNO_3 as compared to Tris-HCl. We have, however, included Tris-HCl and Tris-HNO_3 in our study of series MB2 glasses in an attempt to elucidate kinetic differences according to acid identity.

Degradation experiments ranged from 1 hour to 28 days. In addition to analyses of neat (unused) and blank (glass-free) control solutions, all experiments were performed three times to evaluate uncertainty in final results. The pH of each solution recovered from experiments was measured at room temperature using a pH meter (Mettler Toledo InLab® Pro-ISM). Separate aliquots of recovered solutions were chemically analyzed by ICP-OES (PerkinElmer Optima 8300). ICP-OES detection limits were <0.5 ppm for Na, <0.2 ppm

for B, <0.5 for P, and <0.2 ppm for Si. The normalized loss (NL) of each element (Na, B, and Si) released from glasses into the surrounding solution was calculated using equation (1),

$$NL_i = \frac{C_i - C_o}{\left(\frac{SA}{V}\right) f_i} \qquad (1)$$

where C_i is the mass concentration of element *i* in the solution as detected by ICP-OES; f_i is the mass fraction of the element *i* in the glass; C_o is the background concentration (as determined from blank solutions). Normalized loss data were plotted against time and linearly fit over the apparent linear regimes of release at early times to evaluate forward dissolution rates for each glass composition.

5.2.3.2 Structural evolution of the glass powders due to degradation

To study the kinetics and mechanisms of glass degradation in simulated body environments, bulk and surface characterization were performed on both pre- and post-degradation glass specimens. The glass powders remaining after the dissolution experiments *(from section 5.2.2.1)* were rinsed three times with the deionized (DI) water, followed by rinsing in ethanol (Fisher Chemical, anhydrous) to remove any water sticking to the surface of glass particles. The powders were dried at room temperature in an ambient atmosphere. The powders recovered from these experiments were analyzed by X-ray diffraction (XRD; PANalytical – X'Pert Pro; Cu K_α radiation; 2θ range: 10–90º; step size: 0.01313º s^{-1}) to determine the presence/absence of deposited secondary crystalline phases. Furthermore, single resonance ^{23}Na, ^{11}B, ^{31}P, and ^{29}Si MAS NMR spectroscopy was performed recovered powders to assess the amorphous structural changes occurring as a result of degradation processes. The parameters used in single resonance MAS NMR experiments of post-degradation samples have been summarized in Table 5.2.

Furthermore, surface-probing $^{1}H \rightarrow ^{31}P$ and $^{1}H \rightarrow ^{29}Si$ cross-polarization (CP) MAS NMR experiments were performed to assess structural changes occurring in hydrated layers exposed to simulated body environments. The $^{1}H \rightarrow ^{31}P$ CP-MAS NMR experiments were performed for selected samples on a 5.7 T Varian 240-MR DD2 spectrometer (242.4 MHz and 98.1 MHz resonance frequencies for ^{1}H and ^{31}P, respectively) using a commercial 3.2 mm triple resonance MAS NMR probe. The powdered samples/specimen were spun at 10 kHz. The optimal matching conditions for CP experiments were optimized with regard to solid NaH_2PO_4. Contact times between 300-1500 μs were used along with π/2 radio frequency pulses of 4.3 μs duration. One second recycle delays were implemented in between acquisitions, with a minimum of 27000 acquisitions collected per sample. The measured ^{31}P chemical shifts are reported relative to solid BPO_4 as secondary standard (measured as -29.3 ppm relative to 85% H_3PO_4). The $^{1}H \rightarrow ^{29}Si$ CP-MAS NMR experiments were performed for selected samples on a 9.4 T Varian Unity INOVA spectrometer (400.1 MHz and 79.5 MHz resonance frequencies for ^{1}H and ^{29}Si, respectively) using a 7 mm wide-body CP-MAS probe with 7 mm silicon nitride rotors. The powdered samples/specimen were spun at 4.5-4.7 kHz. The optimal matching conditions for CP experiments were optimized with regard to solid kaolinite. Contact times of 3000 μs were used along with π/2 radio frequency pulses of 6.8 μs duration. Five second recycle delays were implemented in between acquisitions, with a minimum of 1600 acquisitions collected per sample. The measured ^{29}Si chemical shifts are reported relative to solid kaolinite as secondary standard (measured as -91.5 ppm relative to tetramethylsilane).

Table 5.2. *Summary of measurement conditions for all nuclei studied by MAS NMR.*

Single Resonance Parameters		
^{23}Na	Magnetic field (T) / Resonance frequency (MHz)	5.7 / 64.1
	Spinning frequency (kHz)	25.0
	Pulse length (μs) / Tip angle	0.8 / (π/6)
	Recycle delay (s)	0.5
	Number of acquisitions	≥4000
	Reference standard	NaCl (7.2 ppm)
^{11}B	Magnetic field (T) / Resonance frequency (MHz)	14.1 / 192.6
	Spinning frequency (kHz)	15.0
	Pulse length (μs) / (Tip Angle)	1.0 / (π/6)
	Recycle delay (s)	15
	Number of acquisitions	≥100
	Reference standard	BPO_4 (-3.5 ppm)
^{31}P	Magnetic field (T) / Resonance frequency (MHz)	5.7 / 98.1
	Spinning frequency (kHz)	10.0
	Pulse length (μs) / (Tip angle)	2.9 / (π/2)
	Recycle delay (s)	150
	Number of acquisitions	≥400
	Reference standard	BPO_4 (-29.3 ppm)
^{29}Si	Magnetic Field (T) / Resonance frequency (MHz)	9.4 / 79.5
	Spinning frequency (kHz)	4.5-4.7
	Pulse length (μs) / (Tip angle)	5.5 / (π/2)
	Recycle delay (s)	150
	Number of acquisitions	≥20
	Reference standard	Kaolinite (-91.5 ppm)

5.2.3.2 Surface evolution of monolithic bulk coupons during degradation experiments

Degradation experiments were additionally performed on polished monolithic glass coupons of MB2-P5 and PB2-P5 samples (two per composition) for 3- and 7-day durations. The recovered coupons were subjected to the same drying procedure as was performed for the recovered glass powders.

The X-ray photoelectron spectroscopy (XPS) measurements were performed on monolithic glass coupons to understand the composition and chemical environment of elements within the top 10 nm of sample surfaces – both in polished and degraded samples. The XPS measurements utilized a Thermo Scientific K-Alpha equipment, which used a 1486.6 eV monochromated Al K_α x-ray source to excite core level electrons from the sample. A low energy dual electron/argon-ion beam flood gun was used for charge compensation during measurements. The kinetic energy of the photoelectrons was measured using a 180° double-focusing hemispherical analyzer with a 128-channel detector. Binding energies were referenced to the main component of the adventitious carbon peak at 284.8 eV. The photoelectron spectrometer was calibrated using the $Au4f_{7/2}$ binding energy (83.96 eV) for the etched surface of Au metal reference. The analyzer was operated in the constant resolution mode with a pass energy of 10 eV for high-resolution spectroscopy, while a pass energy of 50 eV was used for the routine survey scans. Peak fitting for the core-level scans was performed using a mixed Gaussian-Lorentzian function (Gaussian: 85%) for obtaining binding energy and FWHM of the peaks. Peak areas were converted to composition using suitable elemental relative sensitivity factors[30] and corrected for attenuation through an adventitious carbonaceous overlayer using a

calculation similar to the method described by Smith.[31] The probe depth of XPS, taken to be three times the inelastic mean free path of photoelectrons, was 3.6 nm for Na 1s, 8.7 nm for P 2p, and 9.3 nm for B 1s and Si 2p.

The hydrogen profiles on the surface of post-degradation samples were determined by elastic recoil detection analysis (ERDA) using a 2.0 MeV He^{++} beam (General Ionex Tandetron accelerator). The beam was oriented in a grazing geometry with an angle of 75º between the incident beam and the surface normal. The detector was mounted at 75º with respect to the surface normal in the specular direction, with a 40 µm mylar foil placed over the active area to block scattered He ions. Hence, only forward-scattered H ions were able to penetrate the detector. The probe depth of ERDA is approximately 350 nm.

The post-degradation PB2-P5 glass coupon was mounted vertically in epoxy resin and polished to 1 µm surface finish (in non-aqueous media) to examine its cross-section and determine the depth and characteristics of the hydrated surface layers. The sample surface was sputter-coated with a 20 nm thick gold layer to reduce the charging effects. Both secondary electron imaging (ZEISS Sigma) and energy dispersive spectroscopy (EDS; X-Max Oxford Instruments; Aztec software) were conducted using an electron beam of 10-20 kV. EDS was employed to perform elemental mapping in the hydrated layers of the glass to assess composition differences between pristine and hydrated glass and supplement our knowledge of dissolution mechanisms and layer formation.

5.3 Results

5.3.1 Glass formation

The synthesized glasses which were ultimately selected for degradation experiments were visibly transparent in appearance and did not show any evidence of sharp

peaks in XRD. We observed that series MB2 and PB2 can incorporate 5 mol. % P_2O_5 while series PA2 glasses can only incorporate 3 mol. % P_2O_5 before visible phase separation and/or crystallization. The absence of visible glass-in-glass phase separation allows for an unambiguous examination of degradation behavior and glass structural evolution.

5.3.2 Elemental release behavior of glasses in simulated body environments

All the pH, elemental concentrations, and normalized loss (NL) data are displayed for each composition as a function of the experimental duration in Table 5.3. It is observed through the course of 28 days of experiments that the solution pH rises slightly and maintains between 7.3 and 7.7, indicating that the Tris-HCl and Tris-HNO_3 solutions exhibit a good buffering ability and can closely replicate the pH of human body fluids. Figure 5.1a-f display NL vs. time curves of $x = 0$ and x = maximum samples submerged in Tris-HNO_3 environments. All glasses display clear linear, forward release behavior within the first 12-24 hours of experiments, followed by a rate drop and rapid or gradual transition into the pseudo-equilibrium residual rate regime, typically attributed to the presence of a passivating gel layer on the surface of the glass. The residual rate regime is reached within 3-14 days of submersion, depending on the glass composition and dissolution kinetics. As expected, for the sodium borosilicate compositions ($x = 0$), Na and B NL curves exhibit close overlap, marked by rapid elemental release kinetics, meanwhile, Si is released from the glasses at a much slower rate. This is evidenced by the 200-250 g/m^2 NL values of Na and B after 28 days in $x = 0$ glasses compared to only 40-60 g/m^2 for Si (see Figure 5.1a, c, and e). The magnitude of release is also observed to be highly dependent upon the *R* compositional regime, which will be discussed further below. Upon substitution of P_2O_5 into the glass, P release closely follows that of Na and B in all compositions, thus, Na, P,

and B exhibit congruently degradation from the glass while Si is released incongruently at a significantly suppressed rate.

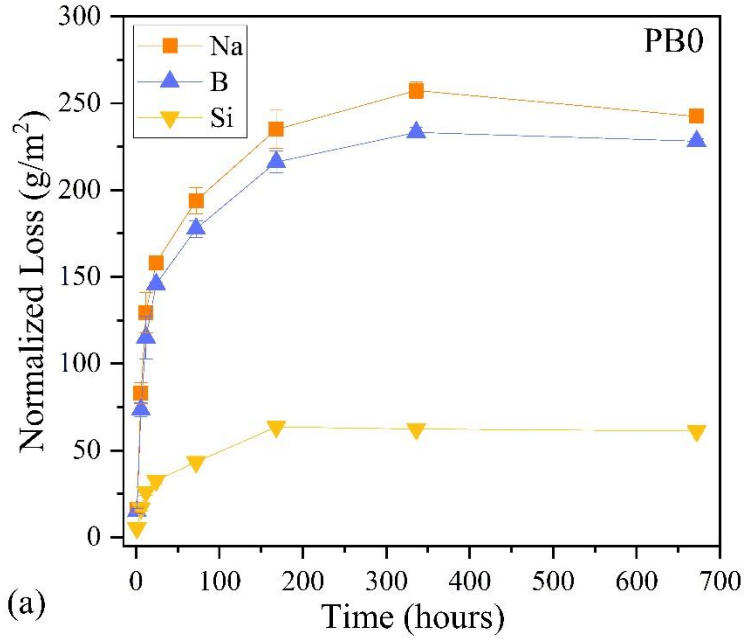

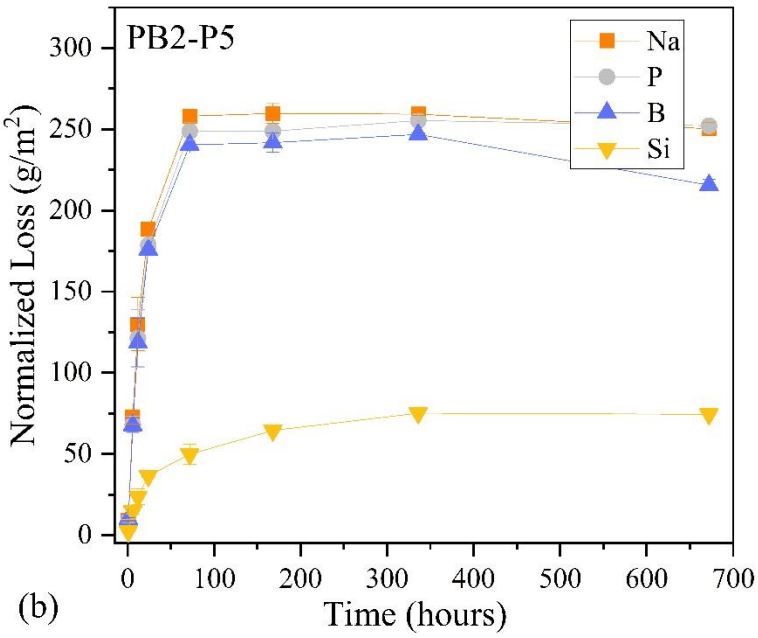

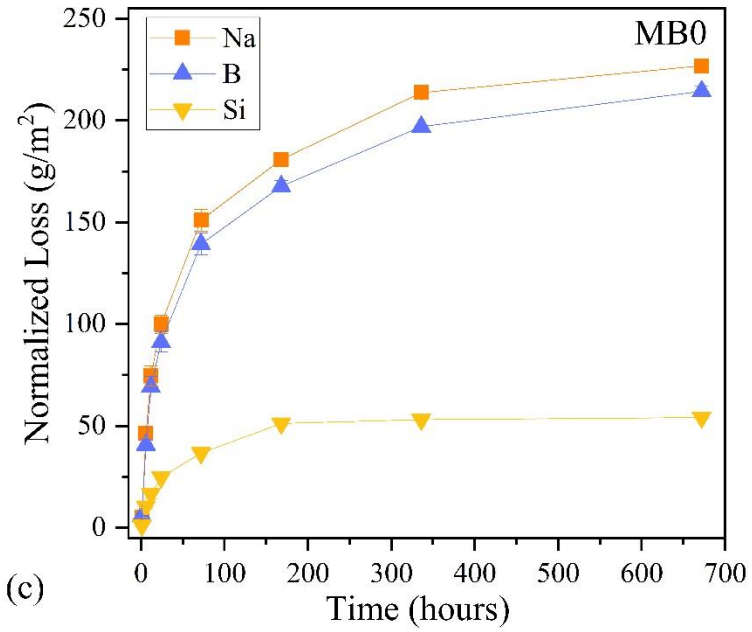
MB0
Na
B
Si
Normalized Loss (g/m^2)
Time (hours)
0
50
100
150
200
250
0
100
200
300
400
500
600
700

(c)

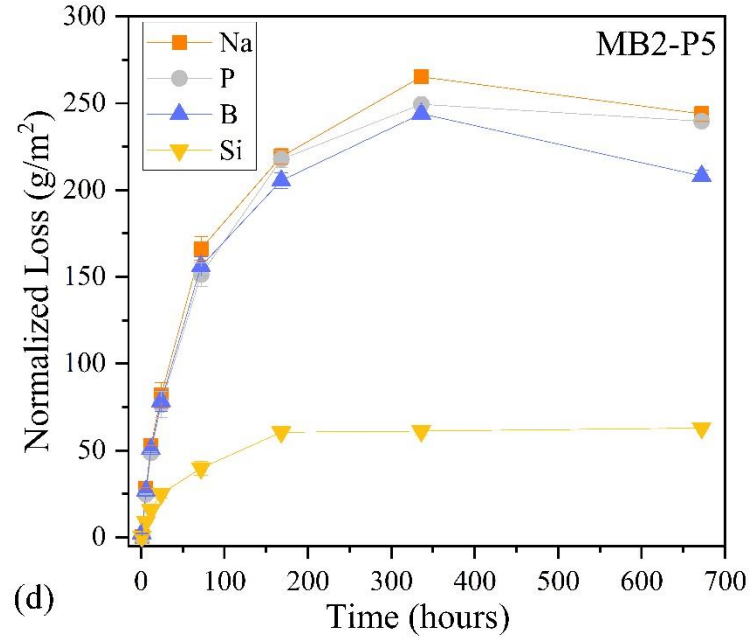
MB2-P5
Na
P
B
Si
Normalized Loss (g/m^2)
Time (hours)
0
50
100
150
200
250
300
0
100
200
300
400
500
600
700

(d)

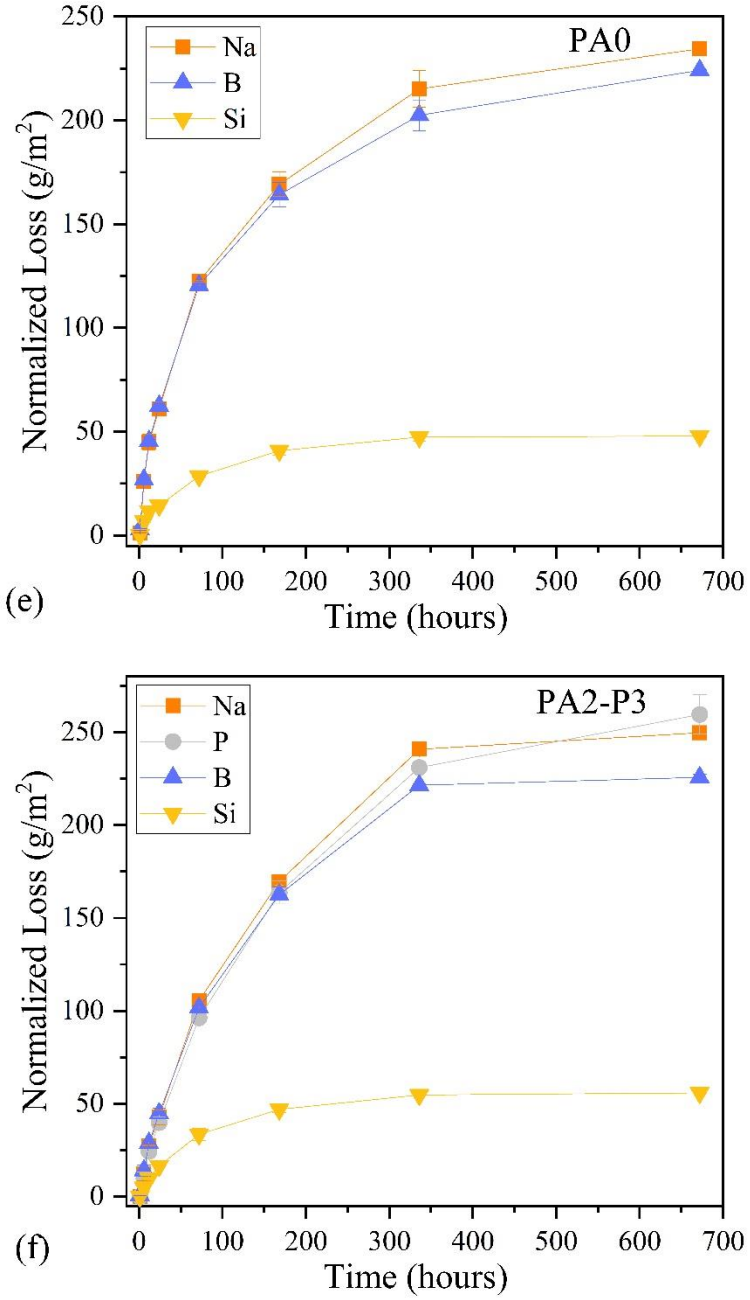

Figure 5.1. *Plots of normalized loss (g/m^2) of each element present in the glass as a function of time (hours) for (a) PB0, (b) PB2-P5, (c) MB0, (d) MB2-P5, and (e) PA0 and (f) PA2-P3.*

Table 5.3. *Average concentration (ppm), averaged normalized loss (g/m^2), and pH as a function of time (h) for all glasses in simulated body solutions. The reported errors are calculated 1σ standard deviation for duplicate samples.*

PB0 – Tris-HNO_3		Concentration, ppm							Normalized Loss, g/m^2						
Time (h)	pH	Na	Na-error	P	P-error	B	B-error	Si	Si-error	Na	Na-error	P	P-error	B	B-error	Si	Si-error
1	7.39±0.02	14.4	±1.6	--	--	8.1	±0.7	5.3	±0.7	15.9	±1.8	--	--	15.0	±1.4	5.3	±0.7
6	7.50±0.01	75.3	±5.4	--	--	37.9	±2.1	16.5	±1.8	83.1	±6.0	--	--	73.4	±4.1	16.6	±1.8
12	7.46±0.03	117.2	±10.4	--	--	59.2	±6.3	26.0	±2.0	129.4	±11.5	--	--	115.1	±12.3	26.1	±2.1
24	7.50±0.00	143.4	±1.6	--	--	74.9	±0.7	32.5	±1.8	158.2	±1.7	--	--	145.7	±1.3	32.6	±1.8
72	7.69±0.01	175.8	±6.9	--	--	91.3	±2.5	43.2	±1.3	193.9	±7.6	--	--	177.7	±4.8	43.3	±1.3
168	7.5±0.01	213.0	±10.0	--	--	111.0	±3.2	63.4	±1.4	235.0	±11.0	--	--	216.2	±6.3	63.6	±1.4
336	7.56±0.00	233.4	±4.3	--	--	119.7	±1.4	62.1	±0.8	257.5	±4.8	--	--	233.3	±2.8	62.4	±0.8
672	7.67±0.01	219.8	±1.3	--	--	118.1	±0.7	61.0	±0.2	242.5	±1.5	--	--	228.2	±1.4	61.2	±0.3
PB2-P1 – Tris-HNO_3		Concentration, ppm								Normalized Loss, g/m^2							
Time (h)	pH	Na	Na-error	P	P-error	B	B-error	Si	Si-error	Na	Na-error	P	P-error	B	B-error	Si	Si-error
1	7.39±0.01	13.0	±2.8	<0.5	--	7.5	±1.3	4.7	±1.1	14.7	±3.2	--	--	14.1	±2.6	4.8	±1.2
6	7.48±0.01	71.9	±11.5	3.1	±0.5	36.0	±5.7	15.0	±2.4	81.1	±12.9	64.2	±11.0	71.1	±11.3	15.4	±2.4
12	7.43±0.01	119.7	±11.8	5.7	±0.5	60.6	±4.2	24.6	±2.7	135.1	±13.4	117.5	±10.5	120.3	±8.4	25.3	±2.8
24	7.58±0.01	158.1	±8.1	7.9	±0.3	81.4	±4.7	33.7	±2.4	178.4	±9.2	163.1	±6.5	161.9	±9.5	34.6	±2.5
72	7.68±0.01	201.6	±3.8	9.9	±0.3	103.1	±2.2	44.5	±2.4	227.4	±4.3	204.7	±6.6	205.3	±4.3	45.7	±2.5
168	7.47±0.02	218.7	±12.1	11.2	±0.5	112.8	±5.5	55.7	±4.8	246.7	±13.7	232.6	±10.3	224.8	±11.1	57.2	±5.0
336	7.45±0.01	238.1	±2.6	12.1	±0.0	122.6	±0.8	64.3	±0.1	268.6	±2.9	250.5	±0.7	244.4	±1.7	65.9	±0.1
672	7.66±0.01	219.8	±3.3	11.7	±0.1	116.8	±1.9	61.1	±0.9	248.1	±3.7	243.2	±1.1	225.6	±3.7	62.7	±0.9
PB2-P3 – Tris-HNO_3		Concentration, ppm								Normalized Loss, g/m^2							
Time (h)	pH	Na	Na-error	P	P-error	B	B-error	Si	Si-error	Na	Na-error	P	P-error	B	B-error	Si	Si-error
1	7.37±0.02	8.0	±0.5	1.0	±0.0	5.0	±0.3	2.7	±0.1	9.4	±0.6	6.8	±0.3	9.7	±0.6	2.9	±0.1
6	7.46±0.00	60.8	±4.6	8.9	±0.8	31.6	±2.1	13.7	±0.5	71.7	±5.4	63.3	±5.9	65.2	±4.3	14.7	±0.6
12	7.39±0.01	109.3	±3.1	16.5	±0.9	56.0	±1.5	23.8	±0.7	129.0	±3.7	117.1	±6.4	116.3	±3.2	25.6	±0.8
24	7.53±0.01	149.6	±3.2	22.4	±0.8	76.9	±2.6	30.6	±1.7	176.5	±3.8	158.8	±5.7	159.9	±5.3	32.8	±1.9
72	7.64±0.01	212.0	±16.0	31.7	±2.4	109.0	±7.6	43.2	±4.9	250.2	±18.9	224.6	±16.6	227.0	±15.8	46.3	±5.3
168	7.45±0.00	221.6	±1.9	35.0	±0.1	114.8	±0.6	59.3	±1.8	261.5	±2.2	248.1	±0.7	239.2	±1.3	63.6	±2.0
336	7.50±0.01	222.2	±1.2	36.3	±1.0	116.6	±0.6	64.5	±1.3	262.1	±1.4	256.7	±6.7	242.9	±1.2	69.2	±1.4
672	7.60±0.00	212.9	±3.6	35.1	±1.6	114.1	±2.1	63.2	±0.9	251.2	±4.2	248.1	±11.4	220.3	±4.0	67.8	±0.9

PB2-P5 – Tris-HNO_3		Concentration, ppm								Normalized Loss, g/m²							
Time (h)	pH	Na	Na-error	P	P-error	B	B-error	Si	Si-error	Na	Na-error	P	P-error	B	B-error	Si	Si-error
1	7.36±0.01	7.6	±0.5	2.0	±0.3	4.9	±0.4	2.2	±0.4	9.3	±0.6	8.6	±1.2	9.9	±0.8	2.4	±0.4
6	7.45±0.00	59.1	±3.5	15.7	±1.2	31.4	±2.0	13.2	±1.7	72.9	±4.4	68.1	±5.3	67.7	±4.5	14.8	±1.9
12	7.35±0.00	105.4	±13.4	27.9	±4.1	54.7	±6.8	21.1	±4.3	130.0	±16.5	121.2	±17.7	118.6	±14.9	23.7	±4.9
24	7.5±0.01	152.8	±0.5	41.1	±0.8	80.9	±0.2	32.6	±0.8	188.5	±0.7	178.7	±3.4	175.9	±0.3	36.6	±0.9
72	7.64±0.01	209.3	±3.5	57.2	±1.2	110.4	±2.2	44.4	±5.6	258.1	±4.3	248.8	±5.1	240.5	±4.9	49.8	±6.3
168	7.4±0.01	210.6	±4.9	57.2	±0.2	111.0	±2.7	57.5	±0.7	259.7	±6.0	248.8	±0.7	241.7	±5.9	64.4	±0.8
336	7.45±0.01	210.3	±0.5	58.7	±0.1	113.3	±0.5	67.0	±0.1	259.3	±0.6	255.4	±0.6	246.9	±1.0	75.1	±0.2
672	7.54±0.01	203.0	±3.0	58.0	±0.5	111.7	±1.8	66.4	±0.5	250.3	±3.7	252.1	±2.3	215.5	±3.5	74.5	±0.6
MB0 – Tris-HCl		Concentration, ppm								Normalized Loss, g/m²							
Time (h)	pH	Na	Na-error	P	P-error	B	B-error	Si	Si-error	Na	Na-error	P	P-error	B	B-error	Si	Si-error
1	7.41±0.00	4.8	±0.2	--	--	4.3	±0.0	1.3	±0.0	5.3	±0.2	--	--	5.3	±0.0	1.1	±0.0
6	7.49±0.00	35.4	±2.1	--	--	16.2	±0.9	9.3	±0.5	38.7	±2.3	--	--	33.0	±2.0	8.3	±0.4
12	7.48±0.01	58.6	±1.4	--	--	25.9	±0.7	17.4	±0.1	64.2	±1.5	--	--	55.7	±1.6	15.6	±0.1
24	7.64±0.00	84.9	±1.3	--	--	36.5	±0.2	27.9	±4.2	92.9	±1.4	--	--	80.3	±0.6	25.0	±3.7
72	7.64±0.01	132.7	±8.7	--	--	57.0	±3.3	44.0	±5.0	145.3	±9.5	--	--	128.1	±7.6	39.4	±4.5
168	7.58±0.01	162.1	±2.6	--	--	70.9	±0.9	52.6	±3.0	177.5	±2.8	--	--	160.3	±2.1	47.1	±2.7
336	7.64±0.01	206.7	±0.6	--	--	87.9	±0.8	61.1	±0.0	226.4	±0.6	--	--	200.1	±1.8	54.8	±0.0
672	7.75±0.02	205.3	±1.6	--	--	90.7	±0.8	60.9	±1.3	224.8	±1.8	--	--	207.9	±1.9	54.6	±1.1
MB2-P1 – Tris-HCl		Concentration, ppm								Normalized Loss, g/m²							
Time (h)	pH	Na	Na-error	P	P-error	B	B-error	Si	Si-error	Na	Na-error	P	P-error	B	B-error	Si	Si-error
1	7.43±0.02	5.2	±0.2	<0.5	--	4.2	±0.1	1.4	±0.1	5.9	±0.2	--	--	5.3	±0.1	1.3	±0.1
6	7.49±0.00	44.4	±1.4	1.8	±0.0	19.2	±0.3	11.1	±0.5	49.7	±1.5	36.2	±0.4	40.9	±0.8	10.2	±0.5
12	7.48±0.01	58.1	±2.0	2.4	±0.1	24.7	±0.6	13.8	±0.4	65.1	±2.2	49.0	±1.7	54.1	±1.5	12.7	±0.4
24	7.58±0.01	94.0	±1.9	4.3	±0.0	40.6	±0.1	25.8	±0.4	105.3	±2.2	88.5	±0.4	91.9	±0.3	23.6	±0.4
72	7.64±0.01	161.2	±8.7	7.7	±0.3	67.1	±4.1	46.2	±5.2	180.6	±9.7	159.4	±7.1	155.1	±9.7	42.4	±4.7
168	7.54±0.02	196.1	±2.9	9.7	±0.0	82.1	±0.6	55.4	±0.9	219.7	±3.2	198.7	±0.3	190.9	±1.5	50.8	±0.8
336	7.64±0.01	232.2	±4.3	11.3	±0.4	97.0	±1.8	61.6	±0.3	260.1	±4.8	232.6	±8.0	226.2	±4.2	56.5	±0.3
672	7.74±0.01	221.9	±0.7	12.0	±0.1	97.7	±0.0	61.9	±0.5	248.5	±0.8	247.8	±1.1	224.1	±0.0	56.7	±0.5

MB2-P3 – Tris-HCl		Concentration, ppm								Normalized Loss, g/m²							
Time (h)	pH	Na	Na-error	P	P-error	B	B-error	Si	Si-error	Na	Na-error	P	P-error	B	B-error	Si	Si-error
1	7.42±0.00	1.7	±0.1	<0.5	--	2.8	±0.1	0.7	±0.1	2.0	±0.2	--	--	1.9	±0.2	0.7	±0.1
6	7.46±0.02	27.3	±0.7	3.9	±0.1	12.8	±0.2	8.8	±0.1	31.9	±0.9	27.6	±0.7	27.0	±0.5	8.5	±0.1
12	7.46±0.01	46.5	±2.4	6.8	±0.4	20.3	±1.0	14.9	±0.2	54.5	±2.8	48.0	±2.9	45.6	±2.5	14.2	±0.1
24	7.61±0.01	74.0	±10	10.9	±1.8	31.3	±4.2	20.1	±2.7	86.7	±11.7	76.8	±12.4	72.9	±10.5	19.2	±2.6
72	7.57±0.02	152.5	±9.7	23.9	±2.1	64.8	±5.0	40.7	±5.9	178.6	±11.4	167.7	±14.6	156.5	±12.5	39.1	±5.6
168	7.48±0.03	208.8	±1.5	32.6	±0.6	86.7	±0.7	54.3	±2.6	244.6	±1.7	229.3	±4.0	211.1	±1.8	52.1	±2.4
336	7.61±0.03	228.6	±2.6	35.1	±0.9	94.9	±0.6	62.0	±0.5	267.8	±3.0	246.4	±6.3	231.4	±1.5	59.4	±0.5
672	7.70±0.01	210.1	±1.7	36.3	±0.6	93.5	±0.7	62.0	±0.4	246.1	±1.9	255.0	±4.2	214.4	±1.6	59.4	±0.4
MB2-P5 – Tris-HCl		Concentration, ppm								Normalized Loss, g/m²							
Time (h)	pH	Na	Na-error	P	P-error	B	B-error	Si	Si-error	Na	Na-error	P	P-error	B	B-error	Si	Si-error
1	7.42±0.00	<0.5	--	<0.5	--	2.1	±0.0	0.3	±0.0	--	--	--	--	0.2	±0.0	0.3	±0.0
6	7.47±0.01	16.3	±0.6	4.2	±0.0	8.5	±0.2	6.2	±0.8	19.9	±0.8	18.1	±0.2	16.9	±0.6	6.3	±0.8
12	7.46±0.01	27.1	±6.3	7.0	±1.7	12.6	±2.6	8.4	±3.3	33.3	±7.7	30.2	±7.2	27.7	±6.7	8.4	±3.3
24	7.66±0.02	53.1	±0.4	14.2	±0.0	24.2	±0.1	17.7	±0.1	65.0	±0.5	61.1	±0.1	57.7	±0.2	17.8	±0.1
72	7.55±0.02	130.3	±5.5	34.9	±1.1	56.3	±1.8	38.6	±3.2	159.6	±6.8	150.6	±4.9	141.6	±4.7	38.7	±3.2
168	7.37±0.02	183.9	±1.4	47.9	±0.6	78.2	±0.5	51.8	±0.3	225.3	±1.8	206.7	±2.6	198.4	±1.3	51.9	±0.3
336	7.57±0.04	215.5	±2.4	56.3	±0.0	91.4	±1.2	61.0	±1.1	264.1	±3.0	243.0	±0.2	233.0	±3.0	61.2	±1.1
672	7.66±0.01	199.8	±3.7	57.4	±0.7	90.8	±1.9	64.5	±0.9	244.7	±4.6	247.9	±3.1	208.0	±4.3	64.7	±0.9
MB0 – Tris-HNO_3		Concentration, ppm								Normalized Loss, g/m²							
Time (h)	pH	Na	Na-error	P	P-error	B	B-error	Si	Si-error	Na	Na-error	P	P-error	B	B-error	Si	Si-error
1	7.40±0.01	4.7	±0.3	--	--	2.9	±0.1	1.3	±0.1	5.2	±0.3	--	--	5.9	±0.2	1.2	±0.1
6	7.49±0.01	42.2	±1.8	--	--	17.9	±0.9	11.6	±0.5	46.2	±2.0	--	--	40.7	±2.2	10.4	±0.4
12	7.41±0.01	68.1	±4.4	--	--	30.1	±2.2	18.7	±2.6	74.5	±4.8	--	--	69.2	±5.0	16.7	±2.4
24	7.65±0.01	91.2	±4.0	--	--	39.5	±2.1	27.6	±1.4	99.9	±4.4	--	--	91.2	±5.0	24.7	±1.3
72	7.59±0.01	138.0	±4.9	--	--	60.2	±2.3	40.9	±2.4	151.1	±5.4	--	--	139.3	±5.2	36.7	±2.1
168	7.64±0.03	165.1	±2.1	--	--	72.4	±1.2	57.1	±0.9	180.8	±2.3	--	--	167.7	±2.8	51.2	±0.8
336	7.63±0.01	195.1	±1.1	--	--	85.0	±0.3	59.3	±0.4	213.7	±1.2	--	--	197.0	±0.7	53.1	±0.3
672	7.68±0.01	207.3	±1.7	--	--	93.5	±1.0	60.4	±0.4	227.0	±1.8	--	--	214.3	±2.4	54.1	±0.4

MB2-P1 – Tris-HNO_3		Concentration, ppm								Normalized Loss, g/m^2							
Time (h)	pH	Na	Na-error	P	P-error	B	B-error	Si	Si-error	Na	Na-error	P	P-error	B	B-error	Si	Si-error
1	7.41±0.00	5.3	±0.3	<0.5	--	3.0	±0.1	1.3	±0.0	5.9	±0.3	--	--	6.3	±0.3	1.2	±0.0
6	7.48±0.01	46.9	±1.2	1.9	±0.2	19.5	±0.6	11.4	±0.7	52.5	±1.3	38.6	±3.1	45.5	±1.5	10.5	±0.6
12	7.40±0.01	74.4	±1.2	3.2	±0.2	31.5	±0.6	17.4	±0.4	83.4	±1.4	66.6	±4.4	74.0	±1.5	16.0	±0.4
24	7.51±0.03	100.1	±7.9	4.7	±0.6	43.2	±5.2	25.3	±3.9	112.1	±8.9	97.4	±12.3	101.9	±12.3	23.2	±3.6
72	7.63±0.01	158.9	±3.2	7.6	±0.3	68.0	±1.2	38.1	±2.7	178.0	±3.6	155.8	±6.2	161.0	±2.9	34.9	±2.5
168	7.47±0.04	196.8	±3.9	10.4	±0.1	85.6	±1.9	61.3	±2.5	220.5	±4.4	214.4	±2.3	202.9	±4.5	56.2	±2.3
336	7.61±0.03	221.6	±0.8	11.2	±0.0	94.5	±0.9	59.4	±0.3	248.2	±0.9	229.8	±0.2	224.2	±2.2	54.5	±0.3
672	7.67±0.01	224.2	±0.1	11.8	±0.0	99.6	±0.2	61.5	±0.0	251.2	±0.1	243.1	±0.3	228.6	±0.5	56.4	±0.0
MB2-P3 – Tris-HNO_3		Concentration, ppm								Normalized Loss, g/m^2							
Time (h)	pH	Na	Na-error	P	P-error	B	B-error	Si	Si-error	Na	Na-error	P	P-error	B	B-error	Si	Si-error
1	7.40±0.01	2.6	±0.1	<0.5	--	2.1	±0.0	1.0	±0.1	3.0	±0.1	--	--	4.1	±0.1	1.0	±0.1
6	7.47±0.00	35.2	±1.7	5.3	±0.4	15.5	±0.6	12.0	±0.9	41.3	±2.0	37.0	±3.0	37.7	±1.4	11.5	±0.9
12	7.40±0.00	64.2	±1.0	9.4	±0.1	28.1	±0.5	19.0	±0.7	75.2	±1.1	65.8	±0.6	68.9	±1.2	18.2	±0.7
24	7.56±0.00	93.0	±2.4	14.3	±0.8	41.0	±0.7	26.4	±1.5	109.0	±2.8	100.4	±5.7	101.1	±1.6	25.3	±1.4
72	7.70±0.01	143.5	±1.7	24.1	±0.3	66.1	±1.0	38.6	±1.9	168.1	±2.0	169.5	±1.8	150.5	±2.4	37.1	±1.9
168	7.65±0.02	207.1	±4.5	33.8	±0.7	89.3	±2.0	62.1	±0.8	242.6	±5.2	237.5	±4.6	221.4	±4.9	59.6	±0.8
336	7.55±0.02	225.8	±5.9	36.0	±0.3	97.6	±1.1	62.5	±1.3	264.5	±6.9	253.0	±1.9	242.2	±2.6	60.0	±1.3
672	7.62±0.01	211.0	±2.1	35.3	±0.5	94.3	±0.9	61.2	±0.1	247.1	±2.5	248.2	±3.6	216.3	±2.0	58.6	±0.0
MB2-P5 – Tris-HNO_3		Concentration, ppm								Normalized Loss, g/m^2							
Time (h)	pH	Na	Na-error	P	P-error	B	B-error	Si	Si-error	Na	Na-error	P	P-error	B	B-error	Si	Si-error
1	7.41±0.01	<0.5	--	<0.5	--	1.2	±0.1	0.4	±0.0	--	--	--	--	2.2	±0.2	0.4	±0.0
6	7.46±0.00	22.8	±0.5	5.7	±0.1	10.6	±0.1	8.9	±0.5	27.9	±0.6	24.7	±0.3	26.7	±0.3	8.9	±0.5
12	7.38±0.01	43.1	±0.1	11.3	±0.1	19.9	±0.1	15.5	±0.8	52.9	±0.2	48.6	±0.4	50.8	±0.2	15.6	±0.8
24	7.50±0.01	66.8	±5.9	17.7	±1.7	30.5	±2.3	24.9	±2.6	81.8	±7.3	76.5	±7.5	78.3	±6.0	25.0	±2.6
72	7.67±0.00	135.7	±5.5	35.0	±1.5	60.3	±2.1	39.7	±4.0	166.3	±6.7	151.3	±6.7	156.2	±5.4	39.8	±4.0
168	7.60±0.01	179.1	±3.7	50.4	±1.2	79.3	±1.8	60.3	±0.1	219.4	±4.5	217.8	±5.0	205.5	±4.6	60.5	±0.1
336	7.54±0.01	216.5	±0.1	57.7	±0.0	94.1	±0.1	61.0	±2.1	265.3	±0.2	249.4	±0.0	244.0	±0.3	61.2	±2.2
672	7.58±0.01	199.1	±3.4	55.5	±0.6	90.9	±1.5	62.8	±0.4	244.0	±4.2	239.7	±2.4	208.2	±3.5	63.0	±0.4

PA0 – Tris-HNO_3		Concentration, ppm								Normalized Loss, g/m^2							
Time (h)	pH	Na	Na-error	P	P-error	B	B-error	Si	Si-error	Na	Na-error	P	P-error	B	B-error	Si	Si-error
1	7.37±0.00	1.2	±0.2	--	--	1.4	±0.1	0.4	±0.1	1.3	±0.2	--	--	2.9	±0.4	0.4	±0.1
6	7.48±0.00	24.0	±1.4	--	--	9.7	±0.3	8.5	±1.0	26.1	±1.6	--	--	26.9	±0.9	6.9	±0.8
12	7.39±0.01	41.3	±3.5	--	--	16.1	±0.7	14.5	±2.4	44.8	±3.8	--	--	45.5	±2.0	11.8	±2.0
24	7.50±0.00	56.1	±2.9	--	--	22.0	±0.5	17.9	±2.1	61.0	±3.2	--	--	62.5	±1.5	14.4	±1.7
72	7.69±0.00	112.7	±0.3	--	--	42.1	±0.3	35.4	±0.5	122.5	±0.4	--	--	120.6	±0.7	28.7	±0.4
168	7.51±0.01	155.6	±5.5	--	--	57.3	±2.1	50.5	±2.8	169.1	±5.9	--	--	164.3	±6.0	40.8	±2.3
336	7.69±0.03	198.0	±8.2	--	--	70.5	±2.6	58.7	±2.5	215.2	±9.0	--	--	202.5	±7.4	47.5	±2.1
672	7.69±0.01	215.8	±0.6	--	--	79.0	±0.2	59.2	±0.4	234.5	±0.7	--	--	224.2	±0.5	47.9	±0.3
PA2-P1 – Tris-HNO_3		Concentration, ppm								Normalized Loss, g/m^2							
Time (h)	pH	Na	Na-error	P	P-error	B	B-error	Si	Si-error	Na	Na-error	P	P-error	B	B-error	Si	Si-error
1	7.47±0.02	0.9	±0.2	<0.5	--	1.2	±0.1	0.4	±0.1	1.0	±0.3	--	--	2.3	±0.2	0.4	±0.1
6	7.48±0.01	17.4	±2	<0.5	--	7.3	±0.8	7.0	±0.8	19.4	±2.2	--	--	20.5	±2.4	5.8	±0.7
12	7.40±0.01	37.4	±1.1	1.5	±0.0	14.5	±0.5	15.9	±0.5	41.6	±1.2	30.5	±0.1	41.8	±1.5	13.2	±0.4
24	7.47±0.01	56.2	±2.8	2.4	±0.2	21.8	±2.2	23.2	±3.9	62.4	±3.1	48.7	±5.0	63.3	±6.6	19.2	±3.2
72	7.68±0.02	108.4	±5	5.1	±0.3	41.3	±2.4	41.4	±3.5	120.6	±5.5	103.7	±7.0	120.8	±7.0	34.3	±2.9
168	7.57±0.03	154.3	±5.4	7.6	±0.1	55.7	±1.9	52.1	±3.1	171.5	±6.0	155.8	±1.8	163.4	±5.5	43.1	±2.6
336	7.66±0.01	205.9	±4.3	10.4	±0.1	73.3	±0.8	60.6	±0.6	228.9	±4.7	212.1	±2.2	215.5	±2.4	50.1	±0.5
672	7.68±0.02	211.6	±1.9	11.5	±0.0	78.1	±0.8	60.4	±1.6	235.3	±2.1	234.3	±0.5	221.5	±2.3	50.0	±1.3
PA2-P3 – Tris-HNO_3		Concentration, ppm								Normalized Loss, g/m^2							
Time (h)	pH	Na	Na-error	P	P-error	B	B-error	Si	Si-error	Na	Na-error	P	P-error	B	B-error	Si	Si-error
1	7.47±0.01	<0.5	--	<0.5	--	0.6	±0.0	<0.2	--	--	--	--	--	0.7	±0.1	--	--
6	7.46±0.01	10.5	±3.2	1.4	±0.5	4.9	±1.0	5.6	±2.1	12.2	±3.7	9.8	±3.4	14.1	±3.0	4.9	±1.8
12	7.39±0.01	23.6	±0.2	3.5	±0.0	9.7	±0.2	11.1	±0.4	27.4	±0.2	24.3	±0.2	28.8	±0.6	9.6	±0.3
24	7.53±0.00	36.7	±3.4	5.7	±0.4	14.9	±0.9	19.1	±0.8	42.7	±3.9	39.8	±2.9	44.8	±2.9	16.5	±0.7
72	7.68±0.02	90.8	±1.1	13.8	±0.2	33.3	±0.3	38.7	±3.8	105.6	±1.3	96.3	±1.2	101.7	±0.9	33.5	±3.3
168	7.54±0.01	145.9	±2.2	23.5	±0.9	53.0	±1.3	54.3	±2.2	169.7	±2.5	163.7	±6.2	162.6	±4.1	47.0	±1.9
336	7.65±0.01	207.1	±0.9	33.1	±0.1	72.0	±0.3	63.2	±0.3	240.9	±1.0	231.0	±0.7	221.5	±0.8	54.7	±0.3
672	7.64±0.01	214.7	±1.2	37.2	±1.5	79.6	±0.6	64.6	±0.2	249.7	±1.3	259.6	±10.6	225.7	±1.6	55.9	±0.2

To quantify the glass dissolution kinetics and provide an estimate of the forward rate, the linear portion of the NL data were fit using linear regression (within the first 12 hours of experiments). The extracted rates are displayed in Table 5.4. The error expressed in the table represents standard uncertainty in linear regression, where the standard deviation of each NL data point was considered, and the relative impact of fitting a slope to uncertain data was summed to determine the overall fitted-slope uncertainty, similar to the method discussed by Kragten.[32] In general, it is observed that dissolution rate is highly dependent upon the *R* regime, where dissolution rate is inversely proportional to *R* and increases in the order PA < MB < PB. Figure 5.2a displays a representative picture of the Na and B dissolution rates in each regime as a function of P_2O_5 content in the glass, in which the Na, P and B release rates show very good agreements and are between 2-4 $gm^{-2}h^{-1}$ for PA glasses, between 4-7 $gm^{-2}h^{-1}$ for MB glasses, and are between 9-11 $gm^{-2}h^{-1}$ for PB glasses in Tris-HNO_3 solutions. Si is consistently released at rates between 1-2 $gm^{-2}h^{-1}$, representing between 50-80 % reduction in Si rate as compared to all other species. Upon the addition of P_2O_5 into glasses, degradation rates were impacted differently based upon the *R* regime. For instance, PB glasses did not show any clear change in dissolution rates regardless of P_2O_5 content, meanwhile, MB and PA degradation rates: (i) maintained similar or slightly increased upon addition of 1 mol. % P_2O_5 and (ii) decrease steadily in glasses beyond $x = 1$. Although not shown in Figure 5.2a, please note that P rates observe the same trends as Na and B, while Si does not undergo significant rate changes upon additions of P_2O_5, independent of *R* regime. In the upcoming sections, these changes in the dissolution rate will be explained from a glass structural standpoint, as several competing factors can greatly impact dissolution kinetics and behavior.

Table 5.4. *Degradation rates of Na, P, B, and Si for the studied glasses in simulated body environments. These rates were determined by linearly fitting the first 12 hours of normalized loss vs. time plots.*

		Degradation Rates (g/[m^{2}h])							
Sample ID	**Solution**	**Na**	**Na-error**	**P**	**P-error**	**B**	**B-error**	**Si**	**Si-error**
PB0	Tris-HNO_3	10.2	±1.1	--	--	9.0	±1.2	1.9	±0.2
PB2-P1		10.9	±1.3	10.3	±1	9.6	±0.8	1.8	±0.3
PB2-P3		10.8	±0.3	10.0	±0.6	9.7	±0.3	2.0	±0.1
PB2-P5		10.9	±1.5	10.2	±1.7	9.8	±1.4	1.9	±0.5
MB0	Tris-HCl	5.3	±0.1	--	--	4.6	±0.1	1.3	±0.0
MB2-P1		5.3	±0.2	4.4	±0.2	4.4	±0.1	1.0	±0.0
MB2-P3		4.7	±0.3	4.3	±0.3	3.9	±0.2	1.2	±0.0
MB2-P5		3.0	±0.7	2.7	±0.7	2.5	±0.6	0.7	±0.3
MB0	Tris-HNO_3	6.3	±0.5	--	--	5.7	±0.5	1.4	±0.2
MB2-P1		7.0	±0.1	6.0	±0.4	6.1	±0.1	1.3	±0.0
MB2-P3		6.5	±0.1	5.9	±0.1	5.9	±0.1	1.5	±0.1
MB2-P5		4.7	±0.0	4.4	±0.0	4.4	±0.0	1.4	±0.1
PA0	Tris-HNO_3	3.9	±0.4	--	--	3.8	±0.2	1.0	±0.2
PA2-P1		3.7	±0.1	2.8	±0.0	3.6	±0.1	1.2	±0.0
PA2-P3		2.5	±0.0	2.2	±0.0	2.6	±0.1	0.9	±0.0

Figure 5.2b displays a comparison between Na, B, and Si rates extracted from MB glasses in Tris-HCl vs. Tris-HNO_3 based solutions with each of the other experimental parameters carefully controlled (i.e. temperature, pH, SA/V, etc.). Interestingly, it is observed that degradation rates are higher in Tris-HNO_3 solutions as compared to Tris-HCl solutions, which is contrary to that found in Tournié et al.[29] While these kinetic changes are statistically significant based upon the current error analysis, it is uncertain if Tris-HCl vs. Tris-HNO_3 rate differences are significantly different, given the 15-25 % errors typically associated with performing dissolution experiments[33-35] and the well-described challenges in literature with fitting NL data with a single rate.[36, 37] Accordingly, many—but not all—of the rate differences reported for Tris-HCl vs. Tris-HNO_3 in the current compositions are within the typically attributed errors in dissolution experiments;

furthermore, a close agreement is observed for NL values within the residual rate regime. Thus, further exploration is necessary to confirm whether kinetic differences result from the changes in acid identity used simulation body environments.

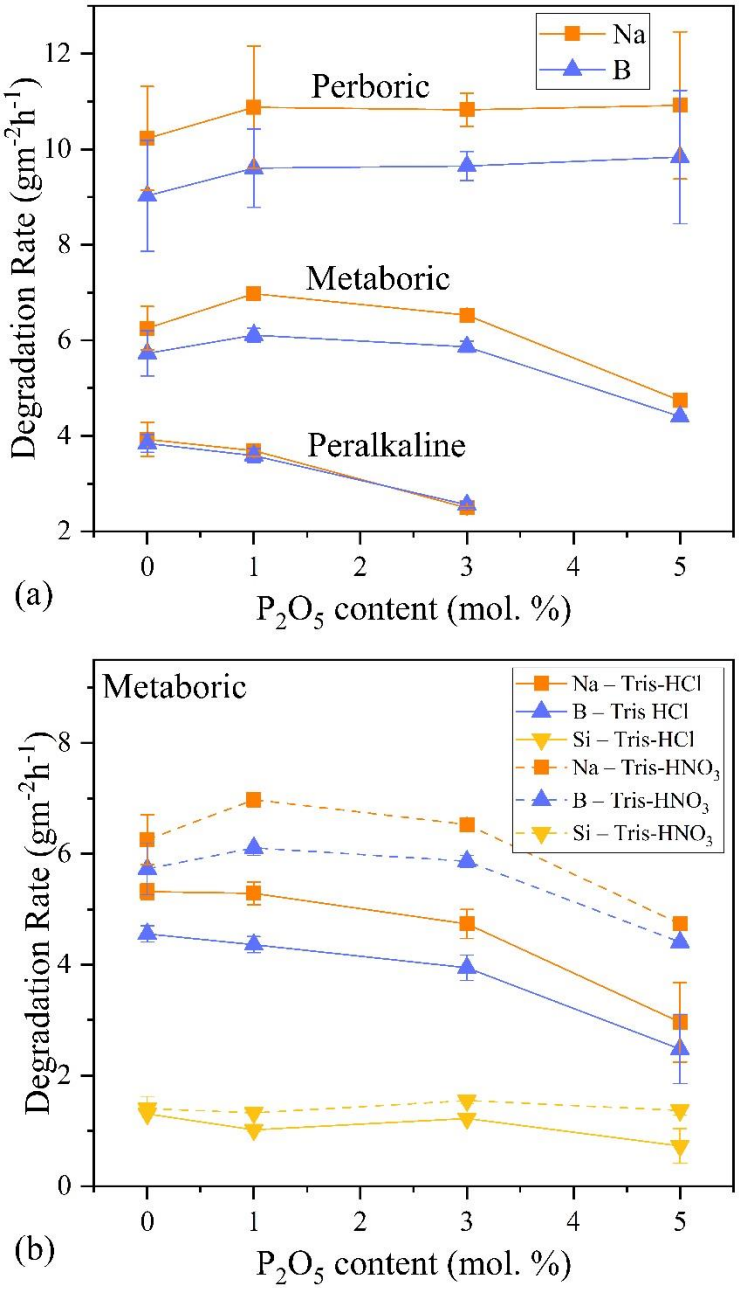

Figure 5.2. *Degradation rates as a function of P_2O_5 content for (a) Na and B in Tris-HNO_3 and (b) for Na, B and Si for MB glasses in Tris-HCl and Tris-HNO_3.*

5.3.3 Structural evolution of the glass and surface layers during dissolution processes

The initial glass structures (pre-dissolution) have been extensively studied in Chapter 4 for their short- and intermediate-range order characteristics. The structural species discussed are labeled in terms of T^n (T = Si, B, P), where *n* denotes the numbers of bridging oxygen atoms to other T species. It was observed for these glasses that adding P_2O_5 into the glass ($x = 1$) promotes the presence of isolated phosphate species (P^0 and P^1; P^n, where *n* indicates the number of bridging oxygen connected to each species). Glasses containing $x > 1$, on the other hand, undergo increases in P-O-B intermixing (as P^2 or P^3 species, linked to P and B^4 species) and promote re-distribution of Na^+ species accompanied by re-polymerization of silicon species and decreases in B^4 fraction (tetrahedral boron). Furthermore, in the order PB >> MB >> PA, it was observed that Si^4 and B^4 fractions increase (as displayed in Table 5.1).

The glass powders recovered from dissolution experiments were first analyzed by XRD to examine for the presence of crystalline secondary phases. As shown in Figure S1, it is observed that all samples displayed amorphous nature, ruling out the significant presence of precipitated crystalline phases. Thus, to understand the evolving amorphous structure, advanced MAS NMR experiments were performed on the glasses to probe the evolving bulk and surface structural characteristics. Figure 5.3 displays the ^{11}B MAS NMR spectra of samples dissolved for 7 days in Tris-HNO_3 (as compared to the initial spectra) which are normalized based upon the upfield peak. These spectra display two main resonances: a broad feature centered near 14 ppm and a narrower peak in the region 0-3 ppm consisting of multiple underlying species. The feature near 14 ppm is associated with B^3 species, which consists of overlapping ring- and non-ring trigonal boron species,

however, this peak may also contain unresolved trigonal boron species containing 1 non-bridging oxygen. Comparing initial spectra to the 7-day dissolved samples, it is observed that the intensity of the B^3 peak decreases in all cases, in which the samples generally undergo larger changes in the order PA < MB < PB. For instance, the B^3 peak presence in the dissolved PB2-P3 and PB2-P5 glasses are not apparent, indicative of a near-zero presence of these species in the glass after degradation. Furthermore, the displayed spectra do not undergo any apparent shape change in the trigonal boron peaks upon dissolution, rather, a uniform intensity reduction. On the other hand, the peaks associated with B^4 undergo clear changes in shape, particularly evident in the PB glasses (Figure 5.3a). In sample PB0, the 7-day dissolved spectrum displays a clear shoulder centered near -1 ppm which was not evident in the initial spectrum. As the P_2O_5 content rises, this peak grows in intensity, marked by sharp peaks at -1 ppm. Additionally, the underlying broad peak reduces in intensity significantly in x = 3 and 5 glasses, explaining the resonance almost exclusively dominated by the sharp B^4 resonance in these samples. Dissolved MB glasses similarly display B^4 peak changes, as evidence of a shoulder near -1 ppm is also observed, however, these changes are not as evident as in PB glasses. Similar changes in dissolved PA spectra are not clearly apparent.

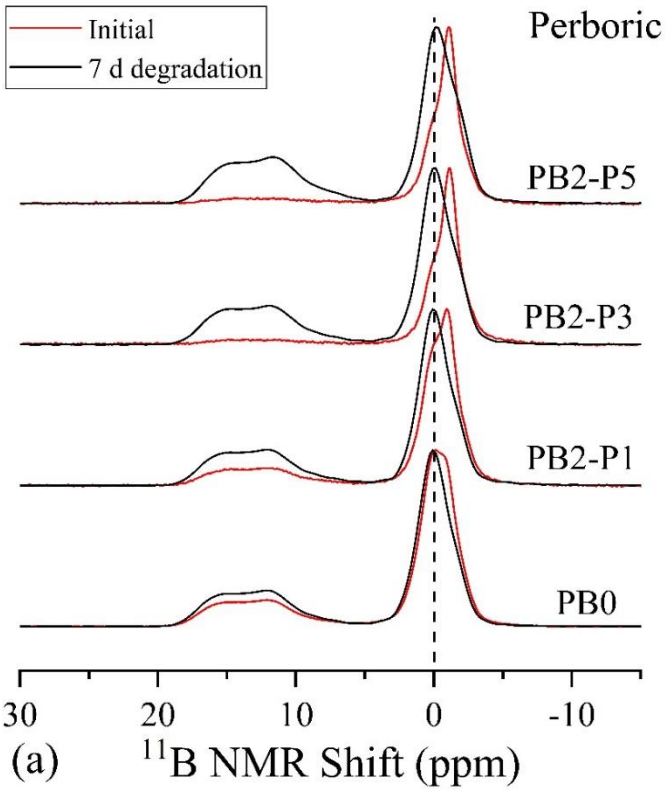
Initial
7 d degradation
Perboric
PB2-P5
PB2-P3
PB2-P1
PB0
30
20
10
0
-10
(a)
^{11}B NMR Shift (ppm)

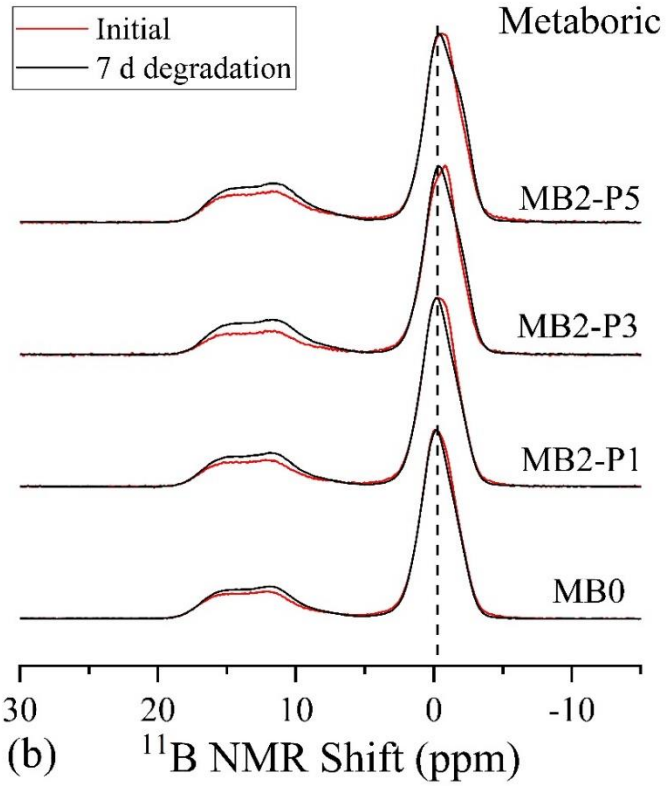
Initial
7 d degradation
Metaboric
MB2-P5
MB2-P3
MB2-P1
MB0
30
20
10
0
-10
(b)
^{11}B NMR Shift (ppm)

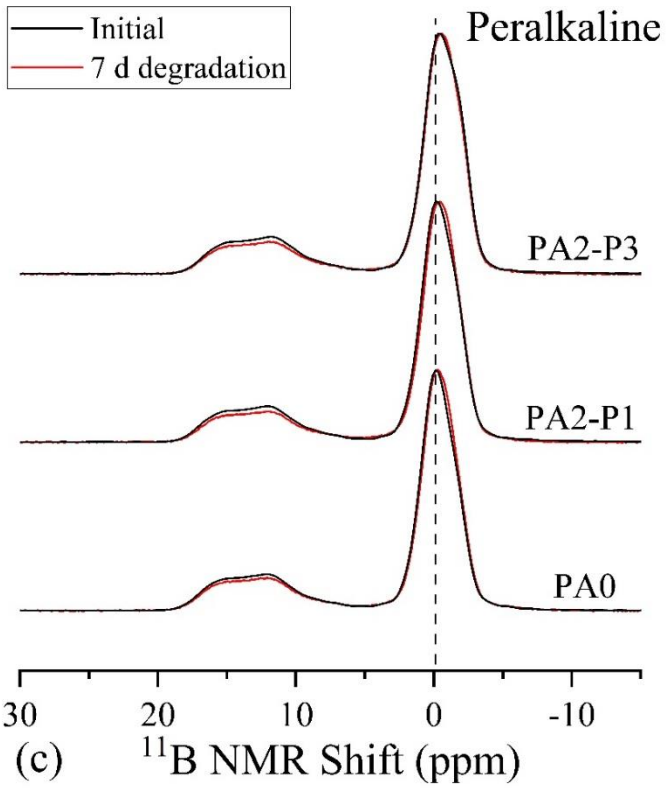

Figure 5.3. *^{11}B MAS NMR spectra of initial glasses vs. glass powders recovered from 7 days of degradation experiments in Tris-HNO_3 solutions.*

The results from ^{11}B MAS NMR (as discussed above) may be explained by one or more of the following standpoints: (i) the glasses undergo preferential dissolution of B^3 species as compared to B^4, (ii) B^3 and B^4 species dissolve at similar rates, with the exception of the B^4 species located at -1 ppm, and (iii) all B species dissolve at similar rates, where the remaining B^4 peak represents a precipitated boron secondary phase near the glass surface. Although precipitated borate species have been hypothesized in literature in highly alkaline solutions (pH > 10.5),[38-40] the formation of these species is unexpected in near-neutral environments, thus, we focus on (i) and (ii) to explain the degradation behavior of borate species in the current system. It is known from literature on sodium borosilicate glasses that species contained within the B^4 resonance with distinct chemical shifts differ in next-nearest neighbor species. For instance, in our system, it is expected that resonances associated with B^4-O-B^3, B^4-O-Si, and B^4-O-P all exist within the region -2 to 1 ppm. For instance, Du and Stebbins[41] attributed a peak near -2 ppm to B^4(0B,4Si), meanwhile greater amounts of boron neighbors led to a downfield shift. Furthermore, it can be inferred from Chapter 4 that a peak near -1 ppm is likely not associated with B^4-O-P linkages, thus, this species is presumably associated with B^4(4Si) species pinned within the silicate network. In an attempt to confirm this peak association, ^{11}B-^{29}Si REDOR experiments were performed on sample PB2-P5 (before and after 7 days of dissolution; data not shown), however, this data was inconclusive due to the low natural abundance of ^{29}Si.

In an attempt to probe the dissolution behavior of phosphate species both in the bulk of the glass and near the surface, ^{31}P MAS NMR and ^{1}H→^{31}P CP-MAS NMR were performed on selected dissolved samples. Comparisons between single resonance and CP-

MAS spectra are displayed in Figure 5.4a-c for PB2-P5, MB2-P5, and PA2-P3 samples degraded for 1 day, 3 days, and 7 days, respectively, as compared to initial glass spectra. These spectra display 3 main resonances centered near 15, 2, and -5 ppm, associated with P^0, P^1, and P-O-B^4 linked species (P^2 and P^3), respectively (discussed in Chapter 4). Following degradation experiments, there is a noticeable sharpening of the P^1 peak for all samples, indicating the possibility of a more highly ordered P^1 species developing upon glass dissolution. While directly quantitative information about speciation cannot be extracted from $^1H \rightarrow ^{31}P$ CP-MAS NMR experiments, the presence of peaks in the same location as the single resonance spectra indicate that each phosphate species displayed shows proximity to protons in the dissolved sample. In other words, the phosphate structure in the hydrated surface layers does not change much during glass dissolution and distinct phosphate species presumably do not undergo preferential extraction. In Figure 5.4d, the PB2-P5 sample which was dissolved for 1 day was examined using varied contact time between ^1H and ^{31}P nuclei, in an attempt to differentiate ^1H-^{31}P interactions in distinct phosphate species, since longer contact times probe larger internuclear distances in the glass. It is observed that the sharp P^1 peak grows in intensity upon stepwise increases in contact time from 300 to 1500 μs, indicating that hydrated P-O-B^4 species undergo greater ^1H-^{31}P heteronuclear dipolar interactions, due to either (i) closer proximity between P-O-B^4 linked species and protons or (ii) a greater amount of proton in the vicinity of P-O-B^4 linked species, as compared to P^1 species.

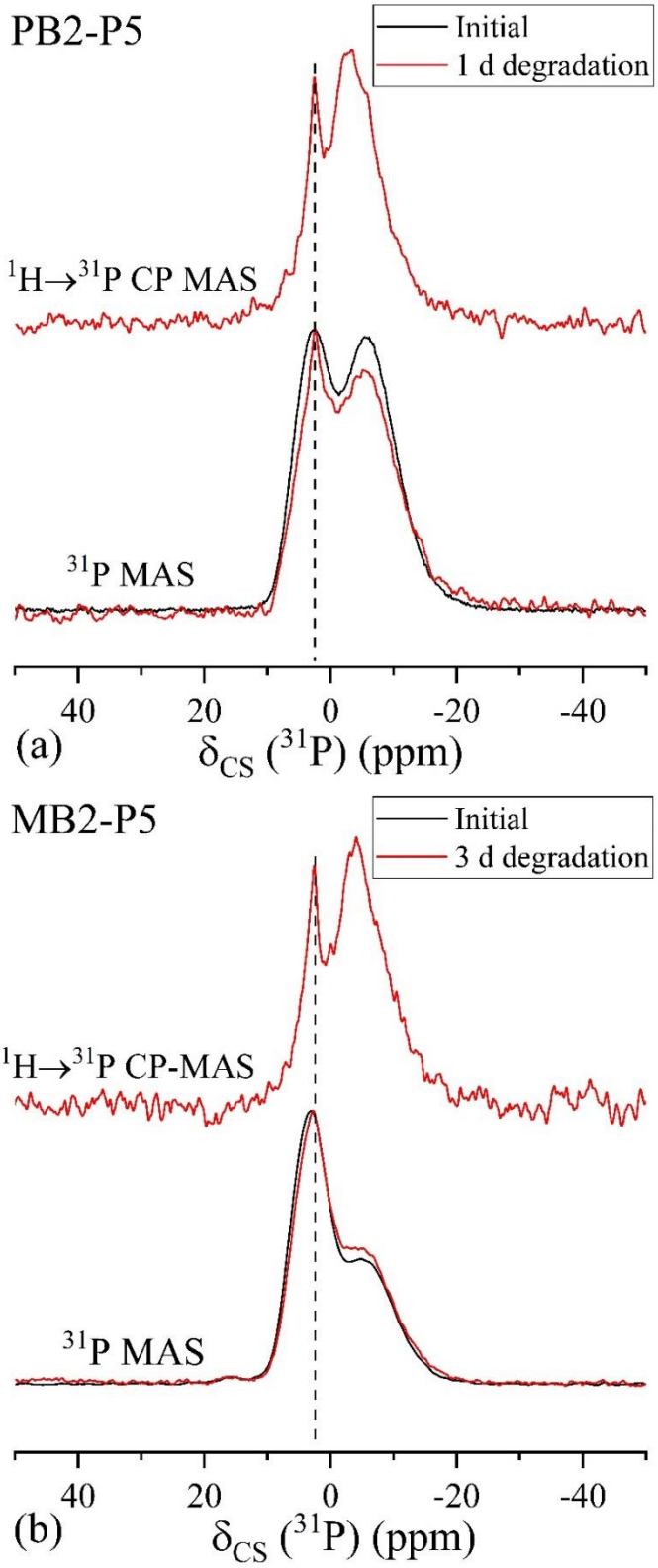
PB2-P5
Initial
1 d degradation
$^{1}H \rightarrow ^{31}P$ CP MAS
^{31}P MAS
40
20
0
-20
-40
(a)
δ_{CS} (^{31}P) (ppm)
MB2-P5
Initial
3 d degradation
$^{1}H \rightarrow ^{31}P$ CP-MAS
^{31}P MAS
40
20
0
-20
-40
(b)
δ_{CS} (^{31}P) (ppm)

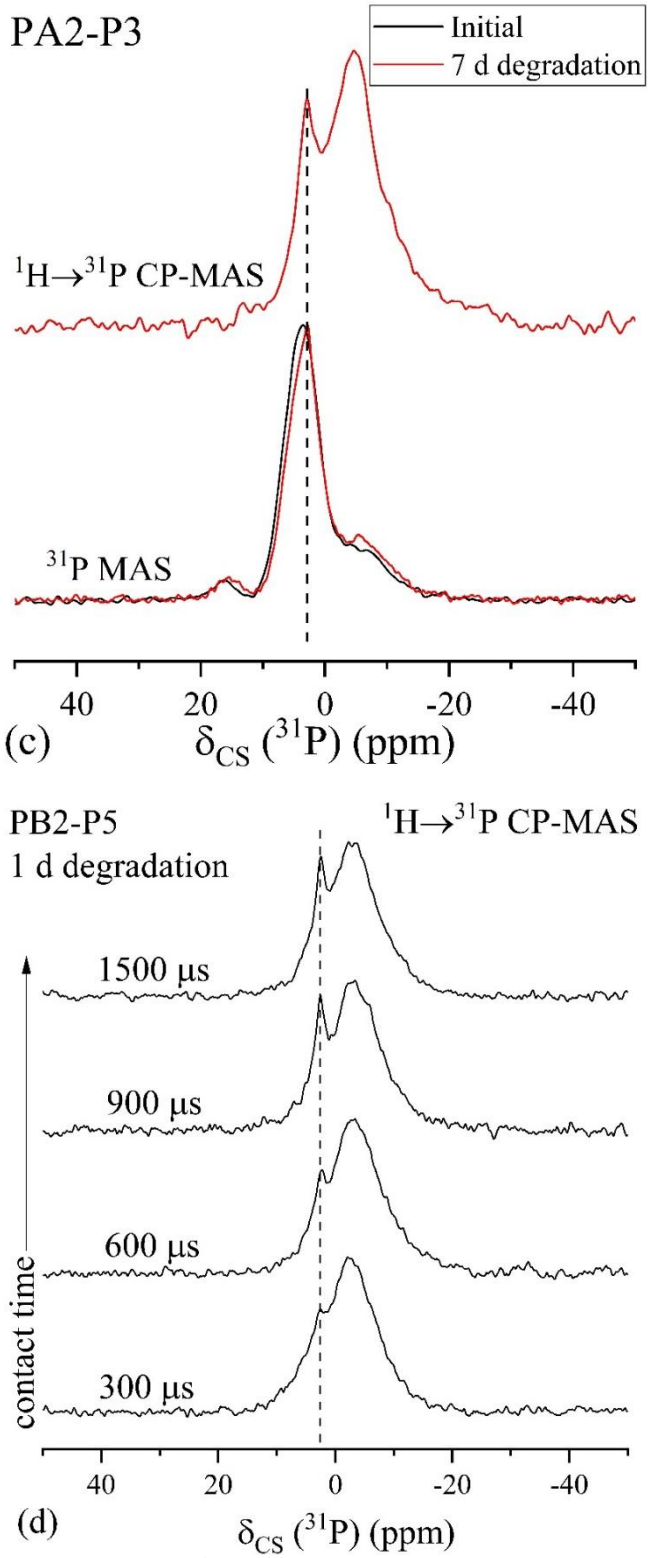

Figure 5.4. *^{31}P MAS NMR and $^{1}H \rightarrow ^{31}P$ MAS NMR spectra of dissolved glasses as compared to their initial ^{31}P MAS spectra, for the samples (a) PB2-P5, (b) MB2-P5, and (c) PA2-P3 dissolved for 1 day, 3 days, and 7 days, respectively, in Tris-HNO_3. (d) displays PB2-P5 1-day sample which was analyzed using varied $^{1}H \rightarrow ^{31}P$ contact times.*

To further explore the glass hydrated layers, $^{1}H \rightarrow ^{29}Si$ CP-MAS NMR experiments were performed on selected samples. The spectra for MB0, and MB2-P5, and PB2-P5 samples recovered from 14-day degradation experiments are shown in Figure 5.5. These samples, which were calculated to initially contain at least 66 % Si^4 with the remaining being Si^3 units, show three main resonances after degradation: -91 ppm (Si^2), -101 ppm (Si^3), and -111 ppm (Si^4). The former two species likely represent silicate species containing hydroxyl groups: Si^2-$(OH)_2$ and Si^3-OH, meanwhile the latter represents fully connected silicate species that undergo ^{1}H-^{29}Si heteronuclear dipolar interactions between more remote nuclei. An idea of the relative fraction of these species can be inferred from the single resonance ^{29}Si MAS NMR spectra of these samples (displayed in Figure S2), in which Si^4 resonances are the most prevalent, however, Si^3 resonances are also observed at smaller intensities (Si^2 species are also observed in the 14-day PB2-P5 sample). As expected, these results indicate that dissolution processes have depolymerized the silicate network, through either ion exchange with NBO sites or silica hydrolysis.

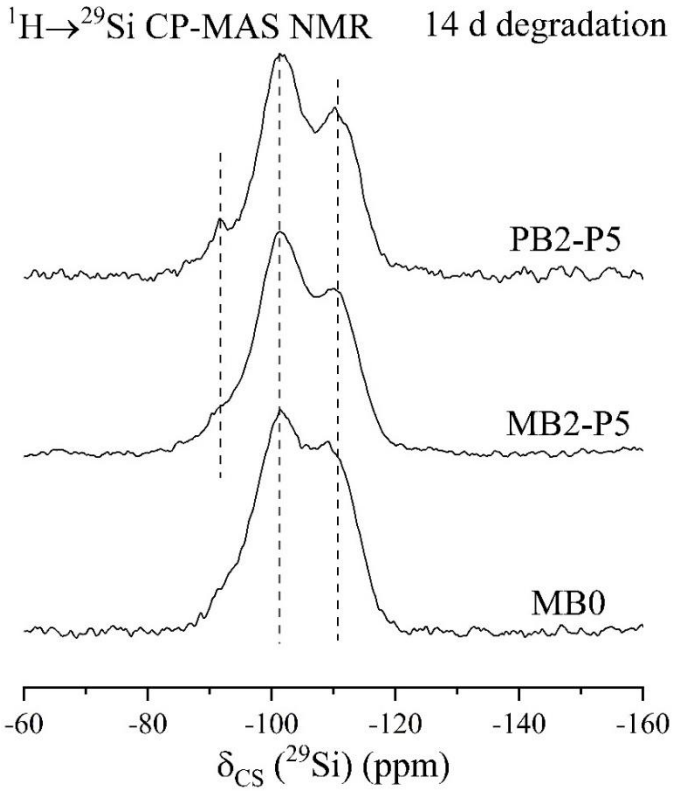

Figure 5.5. *$^{1}H \rightarrow ^{29}Si$ spectra of selected samples dissolved for 14 days in Tris-HNO_3 solutions.*

5.3.4 Glass surface evolution during degradation experiments

In addition to the degradation experiments performed on glass powders, two bulk glass coupons each for PB2-P5 and MB2-P5 glasses were studied for their degradation behavior in Tris-HNO_3 for 3-day and 7-day durations. Both polished (undissolved) and dissolved samples were analyzed for their surface characteristics using XPS and ERDA analyses, whereas the cross-section of the PB2-P5 sample recovered from 7 days of glass dissolution experiments was analyzed for its surface layer characteristics using scanning electron microscopy – energy dispersive spectroscopy (SEM-EDS).

Table 5.5 presents the top surface layer compositions (3-10 nm probe depth) of the analyzed compositions, as compared to the polished and dissolved coupons. The

comparison between the bulk composition and polished surface was generally within ±1 %, however, with slightly higher deviations of 2-4 % in the surface concentrations of B (depleted) and O (enriched). Upon glass degradation for 3 days, both glasses displayed a nearly complete dissolution of P and B from the top surface, coupled with a >85 % reduction in Na content. Likewise, 7-day samples were entirely depleted in P and B, while showing similar amounts of Na remaining in the surface layers. Thus, the remaining surface layers are primarily O and Si, with a stoichiometry ~3:1 (O:Si), which is a much higher stoichiometry than observed in pure SiO_2. This high stoichiometry indicates a significantly depolymerized silicate layer at the surface, since glasses with high non-bridging oxygen content, exhibit O:Si values which approach 3:1, i.e. water glass (Na_2SiO_3). Furthermore, to examine hydrogen content in the surface layers of these samples, ERDA spectra are displayed in Figure 5.6, where the calculated hydrogen contents are listed in Table 5.5. ERDA, which probes a significantly larger depth of the surface (~350 nm), displays that the H content is higher in the dissolved PB2-P5 sample (10.2 %) as compared to the MB2-P5 samples (6.5-6.8 %). The PB2-P5 3-day sample was unexamined using ERDA due to the complete removal of the brittle surface layer upon sample handling. The elevation in hydrogen content in the surface layers of PB2-P5 in comparison to MB2-P5 glass may be explained from a standpoint of elemental release since PB glasses exhibited higher dissolution kinetics / NL curves in comparison to MB glasses. Accordingly, it can be expected that protons and water molecules can diffuse more extensively into the glass surface in the PB2-P5 composition.

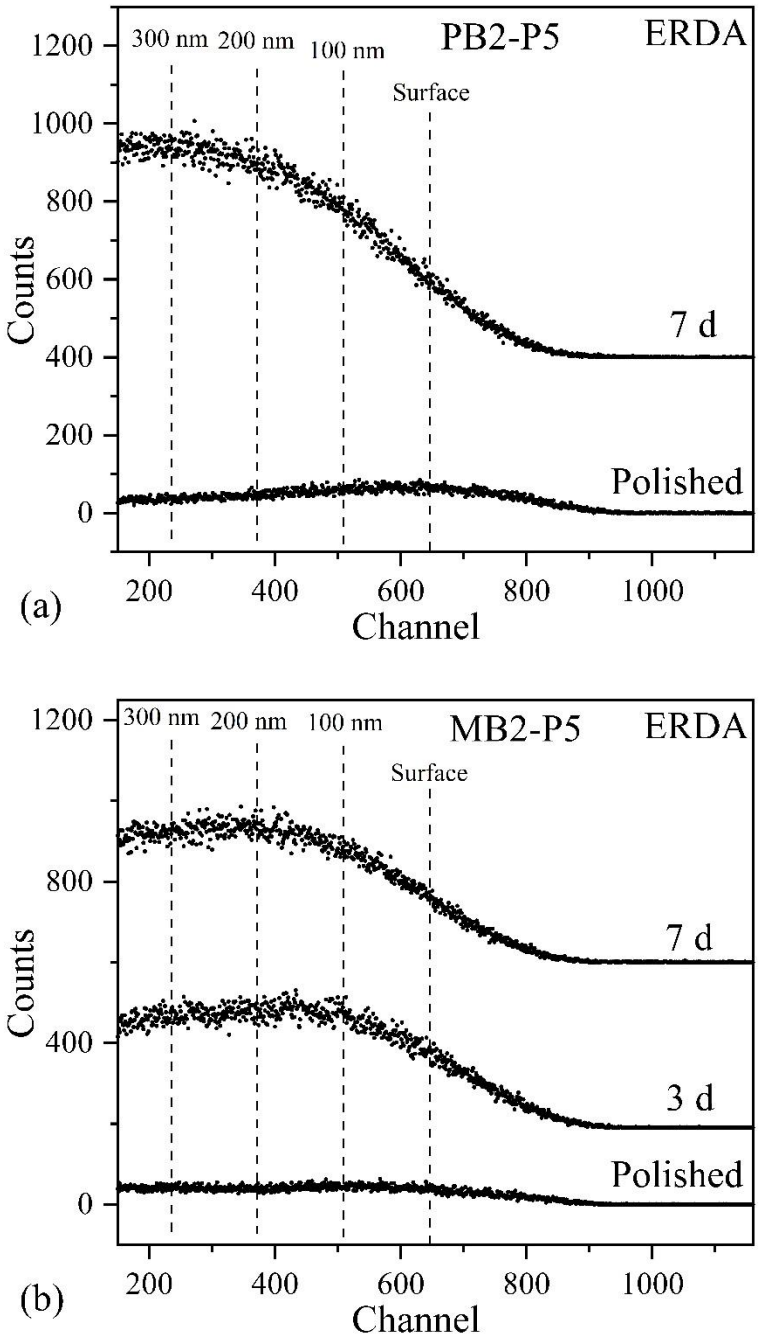

Figure 5.6. *ERDA spectra of (a) PB2-P5 and (b) MB2-P5 polished glass coupons and dissolved glasses for 3- and 7-day durations.*

Table 5.5. *Surface compositions of PB2-P5 and MB2-P5 samples as measured in the top 3–10 nm via XPS analysis (atomic percentages accurate within ±5%). In each sample, we have compared compositions of polished and corroded samples to the bulk compositions measured using ICP-OES. H concentrations were measured using ERDA analysis.*

Element (at. % by XPS)	**Sample**							
	PB2-P5				**MB2-P5**			
	Bulk	**Polished Surface**	**3 d**	**7 d**	**Bulk**	**Polished Surface**	**3 d**	**7 d**
Na	13.7	14.4	1.9	1.6	13.4	13.6	1.3	1.3
P	2.6	2.1	0.2	0.4	2.7	2.0	0.0	0.0
B	15.4	12.5	0.9	0.0	13.0	11.2	0.0	0.0
Si	10.6	9.5	22.1	22.6	12.6	11.5	23.7	23.3
O	57.7	61.5	74.9	75.3	58.2	61.6	74.9	75.5
H[*]	--	<0.1	n.d.[‡]	10.2	--	<0.1	6.5	6.8

[*]H concentration in the top ~350 nm as determined from ERDA (within ±5 %)
[‡]Not determined

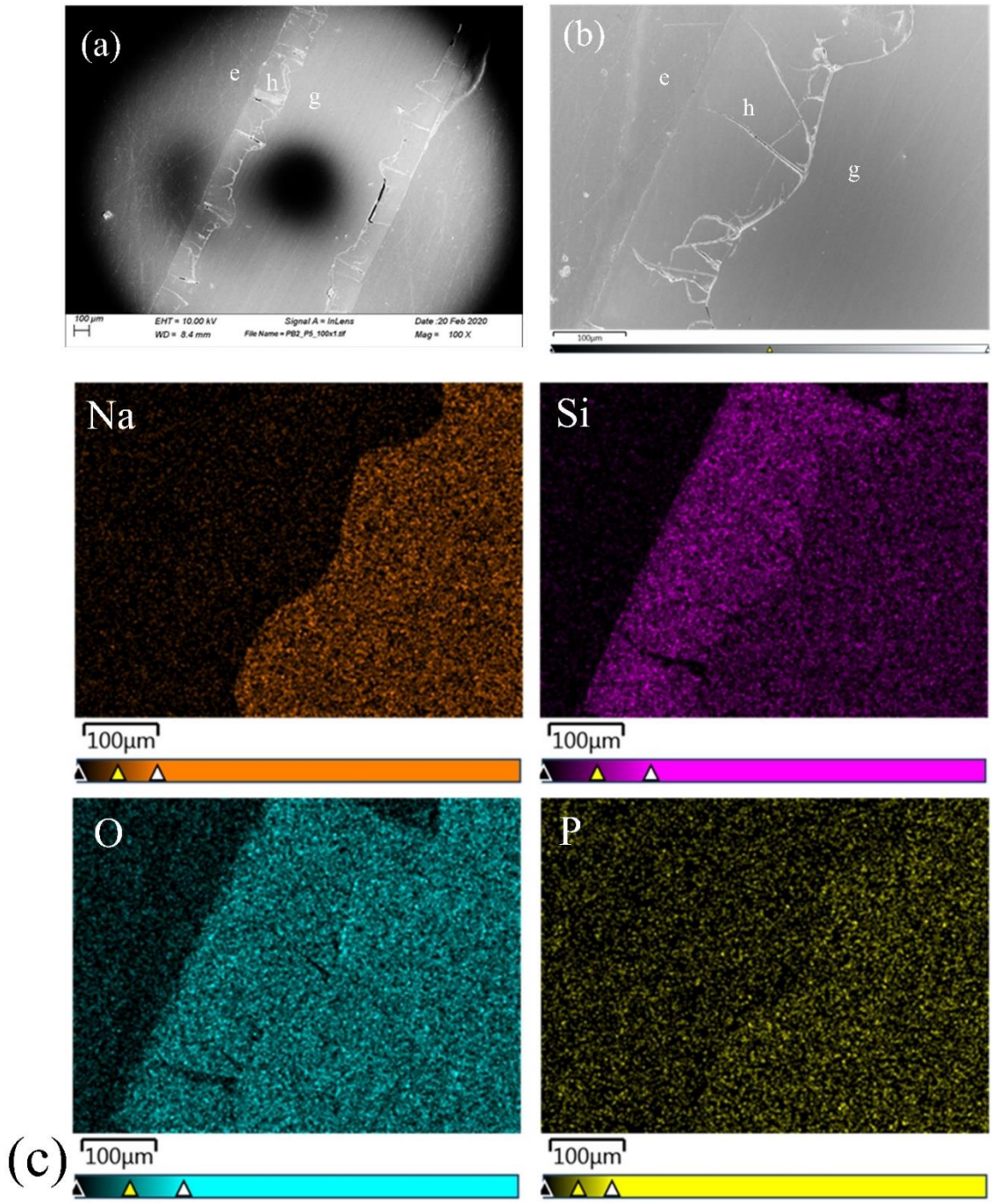

Figure 5.7. *SEM cross-sectional images of the PB2-P5 glass dissolved for 7 days at (a) 100x and (b) 500x magnification. (c) displays the EDS maps of the region depicted in the SEM image of (b).*

The cross-sectional SEM and EDS analysis of the PB2-P5 7-day composition dissolved for 7 days was performed to probe the entire depth of hydrated glass layers, to supplement the XPS and ERDA studies of the top surface layers. In this way, it is possible to understand the entire interface between the pristine glass and fluid, including the reactive interface alongside the established gel layers. Accordingly, Figure 5.7 displays SEM images and EDS maps the glass cross-section. Figures 5.7a and b contain three regions, labeled ‘g’ for pristine glass, ‘h’ for hydrated layer, and ‘e’ for epoxy resin. It is evident from these images that the full hydrated layer varies between 150 and 200 μm, thus, orders of magnitude greater than the probe depth of either XPS or ERDA. Additionally, this layer is observed to undergo thickness fluctuation and contains significant cracking behavior, where many of the propagated cracks are perpendicular to the interface between the pristine glass and the hydrated layer. The presence of cracking throughout this layer is consistent with our observations of apparent brittleness in the surface layers, which may indicate weak bonding to the pristine glass surface and/or weakly bound silicate species. To verify the composition of this layer, Figure 5.7c displays the EDS maps in this region, which confirms that although the pristine glass layers consist of Na, P, Si, and O, the hydrated layer exclusively contains Si and O (in the absence of Na and P), agreeing with the findings from XPS in the top 3-10 nm of the surface. It should be noted that although B content is not readily detectable in EDS maps due to its low K_α energy, the ^{11}B MAS NMR results previously discussed, indicate that certain B species are likely contained within the gel layer.

5.4 Discussion

Recent years have experienced a significant rise in the research interest of borosilicate-based bioactive glasses as potential novel third generation biomaterials, however, many of the studies performed have examined a limited composition-space, largely based on known silicate bioactive glass formulations such as 45S5 or 13-93. [1, 24, 25] However, this "trial-and-error" approach to designing borosilicate bioactive glasses does not allow for the design of glasses with a tailored ionic release for targeted biomedical applications. Accordingly, it was our aim in the present study to understand the compositional and structural drivers governing chemical degradation of borosilicate- and phospho-borosilicate glasses in simulated body environments over a wide composition-space. In this approach, glasses were designed in three sodium borosilicate (P_2O_5-free) systems, including perboric (Na/B < 1), metaboric (Na/B = 1), and peralkaline (Na/B > 1) regimes, substituting P_2O_5 into the glass using stepwise additions. Degradation behavior in these systems was carefully tracked in simulated body environments using advanced solution, bulk, and surface techniques to understand the dissolution kinetics and structural drivers controlling ionic release from the glass into solution.

In this approach, it is determined that ionic release rates and magnitudes are predominantly controlled by *R* (Na/B) and *K* (Si/B) ratios in the studied glass systems. Accordingly, the degradation rates are inversely proportional to *R* and *K* (as displayed in Figure 5.2a), in the order: PA (*R* = 1.25, *K* = 2.75) < MB (*R* = 1, *K* = 2) < PB (*R* = 0.83, *K* = 1.5). These kinetic differences in the baseline glasses (P_2O_5-free) can be explained by a change in the overall network structure since B species are known to undergo hydrolysis and release from the glass at significantly elevated rates in comparison to silicate units.[42]

Specifically, the overall rates of elemental release varied by at least 2× between the PA and PB extremes, thus, tuning the *R* and *K* compositional ratios allows for the design of glasses with controlled functional ion release within this region. As P_2O_5 is added into the glasses, its impact upon glass degradation differs depending on the compositional regime, requiring a greater understanding of changes occurring in the local and intermediate glass structure and their impacts upon degradation processes.

It is observed that degradation rates reduce by up to 20-35 % in MB and PA glasses as a result of 3-5 mol. % of P_2O_5 addition, whereas PB glass dissolution behavior is seemingly less affected by P_2O_5 content. Structurally, the addition of P_2O_5 into the glass was shown to cause increases in silica polymerization and decreases in B^4 fraction due to the re-distribution of Na^+ towards phosphate units. However, stepwise additions of P_2O_5 also resulted in increased P-O-B^4 intermixing at the expense of isolated phosphate units. In the studied systems, since *R* and *K* ratios are maintained while substituting P_2O_5, direct structural impacts on degradation behavior can be unearthed. Specifically, we have observed using ^{11}B MAS NMR experiments that B^3 species are being preferentially extracted in comparison to B^4 species, as deduced from the significant reductions in B^3 fraction observed for all glasses, but to the largest extent in compositions undergoing greater release magnitudes. Furthermore, it is confirmed that ion-exchange / hydrolysis reactions of Na, P, B, and to a less extent, Si sites, in the glass results in a silicate-rich gel layer on the glass surface containing more significant Si^2/Si^3 fractions with terminal hydroxyl groups. Phosphate species, on the other hand, have not been identified to undergo preferential extraction, however, it can be hypothesized based on our observations from ^{11}B MAS NMR, that P-O-B^4 linked units, which dominate the speciation in higher P_2O_5-

containing compositions, exhibit slower degradation as compared to isolated phosphate species. Based upon our findings and the known literature on chemical dissolution behavior, it is conferred that (i) B^3, isolated P^0/P^1, and Si^2/Si^3 (specifically, non-bridging oxygen sites) species correlate positively to the degradation rate, meanwhile (ii) B^4, P^2/P^3 ($P\text{-}O\text{-}B^4$), and Si^4 species correlate negatively to release rates.

Thus, to rationalize our findings within each compositional regime, the overall dissolution rate is impacted by the weighting between each compositional and structural factor. For instance, PB glasses exhibit minimal changes in degradation rates since the B^3 fraction (and B_2O_3 content) is higher and rise with P_2O_5, thus more effectively balancing out the effects of rising Si^4 and $P\text{-}O\text{-}B^4$ speciation. Furthermore, as *R* and *K* ratios decrease (MB and PA glasses), the drop in B^3 fraction (and B_2O_3 content) results in degradation rates which are more significantly controlled by the rises in Si^4 and $P\text{-}O\text{-}B^4$ linkage, thus causing overall rate decreases with P_2O_5 content. The present comprehensive structural understanding of the degradation behavior in the sodium borosilicate and phospho-borosilicate systems can be utilized to develop novel borosilicate bioactive glasses that contain desired structural features allowing carefully controlled ionic release in human body conditions to promote specific cellular responses.

5.5 Conclusions

Using a systematic and dedicated approach, the present study explored the compositional and structural drivers controlling the chemical degradation behavior of borosilicate bioactive glasses across a wide composition space including perboric (Na/B < 1), metaboric (Na/B = 1), and peralkaline (Na/B > 1) regimes. It has been determined that the glass degradation behavior is predominantly driven by the *R* (Na/B) and *K* (Si/B) ratios,

however, the local and intermediate molecular structure also plays a vital role in the ionic release rates. Stepwise additions of P_2O_5 into sodium borosilicate glasses result in complex glass structural changes which have a varied impact upon degradation behavior. The observed degradation behavior has been explained from the standpoint of the effect that specific structural features (i.e. B^3/B^4, Si^3/Si^4, etc.) have upon ionic release behavior. A combination of the comprehensive compositional and structural understanding acquired in the present study can be utilized to facilitate the development of novel borosilicate bioactive glasses with ionic release tuned for targeted biomedical applications.

Conflicts of interest

The authors confirm the absence of any conflict of interest with this submission.

Acknowledgements

This material is based upon work supported by the National Science Foundation under Grant No. 1507131, the US Department of Energy (DOE) – Offices of Nuclear Energy and Environmental Management through Nuclear Energy University Program under Grant No. DE-NE0008597, and US DOE – Office of River Protection under Grant No. DE-EM0003207. H.E. and H.B. thank FAPESP for support under Grant No. 2013/07793-6. H.B. also thanks the DFG for support. The authors also thank the Characterization Sciences group at Corning Incorporated for compositional analysis of glasses.

Supplementary Information

The supplementary information of this manuscript contains XRD patterns and ^{29}Si MAS NMR spectra of glass powders recovered from dissolution experiments.

References

1. Rahaman, M. N.; Day, D. E.; Bal, B. S.; Fu, Q.; Jung, S. B.; Bonewald, L. F.; Tomsia, A. P., Bioactive glass in tissue engineering. *Acta Biomaterialia* 2011, *7* (6), 2355-2373.
2. Balasubramanian, P.; Buettner, T.; Pacheco, V. M.; Boccaccini, A. R., Boron-containing bioactive glasses in bone and soft tissue engineering. *Journal of the European Ceramic Society* 2018, *38* (3), 855-869.
3. Stone-Weiss, N.; Pierce, E. M.; Youngman, R. E.; Gulbiten, O.; Smith, N. J.; Du, J.; Goel, A., Understanding the structural drivers governing glass–water interactions in borosilicate based model bioactive glasses. *Acta Biomaterialia* 2018, *65*, 436-449.
4. Deshkar, A.; Ahmadzadeh, M.; Scrimshire, A.; Han, E.; Bingham, P. A.; Guillen, D.; McCloy, J.; Goel, A., Crystallization behavior of iron-and boron-containing nepheline (Na2O· Al2O3· 2SiO2) based model high-level nuclear waste glasses. *Journal of the American Ceramic Society* 2019, *102* (3), 1101-1121.
5. Huang, W. H.; Day, D. E.; Kittiratanapiboon, K.; Rahaman, M. N., Kinetics and mechanisms of the conversion of silicate (45S5), borate, and borosilicate glasses to hydroxyapatite in dilute phosphate solutions. *Journal of Materials Science-Materials in Medicine* 2006, *17* (7), 583-596.
6. Hoppe, A.; Gueldal, N. S.; Boccaccini, A. R., A review of the biological response to ionic dissolution products from bioactive glasses and glass-ceramics. *Biomaterials* 2011, *32* (11), 2757-2774.
7. Tilocca, A., Structural models of bioactive glasses from molecular dynamics simulations. *Proceedings of the Royal Society a-Mathematical Physical and Engineering Sciences* 2009, *465* (2104), 1003-1027.
8. Goel, A.; Kapoor, S.; Tilocca, A.; Rajagopal, R. R.; Ferreira, J. M. F., Structural role of zinc in biodegradation of alkali-free bioactive glasses. *Journal of Materials Chemistry B* 2013, *1* (24), 3073-3082.
9. Yun, Y. H.; Bray, P. J., Nuclear magnetic resonance studies of the glasses in the system Na2O-B2O3-SiO2. *Journal of Non-Crystalline Solids* 1978, *27* (3), 363-380.
10. Dell, W. J.; Bray, P. J.; Xiao, S. Z., 11B NMR studies and structural modeling of Na2O-B2O3-SiO2 glasses of high soda content. *Journal of Non-Crystalline Solids* 1983, *58* (1), 1-16.
11. Bray, P. J., Structural models for borate glasses. *Journal of Non-Crystalline Solids* 1985, *75* (1-3), 29-36.
12. Manara, D.; Grandjean, A.; Neuville, D. R., Structure of borosilicate glasses and melts: A revision of the Yun, Bray and Dell model. *Journal of Non-Crystalline Solids* 2009, *355* (50–51), 2528-2531.
13. Martens, R.; Muller-Warmuth, W., Structural groups and their mixing in borosilicate glasses of various compositions - an NMR study. *Journal of Non-Crystalline Solids* 2000, *265* (1-2), 167-175.
14. van Wüllen, L.; Müller-Warmuth, W.; Papageorgiou, D.; Pentinghaus, H. J., Characterization and structural developments of gel-derived borosilicate glasses: a multinuclear MAS-NMR study. *Journal of Non-Crystalline Solids* 1994, *171* (1), 53-67.
15. Yu, Y.; Stevensson, B.; Edén, M., Medium-Range Structural Organization of Phosphorus-Bearing Borosilicate Glasses Revealed by Advanced Solid-State NMR

Experiments and MD Simulations: Consequences of B/Si Substitutions. *The Journal of Physical Chemistry B* 2017, *121* (41), 9737-9752.
16. Yu, Y.; Eden, M., Structure-composition relationships of bioactive borophosphosilicate glasses probed by multinuclear 11B, 29Si, and 31P solid state NMR. *RSC Advances* 2016, *6* (103), 101288-101303.
17. Muñoz, F.; Montagne, L.; Delevoye, L.; Durán, A.; Pascual, L.; Cristol, S.; Paul, J.-F., Phosphate speciation in sodium borosilicate glasses studied by nuclear magnetic resonance. *Journal of Non-Crystalline Solids* 2006, *352* (28–29), 2958-2968.
18. Uesbeck, T.; Eckert, H.; Youngman, R.; Aitken, B., The Structure of Borophosphosilicate Pure Network Former Glasses Studied by Multinuclear NMR Spectroscopy. *The Journal of Physical Chemistry C* 2017, *121* (3), 1838-1850.
19. Storek, M.; Adjei-Acheamfour, M.; Christensen, R.; Martin, S. W.; Böhmer, R., Positive and negative mixed glass former effects in sodium borosilicate and borophosphate glasses studied by 23Na NMR. *The Journal of Physical Chemistry B* 2016, *120* (19), 4482-4495.
20. Gan, H.; Hess, P. C.; Kirkpatrick, R. J., Phosphorus and boron speciation in K2O-B2O3-SiO2-P2O5 glasses. *Geochimica et Cosmochimica Acta* 1994, *58* (21), 4633-4647.
21. Fluegel, A.; Spinelli, I. M.; LaCourse, W., Study of the Kinetics of Phase Separation in 3.25 Na2O-3.25 Li2O/Na2O-33.5 B2O3-60 SiO2 Glasses by Skeletonization. *Advances in Fusion and Processing of Glass III* 2006, *141*, 363-370.
22. Christensen, R.; Byer, J.; Kaufmann, T.; Martin, S. W., Structure–property relationships in the mixed glass former system Na2O–B2O3–P2O5. *Physics and Chemistry of Glasses-European Journal of Glass Science and Technology Part B* 2009, *50* (4), 237-242.
23. Crovace, M. C.; Souza, M. T.; Chinaglia, C. R.; Peitl, O.; Zanotto, E. D., Biosilicate®—A multipurpose, highly bioactive glass-ceramic. In vitro, in vivo and clinical trials. *Journal of Non-Crystalline Solids* 2016, *432*, 90-110.
24. Fu, Q.; Rahaman, M. N.; Fu, H.; Liu, X., Silicate, borosilicate, and borate bioactive glass scaffolds with controllable degradation rate for bone tissue engineering applications. I. Preparation and in vitro degradation. *Journal of Biomedical Materials Research Part A* 2010, *95A* (1), 164-171.
25. Huang, W.; Day, D. E.; Kittiratanapiboon, K.; Rahaman, M. N., Kinetics and mechanisms of the conversion of silicate (45S5), borate, and borosilicate glasses to hydroxyapatite in dilute phosphate solutions. *Journal of Materials Science: Materials in Medicine* 2006, *17* (7), 583-596.
26. White, A., The Materials Genome Initiative: One year on. *Mrs Bulletin* 2012, *37* (8), 715-716.
27. Lusvardi, G.; Malavasi, G.; Tarsitano, F.; Menabue, L.; Menziani, M. C.; Pedone, A., Quantitative Structure-Property Relationships of Potentially Bioactive Fluoro Phospho-silicate Glasses. *Journal of Physical Chemistry B* 2009, *113* (30), 10331-10338.
28. American Society for, T.; Materials, W. C. P. A. *Standard test method for static leaching of monolithic waste forms for disposal of radioactive waste ASTM standard*; United States, 1998; p 16.
29. Tournié, A.; Majérus, O.; Lefèvre, G.; Rager, M. N.; Walmé, S.; Caurant, D.; Barboux, P., Impact of boron complexation by Tris buffer on the initial dissolution rate of borosilicate glasses. *Journal of Colloid and Interface Science* 2013, *400*, 161-167.

30. Scofield, J. H. *Theoretical photoionization cross sections from 1 to 1500 keV*; California Univ., Livermore. Lawrence Livermore Lab.: 1973.
31. Smith, G. C., Evaluation of a simple correction for the hydrocarbon contamination layer in quantitative surface analysis by XPS. *Journal of Electron Spectroscopy and Related Phenomena* 2005, *148* (1), 21-28.
32. Kragten, J., Tutorial review. Calculating standard deviations and confidence intervals with a universally applicable spreadsheet technique. *Analyst* 1994, *119* (10), 2161-2165.
33. Ebert, W. L. *Comparison of the results of short-term static tests and single-pass flow-through tests with LRM glass (ANL-06/51)*; Argonne National Laboratory: Argonne, IL, USA, 2006.
34. Gin, S.; Frugier, P.; Jollivet, P.; Bruguier, F.; Curti, E., New Insight into the Residual Rate of Borosilicate Glasses: Effect of S/V and Glass Composition. *International Journal of Applied Glass Science* 2013, *4* (4), 371-382.
35. Fournier, M.; Ull, A.; Nicoleau, E.; Inagaki, Y.; Odorico, M.; Frugier, P.; Gin, S., Glass dissolution rate measurement and calculation revisited. *Journal of Nuclear Materials* 2016, *476*, 140-154.
36. Ebert, W. L. *The effects of the glass surface area/solution volume ratio on glass corrosion: a critical review*; Argonne National Laboratory: 1995.
37. Ebert, W. L.; Bates, J. K., A comparison of glass reaction at high and low glass-surface solution volume. *Nuclear Technology* 1993, *104* (3), 372-384.
38. Gin, S.; Neill, L.; Fournier, M.; Frugier, P.; Ducasse, T.; Tribet, M.; Abdelouas, A.; Parruzot, B.; Neeway, J.; Wall, N., The controversial role of inter-diffusion in glass alteration. *Chemical Geology* 2016, *440*, 115-123.
39. Andriambololona, Z.; Godon, N.; Vernaz, E., R717 Glass Alteration in the Presence of Mortar: Effect of the Cement Grade. *MRS Online Proceedings Library Archive* 1991, *257*.
40. Mercado-Depierre, S.; Angeli, F.; Frizon, F.; Gin, S., Antagonist effects of calcium on borosilicate glass alteration. *Journal of nuclear materials* 2013, *441* (1-3), 402-410.
41. Du, L.-S.; Stebbins, J., Nature of Silicon−Boron Mixing in Sodium Borosilicate Glasses: A High-Resolution 11 B and 17 O NMR Study. *Journal of Physical Chemistry B - J PHYS CHEM B* 2003, *107*, 10063-10076.
42. Stone-Weiss, N.; Youngman, R. E.; Thorpe, R.; Smith, N. J.; Pierce, E. M.; Goel, A., An insight into the corrosion of alkali aluminoborosilicate glasses in acidic environments. *Physical Chemistry Chemical Physics* 2020, *22* (4), 1881-1896.

Chapter 6. Influence of Tris buffer solution chemistry upon dissolution behavior of a model borosilicate bioactive glass

Nicholas Stone-Weiss,[1] Nicholas J. Smith,[2] Randall E. Youngman,[2] Eric M. Pierce,[3] Ashutosh Goel[1,**]

[1]Department of Materials Science and Engineering, Rutgers, The State University of New Jersey, Piscataway, NJ 08854, United States

[2]Science and Technology Division, Corning Incorporated, Corning, NY 14831, United States

[3]Environmental Sciences Division, Oak Ridge National Laboratory, Oak Ridge, TN 37831, United States

[**] Corresponding author:
Email: ag1179@soe.rutgers.edu; Ph: +1-848-333-1523

6.1 Introduction

Simulated body fluid (SBF) has been traditionally utilized in the biomaterials community as the dissolution medium to assess in vitro bioactivity (ISO 23317), marked by the material's ability to form hydroxyapatite on its surface, which bonds with bone tissue and has a similar structure as the mineral component of bone.[1] Accordingly, after a thorough review of in vitro studies of bioactive glasses reported in the literature, it is observed that a large subset of these studies has utilized SBF to maintain stable pH and replicate human body conditions. Although hydroxyapatite-forming ability in SBF has been largely successful in assessing bioactivity of glass compositions similar to 45S5, recent literature has rather suggested that (i) ionic dissolution products which release from the glass into the body can promote specific biological responses at critical ion concentrations, i.e. gene activation for osteoblast or angioblast proliferation,[2,3] and that (ii) SBF tests may not always be valid in accurately predicting glass bioactivity or degradation behavior.[4-6] Since the functioning of third-generation biomaterials necessitates controlled ion release for stimulation of specific processes in the body, understanding glass dissolution kinetics is essential for developing novel bioactive glasses. Thus, aqueous media must be chosen which minimally impact glass degradation behavior and allow for accurate prediction of in vitro and in vivo release kinetics.

Given these developments, to assess both glass bioactivity and degradation behavior, the bioactive glass community has begun to explore alternative buffer solutions which are suitable buffers in the pH range necessary to replicate human body environments.[7-10] Consequently, in today's date, the buffer solutions most commonly used in bioactive glass literature are Tris-based ($C_4O_3NH_{11}$, in combination with acids such as

HCl or HNO_3). Tris buffer, which is also contained within SBF solutions, has been chosen since it is the most widely used buffer for studying glass dissolution in near-neutral pH conditions across many glass applications[2,11-17] and its solutions do not contain dissolved cations (i.e. Na^+ or Ca^{2+}) which can convolute experimental results due to solution feedback effects.[18] Tris-HCl, for instance, has been adopted by ISO 10993-14 as the recommended solution for studying biomaterials. For this reason, it has been extensively utilized in bioactive glass studies and alongside SBF, has been a generally successful aqueous media for assessing degradation behavior of traditional (45S5-based) bioactive glasses. However, uncertainties have been raised as to the validity of Tris as a buffer which minimally impacts bioactivity, particularly with regards to the accelerated kinetic effects it has displayed for bioactive glass and glass-ceramic scaffolds as compared to analogous samples exposed to Tris-free solutions.[6-8,10,19] Furthermore, with the advent of boron-containing glass compositions as potential third-generation bioactive glasses due to their promising and flexible bioactive properties,[20,21] additional challenges are presented, since both Tris-HCl and SBF contain Tris, which is particularly acknowledged to create adverse artificial effects when in contact with boron in glass.[22] The focus of the present study will encompass each of these concerns raised about Tris buffer, with a specific emphasis placed on borosilicate bioactive glass.

Borosilicate glass dissolution kinetics have been shown to accelerate by as much as 8× when in contact with Tris-containing solutions as compared to Tris-free solutions.[22] In their study, Tournié et al.[22] determined that this drastic increase in dissolution rate, which was not observed for a soda-lime silicate glass, was detected for a sodium borosilicate glass in both Tris-HCl and Tris-HNO_3 environments, although to a more pronounced extent in

Tris-HCl.[22] Such a rapid acceleration of dissolution kinetics was attributed to the formation of Tris-boron complexes (at 1:1 stoichiometry), which, while still not fully understood, was assumed to occur either by (i) complexation of boron with Tris in solution or (ii) by adsorption of Tris molecules on boron sites at the glass surface, thus increasing the rate of boron release and causing more a rapid hydrolysis of the surrounding glass network.[22] Since Tris-based solutions have been shown to exhibit such tremendous impacts upon borosilicate degradation kinetics, it is of vital importance to understand the mechanisms by which Tris effects glass dissolution behavior, especially to aid in selecting aqueous media adequate to study and accurately predict the chemical durability of borosilicate glasses.

Borosilicate glasses are utilized not only in bioactive glasses but also in several other technological applications[23]; therefore, it is particularly ideal to uncover a better suited neutral pH buffer solution which minimally impacts dissolution kinetics of borosilicate glasses. Unfortunately, the present consensus in the glass community is that Tris-based solutions are the best choice when studying this pH regime since these solutions provide the buffering properties needed in the absence of dissolved cations which may impact dissolution behavior. Presented with this challenge, the current focus of our study is to understand the mechanisms by which Tris interacts with boron in glass, particularly aiming to address the following open questions: (1) How does the identity of the acid in Tris-based solutions impact dissolution behavior? (2) What suppressing or accelerating effects upon dissolution kinetics are observed as the ratio of Tris/Acid in solution is varied? Accordingly, the present study focuses on the dissolution behavior of a sodium borosilicate glass in Tris-based (pH 7-9) solution environments with varied Tris concentrations (0.01 – 0.5 M) and acid identities (HCl vs. HNO_3). In this pursuit, we particularly seek to

understand the mechanisms by which Tris impacts the dissolution of boron-containing glasses, i.e. whether Tris-boron complexation occurs on the surface or in solution and how glass degradation kinetics are influenced.

6.2 Experimental

6.2.1 Synthesis of the glass

A sodium borosilicate composition (25 Na_2O–25 B_2O_3–50 SiO_2; in mol. %) was synthesized using the melt-quench technique, using high-purity powders of SiO_2 (Alfa Aesar; >99.5 %), H_3BO_3 (Alfa Aesar; ≥98 %), and Na_2SiO_3 (Alfa Aesar; >99 %) as precursors. Oxide precursors were mixed in a 70 g batch and melted in a Pt-Rh crucible for 1-2 h in air at 1450 ºC. The glass melt was quenched on a metallic plate and coarse-annealed at a temperature of T_g^*-50 °C, where T_g^* is the estimated glass transition temperature as obtained from the SciGlass database.[24] The amorphous nature of the glass sample was confirmed by X-ray diffraction (XRD) (PANalytical – X'Pert Pro; Cu K_α radiation; 2θ range: 10–90º; step size: 0.01313º s^{-1}). The actual concentration of SiO_2 and B_2O_3 in the synthesized glasses was determined by ICP–OES (PerkinElmer Optima 7300V), while sodium concentration was determined by flame emission spectroscopy (Perkin Elmer Flame Emission Analyst 200).

6.2.2 Glass transition temperature measurements and annealing

Differential scanning calorimetry (DSC) data were collected on fine glass powders (<45µm diameter) using a Simultaneous Thermal Analyzer (STA 8000; PerkinElmer) from room temperature to 1500 ºC at a heating rate of 20 ºC/min under a constant flow of nitrogen gas. The glass transition

temperature (T_g) was deduced from the inflection point of the endothermic dip in the DSC spectra, where the reported T_g is the average value from two thermal scans. After experimental T_g measurements, the glass was re-annealed for several hours at a temperature corresponding to T_g-50 ºC and slow-cooled to room temperature until most of the residual stresses were removed, as visualized under a polariscope. A more detailed description of the method used to anneal the glasses has been described in our previous article.[25]

6.2.3 Bulk structural analysis of the as-synthesized and post-dissolution glass samples

The structure of glass—both before and following chemical dissolution—has been studied using ^{11}B MAS NMR spectroscopy. Spectra were acquired using a commercial spectrometer (VNMRs, Agilent) and a 3.2-mm MAS NMR probe (Agilent). The samples were powdered in an agate mortar, packed into 3.2 mm zirconia rotors, and spun at 20 kHz. Experiments were conducted at 16.4 T (224.52 MHz resonance frequency), incorporating a 4 s recycle delay, short radio frequency pulses (0.6 μs) corresponding to a $\pi/12$ tip angle, and signal averaging of 400 to 1000 scans. The acquired spectra were processed with minimal apodization and referenced to aqueous boric acid (19.6 ppm). Fitting of the MAS NMR spectra was performed using DMFit.[26] The "Q MAS ½" and Gaus/Lor functions were used to fit 3- and 4-fold coordinated boron resonances in the ^{11}B MAS NMR data, respectively, and N_4 was calculated from the relative areas of these peaks, with a small correction due to the overlapping satellite transition of the 4-fold coordinated boron peak.[27]

6.2.4 Chemical durability of glasses

6.2.4.1 Surface area analysis of glass powder specimens

The studied glass was crushed and sieved to obtain powders with particle size varying between 300 – 425 μm. The glass particles were ultrasonically washed in acetone

to remove any fine powder residue sticking to the surface of larger particles. This process was repeated at least three times or until the supernatant was clear to ensure the removal of all fine particles. The ultrasonically washed glass particles were dried overnight at room temperature in ambient air and analyzed for any structural changes before versus after acetone-washing using Fourier Transform Infrared (FTIR) spectroscopy. The IR spectra were acquired using a single-bounce diamond attenuated total reflectance (ATR) apparatus (FTIR-UATR, Frontier™, PerkinElmer, Inc.; scanning resolution 4 cm^{-1}, 32 scans for background and samples). Average three-dimensional (3D) geometric surface area of washed particles was determined using ImageJ software (as explained in more detail in Ref.[25]) after capturing images of ~1000 particles via an optical microscope (Zeiss Axioskop 40) at ~50X magnification. Experimental density values (measured using Archimedes' method by measuring the mass of sample in air and d-limonene solution; number of samples = 3, standard deviation <0.009 g cm^{-3}) were used together with the 3D surface area calculations to determine the specific surface area of the washed powders (~4100 mm^2/g). Finally, the mass of glass particles resulting in the desired surface area–to–volume ratio (SA/V) was calculated.

6.2.4.2 Dissolution behavior and kinetics of glass corrosion

The dissolution behavior and kinetics of glasses was studied in Tris-HCl and Tris-HNO_3 solutions with pH 7, 8, and 9. In each experiment, 30.0 mg of acetone-washed glass particles were immersed in 50 mL of solution, corresponding to SA/V = 2.5 m^{-1}. pH 7 and 9 solutions consisted of 0.1 M Tris, whereas pH 8 solutions contained 0.01, 0.05, 0.1, 0.3, and 0.5 M Tris. Each solution studied was duplicated with both HCl and HNO_3 as the acid identity in the buffer solution. Solutions were prepared by dissolving the required amount of Tris in DI water and adjusting the pH to the desired value with 1 M of HCl or HNO_3.

Solutions were prepared as target pH ±0.02 in batches with a total volume of 2±0.05 L to maintain accurate Tris molarity in solution. All powder–solution mixtures were immediately sealed into sterilized polypropylene flasks and placed in an oven at 65 ºC. Experiments ranged from 15 minutes to 24 hours. In addition to analyses of neat (unused) and blank (glass-free) control solutions, all experiments were performed three times to evaluate uncertainty in final results. The pH of each solution recovered from experiments was measured at room temperature using a pH meter (Mettler Toledo InLab® Pro-ISM). Separate aliquots of recovered solutions were chemically analyzed by ICP-OES (PerkinElmer Optima 8300). ICP-OES detection limits were <0.5 ppm for Na, <0.2 ppm for B, and <0.2 ppm for Si. The normalized loss (NL) of each element (Na, B, and Si) released from glasses into the surrounding solution was calculated using equation (1),

$$NL_i = \frac{C_i - C_o}{\left(\frac{SA}{V}\right) f_i} \qquad (1)$$

where C_i is the mass concentration of element i in the solution as detected by ICP-OES; f_i is the mass fraction of the element i in the glass; C_o is the background concentration (as determined from blank solutions). Normalized loss data were plotted against time and linearly fit over the apparent linear regimes of release at early times to evaluate forward dissolution rates as a function of glass composition and initial solution pH.

To study the mechanisms of glass degradation, solution and bulk structural characterization of pre- and post-dissolution glass specimens were performed. For examination of dissolved structural species, selected liquid aliquots were studied using ^{11}B solution NMR. These experiments were performed at 11.7 T (160.46 MHz resonance frequency), incorporating a 1 s recycle delay, π/4 tip angle pulses, and signal averaging over at least 1000 scans. These experiments were performed at 25 ºC (room temperature),

37 °C (human body temperature), and 65 ºC (to reproduce dissolution conditions). For bulk analyses, the glass powders remaining after dissolution experiments *(from section 2.4.2)* were rinsed thoroughly with DI water three times and then submerged in ethanol (Fisher Chemical, anhydrous) to (i) facilitate drying the samples at room temperature and (ii) effectively cease glass-water reactions near the glass surface. The samples were then characterized using XRD and ^{11}B MAS NMR spectroscopy.

6.3 Results

6.3.1 Glass formation behavior and bulk properties

The as-synthesized glass sample was transparent in appearance and determined to be amorphous via XRD analysis (as shown in Figure S1). The experimentally measured glass composition (25.2 Na_2O–25.0 B_2O_3–49.8 SiO_2) was in very close agreement with the batched target (within ±0.2 mol. %). T_g and density were measured to be 565±6 °C and 2.487±0.003 g/cm^3, which are both agree well with literature on similar compositions.[28] After analyzing the annealed glass under a polariscope, it was estimated to have less than 10 MPa of remaining residual stresses, as calculated from its ~5 mm sample thickness and considering the absence of first-order fringes under cross-polarized light.

6.3.2 Structural analysis of glasses

Figure 6.1 presents the ^{11}B MAS NMR spectra and fitted peaks for the studied glass. This spectrum displays two main resonances: a broad peak centered near 14.5 ppm associated with trigonal boron species and a strong, relatively narrow peak centered near 0 ppm associated with tetrahedral boron species in the glass. The trigonal boron peak contains contributions from both ring and non-ring species, where ring species are shifted downfield from non-ring species (18.5 vs. 16.2 ppm in the fitted spectra, respectively).[29]

The tetrahedral boron peak consists of resonances likely associated with B^4 units with bridging oxygen (BO) to either 3Si/1B or 4 Si. The former unit is typically shifted downfield from the latter, as evidenced from the 0.0 vs. -1.9 ppm chemical shifts in the fitted spectrum.[29] The N_4 fraction (percentage of B^4 species) in the studied glass was calculated to be 68.2 %, which requires charge compensation by Na^+ in the glass. Using this result in combination with the –Dell, Yun, and Bray model,[30-32] the silicate structure of the studied glass includes 67.3 % Q^4 (Q^n, where *n* is the number of BO per Si tetrahedron), with the remainder being Q^3 units with 1 non-bridging oxygen (NBO) charge-balanced by the remaining Na^+ in the glass. The glass structural characteristics will be revisited in the next section as structural evolution upon glass dissolution will likewise be assessed by ^{11}B MAS NMR.

6.3.3 Chemical dissolution behavior

6.3.3.1 Buffering capacity as a function of solution chemistry

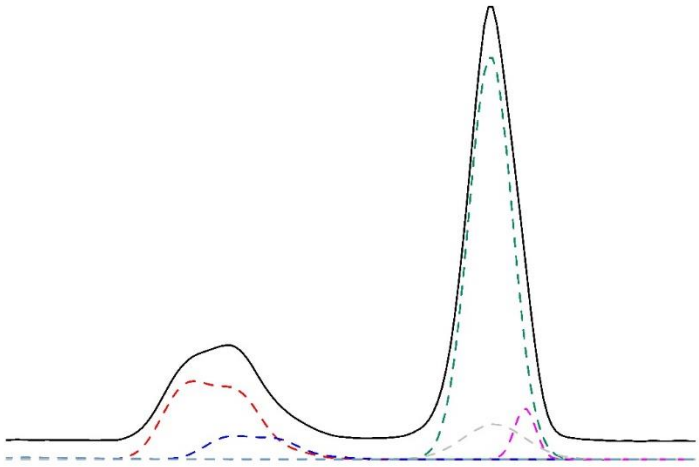

Figure 6.1. *^{11}B MAS NMR spectra of the studied glass and deconvolution for the central transition. The minor fitted peak displayed near 0 ppm represents the overlapping satellite transition within the B^4 resonance, whose area was not considered while calculating N_4.*

The pH readings for all dissolution experiment durations and solution environments are presented in Table S1. Figure 6.2 graphically depicts the pH evolution in solutions with initial pH = 8, as a function of Tris molarity. As the glass dissolves, Na and B from the glass are characteristically released as Na^+ and boric acid (H_3BO_3), where Na^+ tends to increase alkalinity and boric acid reduces the surrounding solution pH. However, the impact that these dissolved species have upon solution pH will largely be defined by the buffer solution chemistry and interactions taking place between the buffering agent and species released from the glass. In our studies at pH = 8, it is observed that between Tris molarities of 0.1–0.5 in solution, pH within 24 h of glass submersion does not change by more than ±0.1 (~8.0-8.1). In 0.01 and 0.05 M Tris solutions, on the other hand, pH changes by as much as ±0.6 and ±0.2, respectively (~8.0-8.6 and ~8.0-8.2). Similar pH evolution behavior is observed regardless of the acid identity, i.e. Tris-HCl vs. Tris-HNO_3 solutions. In pH = 7 and 9 solutions, which are all 0.1 M Tris, pH varies by less than ±0.2 and ±0.1, respectively, regardless of the acid identity in solution or the duration of glass submersion. Thus, as expected, it is exhibited that as more significant fractions of Tris are dissolved in solution, the solution displays enhanced buffering ability, given by the exceptional buffering ability of 0.3 and 0.5 M Tris solutions, while 0.01 and 0.05 M solutions do not enable exceptional pH stability over time. Solutions containing 0.1 M Tris, on the other hand, do not buffer as well at pH = 7 as compared to pH = 8-9. This fundamental difference may be driven by the molarity of acid in solution, where pH = 7 is ~0.09 M, pH = 8 is ~0.06 M, and pH 7 is ~0.01 M concerning the acid contained. Thus, the ratio of [Tris]/[H^+] is significantly lower in pH = 7 solution (near 1:1 in pH = 7) as

compared to pH = 8-9, which likely contributes to the higher buffering abilities observed in pH > 7 solutions.

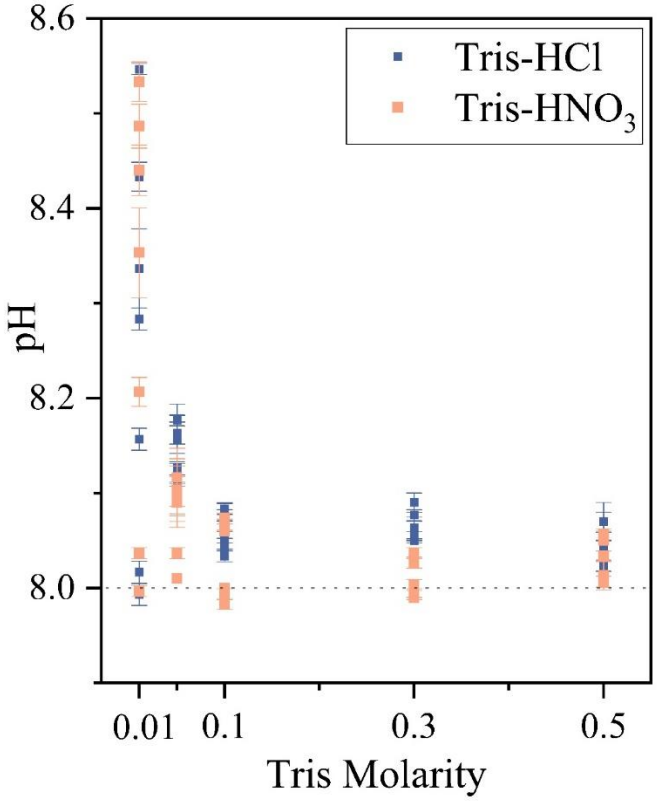

Figure 6.2. *pH spread during pH = 8 dissolution experiments, as a function of the Tris molarity.*

6.3.3.2 Elemental release behavior of glass in varied solution environment

All elemental concentrations and normalized mass loss (NL) data are similarly presented in Table S1. As the glass is brought in contact with Tris-based solutions (pH = 7-9), ion exchange and hydrolysis promote rapid, linear increases in NL with time (forward rate regime). This is followed by concave downward behavior and transition into the slower residual rate regime, which consists of a pseudo-equilibrium between glass and solution. The transition from forward to residual rate may be attributed to the following: the development of secondary phases near the glass surface (i.e. gel/precipitate layer) and/or

solution feedback effects as dissolved species approach saturation limits in the surrounding solution.[33-35]

Figure 6.3a-c displays example NL vs. time curves for the studied glass; in this case, 0.1 M Tris-HNO_3 solutions of pH = 7-9 are depicted. It is observed that Na and B undergo nearly identical release behavior from the glass, while Si curves lie significantly below that of Na and B. This trend was detected in all studied solutions, regardless of initial solution characteristics. We will next compare both forward and residual rate behavior among the varied solution chemistries explored, specifically comparing the impacts of (i) Tris concentration, (ii) acid identity, and (iii) starting solution pH.

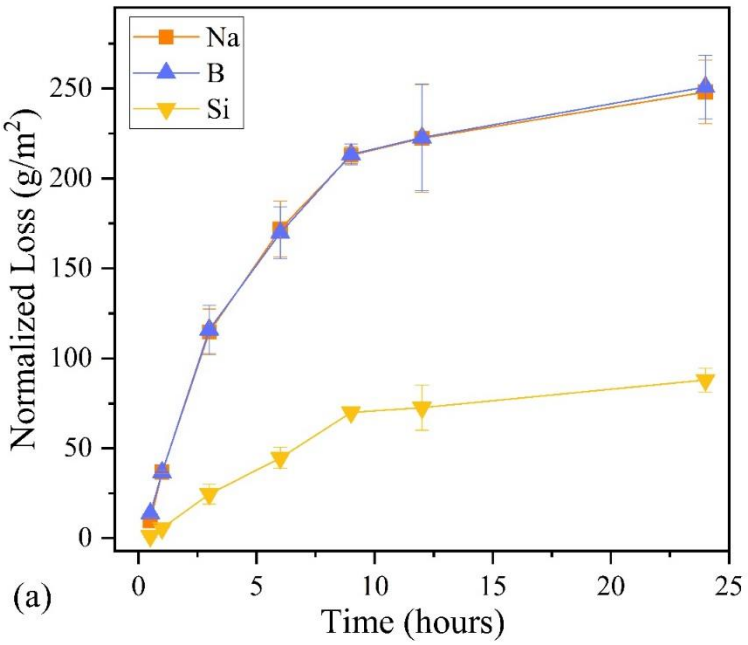

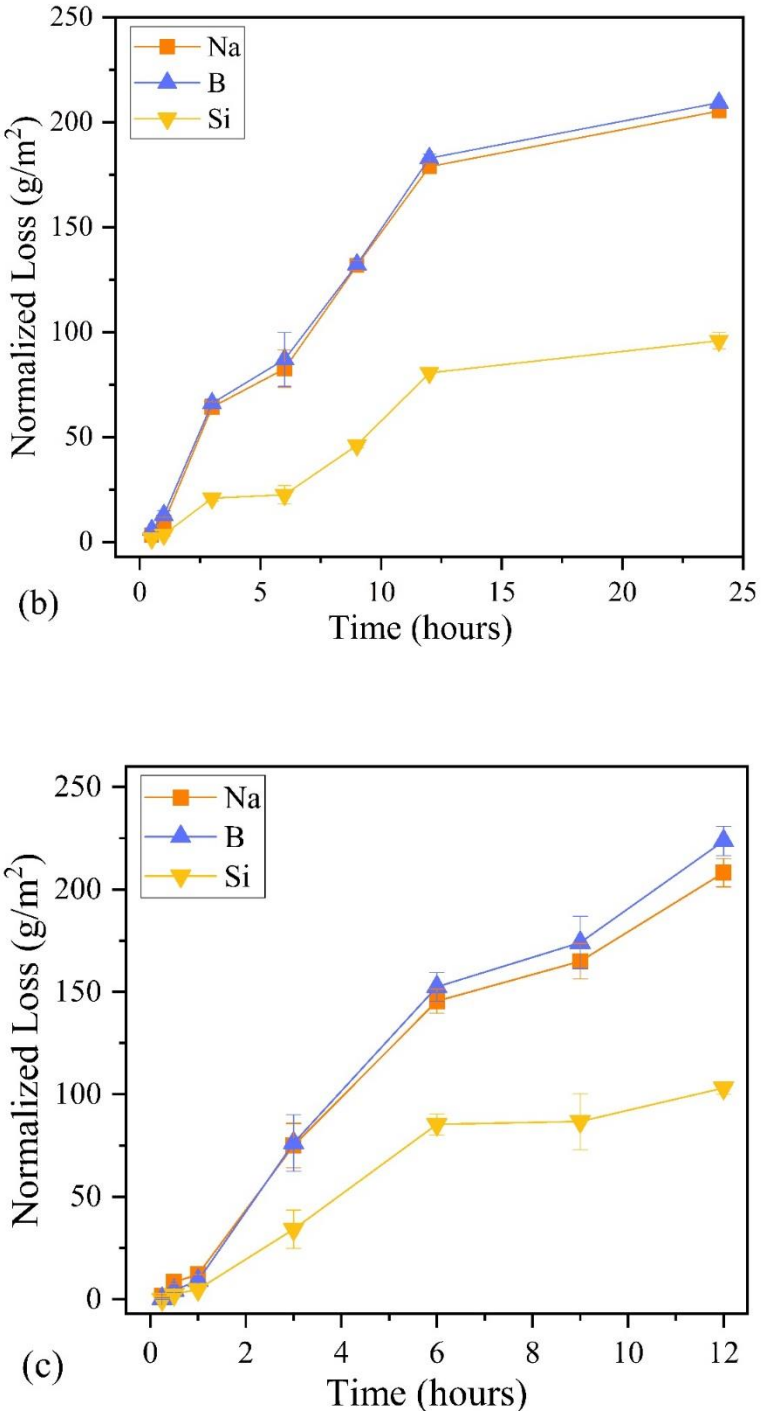

Figure 6.3. *NL vs. time curves for the studied glass in (a) pH = 7, (b) pH = 8, and (c) pH = 9 Tris-HNO_3 solutions.*

The impacts of Tris concentration upon elemental release kinetics are represented in Figure 6.4a and b as boron NL curves of the studied pH 8 solutions (Tris-HCl and Tris-HNO_3, respectively). It is evidenced in both Tris-HCl and Tris-HNO_3 solutions that as Tris molarity in solution increases sequentially, the NL curves undergo gradual downward shifts. For instance, after 24 h of dissolution, 0.01 and 0.5 M Tris solutions possess NL values of near 215-250 g/m^2 and 125-140 g/m^2, respectively, representing a reduction in Na/B release by a factor of ~2 in Tris concentration extremes. Normalized loss values for Si similarly show significant suppression between 0.01 and 0.5 M Tris solutions. Dissolution media with intermediate concentrations of Tris generally undergo release behavior which lies in between that observed in the extreme Tris concentrations (0.01 and 0.5 M). To better quantify the impact of Tris concentration upon forward rate behavior, linear regression has been performed in the first 3 h of dissolution for these curves; the rates extracted from the slopes of these fitted curves are presented in Figure 6.5, while rate values can be found in Table 6.1. Error bars displayed in this plot were calculated from the uncertainty in the least-squares fitting method (discussed by Kragten[36]) using a similar approach as that described in our previous publication.[37] We observe a general decrease in the estimated forward rates with increased Tris concentration for each element in the glass, where these decreases are particularly evident in the contrast of Na and B rates between low Tris concentrations (0.01–0.1 M) and high Tris concentrations (0.3–0.5 M). For instance, the Na forward rates calculated for 0.01 and 0.5 M Tris-HCl were ~30 and ~15 g m^{-2} h^{-1}, respectively. Dissolution rates maintained at least 2× higher for Na and B as compared to Si in all studied pH = 8 solutions. The suppression of elemental release in

solutions containing higher Tris concentrations, which was observed in both the forward rate values and in the magnitude of NL values in the residual rate regime, is likely associated either with (i) a reduction of the rate of dissolution mechanisms (i.e. ion exchange/hydrolysis) due to solution feedback effects or (ii) modifications in the rate of formation or characteristics of the gel layer. The mechanisms of dissolution suppression will be further explored in the next section.

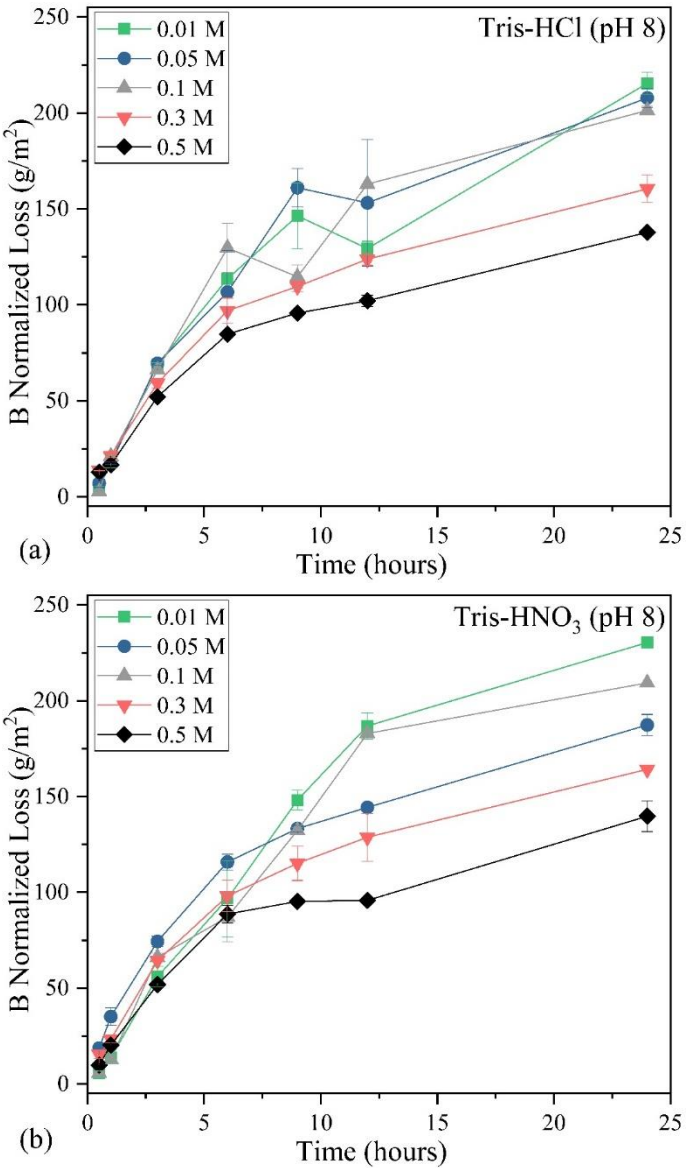

Figure 6.4. *NL vs. time for B (a) Tris-HCl and (b) Tris-HNO_3 solutions at pH = 8. Each plot displays the NL curve differences in Tris molarities ranging from 0.01 – 0.5 M.*

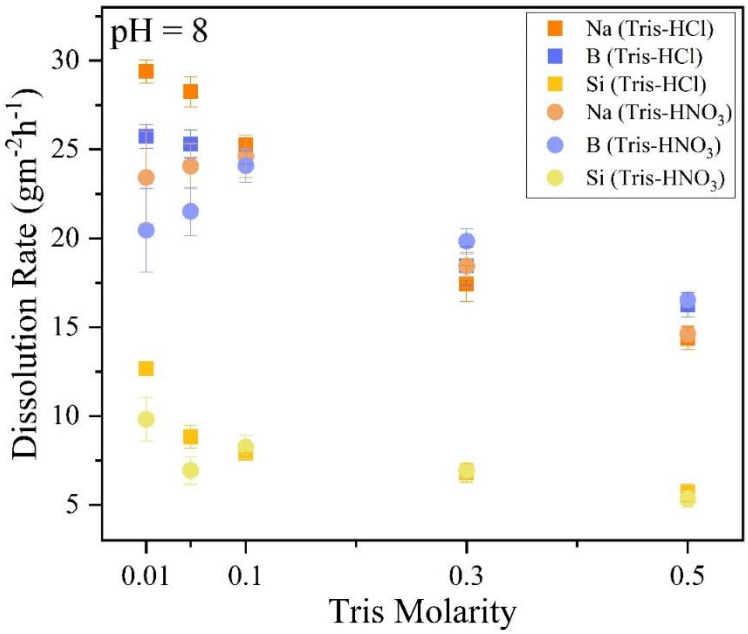

Figure 6.5. *Dissolution rate vs. Tris molarity for all elements in pH = 8 Tris-HCl and Tris-HNO_3 solutions.*

Table 6.1. *Estimated forward rates of Na, B, and Si for the studied glass in Tris-based solutions. N_4 fraction of the recovered glassy grains after dissolution experiments, as assessed by ^{11}B MAS NMR studies.*

		Normalized Loss Rates (g-glass/[m^2h])						
Aqueous Media	**Starting pH**	**Na**	**Na-error**	**B**	**B-error**	**Si**	**Si-error**	***N_4* (24 h[*])**
0.1 M Tris-HCl	7	47.5	±0.7	46.1	±0.9	12.6	±0.3	70.3
0.1 M Tris-HNO_3	7	41.1	±5.5	40.6	±5.8	9.4	±2.4	71.3
0.01 M Tris-HCl	8	29.4	±0.6	25.7	±0.7	12.7	±0.2	71.0
0.01 M Tris-HNO_3	8	23.4	±2.6	20.5	±2.3	9.8	±1.2	70.2
0.05 M Tris-HCl	8	28.3	±0.8	25.3	±0.8	8.8	±0.7	n.d.[†]
0.05 M Tris-HNO_3	8	24.6	±1.2	24.1	±1.0	8.3	±0.7	n.d.
0.1 M Tris-HCl	8	25.3	±0.4	24.6	±0.4	7.92	±0.03	69.8
0.1 M Tris-HNO_3	8	24.6	±1.2	24.1	±1.0	8.3	±0.7	69.7
0.3 M Tris-HCl	8	17.4	±1.0	18.4	±1.1	6.8	±0.5	n.d.
0.3 M Tris-HNO_3	8	18.5	±0.7	19.8	±0.7	6.9	±0.3	n.d.
0.5 M Tris-HCl	8	14.4	±0.6	16.3	±0.7	5.7	±0.5	69.5
0.5 M Tris-HNO_3	8	14.6	±0.4	16.5	±0.4	5.3	±0.5	69.5
0.1 M Tris-HCl	9	26.7	±2.9	28.8	±3.0	15.1	±3.0	69.1 (12 h)
0.1 M Tris-HNO_3	9	26.4	±1.3	28.4	±1.5	16.2	±1.1	69.2 (12 h)

[*]Unless otherwise marked

To compare dissolution behavior and kinetics between buffer solutions of different acid identity, Figures 6.6a-c display a direct comparison between B and Si normalized loss curves of Tris-HCl and Tris-HNO_3 solutions at pH = 7, 8, and 9, respectively. From the close overlap in these curves—especially in the forward rate regime—and considering the 15-25 % errors typically associated with performing static dissolution experiments,[38-40] we determine that release behavior shows close consistency regardless of the acid identity (i.e. HCl vs. HNO_3) used in Tris buffer solutions. Similarly, comparing Figure 6.4a and b in pH = 8 solutions, nearly identical NL curves are seen in HCl- and HNO_3-based solutions, with slight apparent variations occurring in low Tris concentration solutions (0.01 and 0.05 M). Comparisons of estimated forward rates of Tris-HCl and Tris-HNO_3 solutions can be extracted from Figures 6.5 and 6.6d (and Table 6.1). In pH = 8 solutions with ≥0.1 M Tris, HCl- and HNO_3-based solutions with equimolar concentrations show close overlap in Na, B, and Si rate (within ±10 %). Solutions of <0.1 M Tris, on the other hand, show up to 15-20 % reduction in the Tris-HNO_3 rate as compared to Tris-HCl. These disparities in both rate and NL of <0.1 M Tris solutions, which occur both in the forward and residual rate regimes and may result from experimental uncertainty, can likewise be explained by pH drift of the surrounding solution (i.e. differences in pH between identical Tris molarity Tris-HCl and Tris-HNO_3 solutions) since the aforementioned solutions do not buffer as well as those with ≥0.1 M Tris concentrations. It is observed in Figure 6.6d that 0.1 M pH = 8 and 9 solutions display a direct overlap between Tris-HCl vs. Tris-HNO_3 rates. However, pH = 7 exhibits 15-25 % reductions in Tris-HNO_3 rates as compared to Tris-HCl. Despite this disparity, the high uncertainties displayed in the Tris-HNO_3 rates show near overlap with Tris-HCl fitted rates and their uncertainties (±1σ; 95 % confidence

interval), demonstrating close statistical similarities between estimated rates at pH = 7. Thus, we observe that regardless of pH (in the range 7-9), the identity of acid used in Tris-based buffer solutions (i.e. HCl vs. HNO_3)-based buffer solutions exhibit largely similar glass dissolution behavior.

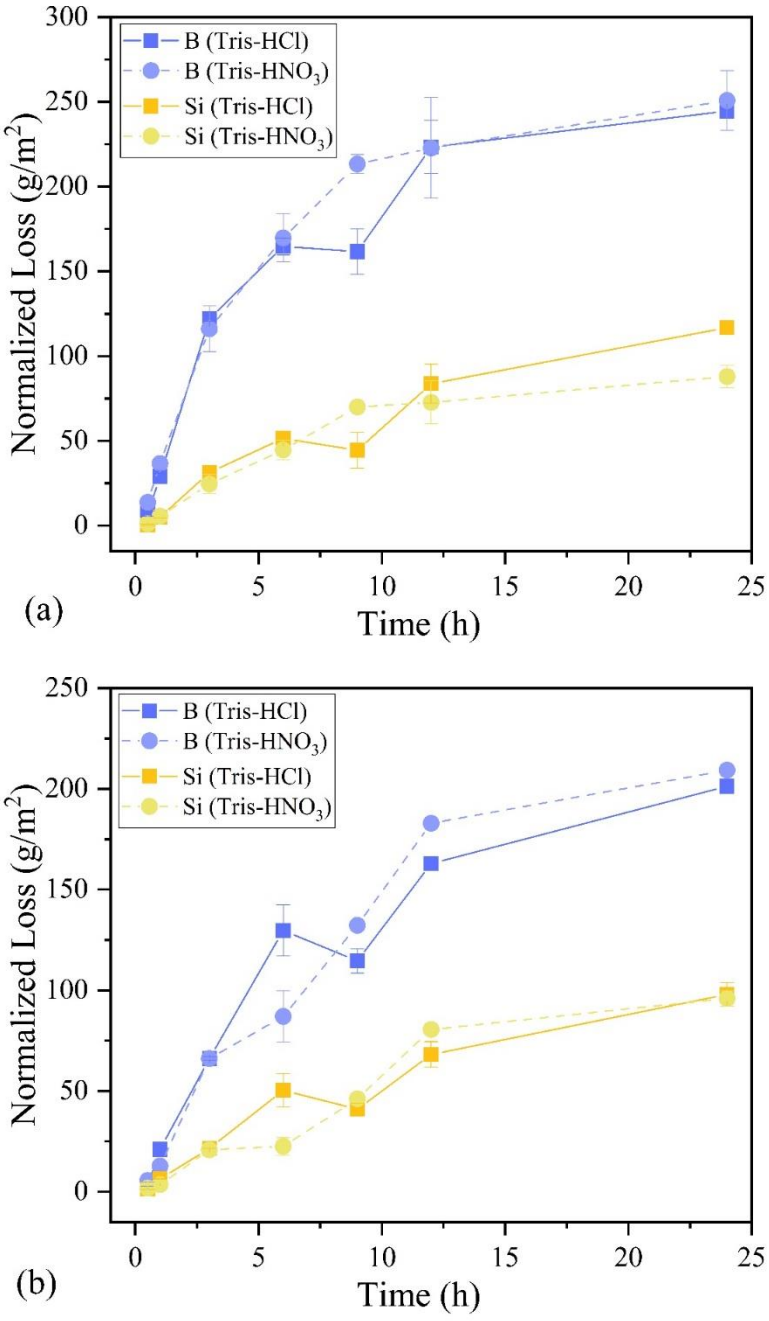

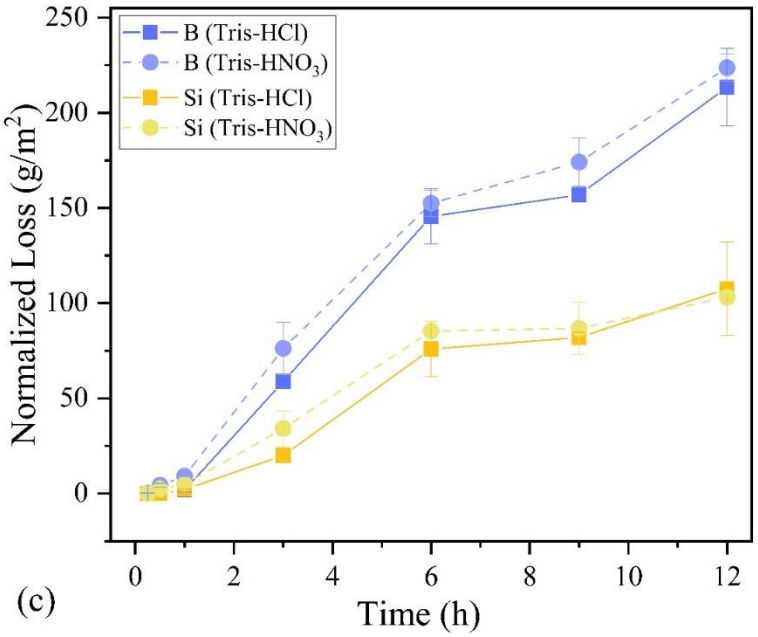

Figure 6.6. *NL vs. time for 0.1 M Tris-based solutions at (a) pH = 7, (b) pH = 8, and (c) pH = 9. Direct comparisons between B and Si release from Tris-HCl and Tris-HNO_3 solutions are displayed.*

The impact that the starting pH of Tris-based buffer solutions has upon dissolution behavior and kinetics is depicted in NL curves in Figure 6.6a-c, with the corresponding estimated forward rates shown in Figure 6.6d. In each solution pictured, the glass undergoes linear, forward rate behavior within the first 3-6 h, followed by a transition into the residual rate regime. After 24 h of dissolution for pH = 7 and 8 (and 12 h for pH = 9), the NL values for Na and B reach 240-250, 200-210, and 200-220 g/m^2 for pH = 7, 8, and 9, respectively. Forward rate comparisons presented in Figure 6.6d similarly show that Na and B dissolution rates remain significantly higher for pH = 7 than pH = 8 and 9, whose rates remain statistically similar. Si rates, however, generally show a minimum at pH = 8, where dissolution rates are higher in pH = 7 and 9 solutions. Although previous studies of glass dissolution in varied pH environments (in a wide range of compositions) have suggested that neutral pH exhibits the slowest dissolution rates in comparison to acidic and

alkaline media,[41] our trends suggest that neutral pH does not necessarily imply slowest dissolution rate. Rather, our results can be explained by the concept that forward rates are largely dependent upon the glass structural details and mechanisms which dominate the network breakdown and elemental release at the studied pH—i.e. ion exchange vs. hydrolysis.

As the starting solution pH rises from neutral, proposed silicate glass dissolution mechanisms involve deprotonation and hydrolysis of terminal Si sites[42,43] and nucleophilic attack of Si sites by OH^- to form a five-coordinated Si intermediate followed by Si hydrolysis.[33] These mechanisms are facilitated by the presence of depolymerized NBO sites in the glass network; in the studied glass, roughly one out of every three Si tetrahedra has one NBO in which either mechanism can prevail following $Na^+ \leftrightarrow H^+$ ion exchange. It is possible that in higher pH solutions, lower proton presence promotes slower rates of ion exchange and B unit hydrolysis, thus delaying the OH^- attack at NBO sites, explaining a dissolution rate minimum shifted from neutral towards pH = 8 or 9.

6.3.3.3 Evolution of bulk and liquid structural characteristics

Glassy grains recovered from dissolution experiments were analyzed via XRD and MAS NMR spectroscopy. XRD scans of all recovered samples after 12 or 24 hours were completely amorphous, thus ruling out the significant presence of crystalline secondary phases (not shown). To quantitatively understand structural changes taking place in the glass structure following dissolution, ^{11}B MAS NMR was performed on selected samples which were subjected to the maximum time duration of aqueous submersion (spectra are shown in Figure 6.7). These spectra were used to track the structural changes in the boron network, particularly the changes in N_4 fraction in the glass based on integrated areas of BO_3 and BO_4 associated peaks *(as has been discussed more in-depth in Section 3.2)*. Table

6.1 presents the N_4 fraction of recovered samples, as compared to that of the as-synthesized glass. It is seen that all samples underwent a statistically significant increase in N_4 (by ~1-3 %), considering the ±0.5 % N_4 error typically associated with fitting ^{11}B MAS NMR spectra. These results are consistent with recent literature on aluminoborate and boroaluminosilicate glass compositions,[44,45] which observe that when the glass comes in contact with water (either from solution or from the atmosphere) increases in the fraction of tetrahedral B occurs near the glass surface. Generally, in the present study, samples that dissolved at faster rates exhibited larger increases in N_4 than samples which dissolved more slowly; thus, more reaction progress leads to larger average B coordination changes. For instance, 0.01 M pH = 8 solutions showed nearly 3 % decreases in N_4, while 0.01 M pH = 8 solutions decreased by only 1.3 %. Furthermore, B coordination changes were relatively independent of acid identity used. This finding suggests either that: (i) BO_3 units are preferentially hydrolyzed and released from the glass in comparison to BO_4 or (ii) that amorphous tetrahedral boron units exist near the glass surface as either adsorbed or precipitated species. In addition to the changes in relative BO_3/BO_4 peak intensities upon glass dissolution, slight changes in the shape of the BO_4 peak of recovered samples are observed, with trends indicating the rise in an upfield shoulder peak (of varying magnitude, depending on the solution environment). This shoulder likely indicates the existence of higher fractions of BO_4 species with 4Si neighbors (near in comparison to species with 3Si/1B neighbors.[29] This may indicate that BO_4 species that are “trapped” within a fully silicate network demonstrate a relative inability to be hydrolyzed and released into solution, as compared to either BO_3 species or BO_4 bonded to at least one other B.

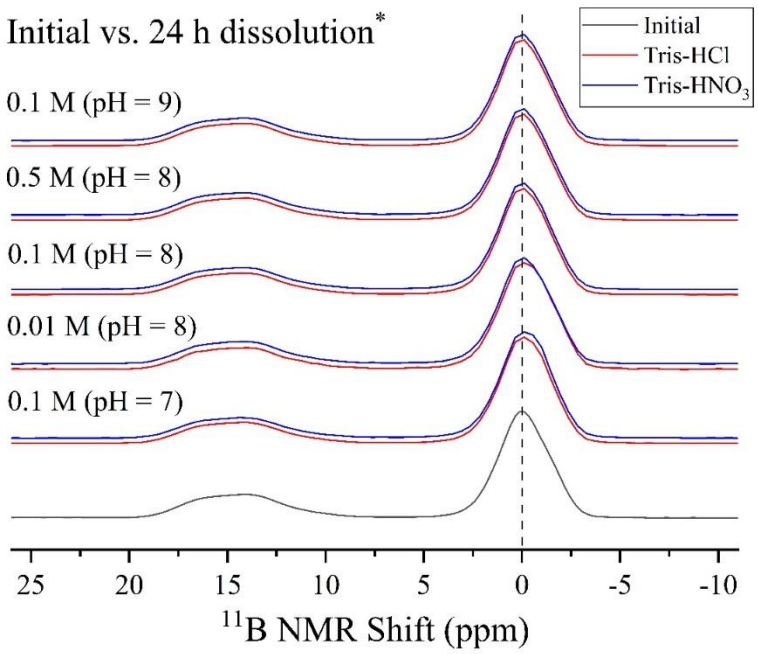

Figure 6.7. *^{11}B MAS NMR spectra of powders recovered from 24 h of selected dissolution experiments. *Denotes that the powders were recovered from 12 h experiments.*

In an attempt to understand the identity of dissolved boron species as a result of glass dissolution processes (i.e. H_3BO_3 vs. Tris-boron complexes), recovered solution aliquots were analyzed via ^{11}B NMR. It should be noted that although the identity of dissolved B species is being probed in solution environments, these species may initially form either near the glass surface or merely after boron is released into the surrounding solution. The NMR experiments were performed at both room temperature and 65 °C; the latter temperature was selected to reproduce the glass submersion conditions and the evolving solution environment in the performed dissolution experiments, to identify the dissolved species resulting from glass dissolution processes.

Figure 6.8a displays ^{11}B spectra of selected solutions at 25 °C, which have been compared to a solution utilized as a reference medium: an equivalent mixture of a 0.1 M H_3BO_3 solution (adjusted to pH = 8 with NaOH) and a 0.1 M Tris-HCl (pH = 8) solution.[22]

This solution mixture, which has a Tris/B = 1 ratio, displays peaks in two main regions, (i) an intense sharp peak associated with H_3BO_3 (near 19.0 ppm) and (ii) two additional sharp peaks at in the range 0.6-1.2 ppm. The peaks observed in our reference medium notably show consistency with an identical solution mixture (pH = 7.5) in the study by Tournié et al.,[22] where the upfield peaks depicted were attributed to Tris-boron complexes. While the attributed H_3BO_3 and Tris-boron complex peaks in our reference sample do not show direct chemical shift alignment with those in the previous study (~22 and ~4 ppm, respectively[22]), the ~18 ppm chemical shift difference between H_3BO_3 and the Tris-boron complex peaks is, however, observed in both studies. Thus, we attribute these peaks to the same aqueous species as discussed by Tournié et al.[22] The solutions recovered from selected dissolution experiments are also pictured in Figure 6.8a. These solutions, interestingly, consist of either one or two sharp peaks at 0.5-0.6 and 1.1-1.2 ppm of varying intensities (typical of Tris-boron complexes) and are marked by the absence of clear H_3BO_3 peaks (except for 0.1 M Tris-HNO_3 at pH = 7). This finding signifies that, at room temperature, dissolved boron from the glass exists predominantly as Tris-boron complexes as opposed to boric acid species.

Figure 6.8b, on the other hand, depicts ^{11}B spectra of the same solutions at 65 °C (the temperature at which dissolution experiments were performed). These spectra have also been compared to the same 1:1 Tris/B mixture as described above. At 65 °C, the Tris/B mixture at pH = 8 solely displays a peak associated with H_3BO_3 centered near 19.7 ppm. However, this spectrum notably lacks any additional peaks associated with Tris-boron complexes, which were observed in all samples at room temperature. Similarly, the spectra of liquid aliquots recovered from 24 h of dissolution experiments (examined at 65 °C) also

lack Tris-boron complex peaks in the range 0.5-1.2, rather displaying only one peak associated with H_3BO_3 species (in the range 19.4-19.8 ppm). This key difference between ^{11}B NMR spectra acquired at room temperature and 65 °C implies that while Tris-boron complexes which were found to be stable at lower temperatures, dissolved boric acid species exist in place of Tris-boron complexes at higher temperatures.

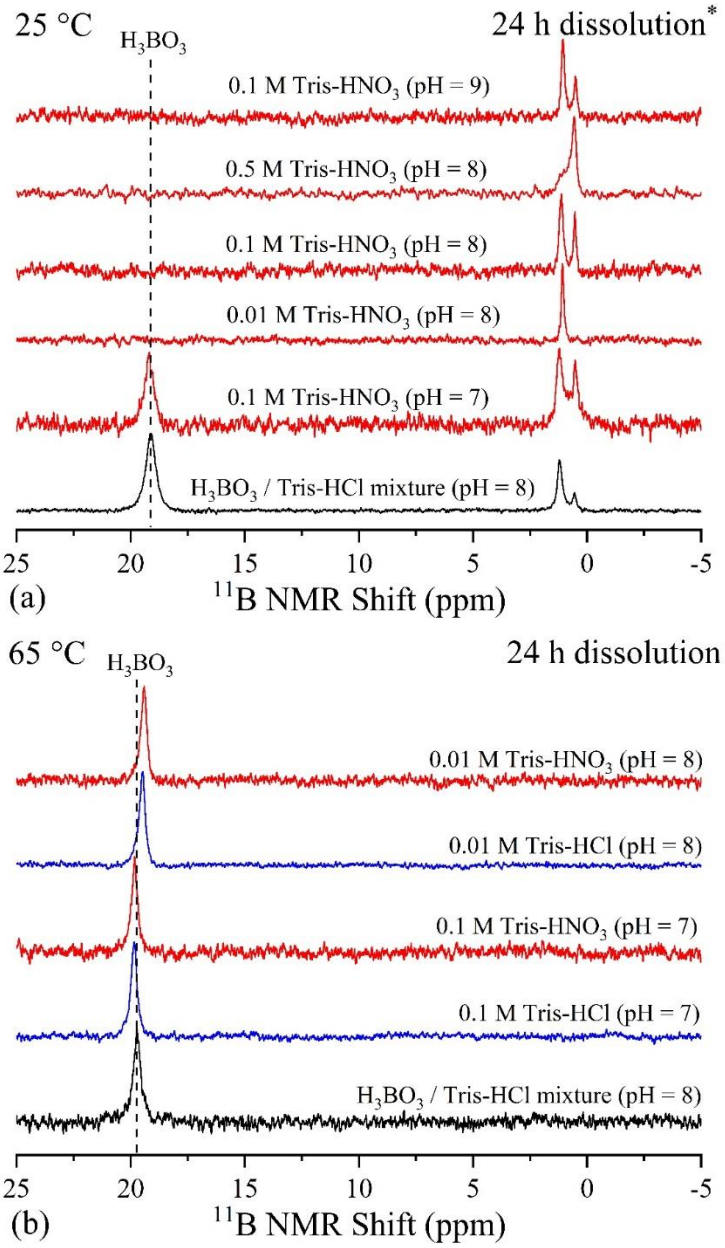

Figure 6.8. *^{11}B liquid NMR of liquid aliquots recovered from 24 h of dissolution experiments. *Denotes that the solutions were recovered from 12 h experiments.*

The absence of peaks associated with Tris-boron complexes from both experimentally recovered solutions and prepared mixtures at 65 °C is particularly intriguing since this temperature coincides with experimental dissolution conditions. This nonexistence may indicate that, in the studied conditions, zero or negligible concentrations of Tris-boron complexes are present in solution, even in samples with higher reaction progress (liquids recovered from dissolution experiments approaching the residual rate regime). Thus, even though the presence of Tris-boron complexes was determined to be extensive at room temperature, their absence in higher temperature conditions may indicate that the formation of Tris-boron complexes does not serve as the primary mechanism governing dissolution behavior of borosilicate glasses in Tris-based solutions in elevated temperatures.

It should also be noted that only spectra of selected solutions are shown in Figure 6.8b since these spectra were able to display resolved boric acid peaks. Tris-HCl and Tris-HNO_3 solution aliquots from 0.1 M Tris (pH = 8 and 9) and 0.5 M Tris (pH = 8) dissolution experiments were similarly attempted; however, the low ppm concentrations of aqueous ^{11}B nuclei in these samples were below detection limits necessary to resolve and identify dissolved boron species. Therefore, at present, we cannot comment on the dissolved species removed from glass submerged in these solutions.

6.4 Discussion

It is generally agreed in the glass community that Tris-based buffer solutions adversely affect the dissolution of boron-containing glasses due to Tris-boron complexation, which is hypothesized to accelerate the release of glassy products from the

sample surface. However, this consensus is largely attributed to a single study that observed (i) Tris-boron complexes in 1:1 Tris/B solution mixtures and (ii) significant forward rate acceleration for a sodium borosilicate glass in Tris-based solutions vs. Tris-free solutions.[22] However, many aspects of Tris–glass interactions are still uncertain, for instance, how does the concentration of the Tris/acid mixture impact dissolution behavior? Furthermore, does the acid identity play a role in the altered dissolution kinetics?

The present study aims to address these questions by investigating the dissolution behavior of a sodium borosilicate composition in a range of aqueous environments, in which the impacts of acid identity, Tris molarity, and solution pH were each examined. Contrary to the findings by Tournié et al.,[22] which displayed 2× quicker elemental release in Tris-HCl as compared to Tris-HNO_3, the present contribution does not illustrate significant differences in dissolution behavior based on acid identity. This is evidenced by the close overlap in elemental release behavior between 0.1 M Tris-HCl and 0.1 M Tris-HNO_3 solutions, as displayed at pH = 7 – 9 in Figure 6.6. Furthermore, all estimated forward rates (Tris-HCl vs. Tris-HNO_3) displayed close agreement, well within the generally accepted error limits while assessing dissolution behavior.[38-40] Thus, our findings indicate that the acid identity does not greatly impact borosilicate dissolution behavior in Tris buffer solutions.

Further, glass dissolution kinetics were investigated at pH = 8 in Tris molarities varying from 0.01 – 0.5 M. As anticipated, higher Tris molarities were more effective in buffering the solution pH, as ≥0.1 M Tris-based solutions maintained pH within ±0.1 after 24 h of dissolution experiments. Conversely, it is observed that increasing the Tris molarity from 0.01 to 0.5 M results in reductions in the extent of elemental release, as is particularly

evident from the contrast between 0.01-0.1 M Tris solutions and 0.3-0.5 M solutions (see Figure 6.5). It is inferred from these results that the substantial presence of dissolved species in 0.3 and 0.5 M solutions provokes solution feedback effects, suppressing the extent of glass dissolution. According to these results, it is deduced that the ideal Tris concentration required to provide a balance between (i) optimal buffering ability and (ii) minimally impacting dissolution kinetics is ~0.1 M Tris, independent of acid identity (Tris-HCl vs. Tris-HNO_3). This value corresponds well with the recommended Tris concentration as discussed in ISO 10993-14 for studying biomaterials.

In addition to examining the impact of Tris solution chemistry upon dissolution behavior, ^{11}B liquid NMR is investigated for recovered solution aliquots in an attempt to understand the mechanism of Tris–glass interaction and confirm the presence of Tris-B complexes. In accordance with the findings by Tournié et al.,[22] Tris-B complex presence is confirmed in the examined solution aliquots. Interestingly, these species are observed to demonstrate clear temperature-dependence, marked by omnipresence in aliquots at room temperature and complete absence in the same aliquots at 65 ºC. Rather, NMR experiments at elevated temperatures indicate that Tris-B complexes are unstable due to the lone presence of boric acid species. This unanticipated temperature-dependence of Tris-boron complexation requires further examination using *in situ* NMR spectroscopy to further examine the mechanisms by which Tris-based solutions impact borosilicate glass dissolution behavior and kinetics.

6.5 Conclusions

In the present study, a sodium borosilicate glass was examined for its dissolution behavior in a wide range of Tris-based solutions. The results have been discussed with

reference to previous studies on this topic and the conclusions from this study were threefold: (i) acid identity does not greatly impact dissolution behavior in Tris-based solutions, (ii) ~0.1 M Tris-based solutions are ideal for sustaining solution pH in the absence of clear adverse solution chemistry effects, and (iii) Tris-boron complexes form as a result of glass dissolution processes, however, these species exhibit a clear temperature-dependence and require further study to unearth the mechanisms by which Tris-based solutions impact dissolution behavior of borosilicate glasses.

Supplementary Information

The supplementary information of this manuscript contains XRD patterns of the as-synthesized glass, in addition to the full set of raw elemental release data.

References

1. Macon, A. L. B.; Kim, T. B.; Valliant, E. M.; Goetschius, K.; Brow, R. K.; Day, D. E.; Hoppe, A.; Boccaccini, A. R.; Kim, I. Y.; Ohtsuki, C.; Kokubo, T.; Osaka, A.; Vallet-Regi, M.; Arcos, D.; Fraile, L.; Salinas, A. J.; Teixeira, A. V.; Vueva, Y.; Almeida, R. M.; Miola, M.; Vitale-Brovarone, C.; Verne, E.; Holand, W.; Jones, J. R., A unified in vitro evaluation for apatite-forming ability of bioactive glasses and their variants. *Journal of Materials Science-Materials in Medicine* 2015, *26* (2).
2. Hoppe, A.; Gueldal, N. S.; Boccaccini, A. R., A review of the biological response to ionic dissolution products from bioactive glasses and glass-ceramics. *Biomaterials* 2011, *32* (11), 2757-2774.
3. Gorustovich, A.; Guglielmotti, M. B.; Lopez, J. M. P.; Cabrini, R. L., Increased osteogenesis elicited by boron-modified bioactive glass particles in the SiO2-CaO-P2O5-Na2O system: A histomorphometric study in rats. *Bioceramics, Vol 17* 2005, *284-286*, 913-916.
4. Bohner, M.; Lemaitre, J., Can bioactivity be tested in vitro with SBF solution? *Biomaterials* 2009, *30* (12), 2175-2179.
5. O'Donnell, M. D.; Hill, R. G., Influence of strontium and the importance of glass chemistry and structure when designing bioactive glasses for bone regeneration. *Acta Biomaterialia* 2010, *6* (7), 2382-2385.
6. Rohanová, D.; Boccaccini, A. R.; Yunos, D. M.; Horkavcová, D.; Březovská, I.; Helebrant, A., TRIS buffer in simulated body fluid distorts the assessment of glass–ceramic scaffold bioactivity. *Acta biomaterialia* 2011, *7* (6), 2623-2630.
7. Horkavcová, D.; Rohanová, D.; Stříbny, A.; Schuhladen, K.; Boccaccini, A. R.; Bezdička, P., Interaction of MOPS buffer with glass–ceramic scaffold: Effect of (PO4) 3− ions in SBF on kinetics and morphology of formatted hydroxyapatite. *Journal of Biomedical Materials Research Part B: Applied Biomaterials* 2019.
8. Rohanová, D.; Horkavcova, D.; Paidere, L.; Boccaccini, A. R.; Bozděchová, P.; Bezdička, P., Interaction of HEPES buffer with glass-ceramic scaffold: Can HEPES replace TRIS in SBF? *Journal of Biomedical Materials Research Part B: Applied Biomaterials* 2018, *106* (1), 143-152.
9. Gomori, G., Buffers in the Range of pH 6.5 to 9.6. *Proceedings of the Society for Experimental Biology and Medicine* 1946, *62* (1), 33-34.
10. Kirste, G.; Brandt-Slowik, J.; Bocker, C.; Steinert, M.; Geiss, R.; Brauer, D. S., Effect of chloride ions in Tris buffer solution on bioactive glass apatite mineralization. *International Journal of Applied Glass Science* 2017, *8* (4), 438-449.
11. Pierce, E. M.; Reed, L. R.; Shaw, W. J.; McGrail, B. P.; Icenhower, J. P.; Windisch, C. F.; Cordova, E. A.; Broady, J., Experimental determination of the effect of the ratio of B/Al on glass dissolution along the nepheline (NaAlSiO4)–malinkoite (NaBSiO4) join. *Geochimica et Cosmochimica Acta* 2010, *74* (9), 2634-2654.
12. Pierce, E. M.; Rodriguez, E. A.; Calligan, L. J.; Shaw, W. J.; Pete McGrail, B., An experimental study of the dissolution rates of simulated aluminoborosilicate waste glasses as a function of pH and temperature under dilute conditions. *Applied Geochemistry* 2008, *23* (9), 2559-2573.
13. Goel, A.; Kapoor, S.; Tilocca, A.; Rajagopal, R. R.; Ferreira, J. M. F., Structural role of zinc in biodegradation of alkali-free bioactive glasses. *Journal of Materials Chemistry B* 2013, *1* (24), 3073-3082.

14. Icenhower, J. P.; McGrail, B. P.; Shaw, W. J.; Pierce, E. M.; Nachimuthu, P.; Shuh, D. K.; Rodriguez, E. A.; Steele, J. L., Experimentally determined dissolution kinetics of Na-rich borosilicate glass at far from equilibrium conditions: Implications for Transition State Theory. *Geochimica et Cosmochimica Acta* 2008, *72* (12), 2767-2788.
15. Goel, A.; Rajagopal, R. R.; Ferreira, J. M., Influence of strontium on structure, sintering and biodegradation behaviour of CaO-MgO-SrO-SiO(2)-P(2)O(5)-CaF(2) glasses. *Acta Biomater* 2011, *7* (11), 4071-80.
16. Kapoor, S.; Goel, A.; Tilocca, A.; Dhuna, V.; Bhatia, G.; Dhuna, K.; Ferreira, J. M., Role of glass structure in defining the chemical dissolution behavior, bioactivity and antioxidant properties of zinc and strontium co-doped alkali-free phosphosilicate glasses. *Acta Biomater* 2014, *10* (7), 3264-78.
17. Kinoshita, M.; Harada, M.; Sato, Y.; Hariguchi, Y., Percolation Phenomenon for Dissolution of Sodium Borosilicate Glasses in Aqueous Solutions. *Journal of the American Ceramic Society* 1991, *74* (4), 783-787.
18. Ebert, W. L. *The effects of the glass surface area/solution volume ratio on glass corrosion: a critical review*; Argonne National Laboratory: 1995.
19. Hlavac, J.; Rohanova, D.; Helebrant, A., The effect of tris-buffer on the leaching behaviour of bioactive glass-ceramics. *CERAMICS SILIKATY* 1994, *38*, 119-119.
20. Rahaman, M. N.; Day, D. E.; Bal, B. S.; Fu, Q.; Jung, S. B.; Bonewald, L. F.; Tomsia, A. P., Bioactive glass in tissue engineering. *Acta Biomaterialia* 2011, *7* (6), 2355-2373.
21. Huang, W. H.; Day, D. E.; Kittiratanapiboon, K.; Rahaman, M. N., Kinetics and mechanisms of the conversion of silicate (45S5), borate, and borosilicate glasses to hydroxyapatite in dilute phosphate solutions. *Journal of Materials Science-Materials in Medicine* 2006, *17* (7), 583-596.
22. Tournié, A.; Majérus, O.; Lefèvre, G.; Rager, M. N.; Walmé, S.; Caurant, D.; Barboux, P., Impact of boron complexation by Tris buffer on the initial dissolution rate of borosilicate glasses. *Journal of Colloid and Interface Science* 2013, *400*, 161-167.
23. Manara, D.; Grandjean, A.; Neuville, D. R., Structure of borosilicate glasses and melts: A revision of the Yun, Bray and Dell model. *Journal of Non-Crystalline Solids* 2009, *355* (50–51), 2528-2531.
24. Mazurin, O.; Streltsina, M.; Shvaiko-Shvaikovskaya, T., Sci Glass-6.5 (Glass Property Information System). *Institute of Theoretical Chemistry, Shrewsbury, MA, USA* 2005.
25. Stone-Weiss, N.; Pierce, E. M.; Youngman, R. E.; Gulbiten, O.; Smith, N. J.; Du, J.; Goel, A., Understanding the structural drivers governing glass–water interactions in borosilicate based model bioactive glasses. *Acta Biomater* 2018, *65* (Supplement C), 436-449.
26. Massiot, D.; Fayon, F.; Capron, M.; King, I.; Le Calvé, S.; Alonso, B.; Durand, J. O.; Bujoli, B.; Gan, Z.; Hoatson, G., Modelling one-and two-dimensional solid-state NMR spectra. *Magnetic Resonance in Chemistry* 2002, *40* (1), 70-76.
27. Massiot, D.; Bessada, C.; Coutures, J.; Taulelle, F., A quantitative study of 27Al MAS NMR in crystalline YAG. *Journal of Magnetic Resonance (1969)* 1990, *90* (2), 231-242.
28. Feller, S. A.; Kottke, J.; Welter, J.; Nijhawan, S.; Boekenhauer, R.; Zhang, H.; Feil, D.; Parameswar, C.; Budhwani, K.; Affatigato, M. In *Physical properties of alkali*

borosilicate glasses, Proceedings of the Second International Conference on Borate Glasses, Crystals, and Melts, Abingdon, United Kingdom, Sheffield (United Kingdom): The Society of Glass Technology: 1997; pp 246-253.
29. Du, L.-S.; Stebbins, J. F., Nature of Silicon−Boron Mixing in Sodium Borosilicate Glasses: A High-Resolution 11B and 17O NMR Study. *The Journal of Physical Chemistry B* 2003, *107* (37), 10063-10076.
30. Yun, Y. H.; Bray, P. J., Nuclear magnetic resonance studies of the glasses in the system Na2O-B2O3-SiO2. *Journal of Non-Crystalline Solids* 1978, *27* (3), 363-380.
31. Dell, W. J.; Bray, P. J.; Xiao, S. Z., 11B NMR studies and structural modeling of Na2O-B2O3-SiO2 glasses of high soda content. *Journal of Non-Crystalline Solids* 1983, *58* (1), 1-16.
32. Bray, P. J., Structural models for borate glasses. *Journal of Non-Crystalline Solids* 1985, *75* (1-3), 29-36.
33. Bunker, B. C., Molecular mechanisms for corrosion of silica and silicate glasses. *Journal of Non-Crystalline Solids* 1994, *179*, 300-308.
34. Hopf, J.; Eskelsen, J. R.; Chiu, M.; Ievlev, A.; Ovchinnikova, O. S.; Leonard, D.; Pierce, E. M., Toward an understanding of surface layer formation, growth, and transformation at the glass–fluid interface. *Geochimica et Cosmochimica Acta* 2018, *229*, 65-84.
35. Vienna, J. D.; Ryan, J. V.; Gin, S.; Inagaki, Y., Current Understanding and Remaining Challenges in Modeling Long-Term Degradation of Borosilicate Nuclear Waste Glasses. *International Journal of Applied Glass Science* 2013, *4* (4), 283-294.
36. Kragten, J., Tutorial review. Calculating standard deviations and confidence intervals with a universally applicable spreadsheet technique. *Analyst* 1994, *119* (10), 2161-2165.
37. Stone-Weiss, N.; Youngman, R. E.; Thorpe, R.; Smith, N. J.; Pierce, E. M.; Goel, A., An insight into the corrosion of alkali aluminoborosilicate glasses in acidic environments. *Submitted* 2019.
38. Ebert, W. L. *Comparison of the results of short-term static tests and single-pass flow-through tests with LRM glass (ANL-06/51)*; Argonne National Laboratory: Argonne, IL, USA, 2006.
39. Gin, S.; Frugier, P.; Jollivet, P.; Bruguier, F.; Curti, E., New Insight into the Residual Rate of Borosilicate Glasses: Effect of S/V and Glass Composition. *International Journal of Applied Glass Science* 2013, *4* (4), 371-382.
40. Fournier, M.; Ull, A.; Nicoleau, E.; Inagaki, Y.; Odorico, M.; Frugier, P.; Gin, S., Glass dissolution rate measurement and calculation revisited. *Journal of Nuclear Materials* 2016, *476*, 140-154.
41. Hamilton, J. P.; Brantley, S. L.; Pantano, C. G.; Criscenti, L. J.; Kubicki, J. D., Dissolution of nepheline, jadeite and albite glasses: toward better models for aluminosilicate dissolution. *Geochimica et Cosmochimica Acta* 2001, *65* (21), 3683-3702.
42. Blum, A. E.; Lasaga, A. C., The role of surface speciation in the dissolution of albite. *Geochimica et Cosmochimica Acta* 1991, *55* (8), 2193-2201.
43. Brady, P. V.; Walther, J. V., Kinetics of quartz dissolution at low temperatures. *Chemical geology* 1990, *82*, 253-264.
44. Kapoor, S.; Youngman, R. E.; Zakharchuk, K.; Yaremchenko, A.; Smith, N. J.; Goel, A., Structural and Chemical Approach toward Understanding the Aqueous Corrosion

of Sodium Aluminoborate Glasses. *The Journal of Physical Chemistry B* 2018, *122*, 10913-10927.

45. Schaut, R. A.; Lobello, R. A.; Mueller, K. T.; Pantano, C. G., Characterization of boroaluminosilicate glass surface structures by B K-edge NEXAFS. *Journal of Non-Crystalline Solids* 2011, *357* (19), 3416-3423.

Chapter 7. Conclusions

The chemical durability of glass is a topic that, while being actively important for identifiable applications such as nuclear waste containment and bioactive glasses, is imperative to understand for predicting the long-term performance of both everyday and cutting-edge technological glass applications. These glasses, however, typically have significant compositional and structural complexity which complicates the development of straightforward models to understand their chemical durability. Given the intricacy of this topic, it is of vital importance to develop an understanding of *composition-structure-chemical durability* relationships in multicomponent oxide glass systems, since chemical durability is highly dependent upon both glass chemistry and its structure at the atomic level. The focus of this research has been to understand these relationships in ternary and quaternary glass systems and addressing some of the remaining fundamental challenges / open questions relating to glass corrosion. Accordingly, glasses designed in the Na_2O-B_2O_3-SiO_2, Na_2O-Al_2O_3-B_2O_3-SiO_2, and Na_2O-P_2O_5-B_2O_3-SiO_2 systems have been the subject of these studies.

In the first study presented in this thesis on Na_2O-B_2O_3-SiO_2 glasses, an attempt has been made to discuss the experimental challenges that need to be carefully navigated to unearth the mechanisms governing the dissolution behavior and kinetics of boron-containing bioactive glasses. It has been shown that the methodology of quenching of the glass melt impacts the dissolution rate of the studied glasses by 1.5× to 3× times (in the studied glass system) in water depending on the changes induced in their molecular structure due to variation in thermal history. The approach proposed to study the dissolution of boron-containing bioactive glasses—which includes maintaining consistent

thermal history, uniform glass particle size range, and following SA/V approach—allows us to gain a new level of conceptual understanding about the composition–structure–property relationships in these glass systems which can be applied to attain a significant leap in designing bioactive glasses with controlled dissolution rates tailored for specific patient and disease states.

The studies of the Na_2O-Al_2O_3-B_2O_3-SiO_2 glass system presented in this thesis has attempted to understand the mechanisms governing corrosion of glasses in acidic environments. Accordingly, it has been shown in pH = 2 environments that, although stepwise addition of B_2O_3 into the glass causes non-linear changes in network structural characteristics—i.e. T_g and fractions of AlO_5/BO_4 in the glass—noticeably linear increases in forward dissolution rates are observed. The results imply that dissolution–re-precipitation processes occur at the glass–fluid interface in both B_2O_3-rich and SiO_2-rich glass compositions, notwithstanding vastly different reaction kinetics. This investigation forms the basis for further study of the glass–fluid interface in wide-ranged glass compositions.

The studies of the Na_2O-P_2O_5-B_2O_3-SiO_2 system in this thesis combine the strengths of MAS NMR and MD studies to provides a comprehensive structural understanding of the short- and intermediate-range order in this system, and its evolution upon successive incorporation of P_2O_5, which effects a significant re-polymerization of the silicon species and a re-structuring of the borate component in the network, driven by the additional demand of phosphate for charge compensation. The detailed analysis of ^{31}P-^{11}B dipole-dipole and ^{31}P-^{31}P indirect spin-spin couplings on selected samples suggests a general picture of the NFU connectivities, which stands in excellent agreement with those

drawn from the MD simulations and expands significantly on previous findings on bioactive P_2O_5-containing silicate and borosilicate glasses.

A comprehensive study of the dissolution behavior of the above glasses has led to the conclusions that glass degradation behavior is predominantly driven by the *R* (Na/B) and *K* (Si/B) ratios, however, specific structural features (i.e. B^3/B^4, Si^3/Si^4, etc.) were determined to have marked impacts upon ionic release behavior. Ultimately, our extensive knowledge of this system will not only facilitate the prediction of structural details and degradation behavior for bioactive glass applications but will also help in identifying novel borosilicate glasses tuned to particular biomedical applications.

In the final study presented in this thesis on a Na_2O-B_2O_3-SiO_2 glass, the impact of Tris-buffer solution was examined across a wide range of Tris-based solutions. It was concluded that: (i) acid identity does not greatly impact dissolution behavior in Tris-based solutions, (ii) ~0.1 M Tris-based solutions are ideal for sustaining solution pH in the absence of clear adverse solution chemistry effects, and (iii) Tris-boron complexes form as a result of glass dissolution processes, however, these species demonstrate a clear temperature-dependence which necessities further study to unearth the mechanisms by which Tris-based solutions interact with borosilicate glasses and impact dissolution behavior and kinetics.

Chapter 8. Recommendations for future work

Future work recommended which relates to this topic involves the expansion of our understanding of *composition-structure-chemical durability* relationships to a wider range of systems and composition-spaces. For instance, building upon the knowledge generated in this thesis research from the Na_2O-Al_2O_3-B_2O_3-SiO_2 and Na_2O-P_2O_5-B_2O_3-SiO_2 systems to expand to the Na_2O-Al_2O_3-P_2O_5-B_2O_3-SiO_2 systems or extending our understanding to B_2O_3-rich Na_2O-P_2O_5-B_2O_3-SiO_2 glasses can significantly the enlarge the composition-space in which chemical dissolution behavior is well-understood for developing novel applications. Furthermore, developing a comprehensive knowledge of the chemical durability of common mixed network-former systems can provide the dataset necessary for generating quantitative structure-property relationships (QSPR) in which chemical dissolution behavior can be predicted based upon the glass composition. Additional recommendations for future work include developing a deeper understanding of the fundamental mechanisms of glass corrosion using *in situ* and/or high resolution studies of the reactive interface and gel layer. Techniques which can supplement our current knowledge are Raman spectroscopy, X-ray absorption near edge structure (XANES) spectroscopy, low energy ion scattering (LEIS) spectroscopy, time-of-flight secondary ion mass spectrometry (ToF-SIMS), atomic force microscopy (AFM), and liquid-state NMR.